Non-Collinear Magnetism in Fe on W(110)

Angularly Resolved Real-Space Imaging and Micromagnetic Data Analysis

Dissertation
zur Erlangung des Doktorgrades
am Fachbereich Physik
der Universität Hamburg

vorgelegt von
Dipl.-Phys. Stefan Meckler
aus Freiburg

Hamburg
2010

Gutachter der Dissertation:	Prof. Dr. Roland Wiesendanger Prof. Dr. Hans Peter Oepen
Gutachter der Disputation:	Prof. Dr. Roland Wiesendanger Prof. Dr. Robert L. Johnson
Datum der Disputation:	17.12.2010
Vorsitzender des Prüfungsausschusses:	Prof. Dr. Michael A. Rübhausen
Vorsitzender des Promotionsausschusses:	Prof. Dr. Jochen Bartels
Leiterin des Fachbereichs Physik:	Prof. Dr. Daniela Pfannkuche
Dekan der MIN-Fakultät:	Prof. Dr. Heinrich Graener

Inhaltsangabe

Spinpolarisierte Rastertunnelmikroskopie und Spektroskopie sind leistungsfähige Werkzeuge zur Untersuchung magnetischer Nanostrukturen mit atomarer Auflösung. Eine wesentliche Schwäche beider Messmethoden liegt jedoch in der nicht bzw. nur eingeschränkt gegebenen Möglichkeit winkelaufgelöster Messungen. Im Rahmen der vorliegenden Arbeit wird demonstriert, dass sich die genannten Methoden um das Element der Winkelauflösung erweitern lassen indem die Messungen im externen Feld eines Drei-Achsen-Vektormagneten durchgeführt werden.

Der im Rahmen der vorliegenden Arbeit entwickelte experimentelle Aufbau wird verwendet um erstmalig die magnetische Struktur einer Oberflächenspinspirale direkt im Realraum zu messen. Es wird gezeigt, dass der magnetische Grundzustand der Eisendoppellage auf der (110)-Oberfläche eines Wolfram-Einkristalls durch eine inhomogene rechtsdrehende zykloidale Spinspirale gegeben ist. Zur detaillierten Untersuchung der beteiligten magnetischen Wechselwirkungen wird ein umfassendes mikromagnetisches Modell vorgeschlagen, das neben magnetischem Austausch und Kristallanisotropie insbesondere die Dzyaloshinskii-Moriya-Wechselwirkung, dipolare Wechselwirkungen sowie die Inhomogenität der Spiralprofile berücksichtigt.

Im Unterschied zu allen zuvor diskutierten Modellen reproduziert das hier vorgeschlagene Modell alle derzeit bekannten experimentellen Beobachtungen bezüglich der Eisendoppellage auf Wolfram(110) widerspruchsfrei und quantitativ korrekt. Aus den Modellrechnungen ergibt sich insbesondere, dass der beobachtete Spiralzustand durch das Zusammenwirken der Dzyaloshinskii-Moriya-Wechselwirkung und dipolarer Effekte induziert wird. Darüber hinaus liefert das Modell eine Erklärung der experimentell beobachteten Temperaturabhängigkeit des Spinspiralzustands sowie dessen Verschwinden in schmalen Eisendoppellagenstreifen.

Im letzten Teil der Arbeit wird ein neuartiger bislang unbekannter zweidimensionaler magnetischer Grundzustand des kombinierten Systems aus Eisenmonolage und Eisendoppellage vorgestellt. Der Zustand unterscheidet sich aufgrund seiner nichttrivialen topologischen Struktur fundamental von der zuvor diskutierten Spinspirale. Es werden Ähnlichkeiten mit den kürzlich beobachteten magnetischen Skyrmiongittern diskutiert und weiterführende Experimente vorgeschlagen.

Abstract

Spin-polarized scanning tunneling microscopy (SP-STM) and spectroscopy (SP-STS) are powerful tools to investigate magnetic nanostructures down to the atomic scale. However, it appears as a fundamental limitation of these techniques that in the existing SP-STM setups the spatial orientation of the probed magnetic moments cannot be determined with full angular resolution. In this thesis it is demonstrated that this experimental limitation can be overcome and that angular resolution can be achieved in SP-STM and SP-STS experiments by operating the microscope in the magnetic field of a triple axes vector magnet.

The instrumental setup developed in the framework of this thesis is used to directly measure the magnetic structure of a surface spin spiral in real-space, for the first time. It is shown that the magnetic ground state of the iron double layer on the (110)-surface of a tungsten single crystal is an inhomogeneous right-rotating cycloidal spin spiral. For the detailed investigation of the relevant magnetic interactions a comprehensive micromagnetic model is suggested. Besides magnetic exchange and crystalline anisotropy this model accounts for the Dzyaloshinskii-Moriya interaction, dipolar interactions and the inhomogeneity of the spin spiral profiles.

In contrast to all previously discussed models the micromagnetic model suggested in this thesis reproduces all hitherto existing experimental observations concerning the iron double layer on the (110)-surface of a tungsten single crystal in a consistent and quantitatively correct way. In particular, the calculations imply that the observed spin spiral state is induced by the joint action of the Dzyaloshinskii-Moriya interaction and dipolar effects. In addition, the model explains the experimentally observed temperature dependence of the spin spiral state as well as its vanishing in narrow iron double layer stripes.

In the last part of this thesis a hitherto unknown two-dimensional magnetic ground state is presented for the combined system of iron mono layer and double layer areas. Due to its non-trivial topological structure this novel state is fundamentally different from the previously discussed spin spiral state. Similarities with the recently observed magnetic skyrmion lattices are discussed and possible subsequent experiments are suggested.

Contents

Introduction **1**

I SP-STM with angular resolution **7**

1 Scanning tunneling microscopy **9**
- 1.1 The tunnel effect 9
- 1.2 Experimental realization 11
- 1.3 The extended Tersoff-Hamann model 13
- 1.4 Spin-polarized scanning tunneling microscopy 18

2 Instrumental developments **25**
- 2.1 Motivation and design concept 25
- 2.2 Substrate cleaning and MBE growth facilities 27
- 2.3 Magnet cryostat and scanning tunneling microscope 30
- 2.4 Software control and automation 35
- 2.5 Demonstration of functionality 39

II The spin spiral in the Fe double layer on W(110) **41**

3 Spin spirals and classical domains **45**
- 3.1 Magnetic interactions in metallic thin films 45
- 3.2 Micromagnetic continuum model 50

4 Fe double layer on W(110): previous studies **67**
- 4.1 Topographic structure 67
- 4.2 Geometry dependence of the magnetic ground state 69
- 4.3 Field dependence of the spiral profile 71
- 4.4 Temperature dependence of the spiral state 71
- 4.5 The physical origin of the spiral state 74
- 4.6 Open questions 76

5 Real-space measurement of spiral type and rotational sense 79
5.1 Topography 79
5.2 The cycloidal character of the spin spiral 80
5.3 The rotational sense of the spin spiral 81
5.4 Homochirality 83

6 Infinitely extended Fe double layer films 85
6.1 Exchange stiffness and effective anisotropy 86
6.2 The Dzyaloshinskii-Moriya vector 88
6.3 Inhomogeneities of the demagnetizing field 97

7 Finite Fe double layer stripes 107
7.1 Extended micromagnetic model calculations 107
7.2 A simplified box model 118

III Two-dimensional complex spin textures in Fe/W(110) 131

8 Skyrmion-lattice-like spin textures 135
8.1 Previous studies 135
8.2 SP-STM experiments in the triple axes magnet 136
8.3 The complex topology of the observed spin texture 138
8.4 Driving forces of the complex spin topology 140
8.5 Measurement of the topological stability 143
8.6 Topological fields and topological Hall effect 146

Summary and perspectives 149

Bibliography 156

Publications 156

Conferences 156

Introduction

The history of magnetism dates back to around 600 B.C. when *Aristoteles* and *Thales* discussed the phenomenon that lodestone attracts other pieces of the same material as well as iron. At about the same time the ancient Indian surgeon, *Sushruta* used magnets for surgical purposes and the first reference to magnetism in Chinese literature is the *Book of the Devil Valley Master* dated to the 4th century B.C. Since then the understanding of magnetic phenomena improved considerably and numerous technical applications of magnetism have become part of our everyday life. For about 2500 years the world of magnetism seemed to be relatively simple since only two magnetic states could be observed in nature: magnetic and non-magnetic.

It was only in 1907 when the French physicist *Pierre-Ernest Weiss* discovered that magnetic materials are not necessarily magnetically homogeneous but can have an internal microscopic structure. Weiss found that this structure consists of small homogeneously magnetized so called *Weiss domains* that can collectively form a complex magnetic domain structure. The transition areas between any two neighboring domains are called domain walls. Under the influence of an external magnetic field the size of those domains being magnetized parallel to the field tends to grow at the expense of those domains being magnetized along other directions. In addition, the magnetization direction of individual domains may eventually be rotated into the direction of the external field. If the external magnetic field increases above a critical value, individual domain walls can annihilate, with neighboring domains being merged. The described process was first observed by the German physicist *Heinrich Barkhausen* in 1910. It is irreversible if the external magnetic field is switched off and thus explains the existence of magnetic remanence, the key property of magnetic materials during the 2500 year old history of magnetism. Although the existence of magnetic domains could explain many properties of magnetic materials the physical origin of magnetic order within the individual domains remained puzzling in classical physics. It could only be explained by introducing the concept of magnetic exchange interaction as a consequence of the quantum mechanical exclusion principle for fermionic particles first discussed by *Wolfgang Pauli* in 1925. Based on the described concept the relative orientations and typical sizes of magnetic domains could finally be explained as a consequence of competing magnetic exchange interaction and dipolar coupling. The magnetically easy axis was ascribed to the so-called magnetic anisotropy, that depends on the crystal structure, the macroscopic shape of a magnetic body, surface properties and various other factors.

With the development of modern spin sensitive imaging techniques, such as neutron scattering, x-ray absorption spectroscopy, magneto-optical techniques like magneto-optical Kerr microscopy, and scanning electron microscopy with polarization analysis the magnetic properties of various materials could be investigated with an ever increasing spatial resolution that finally reached the ultimate atomic limit with the advent of spin-polarized scanning tunneling microscopy (SP-STM) and spectroscopy

(SP-STS). In recent years SP-STM and SP-STS turned out to be extremely valuable tools for the experimental investigation of atomic scale magnetic surface structures. However, it comes as a major drawback of the technique that, due to the underlying contrast mechanism, the local magnetization direction at the sample surface can only be measured relative to the magnetization direction at the tip apex, which in general is an unknown experimental parameter. Luckily, the problem can be overcome at least partially by applying SP-STM and SP-STS in an external magnetic field being strong enough to align the tip magnetization. However, up to now there is no SP-STM setup where the external field can be applied along arbitrary spatial directions. Thus, in all previous experiments the direction of the tip magnetization could only be controlled partially. Consequently, the measurement of magnetic surface structures was hitherto not feasible with full angular resolution.

Part I of this thesis describes the design of a novel scanning tunneling microscope for SP-STM experiments in the external field of a triple axes vector magnet at a base temperature of 4.7 K. For the first time, the instrument allows SP-STM experiments in external magnetic fields of arbitrary direction. Consequently, the setup gives rise to a complete control of the magnetization direction of ferromagnetically coated probe tips. This extends the capabilities of SP-STM significantly since for the first time the local magnetization of the sample can be determined with respect to an external coordinate system and with full angular resolution along all spatial directions. In addition to the extended experimental capabilities the novel setup offers various options for automated substrate cleaning, data acquisition and data logging.

Part II addresses the detailed investigation of the magnetic structure of the iron (Fe) double layer (DL) on the (110)-surface of a tungsten (W) single crystal. Although this sample system was the subject of numerous experimental studies since the invention of SP-STM, many details of its magnetic ground state could not be determined due to the limitations of the technique as discussed above. Using the unique capabilities of the novel experimental setup described in Part I, these open questions can now be addressed. In particular, it is shown that the magnetic structure of the Fe DL on W(110) is a flat, inhomogeneous, and right-rotating cycloidal spin spiral with a spiral period of about 50 nm.

Before the advent of SP-STM there was consensus that the typical domain size in Fe DL films on W(110) can be expected to be on the order of several hundred nanometers or even micrometers, whereas smaller domain sizes cannot be explained by competing exchange interaction and dipolar stray fields. Thus, after the experimental discovery of the nanoscale magnetic domain structure the discussion became controversial. On the one hand, it was shown that a dipolar origin of the experimentally observed magnetic structure can be ruled out unambiguously on the basis of the observed magnetic field dependence of domain wall pairs, so-called 360° walls [1]. On the other hand, it was claimed that the observed domain structure is very well explained by competing magnetic dipolar interaction and magnetic exchange, as long as the magnetic exchange stiffness is small [2]. Unfortunately, the assumed weakness of the exchange stiffness is in contradiction to the previously measured magnetic field dependence. Nevertheless, even the domain wall direction was reproduced in Monte-Carlo simulations, with the additional assumption that the weak magnetic exchange stiffness is anisotropic. In order to account for the deficiency that none of the considered micromagnetic models could explain the observed unique rotational sense, and thus the spin spiral character of the magnetic ground state in the Fe DL on W(110), it was suggested to extend the considered micromagnetic models by the so-called Dzyaloshinskii-Moriya (DM) interaction, an antisymmetric magnetic interaction originating from spin-orbit coupling in the presence of the broken inversion symmetry at the sample's surface. The relevant micromagnetic parameter describing this interaction, the so called DM vector, was calculated using density functional theory (DFT) methods. Although, the respective calculations could indeed predict a right-rotating spiral type, the observed domain size in the nanometer regime could neither be reproduced nor ruled out due to numerical limitations [3]. In addition, the results of the DFT calculations are limited by the assumption of sinusoidal magnetic profiles and vanishing long-range dipolar interaction and the disregard of edge effects in Fe DL stripes of finite size.

In this thesis the previously discussed micromagnetic models are combined and extended in order to explicitly account for all potentially relevant interactions, arbitrary spiral profiles, and sample geometries of finite size. A unique set of all relevant model parameters (exchange stiffness, crystalline anisotropy, DM vector, and saturation magnetization) is determined by comparison to the experimental data. On the basis of the suggested micromagnetic model and the determined parameter set all experimental observations can for the first time be explained quantitatively in a mathematically consistent way. In particular, the model explains the experimentally observed vanishing of the spin spiral ground state at elevated temperatures as well as in narrow magnetic stripes.

Part III extends the discussion by considering the magnetic structure of the first atomic Fe layer on W(110) in addition to the previously investigated Fe DL areas. Using the experimental setup described in Part I, the magnetic ground state of the combined system of Fe monolayer (ML) and Fe DL on W(110) is measured. It is shown that for certain Fe coverages the magnetic structure in the Fe ML is strongly correlated to the spin spiral structure in the Fe DL. The observed correlations give rise to a complex two-dimensional spin configuration that is topologically non-trivial and can be described by the same skyrmion number as the recently observed magnetic skyrmion lattices in chiral bulk ferromagnets [4–6] and in the Fe ML on Ir(111) [7]. Two alternative mechanisms are suggested in order to explain the stabilization of the observed topologically non-trivial state. Finally, the topological stability of the observed two-dimensional spin configuration is discussed along with several experiments for its experimental confirmation. In addition, it is argued that, due to its topological complexity, the magnetic field resulting from the observed spin configuration may induce a topological Hall effect that may be measured in electronic transport experiments.

Part I

SP-STM with angular resolution

Chapter 1

Scanning tunneling microscopy

Scanning tunneling microscopy (STM) and spectroscopy (STS) provide insight into the structural and electronic properties of surfaces and nanostructures on surfaces with a resolution down to the atomic scale. For both techniques an atomically sharp metallic tip is brought into the proximity of an electrically conductive sample surface and a bias voltage is applied between sample and tip. At a distance of about 0.5 – 1.5 nm, i.e. without physical contact of sample and tip, one observes a measurable current due to the quantum mechanical tunneling effect that can be exploited for the investigation of the structural and electronic properties of the sample and even the tip electrode.

1.1 The tunnel effect

In the framework of a one dimensional model classical electrons can be described as particles moving in a potential landscape $U(z)$, with z being their spatial position. The total energy of the electron is given by the sum of its kinetic and its potential energy. Fig. 1.1 shows the one dimensional model case of an electron moving in a region of zero potential energy and approaching a potential barrier of height U_0 and width d.

$$\begin{array}{lll} \text{I:} & z < 0, & U(z) = 0 \\ \text{II:} & 0 \leq z \leq d, & U(z) = U_0 \\ \text{III:} & z > d, & U(z) = 0 \end{array} \tag{1.1}$$

Since the movement of classical particles is restricted to areas with $E \geq U(z)$ an electron moving in area I of the model potential can overcome the barrier only if its kinetic energy exceeds U_0. Otherwise it is reflected as illustrated in Fig. 1.1 (a). In quantum mechanics the situation is very different and the electron has a non-vanishing probability of tunneling through the potential barrier if $U_0 < \infty$, as depicted in Fig. 1.1 (b). This counter-intuitive behavior is a consequence of the fact that quantum mechanical objects, such as electrons, do not have a well defined spatial position as long as they are

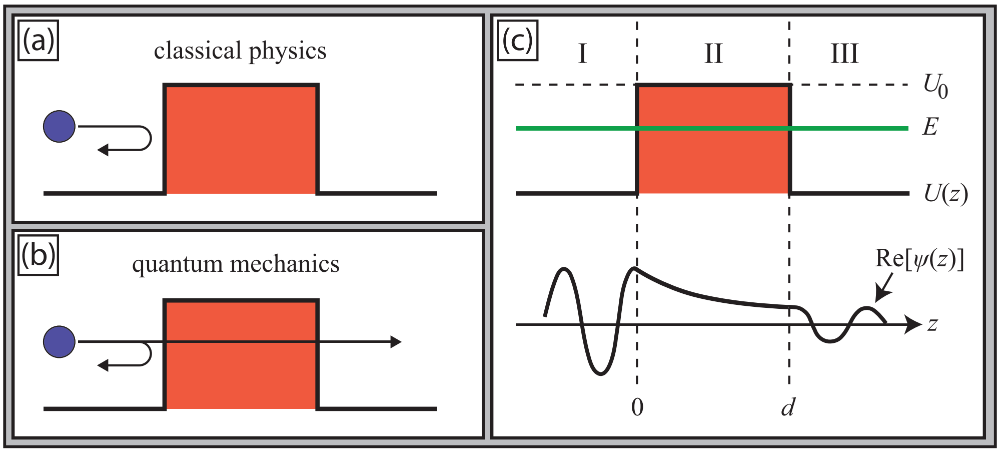

Figure 1.1: Behavior of a particle (blue) when hitting the box shaped potential barrier Eq. (1.1) (red). (a) In classical theory the particle is reflected if its energy is lower than the height of the barrier. (b) In quantum mechanics there is a finite probability T for the particle to tunnel through the barrier. The probability for the reflection is given by $R = 1 - T$. (c) The probability of the particle to be measured in the regions (I, II, III) is given by the square of the wave function $\psi(z)$, as visualized in the lower part of the panel.

not measured. Instead, their position is given by a probability distribution $P(z) = \psi(z)^2$ that can be calculated as a solution of the *Schrödinger* equation:

$$\left(-\frac{\hbar^2}{2m_\mathrm{e}}\frac{\mathrm{d}^2}{\mathrm{d}z^2} + U(z)\right)\psi(z) = E\psi(z)\,, \tag{1.2}$$

Here m_e is the electron mass, $\hbar$ is Planck's constant divided by 2π and $U(z)$ is the individual potential landscape where the electron is moving in. For a particle approaching the potential barrier from the left the solution of Eq. (1.2) is given by

$$\begin{array}{ll|l} \text{I:} & \psi_1 = \mathrm{e}^{\mathrm{i}kz} + r\cdot\mathrm{e}^{-\mathrm{i}kz} & k^2 = \frac{2m_\mathrm{e}E}{\hbar^2} \\ \text{II:} & \psi_2 = \alpha\mathrm{e}^{\kappa z} + \beta\mathrm{e}^{-\kappa z} & \kappa^2 = \frac{2m_\mathrm{e}(U_0-E)}{\hbar^2} \\ \text{III:} & \psi_3 = t\cdot\mathrm{e}^{\mathrm{i}kz} & \end{array} \tag{1.3}$$

In particular, the parameters r and t can now be related to the reflection and transmission probabilities $R = r^2$ and $T = t^2$, respectively. Since the total number of particles is conserved, R and T are related quantities:

$$R + T = 1. \tag{1.4}$$

Starting from Eq. (1.2)-(1.4), the transmission probability T is given by:

$$T = \frac{1}{1 + \frac{\left(k^2+\kappa^2\right)^2}{4k^2\kappa^2}\sinh^2(\kappa d)} \overset{\kappa d \gg 1}{\approx} \frac{16k^2\kappa^2}{\left(k^2+\kappa^2\right)^2} \cdot \mathrm{e}^{-2\kappa d}. \tag{1.5}$$

Here, k and κ are defined according to Eq. (1.3). The approximation is valid in the limit of large tunnel barriers. In the classical limit ($\hbar \to 0$) the transmission coefficient reduces to $T = 0$, in agreement with the classical particle behavior illustrated in Fig. 1.1 (a). According to Eq. (1.5) and the definition of k and κ in Eq. (1.3), the transmission probability T depends exponentially on the product of the barrier width d and the square root of the effective barrier height $U_0 - E$. In STM experiments, where the tunnel barrier is given by the vacuum gap between sample and tip, this exponential behavior results in a very high, i.e. exponential, sensitivity of the tunnel current to the tip-sample distance.

1.2 Experimental realization

In a scanning tunneling microscope (STM) a sharp conducting tip is approached to a conducting sample surface. At distances on the order of a few ångströms electrons can tunnel between sample and tip. With an applied bias voltage this results in a small net current. In the previous section it was shown on the basis of a very simple model that the tunnel current depends exponentially on the width of the tunnel barrier and thus the tip-sample distance. As a major consequence of this exponential dependence the tunnel current essentially flows between the frontmost atom of the tip and the sample atom right underneath, i.e the tunnel current is very much localized. This explains the high spatial resolution of an STM down to the ultimate limit of atomic resolution. The detection of variations in the tip-sample distance via the measurement of the tunnel current is relatively simple. However, the precise positioning of the tip based on the obtained information is very challenging. Experimentally, this highly nontrivial task of adjusting the lateral and vertical position of the tip can be accomplished by an appropriate combination of piezoelectric actuators, which can be elongated and contracted by the application of suitable high-voltages. It was first accomplished by *Gerd Binnig* and *Heinrich Rohrer* in 1981 [8], a technological milestone, for which they were awarded the Nobel Prize in 1986.

Fig. 1.2 visualizes the set-up of a complete STM system schematically. On the left hand side the piezoelectric tube scanner with the tip and the sample are shown. The outer side of the tube scanner is covered by four electrode segments (x^+, x^-, y^+, y^-), whereas the inner side of the tube is contacted by a single electrode (z). By applying identical high voltages between the inner electrode and all outer electrodes the piezoelectric tube can be elongated and contracted depending on the polarity of the voltage. This allows for a precise z-positioning of the tip above the sample surface.

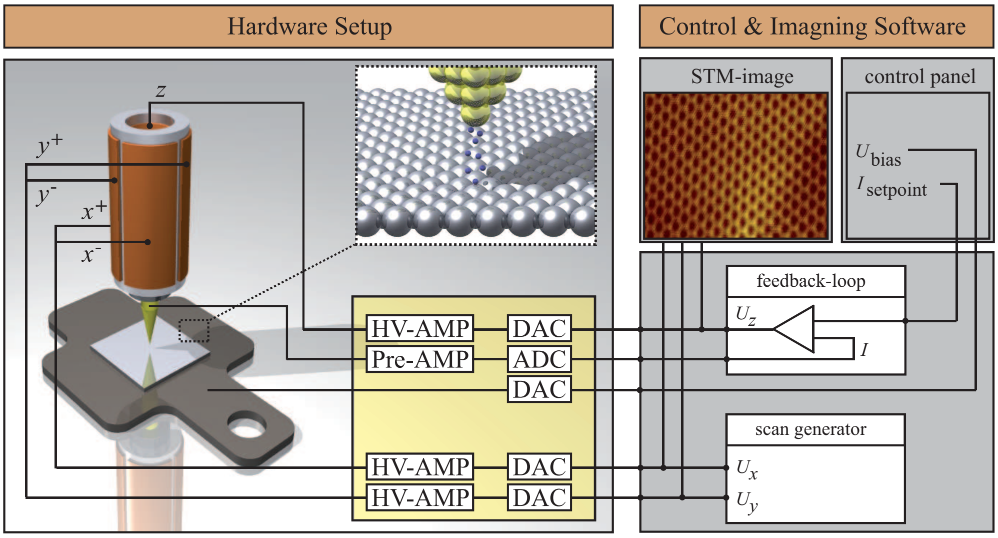

Figure 1.2: Principle of an STM experiment in constant current mode, as used for this thesis. The tip laterally scans across the sample surface controlled by the software based scan generator. During the scanning process the tunnel current is kept at a constant value I_{bias} using the feedback loop of the control software. At the interface between the microscope and the control software all currents and voltages are converted from analog to digital signals and vice versa using digital analog converters (DAC) and analog digital converters (ADC), respectively. In addition, the analog scanning voltages are amplified before they are applied to the piezos of the tube scanner. Finally, the sample surface is visualized by plotting U_z as a function of U_x and U_y.

Additionally, the tube can be bent along the x-direction by superimposing voltages of opposite polarity between z and x^+ and z and x^-, respectively. In an analogous way the tube can be bent along the y-axis. Consequently, the tip can be scanned laterally across the surface while adjusting the tip-sample distance. The right hand side of Fig. 1.2 visualizes the software concept for the data acquisition and the controlling of the tube scanner. The central modules of this software are a digital feedback-loop for the control of the z-voltage, a digital scan generator for the scanning voltages applied to the outer electrode segments of the tube scanner, a control panel for user inputs, and an imaging software. Since the control software is working on a digital basis and the STM is a purely analog device, an appropriate conversion and amplification electronics is needed as shown in the center of the figure. The abbreviations DAC and ADC stand for digital analog converter and analog digital converter, respectively.

Based on the measurement of the tunnel current during the scanning process, topographic image recording can be realized in two different data acquisition modes: *constant height* mode and *constant current* mode.

Constant height mode: In constant height mode the z-voltage is kept constant while the tip is being scanned across the sample surface, i.e the feedback-loop in the control software is switched off during scanning. The measured quantity is the tunnel current $I(x, y)$. It is usually visualized as a function of the tip position along the sample surface using two dimensional intensity maps.

Constant current mode: In constant current mode the tunnel current is kept constant by adjusting the tip-sample distance using the feedback-loop of the control software. Consequently, now the available information about the sample structure is contained in the z-coordinate $z(x, y)$ of the tip. Like the tunnel current in the constant height mode it can be visualized as a function of the tip coordinates along the sample surface using two dimensional intensity maps.

From a very general point of view both modes are equivalent since they are both based on the measurement of the tunnel current. However, from an experimental point of view the concept of constant-current imaging is preferable since tip crashes into the sample surface are effectively avoided due to the perpetual adjustment of the tip-sample distance.

1.3 The extended Tersoff-Hamann model

The simple textbook example of the quantum mechanical tunnel effect, as introduced in section 1.1, nicely explains the exponential dependence of the tunnel current on the tip-sample distance. However, it does not consider any influence of the electronic band structure at the sample and tip electrode. To account for this deficiency Bardeen [9] investigated the tunneling of electrons between two weekly coupled electrodes using first-order time-dependent perturbation theory. Following Bardeen's approach Tersoff and Hamann [10, 11] describe the tunnel process in an STM. Their model is based on four approximations:

- The tip wave function is spherically symmetric, i.e. it is of s-type.
- The tip's local density of states is a constant function of energy.
- The limit of small bias voltage and low temperature is considered.
- The work function of the tip and sample electrode are assumed to be equal.

The following discussion refers to the extension of the Tersoff-Hamann model by Lang [12], where the third and fourth approximations have been dropped.

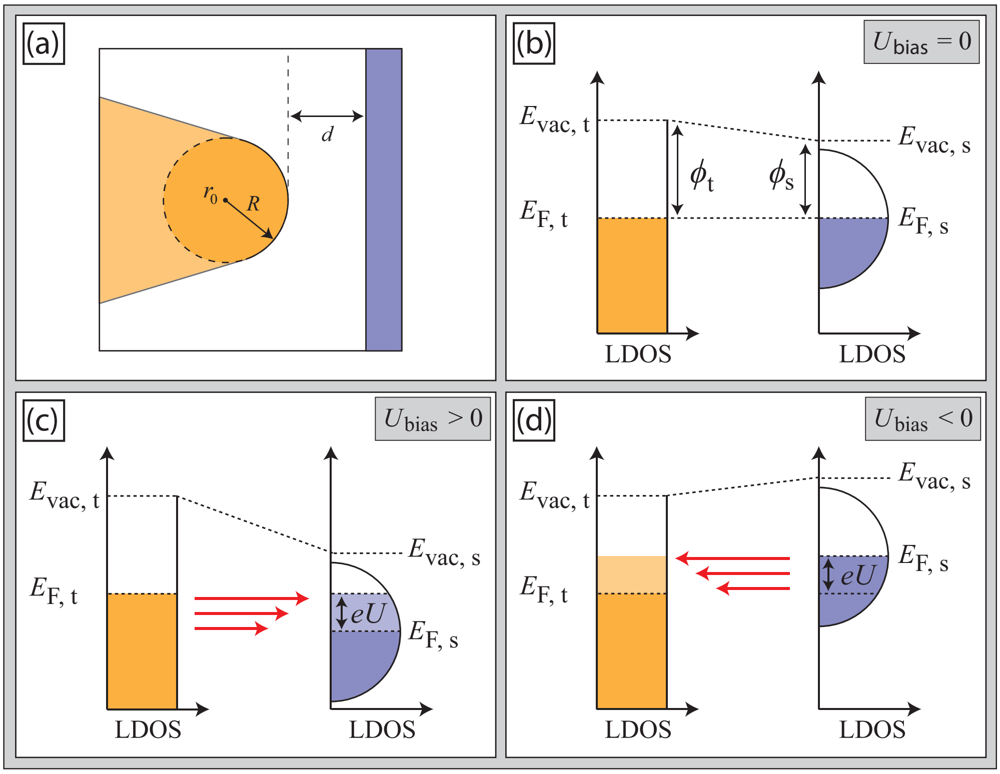
(a)
r_0
R
d
(b)
$U_{\text{bias}} = 0$
$E_{\text{vac, t}}$
$E_{\text{F, t}}$
ϕ_t
ϕ_s
$E_{\text{vac, s}}$
$E_{\text{F, s}}$
LDOS
LDOS
(c)
$U_{\text{bias}} > 0$
$E_{\text{vac, t}}$
$E_{\text{F, t}}$
$E_{\text{vac, s}}$
eU
$E_{\text{F, s}}$
LDOS
LDOS
(d)
$U_{\text{bias}} < 0$
$E_{\text{vac, t}}$
$E_{\text{F, t}}$
$E_{\text{vac, s}}$
$E_{\text{F, s}}$
eU
LDOS
LDOS

Figure 1.3: Vacuum tunneling in the extension to the Tersoff-Hamann-model by Lang [12]. (a) Schematic drawing of the tunnel geometry, with R being the effective tip radius, r_0 the center of curvature of the tip, and d is the tip-sample distance. (b-d) Energy level diagrams for $U_{\text{bias}} = 0$, $U_{\text{bias}} < 0$, and $U_{\text{bias}} > 0$, respectively. The red arrows in (b,d) visualize the tunneling electrons, with their length indicating the probability of tunneling, as defined by the transmission coefficient T.

Tunnel current and total density of states

According to the Tersoff-Hamann model and its extension by Lang [12], the tunnel current can be calculated based on the geometry of the tunnel junction given in Fig. 1.3 (a) and the energy level diagrams shown in (b-d) for three different bias voltage regimes. According to the given model assumptions, the local density of states (LDOS) at the tip is constant while the LDOS at the sample varies with energy as illustrated by the half spheres. At $U_{\text{bias}} = 0$ the Fermi energies of sample and tip become equal due to electron tunneling through the vacuum barrier in both directions (b). With positive sample bias the sample's LDOS is rigidly shifted into the direction of lower energies (c). Consequently, electrons can tunnel from occupied tip states into empty sample states as indicated by the red arrows. For negative sample bias the sample's LDOS is rigidly shifted into the direction of higher energies (d). Thus the direction of the tunnel current is reversed with respect to (c), i.e. now the electrons tunnel from occupied sample states into empty tip states.

Under the given model assumptions the tunnel current is given by

$$\begin{aligned} I\,(U) &\propto n_{\mathrm{t}} \cdot \int_{E_{\mathrm{F}}}^{E_{\mathrm{F}}+eU} n_{\mathrm{s}}\,(E') \cdot T_{(d,R)}\,(E', eU)\,\mathrm{d}E' \\ T_{(d,R)}\,(E, eU) &:= \mathrm{e}^{-2(d+|R|)\cdot\overline{\kappa}(E,eU)} \\ \overline{\kappa}\,(E, eU) &:= \sqrt{\frac{2m}{\hbar^2}\left(\frac{\phi_{\mathrm{t}}+\phi_{\mathrm{s}}}{2}+\frac{eU}{2}+E_{\mathrm{F}}-E\right)} \end{aligned} \tag{1.6}$$

Here, n_{t} is the LDOS of the tip and n_{s} is the LDOS of the sample. As mentioned before n_{t} is assumed to be constant while n_{s} is a function of energy, i.e. n_{s} reflects the electronic band structure of the sample while the band structure of the tip is assumed to be featureless. Since electronic states are spatially extended entities the LDOS is in general a spatially varying quantity. In Eq. (1.6) n_{t} is defined at the center of curvature of the tip (r_0, in Fig. 1.3 (a)), whereas n_{s} indicates the sample's LDOS at the sample surface right underneath the tip apex. E_{F} denotes the Fermi energy of the sample, ϕ_{s} and ϕ_{t} are the work functions of the sample and tip electrode, respectively. U is the applied bias voltage. The parameters R and d describe the geometry of the tunnel junction as visualized in Fig. 1.3 (a).

According to Eq. (1.6) the Tersoff-Hamann model extends the previously discussed simplified textbook example of the tunnel process (Eq. (1.1)-(1.4)) into two directions. First of all, it considers the energy dependence of the LDOS at the sample electrode $n_{\mathrm{s}}\,(E)$ and second it accounts for the energy dependence of the tunnel barrier and thus the energy dependence of the transmission probability T. Like the dependence on the width of the tunnel barrier the energy dependence, i.e. the dependence on the barrier height, shows an exponential behavior. Thus, the total tunnel current is dominated by the tunneling electrons of highest energy and can be interpreted as sum of partial currents at different energies weighted by the respective energy dependent transmission probabilities. These partial tunnel currents are illustrated by the red arrows in Fig. 1.3 (c, d). The exponential damping is indicated by the variable length of the arrows.

In addition to the sample's LDOS (n_{s}) one can define its total density of states $\tilde{n}_{\mathrm{s}}$ in the energy interval between E_{F} and $E_{\mathrm{F}} + eU$:

$$\tilde{n}_{\mathrm{s}}\,(eU) := \int_{E_{\mathrm{F}}}^{E_{\mathrm{F}}+eU} n_{\mathrm{s}}\,(E')\,\mathrm{d}E' \tag{1.7}$$

Using the transmission probability T, as defined in Eq. (1.6), both n_{s} and $\tilde{n}_{\mathrm{s}}$ can be calculated at the center of curvature of the tip r_0:

$$\begin{aligned} n_{\mathrm{s}}\left(\mathbf{r}_0, E, eU\right) &:= n_{\mathrm{s}}\left(E\right) \cdot T_{(d,R)}\left(E, eU\right) \\ \tilde{n}_{\mathrm{s}}\left(\mathbf{r}_0, eU\right) &:= \int_{E_{\mathrm{F}}}^{E_{\mathrm{F}}+eU} n_{\mathrm{s}}\left(E'\right) \cdot T_{(d,R)}\left(E', eU\right)\ \mathrm{d}E' \end{aligned} \tag{1.8}$$

Using these definitions, the tunnel current (Eq. (1.6)) can be rewritten:

$$\boxed{I\left(U\right) \propto n_{\mathrm{t}} \cdot \tilde{n}_{\mathrm{s}}\left(\mathbf{r}_0, eU\right) \overset{U\to 0}{\propto} n_{\mathrm{t}} \cdot n_{\mathrm{s}}\left(\mathbf{r}_0, E_{\mathrm{F}}, eU = 0\right)} \tag{1.9}$$

From Eq. (1.6)-(1.9) it follows that the tunnel current, and thus the z-position of the tip in constant current mode, is a direct measure of $\tilde{n}\left(\mathbf{r}_0, eU\right)$ that on its part depends on both the tip-sample distance, and the energy dependent structure of n_{s}. Thus the interpretation of STM images as topographic images can be misleading, since inhomogeneities in n_{s} may be superimposed to the purely topographic height information. Only in a scenario where n_{s} is spatially homogeneous, $\tilde{n}\left(\mathbf{r}_0, eU\right)$ is a direct measure for the tip-sample distance and thus the topography of the sample surface.

Differential conductivity and local density of states

In the previous section it was shown that the tunnel current I essentially probes the sample's total density of states ($\tilde{n}_{\mathrm{s}}$) at the center of curvature of the tip (r_0). In the limit of low bias voltage, I is proportional to the sample's LDOS (n_{s}) at the Fermi energy. However, in order to investigate the electronic structure of the sample in more detail, it is crucial to determine n_{s} even in the regime of finite energy, i.e. at $E \neq E_{\mathrm{F}}$. This can be achieved by measuring the differential conductivity $\mathrm{d}I/\mathrm{d}U\left(U\right)$ instead of the total tunnel current I. A mathematical expression of the differential conductivity can be derived by differentiation of Eq. (1.6):

$$\begin{aligned} \frac{\mathrm{d}I}{\mathrm{d}U}\left(U\right) \propto\ & n_{\mathrm{t}} \cdot n_{\mathrm{s}}\left(E_{\mathrm{F}} + eU\right) \cdot T_{(d,R)}\left(E_{\mathrm{F}} + eU, eU\right) \\ & + n_{\mathrm{t}} \cdot \int_{E_{\mathrm{F}}}^{E_{\mathrm{F}}+eU} n_{\mathrm{s}}\left(E\right) \cdot \frac{\mathrm{d}}{\mathrm{d}U} T_{(d,R)}\left(E, eU\right) \mathrm{d}E \end{aligned} \tag{1.10}$$

Since $\frac{\mathrm{d}}{\mathrm{d}U}T\,(E,eU)$ is usually small, the second summand in Eq. (1.10) can often be neglected. Consequently, using Eq. (1.8), the differential conductivity can be rewritten:

$$\boxed{\frac{\mathrm{d}I}{\mathrm{d}U}\,(U) \propto n_{\mathrm{t}} \cdot n_{\mathrm{s}}\,(\mathbf{r}_0, E_{\mathrm{F}} + eU, eU)} \tag{1.11}$$

In contrast to the tunnel current, the differential conductivity is proportional to $n_{\mathrm{s}}\,(\mathbf{r}_0, E, eU)$ instead of $\tilde{n}_{\mathrm{s}}\,(\mathbf{r}_0, eU)$, thus $n_{\mathrm{s}}\,(\mathbf{r}_0, E, eU)$ can be determined as a function of energy by measuring $\mathrm{d}I/\mathrm{d}U$ as a function of the applied bias voltage. Experimentally this can in principle be achieved by measuring the tunnel current I as a function of the applied bias voltage while keeping the tip-sample distance fixed. Finally, the differential conductivity $\mathrm{d}I/\mathrm{d}U\,(U)$ can be calculated by numerical differentiation. However, in order to improve the signal to noise ratio the differential conductivity is usually measured directly using a lock-in technique. Here, an alternating (ac) modulation voltage is superimposed to the direct (dc) bias voltage and the response in the tunnel current at the modulation frequency is analyzed using a lock-in amplifier. By repeating this procedure for various values of the dc bias voltage the differential conductivity, and thus $n_{\mathrm{s}}\,(\mathbf{r}_0, E, eU)$, can be determined as a function of energy. The described measurement technique is known as scanning tunneling spectroscopy. Since in the framework of this thesis spectroscopic measurements do not play a role, a more detailed discussion of the technique is omitted here. For further reading see for instance [13] and references therein.

The measurements to be discussed in the following chapters were done using a related technique, that also relies on Eq. (1.10) and Eq. (1.11). For this type of measurement the $\mathrm{d}I/\mathrm{d}U$signal is measured using the lock-in technique discussed above. However, now the measurement is only done at one specific value of the dc bias voltage. This allows to scan the sample surface with the feedback-loop being switched on while measuring $\mathrm{d}I/\mathrm{d}U\,(x,y)$ as well as $z\,(x,y)$. As a result one obtains a topographic image as well as a two-dimensional map of the spatially resolved $\mathrm{d}I/\mathrm{d}U$-signal, a so called $\mathrm{d}I/\mathrm{d}U$-map. Since, according to Eq. (1.11), the $\mathrm{d}I/\mathrm{d}U$-signal is proportional to $n_{\mathrm{s}}\,(\mathbf{r}_0, E, eU)$, a $\mathrm{d}I/\mathrm{d}U$-map visualizes the spatially resolved LDOS at the specific energy corresponding to the acquisition voltage. In particular, the LDOS information can be related to the topography of the sample due to the simultaneous acquisition of $\mathrm{d}I/\mathrm{d}U\,(x,y)$ and $z\,(x,y)$.

Although the Tersoff-Hamann model is a powerful tool for the understanding of STM experiments, it is limited due to the discussed model assumptions. In particular the model only applies to the case of constant n_t. Consequently, the derived equations are not useful when it comes to the interpretation of effects resulting from tunnel processes involving specific tip states. In addition, the model is based on the assumption that the energy of the tunneling electrons is conserved during the tunnel process. It can therefore not be applied for the description of inelastic tunnel processes, as reported recently [14–20]. However, in the framework of this thesis both the electronic structure of the tip and inelastic tunnel processes are negligible. Thus, the discussed model gives a good description of the tunnel experiments to be discussed in the subsequent chapters.

1.4 Spin-polarized scanning tunneling microscopy

Thus far, the tunneling electrons were considered as charge carriers while their spin was neglected. However, it turns out that in electron tunneling experiments with magnetic tip and sample electrodes the spin degree of freedom must be taken into account for a proper description of the tunnel process. In particular the consideration of the electron spin in STM-experiments allows to experimentally investigate the magnetic properties of nanostructures at surfaces down to the atomic limit [21–25].

In the limit of vanishing bias voltage and under the assumption of a free-electron behavior of the conduction electrons, the tunnel current between two magnetic electrodes was first derived for planar tunnel junctions [26, 27]. The following discussion refers to a more recent study where the tunnel current was investigated for a tunnel junction in an STM by extending the Tersoff-Hamann model in an appropriate way [28]. The approach is based on the previously discussed approximations [10–12] plus three additional assumptions:

- During the tunnel process the spin of the tunneling electron is conserved.
- The transmission coefficient T (Eq. (1.6)), is independent of the spin direction.
- Both the spin-up and the spin-down contribution to the tip's LDOS are constant as a function of energy.

If the electron spin is taken into account the LDOS of the sample and tip electrode splits up into a spin-up and a spin-down contribution:

$$n_{\mathrm{t,s}}(E) = n_{\mathrm{t,s}}^{\uparrow}(E) + n_{\mathrm{t,s}}^{\downarrow}(E) \tag{1.12}$$

In general $n_{\mathrm{s}}^{\uparrow}$ and $n_{\mathrm{s}}^{\downarrow}$ are not necessarily equal, resulting in a non-vanishing local spin density of states:

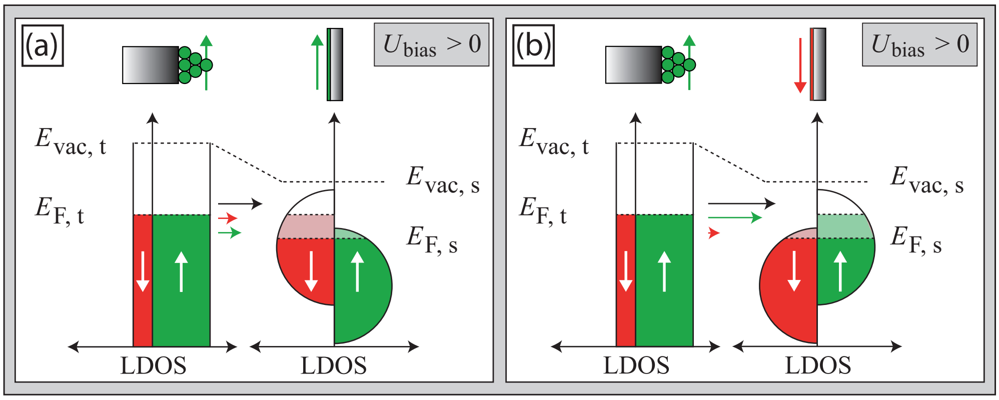

Figure 1.4: Spin-polarized scanning tunneling microscopy with spin and energy conservation for the case of positive sample bias. (a) Energy level diagram for the case of a parallel magnetization of the sample and tip electrode. The spin-polarization of both tunnel electrodes is reflected by the unequal LDOS of spin up (green) and spin down (red) states. Due to spin-conservation the total tunnel current is split into a spin-up and a spin-down contribution. The strength of the respective spin currents is indicated by the length of the red and green horizontal arrows. The black arrow illustrates the total tunnel current. (b) Analogous energy level diagram for the case of an antiparallel magnetization of the sample and tip electrode.

$$m_{\mathrm{t,s}}(E) \quad := \quad n^{\uparrow}_{\mathrm{t,s}}(E) - n^{\downarrow}_{\mathrm{t,s}}(E) \tag{1.13}$$

In particular, a finite value of the integrated local spin density of states in the energy interval below E_{F} corresponds to a net magnetization at the respective tunnel electrode.

$$M_{\mathrm{t,s}} \quad \propto \quad \int_0^{E_{\mathrm{F}}} m_{\mathrm{t,s}}(E')\ \mathrm{d}E' \tag{1.14}$$

Fig. 1.4 illustrates the tunnel process between a magnetic sample and a magnetic tip. The spin-splitting of $n_{\mathrm{s}}(E)$, i.e. the inequivalence of $n^{\uparrow}_{\mathrm{s}}$ and $n^{\downarrow}_{\mathrm{s}}$, is illustrated by the vertically displaced half spheres. The energy level diagrams refer to a parallel and antiparallel alignment of the magnetization at the sample and tip electrode, as indicated in the upper part of each panel.

As a consequence of the assumption, that during the tunnel process the electron spin is a conserved quantity, electrons can only tunnel between states of the same spin-orientation. Consequently, the tunnel current is split into a spin-up and a spin-down contribution. With $n^{\uparrow}_{\mathrm{t}}$ and $n^{\downarrow}_{\mathrm{t}}$ being constant both contributions can essentially be calculated independently in formal analogy to the spin-averaged case. Finally, the total spin-polarized tunnel current is given by[1]

$$I_{\mathrm{sp}} = I^{\uparrow}(U) + I^{\downarrow}(U) \propto n_{\mathrm{t}}^{\uparrow} \cdot \tilde{n}_{\mathrm{s}}^{\uparrow}(\mathbf{r}_0, \mathbf{eU}) + n_{\mathrm{t}}^{\downarrow} \cdot \tilde{n}_{\mathrm{s}}^{\downarrow}(\mathbf{r}_0, \mathbf{eU})$$

$$\begin{aligned} \tilde{n}_{\mathrm{s}}^{\uparrow}(\mathbf{r}_0, eU) &:= \int_{E_{\mathrm{F}}}^{E_{\mathrm{F}}+eU} n_{\mathrm{s}}^{\uparrow}(E')\, T_{(d,R)}(E, eU)\, \mathrm{d}E' \\ \tilde{n}_{\mathrm{s}}^{\downarrow}(\mathbf{r}_0, eU) &:= \int_{E_{\mathrm{F}}}^{E_{\mathrm{F}}+eU} n_{\mathrm{s}}^{\downarrow}(E')\, T_{(d,R)}(E, eU)\, \mathrm{d}E'. \end{aligned} \tag{1.15}$$

Eq. (1.15) is valid independent of the relative magnetization direction of sample and tip. Nevertheless, the total tunnel current changes upon inversion of the magnetization at the sample electrode, since such an inversion essentially corresponds to an exchange of $\tilde{n}_{\mathrm{s}}^{\uparrow}$ and $\tilde{n}_{\mathrm{s}}^{\downarrow}$ as indicated in Fig. 1.4. Consequently, the total tunnel current for the parallel and antiparallel configuration can be rewritten:

$$\begin{aligned} I_{\mathrm{sp}}^{\uparrow\uparrow}(U) &\propto n_{\mathrm{t}}^{\uparrow} \cdot \tilde{n}_{\mathrm{s}}^{\uparrow}(\mathbf{r}_0, \mathbf{eU}) + n_{\mathrm{t}}^{\downarrow} \cdot \tilde{n}_{\mathrm{s}}^{\downarrow}(\mathbf{r}_0, \mathbf{eU}) \\ I_{\mathrm{sp}}^{\uparrow\downarrow}(U) &\propto n_{\mathrm{t}}^{\uparrow} \cdot \tilde{n}_{\mathrm{s}}^{\downarrow}(\mathbf{r}_0, \mathbf{eU}) + n_{\mathrm{t}}^{\downarrow} \cdot \tilde{n}_{\mathrm{s}}^{\uparrow}(\mathbf{r}_0, \mathbf{eU}) \end{aligned} \tag{1.16}$$

In particular, the total spin-polarized tunnel current can be expressed by a single equation that reduces to the two cases of Eq. (1.16) for the (+) and (-) case, respectively:

$$\begin{aligned} I_{\mathrm{sp}}(U) &\propto \frac{I_{\mathrm{sp}}^{\uparrow\uparrow} + I_{\mathrm{sp}}^{\uparrow\downarrow}}{2} \pm \frac{I_{\mathrm{sp}}^{\uparrow\uparrow} - I_{\mathrm{sp}}^{\uparrow\downarrow}}{2} \\ &\propto n_{\mathrm{t}} \cdot \tilde{n}_{\mathrm{s}} \pm m_{\mathrm{t}} \cdot \left(\tilde{n}_{\mathrm{s}}^{\uparrow}(\mathbf{r}_0, eU) - \tilde{n}_{\mathrm{s}}^{\downarrow}(\mathbf{r}_0, eU)\right) \end{aligned} \tag{1.17}$$

In order to simplify this equation, one can define the sample's total spin density of states $\tilde{m}_{\mathrm{s}}$ in the energy interval between E_{F} and $E_{\mathrm{F}} + eU$ in addition to its local spin density of states m_{s}:

$$\tilde{m}_{\mathrm{s}}(eU) := \int_{E_{\mathrm{F}}}^{E_{\mathrm{F}}+eU} m_{\mathrm{s}}(E')\, \mathrm{d}E' \tag{1.18}$$

In analogy to Eq. (1.8) and Eq. (1.15) both m_{s} and $\tilde{m}_{\mathrm{s}}$ can be calculated at the center of curvature of the tip $\mathbf{r}_0$

---

[1] Note, that here the transmission coefficient $T_{(d,R)}(E, eU)$ is defined according to Eq. (1.6). It is assumed to be independent of the spin-direction in agreement with the additional assumptions extending the Tersoff-Hamann model to the spin-polarized case.

$$\begin{aligned}
m_{\mathrm{s}}(\mathbf{r}_0, E, eU) &:= m_{\mathrm{s}}(E)\cdot T_{(d,R)}(E, eU)\\
\tilde{m}_{\mathrm{s}}(\mathbf{r}_0, eU) &:= \int_{E_{\mathrm{F}}}^{E_{\mathrm{F}}+eU} m_{\mathrm{s}}(E')\cdot T_{(d,R)}(E', eU)\,\mathrm{d}E' \\
&= \tilde{n}_{\mathrm{s}}^{\uparrow}(\mathbf{r}_0, eU) - \tilde{n}_{\mathrm{s}}^{\downarrow}(\mathbf{r}_0, eU)
\end{aligned} \tag{1.19}$$

By inserting Eq. (1.19) into Eq. (1.17) the spin-polarized tunnel current can be rewritten:

$$I_{\mathrm{sp}}(U) \propto n_{\mathrm{t}}\cdot\tilde{n}_{\mathrm{s}}(\mathbf{r}_0, eU) \pm m_{\mathrm{t}}\cdot\tilde{m}_{\mathrm{s}}(\mathbf{r}_0, eU) \tag{1.20}$$

According to Eq. (1.20) the tunnel current $I_{\mathrm{sp}}(U)$ is given by the sum of the spin-averaged contribution Eq. (1.9) and an additional contribution that depends on the tip's local spin density of states, the sample's integrated spin density of states, and the relative magnetization directions at the sample and tip electrode. In Fig. 1.4 the angular dependence of $I_{\mathrm{sp}}(U)$ is illustrated by the size of the black horizontal arrow. The contributions of the spin-up and spin-down electrons to $I_{\mathrm{sp}}(U)$ are visualized by green and red arrows, respectively.

The preceding discussion was limited to the case of a parallel and antiparallel alignment of the sample and tip magnetization. This collinear special case can easily be generalized to configurations with an arbitrary angle α between the magnetization directions of sample and tip [28].

$$\boxed{\begin{aligned}
I_{\mathrm{sp}}(U) &\propto n_{\mathrm{t}}\cdot\tilde{n}_{\mathrm{s}}(\mathbf{r}_0, eU) + m_{\mathrm{t}}\cdot\tilde{m}_{\mathrm{s}}(\mathbf{r}_0, eU)\cdot\cos(\alpha)\\
&\propto n_{\mathrm{t}}\cdot\tilde{n}_{\mathrm{s}}(\mathbf{r}_0, eU) + \mathbf{m}_{\mathrm{t}}\cdot\tilde{\mathbf{m}}_{\mathrm{s}}(\mathbf{r}_0, eU)
\end{aligned}} \tag{1.21}$$

Here, the vectorial quantities $\mathbf{m}_{\mathrm{t,s}}$ and $\tilde{\mathbf{m}}_{\mathrm{t,s}}$ are calculated as the product of $m_{\mathrm{t,s}}$ ($\tilde{m}_{\mathrm{t,s}}$) and the unit vector along the respective magnetization direction. Differentiating Eq. (1.21) finally yields the spin-polarized differential conductivity:

$$\boxed{\begin{aligned}
\left(\frac{\mathrm{d}I}{\mathrm{d}U}\right)_{\mathrm{sp}}(U) &\propto n_{\mathrm{t}}\cdot n_{\mathrm{s}}(E_{\mathrm{F}}+eU) + m_{\mathrm{t}}\cdot m_{\mathrm{s}}(E_{\mathrm{F}}+eU)\cdot\cos(\alpha)\\
&\propto n_{\mathrm{t}}\cdot n_{\mathrm{s}}(E_{\mathrm{F}}+eU) + \mathbf{m}_{\mathrm{t}}\cdot\mathbf{m}_{\mathrm{s}}(E_{\mathrm{F}}+eU)
\end{aligned}} \tag{1.22}$$

In Eq. (1.21) the spin-averaged contribution depends on the integrated LDOS of the sample, i.e. it increases with the applied bias voltage. In contrast, the spin-polarized contribution to the tunnel current only varies moderately around zero. Consequently, with increasing bias-voltages, the spin-averaged contribution becomes dominating and the observation of a spin-polarized current signal becomes increasingly difficult. In the case of differential conductivity measurements Eq. (1.22) the situation is more favorable, since the spin-averaged contribution only depends on the sample's LDOS without any integration. Consequently, the bias voltage can be optimized such that the spin-polarized contribution is maximized over the spin-averaged one.

SP-STM in an external magnetic field

According to Eq. (1.21) and Eq. (1.22) the experimentally observed spin-contrast for a given magnetic structure of the sample essentially depends on two factors:

- The spin densities of states $m_{\mathrm{t,s}}(\mathbf{r}_0, E, eU)$ and $\tilde{m}_{\mathrm{t,s}}(\mathbf{r}_0, eU)$.
- The magnetization direction at the tip electrode.

Since $m_{\mathrm{t,s}}(\mathbf{r}_0, E, eU)$ and $\tilde{m}_{\mathrm{t,s}}(\mathbf{r}_0, eU)$ are functions of the applied bias voltage, they can be adjusted in an STM-experiment at least to some extent. Concerning the magnetization direction at the tip the experimental options are in general more limited. While for bulk magnetic tips the magnetization direction is governed by the shape anisotropy it can be adjusted for tips with a magnetic thin film coating [24, 29]. It can be chosen to be parallel or perpendicular to the sample surface, depending on the coating material and its thickness, while the azimuthal angle, i.e. the orientation of the magnetization in the plane parallel to the sample surface, is not an experimentally controllable parameter. In particular, once the magnetization direction of the tip is fixed after the tip preparation, it can in general not be adjusted during the SP-STM experiment. Consequently, the observed contrast levels cannot be assigned to specific spatial directions of the sample magnetization.

This lack of angular resolution can in principle be overcome by applying an external magnetic field that aligns the tip magnetization along a specific axis during the measurement [1]. However, in general it is not only the tip magnetization that is affected but also the magnetic structure of the sample to be investigated. There are essentially two extreme cases of experiments that can be done in external magnetic fields.

SP-STM-tips with a hard magnetization compared to the sample:

If the magnetization of the tip is hard it is not affected by external magnetic fields of moderate strength[2]. Consequently, all observed contrast changes can be attributed to changes of the magnetic structure at the sample electrode. Since the magnetic structure of the sample changes into the direction of a parallel alignment along the external field the observed contrast levels can be determined with respect to the direction of the field.

SP-STM-tips with a soft magnetization compared to the sample:

If the magnetization of the tip is soft it can easily be aligned along the external magnetic field without affecting the magnetic structure of the sample. In contrast to the previously described type of measurements now the direction of the tip magnetization is a well defined parameter. Using this approach the observed spin contrast can in principle be maximized and minimized, while the magnetic structure of the sample remains unaffected. However, the observed maxima and minima of the spin-polarized signal can not be unambiguously attributed to a parallel or antiparallel alignment of the tip and sample magnetization, since in general a possible inversion of the observed spin-contrast as a function of the applied bias voltage must be taken into account. Thus, the magnetization direction at the sample can only be determined up to an unknown phase factor of π.

By combining both types of measurements the complete information about the magnetic structure of the sample can in principle be obtained. However, for the existing STM setups the direction of the external magnetic field is in general limited to the direction of the surface normal [31–41]. Consequently, the accessible angular resolution for SP-STM is limited to the polar angle, i.e the angle with respect to the surface normal. In particular in the context of the investigation of complex non-collinear magnetic structures this puts a significant limitation to the number of accessible scientific questions. To date, there are only two SP-STM setups where the magnetic field can be rotated in a two dimensional plane [42, 43] and one where the microscope can be rotated in a plane with respect to the external field [44]. Only two setups give access to arbitrary field orientations in three-dimensional space and thus allow for a measurement of the azimuthal in addition to the polar angle. One of these setups was developed as part of this thesis. The second one was placed into operation shortly afterwards [45].

---

[2] The prototypical example for this type of STM-tip is the case of a Cr-coated W-tip [30].

Chapter 2

Instrumental developments

2.1 Motivation and design concept

Spin-polarized scanning tunneling microscopy (SP-STM) and spectroscopy (SP-STS) are powerful tools to investigate magnetic nanostructures down to the atomic scale. After the first spin-polarized measurements [21, 23] the method became a routinely used technique with the integration of the microscope into a low temperature ultra-high vacuum (UHV) system and the development of a reliable *in-situ* tip exchange mechanism [31] that allowed for the magnetic coating of the STM tips under UHV conditions. The additional integration of strong magnetic fields paved the way towards fascinating investigations of magnetism at the nanoscale [46–48] and even at the level of single atoms [49–51].

Despite their differences, all methods to achieve spin contrast in scanning tunneling experiments [21, 52, 53] rely on the idea that spin contrast depends on the relative orientation of the magnetizations of sample and tip, as discussed in detail in the previous chapter. However, the magnetization direction of the tip is in general not known, thus detailed conclusions about the magnetization directions in magnetic nanostructures have remained a fundamental problem of SP-STM since its beginnings.

A successful and relatively simple way to at least partially overcome this problem has been to apply an external magnetic field while using a ferromagnetically coated STM-tip. Thus the magnetization at the tip apex can be canted or even fully aligned along the direction of the external field [1]. On the other hand, by using antiferromagnetic chromium tips the tip magnetization can be kept stable in external magnetic fields [30, 54] thus allowing to investigate the behavior of a sample system in an external field without any superimposed tip effects [1, 46, 49, 54]. However, so far the direction of the external field has been restricted to specific spatial directions due to

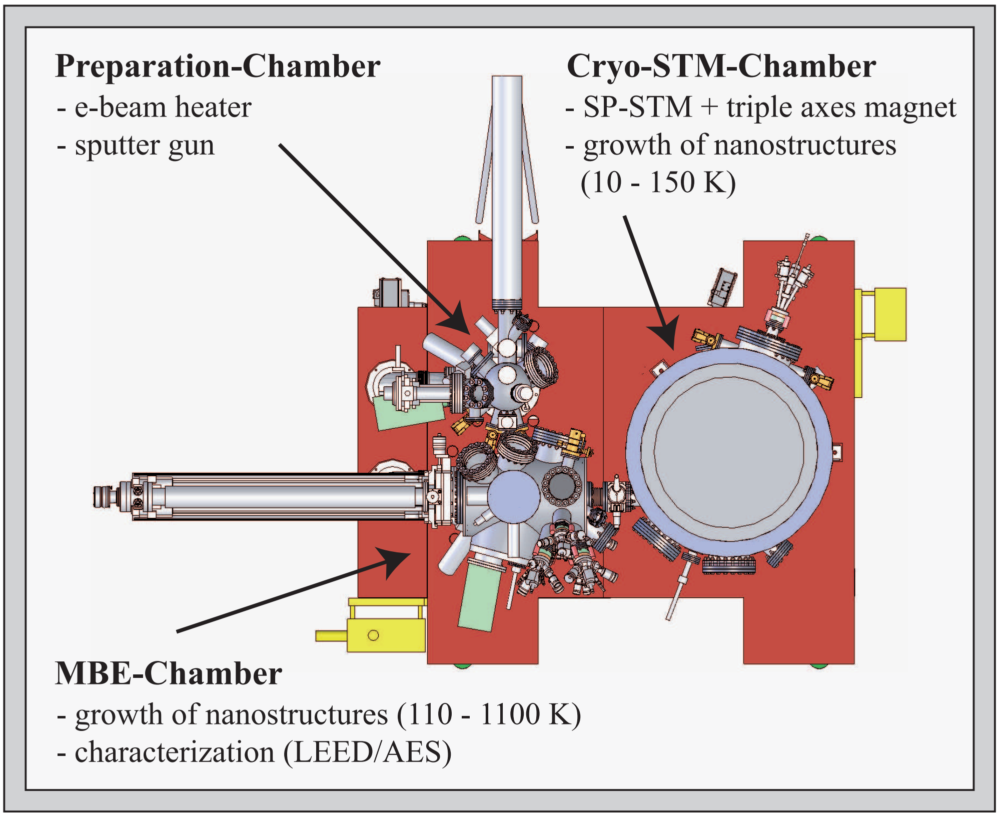
Preparation-Chamber
- e-beam heater
- sputter gun
Cryo-STM-Chamber
- SP-STM + triple axes magnet
- growth of nanostructures (10 - 150 K)
MBE-Chamber
- growth of nanostructures (110 - 1100 K)
- characterization (LEED/AES)

Figure 2.1: Top view of the three chamber UHV system schematics. The system bench rests on a solid foundation of concrete decoupled from the building. Additional air damping legs are installed under the bench.

the limitations of the existing SP-STM setups.

In order to overcome these limitations a novel SP-STM setup has been designed and put into operation as part of this thesis. The STM is rigidly mounted inside the center of a superconducting triple axes vector magnet. The design allows an easy access to the microscope from two sides, which guarantees a fast and easy exchange of samples and tips in the STM as well as the option to deposit single adsorbate atoms directly onto the cryogenic sample surface inside the microscope. It is important to note that due to the requirement of a direct access to the microscope the magnet design is based on three pairs of split coils instead of a configuration with a solenoid as the central coil.

The design focus of the sample and tip preparation facilities outside the microscope has been put on a maximum of flexibility for the self-assembled growth of atomic scale magnetic structures. To increase the throughput of the system, a LabView based software package was developed for monitoring and control of the complete setup as well as for the automation of substrate cleaning processes and measurements.

The UHV system was realized in a fully customized design and consists of three chambers plus loadlock interconnected by gate valves to allow for the transfer of samples and STM-tips (Fig. 2.1). The design was developed in close collaboration with Omicron Nanotechnology GmbH [55] who manufactured the system according to the technical drawings developed in the framework of this thesis. In the laboratory the whole setup is installed on a huge block of concrete, which is vibrationally decoupled from the building. Additionally, the UHV chambers are supported by a bench resting on pneumatic damping legs. All vacuum chambers are pumped by ion getter and titanium sublimation pumps (TSP). In the cryostat chamber the cold surfaces of the cryostat act as an additional cryopump. To counterbalance the desorption of hydrogen during cryostat warm-up the cryostat chamber is equipped with a non-evaporating getter (NEG) pump. The base pressures are below 1×10^{-10} mbar for all vacuum chambers.

2.2 Substrate cleaning and MBE growth facilities

Cleaning Processes

For the investigation of magnetic nanostructures at the atomic scale the cleanliness of the underlying substrate is essential. Since all cleaning procedures inevitably lead to high gas loads they are accomplished in the preparation chamber, which is separated from the other chambers by a gate valve. The preparation chamber is connected to a load lock chamber where up to four substrates or STM tips can be transfered into the system in a single step.

There are two cleaning procedures of major importance, depending on the material of the single crystals in use. An ion source in conjunction with a manipulator equipped with a resistive heating stage providing temperatures up to 1100 K can be used for repeated cycles of Ar^+ ion sputtering and subsequent annealing. For the Ar gas inlet a piezo motor controlled leak valve is used, which can be addressed by an appropriate control electronics. Thus, the desired gas pressure can be accurately adjusted and is stabilized by a feedback loop. This feature allows to run unattended automated sputter and annealing cycles.

In the second cleaning procedure a home-built electron bombardment heating stage is applied to achieve temperatures as high as 2000 °C and more. This facility is designed to enable not only a treatment of samples, but also of STM tips (Fig. 2.2). An advanced cleaning procedure for tungsten single crystals involving high temperatures has been described previously [56]. In short, the tungsten substrate is repeatedly kept at elevated temperatures in an oxygen atmosphere for a certain time, followed by a short flash to high temperature after a recovery of the base pressure to the low 10^{-10} mbar range.

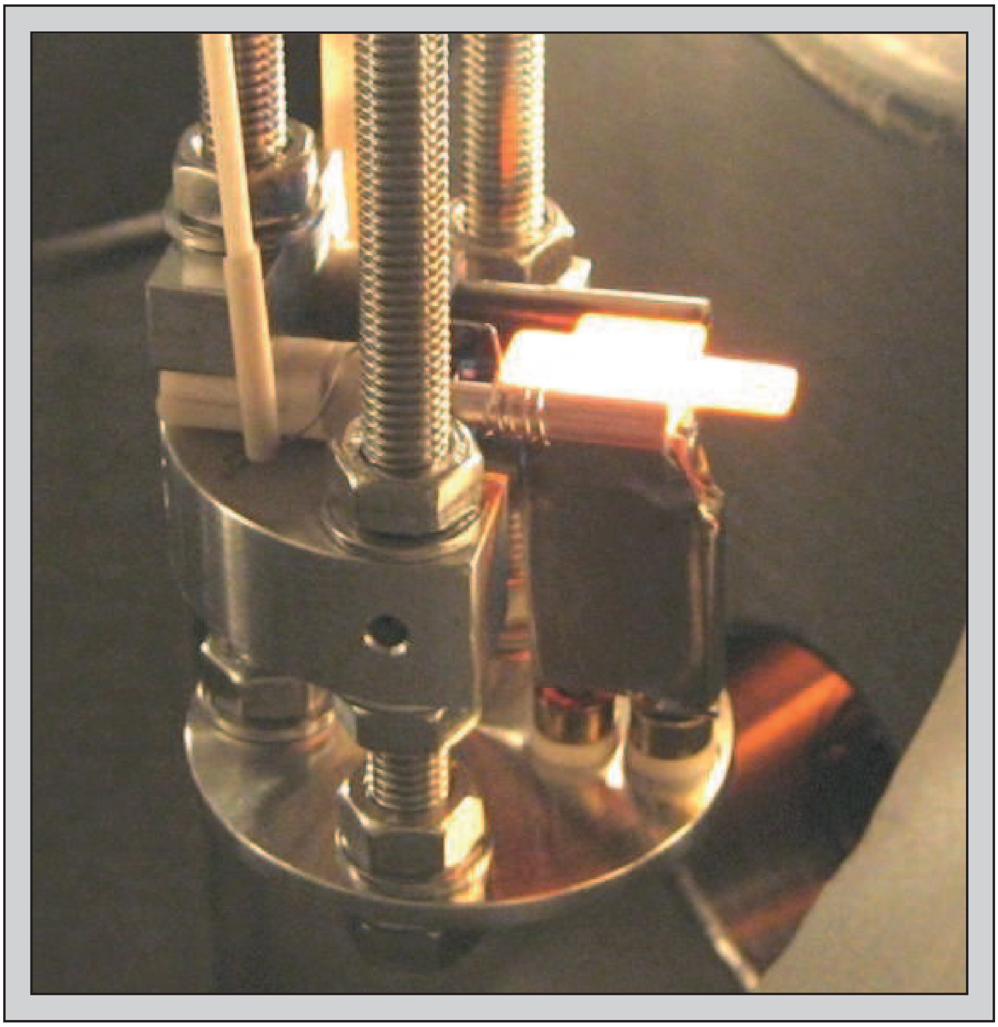

Figure 2.2: An empty sample tray being heated by electron bombardment. Grooves in two tungsten rods receive the sample tray or the tip transporter. The electron-emitting filament is positioned right underneath the tray. With the tungsten rods held at high positive voltage, the electrons get accelerated and release their kinetic energy upon impingement on the tray's back side.

Similar procedures can be applied for other materials. Again, by making use of a piezo-driven leak valve and a suitable home-built control software the time consuming cleaning cycles have been automated.

Nanostructure Growth and Characterization

The main purpose of the MBE-chamber is the growth of magnetic nanostructures on the clean substrates using self-assembly. A process of equal importance is the deposi-

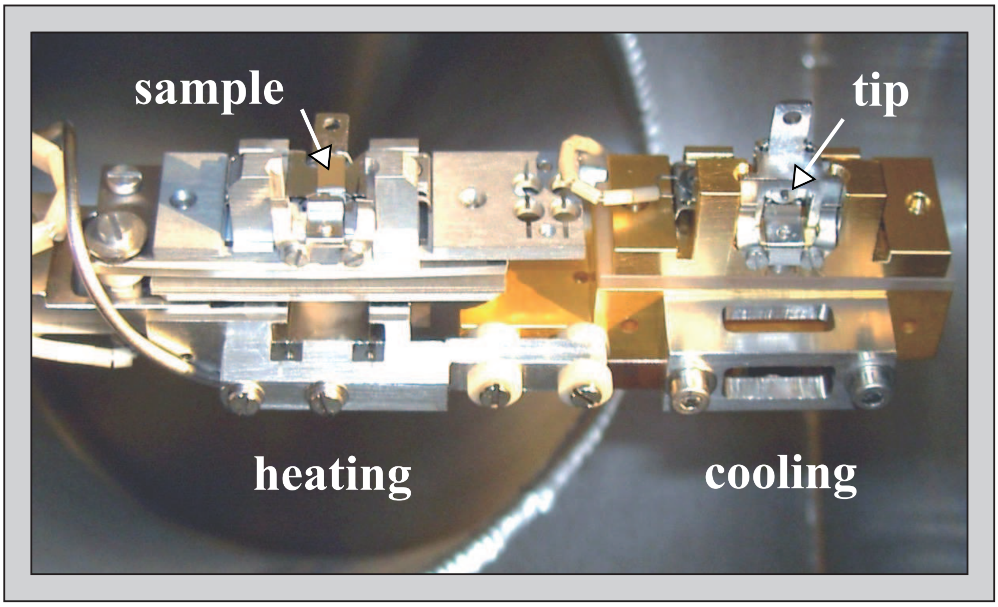

Figure 2.3: The two stages of the manipulator head used for heating or cooling the sample or the tip during evaporation. For illustration purposes both a sample and a tip transporter have been put on the manipulator head at the same time. The overall achievable temperature range is 110 K to 1100 K.

tion of thin magnetic films on the pre-cleaned STM-tips. For controlling the process of self-assembly there are three major parameters, on which the growth result depends crucially: (i) the choice of material combination of the adsorbate/substrate system with a particular surface crystallographic orientation, (ii) the substrate temperature during growth, and (iii) the deposition rate.

The chamber is equipped with five Focus EFM3 e-beam evaporators [57] for submonolayer growth of various magnetic transition metals. They contain flux meters enabling the growth to be controlled by well defined deposition rates. One of the evaporators is of the EFM3i type [58]. As a special feature, this evaporator can generate ions during evaporation. This can be useful to deliberately create nucleation centers at the sample surface. By virtue of this process, smooth heteroepitaxial films can be grown on surfaces where otherwise Vollmer-Weber [59] growth would be present [58]. In the context of the investigation of atomic scale nanostructures this ion assisted deposition technique may be useful to nucleate atomic scale clusters at high areal densities on a substrate surface.

During evaporation sample or tip are held in an Omicron manipulator head, which is mounted to a VG Scienta Omniax manipulator. Essentially, the manipulator head is the standard Omicron design but with a few important modifications to meet the geometry of our custom sample trays and tip transporters (Fig. 2.3). Instead of just one receptacle for the sample there is another one for the tip transporter at an angle of 90°. Furthermore, this manipulator head consists of two stages, one for heating and another one for cooling the sample. Both stages are thermally decoupled at elevated temperature by a sapphire plate. The heater stage is equipped with a PBN-heater enabling us to heat both sample or tip to about 1100 K. At the cooling stage a temperature of 110 K is achieved using cold nitrogen gas that can be circulated through tubes thereby cooling a copper block at the cooling stage. At both stages the temperature is measured by a thermocouple.

At the heater stage the temperature can be adjusted with a precision below 1 K. For low temperatures a precise temperature control is not possible. However, the temperature can be adjusted with some precision by adjusting the nitrogen flux and heating with the PBN-heater. The travel of the manipulator was chosen long enough to allow the transfer of the sample all the way into the cryostat while being cooled. Since the wobble stick for the sample transfer into the microscope can be pre-cooled by direct thermal contact to the nitrogen reservoir the sample can be inserted into the STM without warming up significantly after evaporation.

In addition to the evaporation facilities, standard surface analysis instruments for low energy electron diffraction (LEED) and Auger electron spectroscopy (AES) are available in the MBE chamber.

2.3 Magnet cryostat and scanning tunneling microscope

Triple Axes Magnet Design

At the heart of the UHV system described here is a large vacuum chamber hosting a cryostat system [60] with a superconducting triple axes magnet [61] and a home-built scanning tunneling microscope. The inner diameter of the vacuum chamber amounts to 700 mm and the UHV tight connection between the chamber and the cryostat system is accomplished by a COF700 flange. A three dimensional cutaway view of the setup is given in Fig. 2.4. The vector magnet system consists of three pairs of split coils allowing to apply magnetic fields of 1.3 T along the x- and y-axis (red and green coils) and 5 T along the z-axis (blue coil), respectively. These values can only be achieved when any one of the three split coils is operated in single axis mode. When operated in cooperative mode the magnetic field vector is restricted to values inside a cylinder of radius 1 T and height ± 3.5 T, as illustrated in Fig. 2.4. The maximum sweep rates for the x-, y- and z-coils are limited to 1.2 mT/s, 1.3 mT/s and 5 mT/s, respectively.

There were three major constraints for the design of this vector magnet. First of all, the

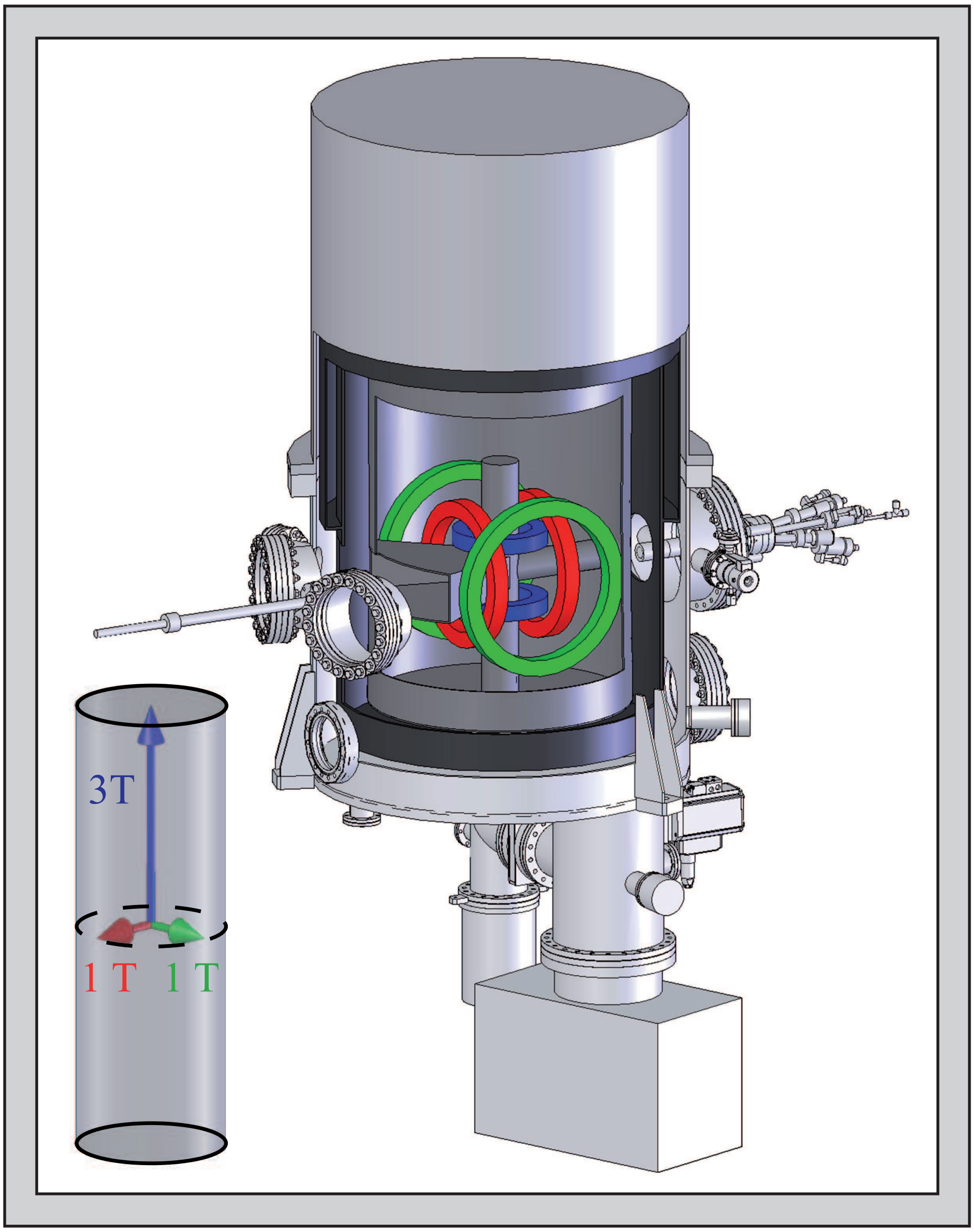

Figure 2.4: Cutaway view of the cryostat chamber hosting the superconducting triple axes magnet with the STM. The split coils of the magnet are shown in red, green and blue, respectively. The sample is inserted into the microscope using the wobble stick to the left. An evaporator for single adsorbate deposition at very low temperatures is mounted opposite to the wobble stick. Inset: Schematic drawing of the accessible magnetic field range.

inner bore of the *z*-coils was demanded to be large enough to mount the microscope. In addition, an opening of 60° was desired to allow an easy access to the microscope for sample and tip exchange, which has proven to be highly beneficial in terms of sample throughput [31]. The third requirement was another, smaller direct access to the microscope from the backside. Since the STM is equipped with a mechanism for sample rotation (Fig. 2.5), this second direct access allows to deposit single adsorbates directly onto the cold sample without removing it from the microscope.

A major task in building a superconducting triple axes magnet is to construct a solid mechanical structure preventing the coils from moving due to their pairwise dipolar interaction. Movements on the order of micrometers can already cause the superconducting magnet to quench. To accomplish the two openings mentioned above a design with a solenoid as the central coil is not appropriate and three pairs of split coils must be used. All split coils must be larger and therefore stronger than in a solenoid geometry resulting in a tendency towards reduced static stability. Thus, building a magnet with the given constraints poses a great challenge to the magnet design. The key issue to meet all the required specifications is a firm steel frame. In combination with the large diameters of the split coils this results in the big overall size of the magnet.

The magnet is mounted inside a ^{4}He bath cryostat, which is shielded by a liquid nitrogen (LN_2) reservoir against thermal radiation. In order to prevent an excessive heat load through the large openings two double-walled shutters are employed, to be operated by vertical linear feedthroughs. The two walls of each shutter are thermally decoupled, with the outer one anchored to LN_2, the inner one to the He bath, by means of copper braids. This shutter system, in conjunction with the efficient cooling of the microscope itself, as discussed below, results in a base temperature of the microscope of 4.7 K. The magnet can only be energized when totally covered by liquid helium, thus the active volume of the He reservoir above the magnet plays a key role in terms of hold time. With an active volume of 80 l of liquid helium a hold time of 36 hours is achieved. The cryostat remains at base temperature for another 20 hours. However, during that time the magnet cannot be operated.

To obtain proper UHV conditions the magnet is designed to safely endure bakeout at 90 °C. During bakeout the surrounding chamber and the nitrogen reservoir are heated up to 130 °C for 60 hours. Due to its large thermal mass the magnet's temperature follows slowly with a delay of about 24 hours. As a consequence, the temperature of the magnet never exceeds 75 °C. The magnet temperature is measured by two temperature sensors close to the central bore and one on top of the magnet. The microscope's temperature is measured by a CERNOX [62] temperature sensor mounted to the sample receptacle, as shown in Fig. 2.5. The signal of either of these sensors can be fed into a control unit that supplies a flow of cold nitrogen gas across the magnet if the temperature is about to surpass a critical value due to some unforeseen event. Thus, a safe bakeout operation is guaranteed. After bakeout and with the cryostat cooled down, a base pressure below 1×10^{-10} mbar is achieved.

To avoid vibrations due to boiling nitrogen the LN_2 reservoir is pumped to below 5 mbar. As a consequence the nitrogen undergoes a transition to its solid phase. The pumping is done by a rotary vane pump with a nominal pumping speed of $65\,\mathrm{m^3/h}$, which is necessary to cope with the very high initial gas load. The pump is located in an adjacent room, which is acoustically isolated from the STM laboratory. Once the gas flow through the pumping line is sufficiently low the acoustic coupling of the cryostat system to the pump is sufficiently suppressed. Besides the significant reduction of vibrations a positive side effect is the reduced temperature of the solid nitrogen compared to the liquid phase. The temperature drops from 77 K down to 63 K, which is of considerable advantage in terms of helium boil-off.

Due to the large area of the cold surfaces exposed to UHV the cryostat itself acts as a very efficient cryo-pump. While this is very advantageous in terms of improving the vacuum, it can be quite problematic during warm-up. In this situation, without any precautions, a pressure rise to the 10^{-3} mbar range may be observed, which is mainly due to hydrogen desorbing from the cryo-surfaces. To avoid this extreme pressure rise an additional NEG-pump, which is very efficient in pumping hydrogen, has been mounted to the chamber. As a result the described pressure rise is limited to the 10^{-8} mbar range.

STM Design

Fig. 2.5 shows a sketch of the STM, which is operated in the center of the triple axes magnet, as illustrated in Fig. 2.4. While the overall design follows the general ideas described previously [31], here the focus is put on some significant modifications.

Instead of the ceramics MACOR, phosphorous bronze ($CuSn_8P$) was chosen for the microscope body. This material is easy to machine, UHV compatible and nonmagnetic. The body is gold-plated to reduce the emissivity of the surface. Compared to MACOR, the metallic body has a much higher thermal conductivity. Thus, after a sample exchange at low temperatures, the microscope reaches thermal equilibrium within a few minutes, while a typical waiting time with a MACOR body amounts to about 45 minutes. The microscope is rigidly mounted on top of an oxygen-free highly conductive (OFHC) copper column resting on a flange of the same material. This allows to mount the microscope inside the magnet by inserting it from the bottom where the microscope's flange is firmly screwed to the liquid helium (LHe) reservoir. All wirings necessary to operate the STM are also fed from the bottom side. The leads are custom made twisted pairs of 0.1 mm stainless steel inside a braided shield, with Kapton insulation [63]. The overall diameter of these very rugged cables is 1 mm. The wires are thermally decoupled from the LN_2 reservoir. Instead, following [64], they are anchored to the LHe bath. They run inside straight grooves in the copper

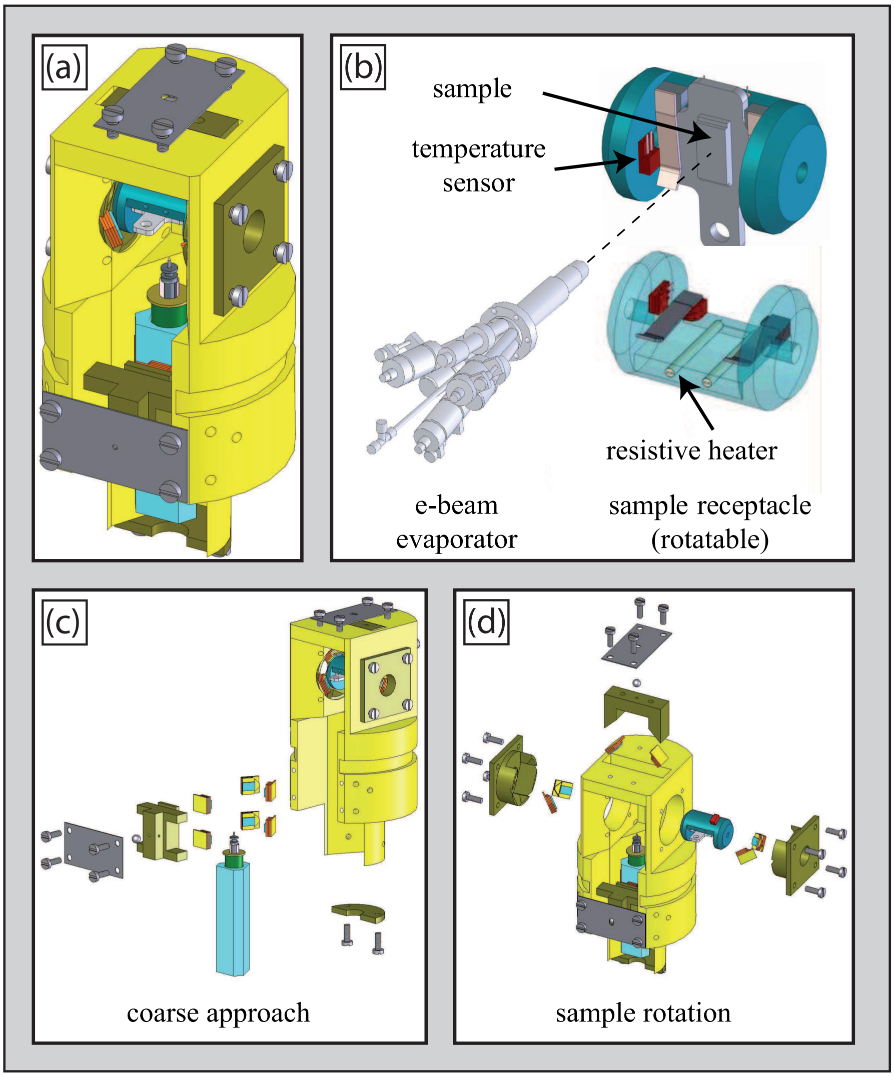
(a)
(b)
sample
temperature sensor
resistive heater
e-beam evaporator
sample receptacle (rotatable)
(c)
coarse approach
(d)
sample rotation

Figure 2.5: (a) Microscope body with the tip approaching from the bottom. b) Adsorbate deposition inside the microscope using the sample rotation mechanism. c) Exploded drawing of the approach mechanism. d) Exploded drawing of the mechanism for sample rotation

column, firmly pressed by screwed-on plates, on a length of 130 mm. As a result, the temperature difference between the wire and the copper column is reduced to less than 1 mK at the wire ends close to the microscope. For comparison, a similar wire made of Cu, would require a length of 670 mm for the same result. The cold wire ends are fixed to a Teflon ring where plug and socket connections allow to proceed using copper wires to finally contact the microscope. In conjunction with the earlier mentioned double-walled radiation shields, which close the access openings to the microscope, the heat load on the microscope is effectively reduced. The equilibrium temperature, as measured by a calibrated Cernox [62] sensor mounted directly to the sample receptacle, is below 4.7 K.

For the coarse approach a stepper motor based on the slip-stick principle is used, similar to the one described in [31], with six shear piezo stacks clamping a sapphire prism, which carries the tube scanner with the tip, as shown in Fig. 2.5. In contrast to the previously described microscope the sample surface is facing downward, the tip points upward. For the scanner a 1/4’ EBL #4 piezo tube [65] with 0.02’ wall thickness and an effective length of 19.5 mm is used. For a maximum applied voltage of ±150 V the scan range amounts to 4.3 μm at room temperature and 2.5 μm at 4.7 K, respectively.

A key requirement for SP-STM experiments is a reliable tip exchange mechanism, allowing an *in situ* preparation of tips with magnetic sensitivity. The scanner houses a tip exchange mechanism, as described in [31]. Taking this additional load into account, the lowest resonance frequency of the tube scanner has been calculated to 4.44 kHz following [66], well above typical cutoff frequencies occurring during scanning.

A special feature of the microscope is its rotatable sample stage made of sapphire (Fig. 2.5b)). Such a stage was already described in [31]. By virtue of this device the sample surface can be reoriented by 90° towards an evaporator, which is mounted on the back side of the cryo-chamber. The radiation shield is equipped with a shutter, which gives access to a bore in the magnet structure providing line-of-sight between the sample surface and the evaporator. With the shutter open, one can supply an atom beam directly onto the cold sample surface while the temperature does not rise above 10 K. On the cold surface, the impinging atoms have no mobility, which is a prerequisite for the preparation of individual magnetic adatoms. To increase the versatility of the STM, a resistive heating was integrated into the sample stage (Fig. 2.5b). The key to do this was to drill two holes 1 mm in diameter through the sapphire stage right underneath the sample receptacle. A tungsten filament of 0.1 mm diameter and about 40 mm length, guided by appropriate alumina tubings, is fixed into the bores. A local temperature of 150 K is easily achieved, allowing to induce a controlled surface diffusion of the adsorbates if desired. Summarizing, together with the variable temperature equipment of the manipulator in the MBE chamber (section 2.2) the temperature range available for sample preparation extends from about 1100 K down to 10 K.

2.4 Software control and automation

The low-temperature STM described above has been installed in a laboratory in the basement of the building. The refill of cryogenic liquids and the operation of the STM and magnet system is done from a second laboratory room one floor above. Therefore, it is essential to have an appropriate software to remotely monitor and control the microscope, the triple axes magnet, the cryostat and some important UHV-related

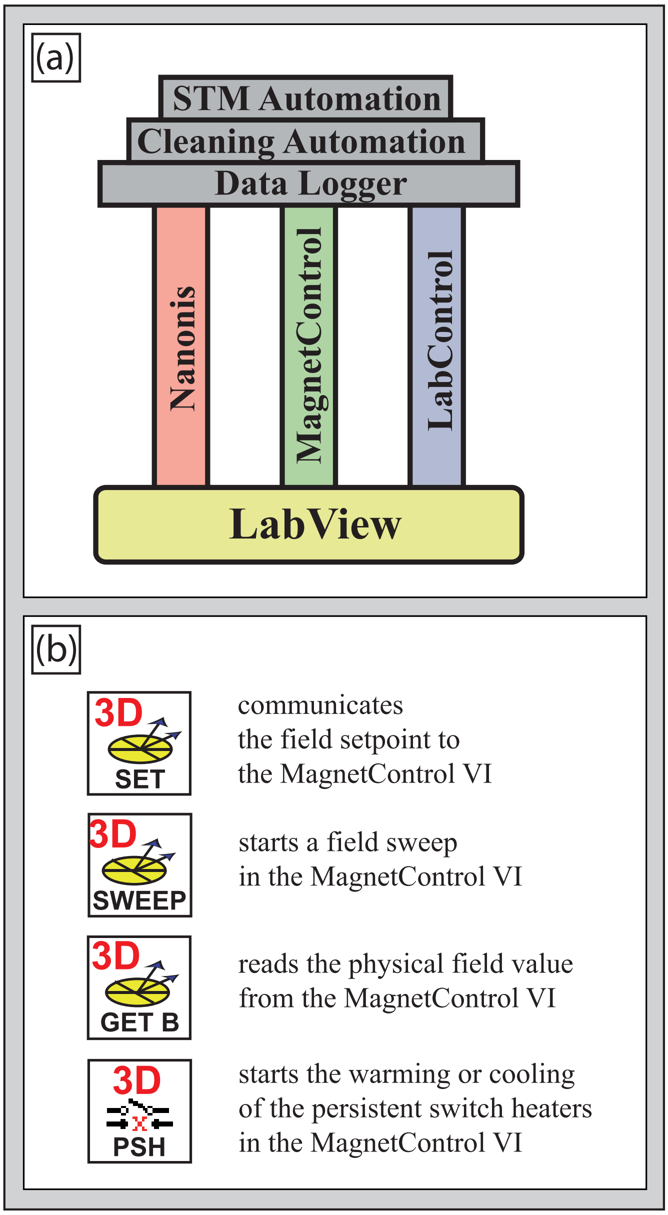
(a)
STM Automation
Cleaning Automation
Data Logger
Nanonis
MagnetControl
LabControl
LabView
(b)
3D SET
communicates the field setpoint to the MagnetControl VI
3D SWEEP
starts a field sweep in the MagnetControl VI
3D GET B
reads the physical field value from the MagnetControl VI
3D PSH
starts the warming or cooling of the persistent switch heaters in the MagnetControl VI

Figure 2.6: (a) Schematics of the software concept. All applications are based on three pillars with LabView as the programming language. b) Overview of the subVIs contained in the programming interface of the Magnet Control VI. The programming interfaces for the other software modules follow the same concept.

devices. In addition, it is desirable to have an automation software to control routine processes such as substrate cleaning. To meet these requirements a monitoring and control software package has been developed, which is based on three software components each realized as a LabView [67] virtual instrument (VI), as illustrated by the pillars in Fig. 2.6 (a):

- LabControl software for control and monitoring of the UHV system and the cryostat.
- MagnetControl software for control and monitoring of the triple axes magnet.
- Nanonis data acquisition software for the control and monitoring of the STM [68].

Each software component provides a programming interface for the communication with other VIs. In that sense the home-built VIs are formally equivalent to the LabView based commercial Nanonis software. A programming interface consists of a set of subVIs, as shown in Fig. 2.6b) for the case of the MagnetControl VI. They can be used in LabView block diagrams just as any other subVI. Every subVI in a programming interface establishes a well defined communication access to set, modify, or read a specific parameter or set of parameters in the respective VI.

Based on these subVIs, customized VIs for various purposes can be developed. Applications that have been accomplished already are shown in gray colors in Fig. 2.6a).

Automated Measurements

Using the Nanonis programming interface one can easily customize STM measurement series and run them in a computer controlled way. In combination with the MagnetControl and LabControl software and their programming interfaces this offers numerous new options for measurements that would not be possible with standard software alone. As a first application our new software package is used as a tool to conduct automated field dependent STM measurement series. This is illustrated in the block diagram shown in Fig. 2.7. A sequence of four STM images is taken using the Nanonis programming interface. Prior to each individual scan the magnetic field is ramped to a new value, i.e. by performing an in-plane rotation of the field vector by 90°. This is accomplished by using the MagnetControl programming interface. After pausing 5 seconds scanning is started. This type of measurement is particularly interesting as it offers a tool to save all relevant parameters of the experiment, i.e. magnetic field values, temperatures, etc. in a single file together with the image data.

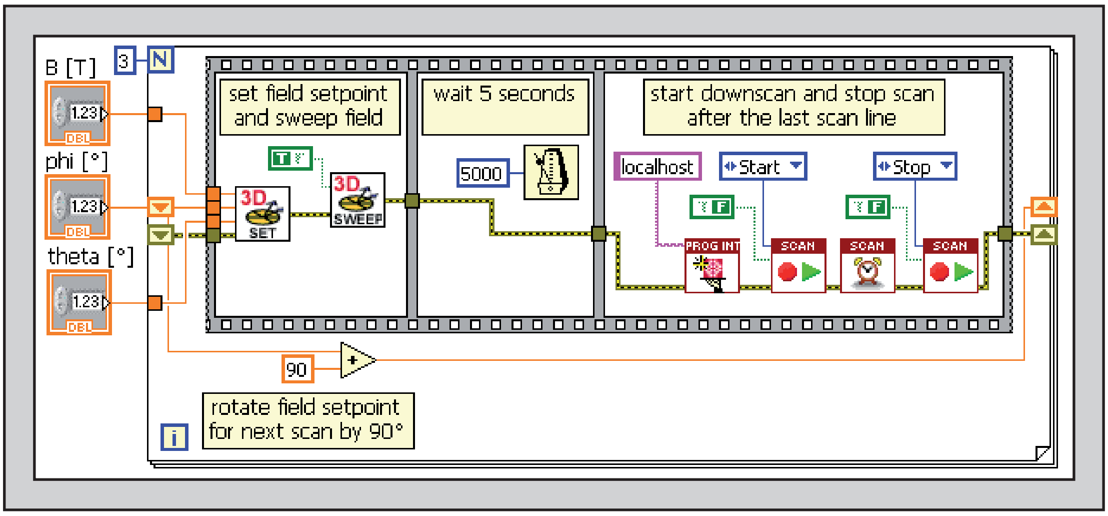
B [T]
phi [°]
theta [°]
3
N
1.23
DBL
set field setpoint and sweep field
wait 5 seconds
start downscan and stop scan after the last scan line
3D SET
3D SWEEP
5000
localhost
Start
Stop
PROG INT
SCAN
90
rotate field setpoint for next scan by 90°
i

Figure 2.7: Block diagram of a LabView VI controlling an automated cycle of STM measurements. Four images are taken at four different orientations of the external magnetic field. Between two image scans the field is rotated in-plane by 90° using the programming interface of the magnet control VI.

Automated Substrate Cleaning

To be able to operate the experimental setup at maximum efficiency it is valuable to run routine processes such as substrate cleaning at night or over the weekend. To increase efficiency the substrate cleaning processes in the preparation chamber were automated as a second application of the software package described above. The CleaningAutomation software is capable of ramping the power of the home-built e-beam heater power supply and thereby stabilizing the substrate temperature at elevated values, as shown in Fig. 2.2. In addition, it contains a PID control loop, which is used to stabilize the oxygen pressure in the preparation chamber at a desired value. This is achieved by applying an appropriate voltage to a piezo-controlled leak valve [69] using the EVC 300 power supply of the Focus evaporators [57]. The software allows to define complete cycles of substrate cleaning, as described previously [56] and run them in an automated fashion. During these cleaning cycles the input data necessary for the pressure control as well as for the operation of TSP and ion getter pump is provided by the programming interface based communication with the LabControl software, as described above.

Data Logging

Due to the MagnetControl and LabControl software all important status parameters of the laboratory are available on the computer at any time. Thus, it was straightforward to implement the option to log the data continuously to a file. The log files acquired so far turned out to be very useful for the analysis of unexpected events and problems.

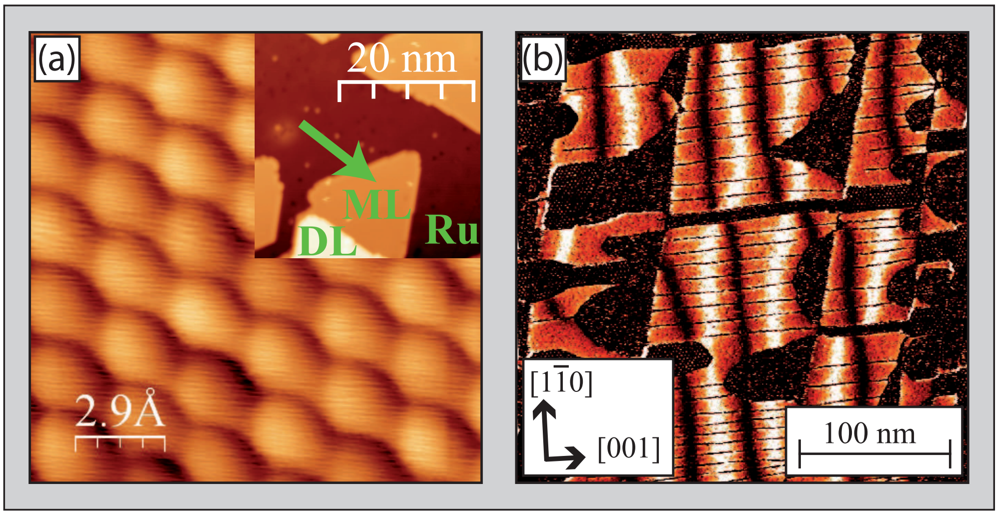

Figure 2.8: (a) STM image of the Fe ML on Ru(0001) demonstrating the atomic resolution capability of the microscope. $U = 10\,\mathrm{mV}$, $I = 7\,\mathrm{nA}$. The inset shows an overview of the sample with ruthenium (Ru), Fe ML, and Fe DL areas. The atomically resolved image was taken on the Fe island marked by the green arrow. (b) Spin-polarized $\mathrm{d}I/\mathrm{d}U$-map of 1.7 AL Fe on W(110) measured with an in-plane sensitive Fe coated W-tip. Domain walls show up in the DL as black and white lines along the [1$\bar{1}$0] axis. Tunneling parameters: I = 500 pA, U_{bias} = 550 mV.

By saving the log file directly to a network drive the current status of the whole experimental setup can be supervised from any remote computer having web access. This is a very convenient feature in particular during system bakeout.

2.5 Demonstration of functionality

Atomic resolution

Fig. 2.8 (a) shows an STM image of an Fe ML on Ru(0001) with atomic resolution, as recorded on the island marked by the green arrow in the inset. The measured lattice constant corresponds to the lattice constant of the underlying Ru(0001) surface confirming pseudomorphic growth in agreement with [70]. The inset shows an overview of the sample where the ruthenium substrate (Ru), Fe ML and Fe DL regions can be identified. As for all other STM images shown in this thesis, image processing has been done using the WSxM software [71].

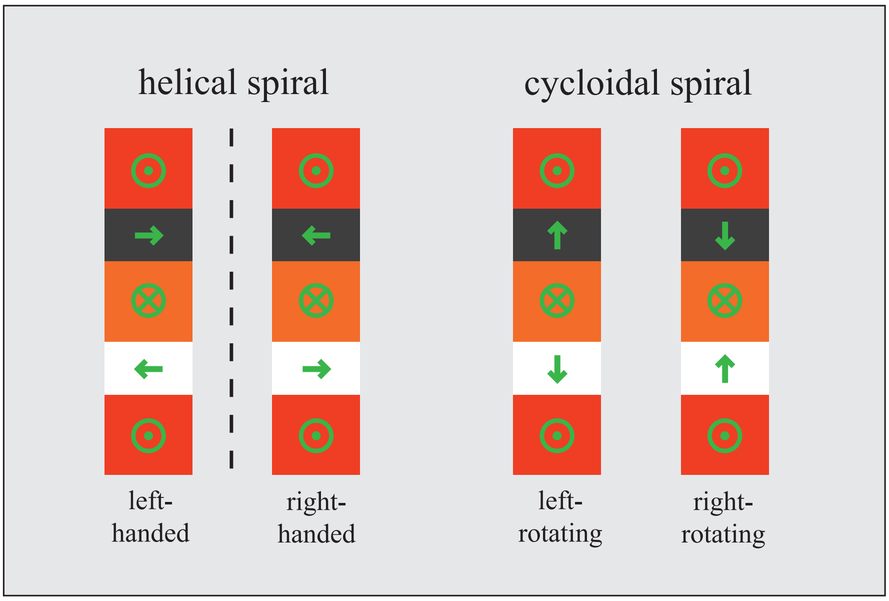

Figure 2.9: Right- and left-rotating helical and cycloidal spin spiral configurations. Due to the limitation to external magnetic fields along only one or at maximum two spatial directions both the spiral type and the rotational sense cannot be measured in traditional SP-STM setups.

Spin contrast

Fig. 2.8 (b) presents a spin-polarized dI/dU map recorded on 1.7 atomic layers of Fe on W(110) using an Fe coated W-tip being sensitive to the in-plane magnetization of the sample. The image shows the well known domain structure [30] with the bright and dark in-plane magnetized domain wall areas being predominantly aligned along the $[1\bar{1}0]$ direction of the underlying W(110) crystal. It was shown in previous studies [29, 30] that the observed domain structure has a unique rotational sense that does not depend on the position on the sample surface. In the following this type of magnetic spiral state is referred to as a unirotational spin spiral. However, both from previous studies and from the measurement in panel (b) it remains unclear if this spin spiral state is of cycloidal or helical type or if it is even a complex combination of both. In addition, it remains unclear if the spiral is right-rotating or left-rotating (cf. Fig. 2.9). Except for local distortions due to surface inhomogeneities, the observed spin spiral structure in the Fe DL on W(110) can essentially be described as a one-dimensional structure where along $[1\bar{1}0]$ all magnetic moments are aligned parallel. In particular, the observed spiral configuration can be described as a spin spiral propagating along [001]. The system will be discussed in much detail in the remainder of this thesis. By making use of the now available rotatable magnetic field it will be shown that the observed magnetic structure is an inhomogeneous right rotating cycloidal spin spiral whereas the other configurations in Fig. 2.9 can be ruled out.

Part II

The spin spiral in the Fe double layer on W(110)

The magnetic structure of the Fe DL on W(110) has been the subject of numerous experimental and theoretical studies during the past decades. Nevertheless, the structural details of the observed magnetic configurations could not be fully determined and the magnetic interactions driving these configurations remained puzzling. In some studies the observed magnetic structures were discussed in terms of classical domain patterns driven by the reduction of dipolar stray field energy [2]. Other studies discussed the observations in terms of spin spirals being driven by the so called DM interaction that results from the broken inversion symmetry at crystal surfaces [3, 72, 73]. However, none of the proposed models gives a consistent description of all experimental observations.

In the following five chapters the magnetic structure of the Fe DL on W(110) is discussed in detail. After introducing some general concepts for the description of magnetic thin films (*Chapter 3*), the results of previous studies on the sample system are summarized (*Chapter 4*). By making use of the unique capabilities of the experimental setup discussed in Part I, some hitherto not accessible experimental questions will be answered (*Chapter 5*). In particular, it will be shown that the spin spiral in the Fe DL on W(110) is flat right-rotating cycloid. Finally, the previously suggested micromagnetic models for the description of the Fe DL on W(110) are combined and extended significantly. It is shown that the resulting model gives the first theoretical description that consistently reproduces all experimental observations. The model is applied to closed Fe DL films (*Chapter 6*) as well as to Fe DL stripe systems, as measured in previous studies [29] (*Chapter 7*)

Chapter 3

Spin spirals and classical domains

The following discussion gives an overview of the magnetic interactions that play a role in ultrathin metallic films at crystal surfaces. The general concepts of spin spirals and classical domain structures are introduced. It is discussed how these structures can be quantitatively described using a micromagnetic model ansatz. In particular, the previously suggested micromagnetic models are summarized, combined and extended by the additional consideration of dipolar energy. The discussed model equations are important prerequisites for the understanding of the previous studies on the Fe DL on W(110), as summarized in *Chapter 4* and the subsequent analysis of closed Fe DL films and finite Fe DL stripe systems in the *Chapters 6-7*.

3.1 Magnetic interactions in metallic thin films

In general, the magnetic structure of magnetic thin film systems, such as the Fe DL on W(110), is determined by two types of interactions:

- Local interactions that result from the overlap of quantum mechanical wave functions, the Pauli exclusion principle, Coulomb interaction, and local spin-orbit coupling effects.
- Long-range dipolar interactions that depend on the magnetic stray field of the individual magnetic moments.

In the following both types of interactions will be discussed in detail.

Local interactions

Around the Fermi energy the band structure of the Fe DL on W(110) is dominated by spin-polarized 3d bands [74–76] and the magnetic properties are governed by the itinerant nature of the delocalized electrons that occupy these bands. The simplest model describing the magnetism of itinerant magnetic systems, such as the Fe DL on W(110), is the Hubbard model [77]:

$$H = -t \cdot \sum_{\langle ij \rangle, \sigma} a^{\dagger}_{i\sigma} a_{j\sigma} + u \cdot \sum_{i} a^{\dagger}_{i\uparrow} a_{i\uparrow} a^{\dagger}_{i\downarrow} a_{i\downarrow} \tag{3.1}$$

The model is described in the framework of second quantization, with $a^{\dagger}_{i\sigma}$ and $a_{j\sigma}$ being the creation and annihilation operators of an electron in a non-degenerate state being localized at the atomic lattice site i. The spin of this state is denoted σ. The first sum describes the hopping of electrons between neighboring lattice sites i and j, as defined by the transition matrix element t. The second sum defines the on-site Coulomb interaction of electrons at the same lattice site i, with u indicating the strength of the Coulomb repulsion. In the atomic limit ($t = 0$) the hopping of electrons is effectively suppressed, and the system is in an insulating state. In the opposite limit the hopping dominates and the system is characterized by the itinerant electrons in the delocalized electronic bands.

All magnetic properties of an itinerant magnetic system can be described in terms of the spatially dependent spin density of states $\mathbf{m}(x, y)$ that can be calculated using spin density functional theory [78, 79] and measured by SP-STM, as discussed in the context of Eq. (1.21)-(1.22). In general, $\mathbf{m}(x, y)$ is relatively homogeneous around the atomic lattice sites and varies mainly along the bonds between the atoms, as could be shown both experimentally [25, 80–82] and theoretically [83, 84] for a number of materials. Consequently, it seems to be well justified to integrate $\mathbf{m}(x, y)$ over the homogeneous areas around each lattice site and consider the resulting macro spins as localized magnetic moments. In particular, such an approach is equivalent to considering the limit $T \ll U$ where the hopping term in Eq. (3.1) is treated as a perturbation with respect to the interaction term. Taking spin-orbit coupling into account, in this limit the Hubbard model can be mapped on an effective Heisenberg Hamiltonian [85–88]:

$$\begin{gathered} H = \sum_{i \neq j} \mathbf{S}_i \mathbf{J}_{ij} \mathbf{S}_j + \sum_{i} \mathbf{S}_i \mathbf{K}_i \mathbf{S}_i \\ \mathbf{S}_i = \begin{pmatrix} S_x \\ S_y \\ S_z \end{pmatrix}_i , \quad \mathbf{S}_j = \begin{pmatrix} S_x \\ S_y \\ S_z \end{pmatrix}_j , \quad \mathbf{J}_{ij} = \begin{pmatrix} J_{xx} & J_{xy} & J_{xz} \\ J_{yx} & J_{yy} & J_{yz} \\ J_{zx} & J_{zy} & J_{zz} \end{pmatrix}_{ij} \end{gathered} \tag{3.2}$$

The first term of the Hamiltonian describes the energy of the pair interactions between individual macro spins. $\mathbf{J}_{ij}$ determines the magnetic coupling energy of one single pair of spins ($\mathbf{S}_i$, $\mathbf{S}_j$) being localized at the lattice positions i and j. $\mathbf{S}_i$ and $\mathbf{S}_j$ are described as vectors and thus refer to classical magnetic moments. They are normalized such that $|\mathbf{S}_i| = \left|\mathbf{S}_j\right| = 1$. The second term of the Hamiltonian describes the on-site crystalline anisotropy energy. It is given as the sum of the anisotropy energies of the individual magnetic moments at the lattice sites i. At each lattice site the anisotropy energy is fully described by the anisotropy tensor $\mathbf{K}_i$ and the respective magnetic moment $\mathbf{S}_i$.

Like every quadratic matrix $\mathbf{J}$ can be decomposed:

$$\begin{gathered}\mathbf{J} = \mathrm{J}\mathbb{1} + \mathbf{J}^{\mathrm{S}} + \mathbf{J}^{\mathrm{A}} \\ \mathrm{J} = \frac{1}{3}\mathrm{Tr}\,(\mathbf{J}) \quad , \quad \mathbf{J}^{\mathrm{S}} = \frac{1}{2}\left(\mathbf{J} + \mathbf{J}^{\mathrm{T}}\right) - J\mathbb{1} \quad , \quad \mathbf{J}^{\mathrm{A}} = \frac{1}{2}\left(\mathbf{J} - \mathbf{J}^{\mathrm{T}}\right)\end{gathered} \tag{3.3}$$

Here, $\mathbf{J}^{\mathrm{S}}$ and $\mathbf{J}^{\mathrm{A}}$ describe the traceless symmetric and the antisymmetric part of $\mathbf{J}$, respectively. In the following the coordinate system is chosen such that $\mathbf{J}^{\mathrm{S}}$ is diagonal.

Based on the definition of the so-called DM vector

$$\mathbf{D} = \begin{pmatrix} D_x \\ D_y \\ D_z \end{pmatrix} := \begin{pmatrix} \frac{J_{yz}-J_{zy}}{2} \\ \frac{J_{zx}-J_{xz}}{2} \\ \frac{J_{xy}-J_{yx}}{2} \end{pmatrix} \tag{3.4}$$

the matrix $\mathbf{J}^{\mathrm{A}}$ can be simplified:

$$\begin{aligned}\mathbf{J}^{\mathrm{A}} &= \begin{pmatrix} 0 & \frac{J_{xy}-J_{yx}}{2} & \frac{J_{xz}-J_{zx}}{2} \\ -\frac{J_{xy}-J_{yx}}{2} & 0 & \frac{J_{yz}-J_{zy}}{2} \\ -\frac{J_{xz}-J_{zx}}{2} & -\frac{J_{yz}-J_{zy}}{2} & 0 \end{pmatrix} \\ &= \begin{pmatrix} 0 & D_z & -D_y \\ -D_z & 0 & D_x \\ D_y & -D_x & 0 \end{pmatrix}\end{aligned} \tag{3.5}$$

Finally, the spin Hamiltonian Eq. (3.2) can be rewritten using Eq. (3.3)-(3.5):

$$\boxed{H = \sum_{i} \mathbf{S}_i \cdot \mathbf{K}_i \cdot \mathbf{S}_i + \sum_{i \neq j} \mathrm{J}_{ij} \mathbf{S}_i \mathbf{S}_j + \sum_{i \neq j} \mathbf{S}_i \mathbf{J}^{\mathrm{S}}_{ij} \mathbf{S}_j + \sum_{i \neq j} \mathbf{D}_{ij} \cdot \left(\mathbf{S}_i \times \mathbf{S}_j \right)} \tag{3.6}$$

In this form the Hamiltonian is more illustrative, since the summands on the right hand side can now be identified with the physical interactions being discussed in this thesis. It was already mentioned that the first term describes the energy contribution of the crystalline anisotropy. The second term corresponds to the Hamiltonian of a classical Heisenberg model and describes the contribution of isotropic magnetic exchange. The third term extends the model by the contribution of anisotropic magnetic exchange. The last term finally represents the so called DM interaction [89–92] that will be discussed in more detail in the following section. It is fully determined by the DM vectors $\mathbf{D}_{ij}$. In analogy to Eq. (3.2) the summations go over magnetic moments at the lattice sites i and j, respectively.

Dzyaloshinskii-Moriya interaction

More than 50 years ago, Dzyakloshinskii derived on the basis of symmetry arguments, that in the presence of broken inversion symmetry spin-orbit coupling gives rise to antisymmetric exchange interactions that can be expressed in formal equivalence to the last term on the right hand side of Eq. (3.6) [89, 90]. Finally, Moriya showed how to calculate this contribution for the special case of localized magnetic moments using a microscopic model relying on direct exchange interactions between two neighboring magnetic sites in the presence of on-site spin-orbit coupling [91, 92]. Both Dzyaloshinskii and Moriya considered the discussed interaction as the driving force of the weak ferromagnetism observed in several antiferromagnetic insulators, such as $\alpha - \mathrm{Fe}_2\mathrm{O}_3$ and CrF_3. Finally, it was proposed that the DM interaction also plays an important role for the observed magnetic order in $\mathrm{La}_2\mathrm{CuO}_4$ and $\mathrm{YBa}_2\mathrm{Cu}_3\mathrm{O}_6$-type perovskite compounds [93–97], as well as in the chiral bulk magnet MnSi [4].

In this thesis the magnetic structure of the Fe DL on W(110) is investigated. However, in this context the microscopic model of Moriya is no longer applicable, since it does not account for the indirect magnetic interactions in itinerant systems, i.e. it does not account for interactions mediated by the W(110) surface. In order to account for this deficiency the special case of two distinct magnetic atoms interacting in a RKKY-like manner via a nonmagnetic atom with strong spin orbit coupling was investigated [98].

The scenario is illustrated in Fig. 3.1, where the orange circles represent the magnetic atoms and the violet circle corresponds to the non-magnetic atom mediating the indirect

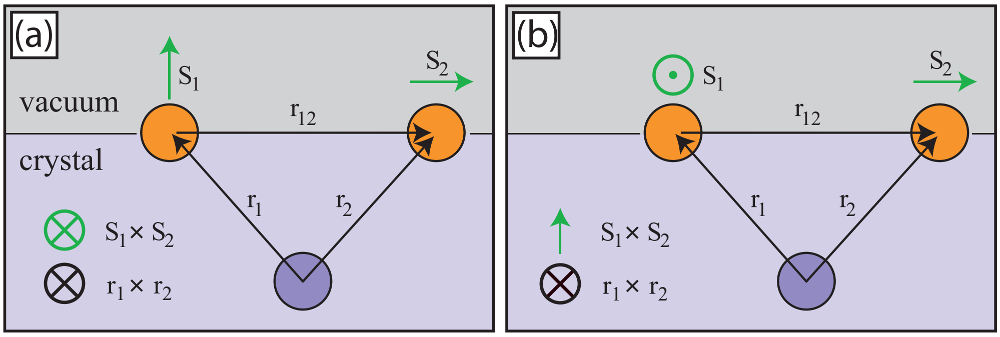

Figure 3.1: Indirect asymmetric exchange interaction between two magnetic atoms (orange) mediated via a non-magnetic atom (violet) with strong spin-orbit coupling. The magnetic moments of the magnetic atoms are illustrated for two different scenarios (green). (a) Rotation of the magnetic moments via the out-of-plane direction. The cross product vectors $\mathbf{S}_1 \times \mathbf{S}_2$ and $\mathbf{r}_1 \times \mathbf{r}_2$ are collinear. Their parallel or antiparallel alignment, and thus the sign of the respective contribution to the DM energy, depends on the rotational sense of the magnetic moments. In (b) the rotation of the magnetic moments is confined to the surface plane, i.e. the cross product vectors have a perpendicular alignment. Consequently, the DM energy vanishes.

coupling. The figure visualizes two different scenarios concerning the relative orientation of the magnetic moments. In (a) the magnetic moments rotate via the out-of-plane direction while in (b) the rotation is confined to the surface plane. Like for the case of direct exchange coupling [91, 92] the Hamiltonian can be written in formal equivalence to the last term on the right hand side of Eq. (3.6). For the case of indirect interaction between two magnetic atoms in spin glasses doped with heavy impurity atoms [99] the Hamiltonian was shown to be of the following form:

$$\boxed{H_{\mathrm{DM}} = -V(\xi)\,\frac{\sin\left[k_{\mathrm{F}}\left(r_1 + r_2 + r_{12}\right) + \eta\right] \cdot \mathbf{r}_1 \cdot \mathbf{r}_2}{r_1 \cdot r_2 \cdot r_{12}}\,(\mathbf{r}_1 \times \mathbf{r}_2)\,(\mathbf{S}_1 \times \mathbf{S}_2)} \tag{3.7}$$

Here, the nomenclature refers to Fig. 3.1, with $r_i = |\mathbf{r}_i|$ and $r_{12} = |\mathbf{r}_2 - \mathbf{r}_1|$. $V(\xi)$ is a prefactor depending on the spin orbit coupling constant ξ of the nonmagnetic atom (violet), k_{F} is the Fermi vector, and η is a parameter indicating a phase shift induced by the indirect interaction.

Eq. (3.7) results in a finite energy contribution only in the case of panel (a) where the cross product vectors $\mathbf{S}_1 \times \mathbf{S}_2$ and $\mathbf{r}_1 \times \mathbf{r}_2$ are collinear. The sign of the energy depends on the parallel or antiparallel orientation of the cross product vectors, i.e. on the rotational sense of the magnetic configuration. The equation is of great value not only for the description of spin glasses but also for itinerant magnetic systems such as metals and semiconductors. In particular, it can be translated to the case of two interacting magnetic atoms on a surface in the presence of strong spin orbit coupling effects, i.e. it can be applied to the case of the Fe DL on W(110) being the subject of the following chapters.

Dipolar interaction

Eq. (3.2) and Eq. (3.6) only contain magnetic interactions of local character. However, a complete description of magnetism in thin films, such as the Fe DL on W(110), is only possible if the long range dipolar coupling of magnetic moments is additionally taken into account. The respective Hamiltonian is given by:

$$\boxed{H_{\text{dip}} = D_{\text{dip}} \sum_{i,j} \left[\frac{\mathbf{S}_i \cdot \mathbf{S}_j}{\left|\mathbf{r}_{ij}\right|^3} - 3 \frac{\left(\mathbf{S}_i \cdot \mathbf{r}_{ij}\right)\left(\mathbf{S}_j \cdot \mathbf{r}_{ij}\right)}{\left|\mathbf{r}_{ij}\right|^5} \right]} \tag{3.8}$$

Here, the summation goes over all pairs of spins $\mathbf{S}_i, \mathbf{S}_j$ with their relative distance being given by $|\mathbf{r}_{ij}|$. D_{dip} is the dipolar coupling constant.

3.2 Micromagnetic continuum model

It was shown above that the interactions driving the ordering of magnetic structures can be described in terms of a discrete model based on single magnetic moments. However, within this approach the calculation of the energy minimum can be extremely complicated, in particular if the number of magnetic moments is large and if long-range dipolar interactions are involved. Thus, in general the magnetic ground state is only accessible on the basis of approximation techniques such as Monte-Carlo simulations.

If a magnetic structure changes on a length scale being large compared to the lattice period of the underlying crystal, it can alternatively be described in terms of a micromagnetic model. Instead of a discrete set of unit vectors $\{\mathbf{S}_i\}$ the magnetic structure is described by the continuous vector field $\mathbf{M}(x, y, z)$ indicating the spatial variation of the magnetization vector. Like the magnitude of the discrete magnetic moments $\mathbf{S}_i$ the magnetization vector is normalized to $|\mathbf{M}| = 1$.

Local spin-spin interactions

For the special case of a magnetization profile varying only along a unique propagation direction x the micromagnetic analogon of Eq. (3.6) is given by: [72, 73][1]

$$E\left[\mathbf{M}(x)\right] = d \cdot b \cdot \int \mathbf{M}(x) \cdot \tilde{\mathbf{K}} \cdot \mathbf{M}(x) + \tilde{A} \cdot \dot{\mathbf{M}}^2(x) + \tilde{\mathbf{D}} \cdot \left(\mathbf{M}(x) \times \dot{\mathbf{M}}(x)\right) \,\mathrm{d}x. \quad (3.9)$$

The calculation of $\tilde{A}$, $\tilde{\mathbf{D}}$ and $\tilde{\mathbf{K}}$ depends on the lattice structure of the underlying crystal. For the W(110) surface a detailed discussion is given in [72]. The integrand denotes the spatial variation of the local energy density per volume along the propagation direction x. The parameters d and b refer to the spatial extensions of the magnetic structure along the directions perpendicular to x. $\dot{\mathbf{M}}$ indicates the derivative of $\mathbf{M}$ by the spatial variable x. Since no time derivative is needed in the framework of this thesis, this notation will be used as a standard abbreviation in the following.

For a spatially periodic magnetic structure the local energy density per volume is periodic as well. Consequently, the average energy density can be calculated by integration over one period and division by the period length λ_x:

$$\varepsilon\left[\mathbf{M}(x)\right] = \frac{\int_0^{\lambda_x} \overbrace{\mathbf{M}(x) \cdot \tilde{\mathbf{K}} \cdot \mathbf{M}(x)}^{\text{anisotropy}} + \overbrace{\tilde{A} \cdot \dot{\mathbf{M}}^2(x)}^{\text{exchange}} + \overbrace{\tilde{\mathbf{D}} \cdot \left(\mathbf{M}(x) \times \dot{\mathbf{M}}(x)\right)}^{\text{DM interaction}} \,\mathrm{d}x}{\lambda_x}. \quad (3.10)$$

In formal analogy to Eq. (3.6) the micromagnetic ansatz considers three types of interactions: crystalline anisotropy, magnetic exchange, and the DM interaction. Compared to the discrete model, the exchange energy is now described by the effective exchange stiffness $\tilde{A}$. In an analogous way, the DM vectors $\mathbf{D}_{ij}$ are replaced by an effective vector $\tilde{\mathbf{D}}$. Finally, the crystalline anisotropy tensor $\mathbf{K}$ is replaced by its micromagnetic counterpart $\tilde{\mathbf{K}}$, as well. In the following the tilde will be omitted since all further discussions will be based on the micromagnetic continuum ansatz and thus a confusion with the discrete model parameters can be excluded. According to Eq. (3.10) the micromagnetic energy density is essentially determined by the tensorial and vectorial quantities $\mathbf{A}$, $\mathbf{K}$ and $\mathbf{D}$. Consequently, the magnetic ground state depends on the relative orientation of the easy, hard and intermediate magnetic axis, the direction of the $\mathbf{D}$-vector and the directional dependence of the magnetic exchange interaction.

According to the short discussion in the context of Fig. 2.8 (b) and Fig. 2.9 the magnetic structure of the Fe DL on W(110) is essentially one-dimensional and propagates along

---

[1] In the context of the Fe DL on W(110) this is a reasonable assumption that has been confirmed by experimental observations [1]. This issue will be discussed in more detail in Chapter 5.

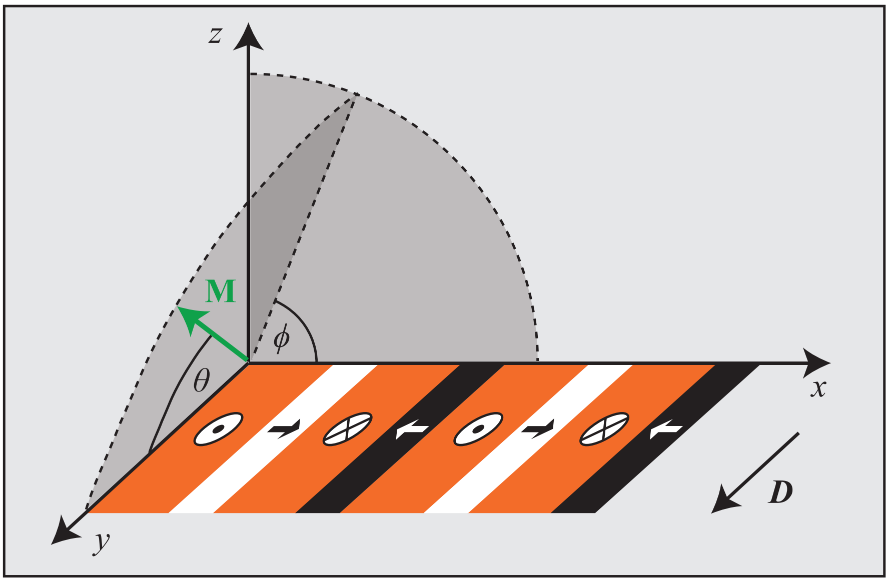

Figure 3.2: Definition of the coordinate system for a magnetic surface structure propagating along one of the high symmetry directions of the underlying crystal surface. The x, y, and z-axis are oriented along the propagation direction, the **D**-vector, and the surface normal, respectively.

the crystallographic high symmetry direction [001]. In a previous study [72, 73] this special case was analyzed in detail. In particular, Eq. (3.10) was investigated, relying on the idea that the observed spiral structure is induced by the DM interaction. This is a reasonable assumption, since all other interactions are symmetric and can therefore not account for the observed unique rotational sense. However, it turns out that, for a propagation direction along one of the high symmetry axes, the DM interaction only results in a non-vanishing energy contribution if the spin spiral is of cycloidal type, and if additionally the effective **D**-vector points in-plane and normal to the propagation direction [91]. For the Fe DL on W(110) the required orientation of the **D**-vector is supported by DFT calculations [3, 72] that indeed suggest an orientation along [1$\bar{1}$0]. The cycloidal character of the spin spiral remains to be confirmed experimentally (cf. Chapter 5). Starting from the required direction of **D**, the observed propagation direction, and the direction of the surface normal, one can chose a right-handed coordinate system, as visualized in Fig. 3.2. With respect to this coordinate system **D** and **K** simplify considerably.

$$\mathbf{D} = \begin{pmatrix} 0 \\ D \\ 0 \end{pmatrix} \quad , \quad \mathbf{K} = \begin{pmatrix} K_x & 0 & 0 \\ 0 & K_\mathrm{D} & 0 \\ 0 & 0 & K_z \end{pmatrix} . \tag{3.11}$$

Finally, the magnetic structure can be described in terms of polar coordinates $\theta(\mathbf{r})$, $\phi(\mathbf{r})$, as visualized in Fig. 3.2. The magnetization **M** is then given by:

$$\mathbf{M}(x) = \begin{pmatrix} M_x(x) \\ M_y(x) \\ M_z(x) \end{pmatrix} = \begin{pmatrix} \sin[\theta(x)] \cdot \cos[\phi(x)] \\ \cos[\theta(x)] \\ \sin[\theta(x)] \cdot \sin[\phi(x)] \end{pmatrix}. \tag{3.12}$$

Using this definition, Eq. (3.10) can be rewritten in terms of polar coordinates as well:

$$\boxed{\begin{aligned} \varepsilon[\theta(x), \phi(x)] \quad = \quad & \frac{1}{\lambda_x} \cdot \int_0^{\lambda_x} A\left(\dot{\theta}^2 + \sin^2\theta\left|\dot{\phi}\right|^2\right) \pm D\sin^2\theta\left|\dot{\phi}\right| \\ & + K_x \sin^2\theta\cos^2\phi + K_\mathrm{D}\cos^2\theta + K_z\sin^2\theta\sin^2\phi \, \mathrm{d}x \end{aligned}} \tag{3.13}$$

Now, the parameters A, K_x, K_y, and K_D are of scalar type in contrast to the tensorial quantities $\mathbf{A}$ and $\mathbf{K}$ used before. In an analogous way, the Dzyaloshinskii parameter D is a scalar as well, in contrast to the previously used vectorial quantity $\mathbf{D}$. Note, that by definition of the coordinate system (Fig. 3.2) D is positive. Thus, in Eq. (3.13) the + (-) refers to a positive (negative) value of $\dot{\phi}$, i.e. the parallel (antiparallel) orientation of the cross product vector $\mathbf{M}(x) \times \dot{\mathbf{M}}(x)$ in Eq. (3.10) with respect to the y-axis of the coordinate system.

There are essentially three different scenarios for the relative alignment of the **D**-vector and the hard, easy, and intermediate magnetic axis, respectively:

- **D** pointing along the easy magnetic axis
- **D** pointing along the hard magnetic axis
- **D** pointing along the intermediate magnetic axis

In the context of the Fe DL on W(110) the first scenario can be ruled out from an experimental point of view, since it could be shown that the easy axis is pointing along the z-axis [29, 100]. Only in extremely narrow Fe DL islands and stripes an in-plane magnetization has been observed [101, 102]. However, instead of an in-plane magnetic easy axis this observation was attributed to the magnetic exchange coupling to the Fe ML. In contrast to the direction of the easy magnetic axis, the directions of the hard and intermediate axis remain unknown from an experimental point of view. Thus, the two remaining scenarios will be discussed in the following.

D pointing along the hard magnetic axis: $K_z < K_x < K_\mathrm{D}$

For this scenario the magnetization vector is confined to the (xz)-plane, since any deviation would increase the energy density contributions of both the anisotropy and the DM interaction. Consequently, the magnetic structure can be described by only one angle $\phi(x)$, with $\theta(x)$ being equal to zero. The energy density functional Eq. (3.13) simplifies to:

$$\boxed{\begin{gathered}\varepsilon\left[\phi(x)\right] = \frac{\int_0^{\lambda_x} A\cdot\left|\dot{\phi}\right|^2 \pm D\cdot\left|\dot{\phi}\right| + K_\mathrm{c}\cdot\cos^2\!\phi\ \mathrm{d}x}{\lambda_x} + \text{constant} \\[2ex] K_\mathrm{c} = K_x - K_z\end{gathered}} \tag{3.14}$$

Eq. (3.14) was discussed in detail in [103, 104]. It was shown that the magnetic ground state is either a collinear single domain state or a spin spiral with the spiral profile being given by:

$$\boxed{\begin{gathered}\phi(x) = \pm\mathrm{am}\left(\frac{1}{\delta\sqrt{\frac{A}{K_\mathrm{c}}}}\cdot x, \delta\right) \\[2ex] \lambda_x = 4\delta\cdot\sqrt{\frac{A}{K_\mathrm{c}}}\cdot\mathrm{F}\left(\frac{\pi}{2},\delta\right) \quad , \quad D = \frac{4}{\pi\delta}\cdot\mathrm{E}\left(\frac{\pi}{2},\delta\right).\end{gathered}} \tag{3.15}$$

Here, am denotes the Jacobi amplitude function. The parameter $\delta \in [0,1]$ defines the inhomogeneity of the profile, i.e. the deviation from a perfect linear behavior of $\phi(x)$. It is related to the spiral period λ_x via F, the incomplete elliptic integral of the first kind [105]. The ±-sign determines the rotational sense of the spin spiral. Since the spiral state is induced by the DM interaction, the spiral period λ_x depends on D. Consequently, there is also a functional relationship between D and the inhomogeneity parameter δ. It is mediated by E, the incomplete elliptic integral of the second kind.

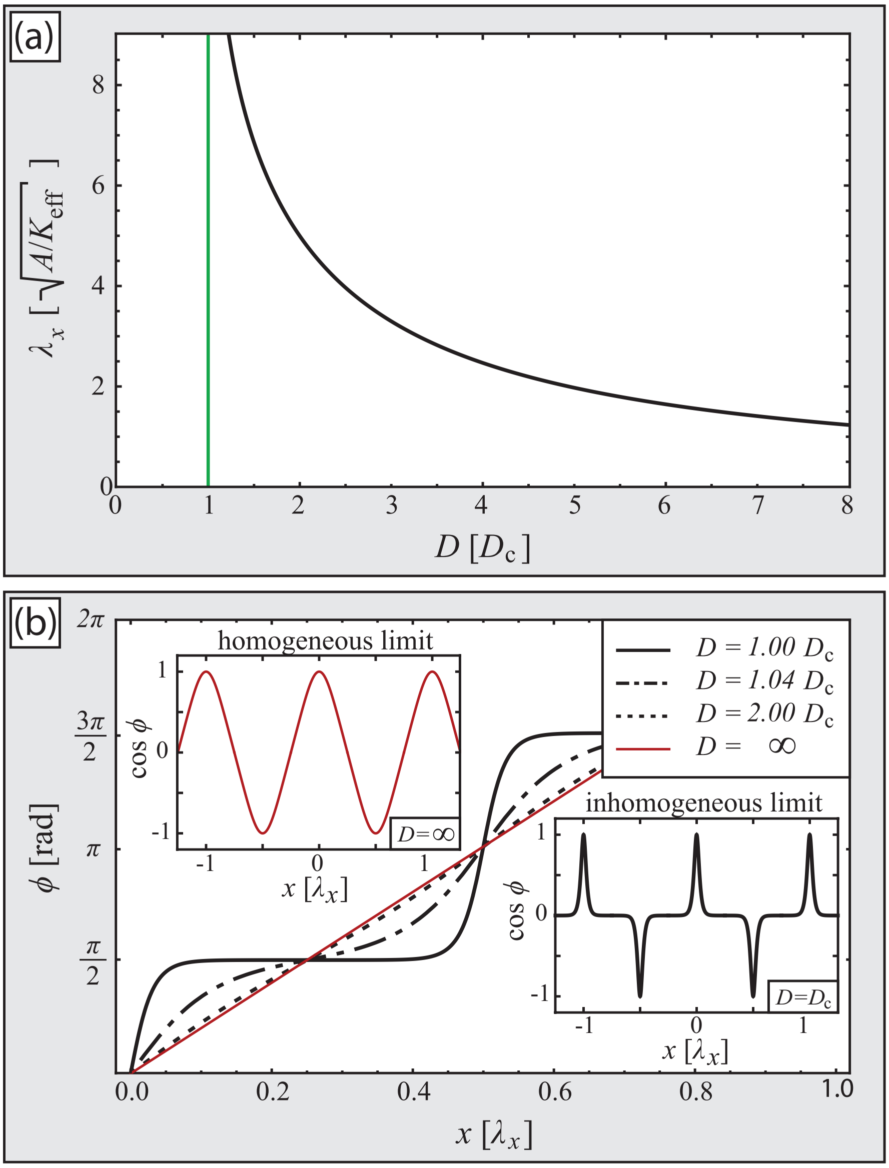

Figure 3.3: (a) Spiral period λ_x as a function of the Dzyaloshinskii parameter D. The value of λ_x diverges with D approaching D_{c} as defined in Eq. (3.16). (b) Inhomogeneity of the spin spiral profile. The figure visualizes the function $\phi\,(x)$ according to Eq. (3.15) for various values of D. In order to allow for a better comparison all lengths are given in units of λ_x. With increasing D the spiral profile approaches the homogeneous limit, where $\phi(x)$ becomes a linear function of x (red line) and the in-plane component of the magnetization is a sinusoidal function of the position along the propagation direction of the spiral (upper inset). In the opposite limit $D \searrow D_{\mathrm{c}}$ the spiral profile converges to a periodic sequence of infinitely spaced classical domain walls, as visualized in the lower inset.

For the phase transition between the collinear and the spin spiral regime (Eq. 3.15) there is a critical value of the DM parameter:

$$\boxed{D = D_\mathrm{c} := \frac{4}{\pi}\sqrt{A \cdot K_\mathrm{c}}.} \tag{3.16}$$

For $D < D_\mathrm{c}$ the magnetic ground state is collinear, the spin spiral state is observed for $D > D_\mathrm{c}$.

Fig. 3.3 (a) visualizes the spiral period λ_x as a function of D. While λ_x is small for large values of D it diverges for $D \searrow D_\mathrm{c}$. Fig. 3.3 (b) shows $\phi(x)$, as given by Eq. (3.15), for three different values of D (and thus three different values of δ and λ_x). For a better comparison of the curves all lengths are given in units of λ_x. With increasing D the spiral profile approaches the homogeneous limit, where $\phi(x)$ becomes a linear function of x (red line) and the in-plane component of the magnetization is a sinusoidal function of the position along the propagation direction of the spiral (upper inset). In the opposite limit $D \searrow D_\mathrm{c}$ the spiral profile converges to a periodic sequence of infinitely spaced classical domain walls, as visualized in the lower inset. The shape and energy of one single domain wall will be discussed below, after considering the second scenario where **D** points along the intermediate magnetic axis.

D pointing along the intermediate magnetic axis: $K_z < K_\mathrm{D} < K_x$

For D pointing along the intermediate magnetic axis the DM interaction continues to favor a rotation of **M** in the xz-plane. However, in contrast to the previously discussed scenario, now the anisotropy energy is minimized by avoiding the magnetically hard x-direction and deviating from the xz-plane, while $\cos\phi$ is large, i.e. while the magnetization is aligned along the xy-plane (Fig. 3.4). Consequently, the resulting magnetic configuration must in general be described by two independent angles (θ, ϕ), according to Eq. (3.13). The values of θ and ϕ depend on the relative strength of the involved magnetic interactions.

The discussed scenario was investigated in detail in [72]. It was shown that for small values of D the magnetic ground state is a collinear single domain state. At $D = D_\mathrm{c}$ the system undergoes a phase transition to the spin spiral regime, in analogy to the previously discussed scenario. However, now the spiral energy can be further minimized by deviating from the flat spin spiral configuration as long as the value of D is

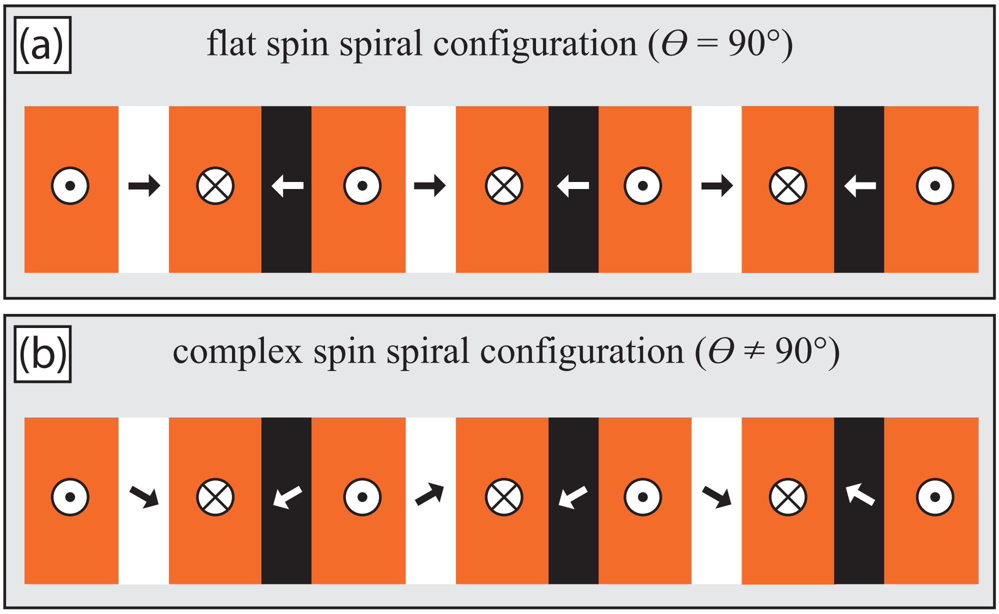
(a)
flat spin spiral configuration (Θ = 90°)
(b)
complex spin spiral configuration (Θ ≠ 90°)

Figure 3.4: (a) Flat spin spiral configuration as discussed for the case of **D** pointing along the hard magnetic axis. (b) Complex spin spiral configuration as discussed for the case of **D** pointing along the intermediate magnetic axis. The complex spiral configuration only exists if Eq. (3.17) is fulfilled. Otherwise, it reduces to the flat configuration shown in (a).

below a certain threshold. Note, that even below this threshold the deviation from the flat configuration can only prevail if the anisotropy energy difference between the x- and y-direction is large compared to the one between the y- and z-direction. The exact condition for the existence of the complex spiral phase was derived in [72]:

$$K_x - K_y > \frac{1}{0.08}\left(K_y - K_z\right). \tag{3.17}$$

Otherwise, the spiral rotation remains confined to the xz-plane for all values of $D > D_\mathrm{c}$ and the magnetic ground state can be described by Eq. (3.14)-(3.16), as discussed before.

It will be shown in Chapter 5 that for the Fe DL on W(110) the complex spin spiral configuration can be ruled out on the basis of measurements using the experimental setup discussed in Part I. Consequently, in Chapter 6-7 the theoretical analysis of the experimental observations can be based on Eq. (3.14)-(3.16) although the direction of the intermediate magnetic axis remains unknown.

Domain wall shape and energy

Even if the Dzyaloshinskii parameter D is too small to induce a spin spiral state, a ferromagnetic structure of sufficient size can decay into domains due to surface defects and additional energy contributions such as the hitherto not considered dipolar, i.e. demagnetizing, energy that will be discussed in the following section. In analogy to the previous scenario with $D > D_\mathrm{c}$ the domain wall shape and energy can be calculated on the basis of Eq. (3.14) using variational techniques. In the following, the domain wall is forced into the system by the choice of appropriate boundary conditions.

$$\lim_{x\to\pm\infty} [\phi(x)] = \pm\frac{\pi}{2} \tag{3.18}$$

Starting from Eq. (3.14) one gets

$$\begin{aligned}
E_\mathrm{wall} &= \int_{-\infty}^{\infty} \left[A\dot{\phi}^2 + K_\mathrm{c}\cos^2\phi\right]\mathrm{d}x + \int_{-\infty}^{+\infty}\left[D\dot{\phi}\right]\mathrm{d}x \\
&= \int_{-\infty}^{\infty} \left[A\dot{\phi}^2 + K_\mathrm{c}\cos^2\phi\right]\mathrm{d}x + D\cdot\int_{-\frac{\pi}{2}}^{+\frac{\pi}{2}} d\phi \\
&= \int_{-\infty}^{\infty} \left[A\dot{\phi}^2 + K_\mathrm{c}\cos^2\phi\right]\mathrm{d}x \pm D\pi. \qquad (3.19)
\end{aligned}$$

Applying variational techniques to the integral remaining on the right hand side [106] results in the domain wall energy E_wall and the domain wall shape $\phi(x)$:

$$\boxed{\begin{aligned}
E_\mathrm{wall} &= 2\int_{-\infty}^{\infty} A\dot{\phi}^2\mathrm{d}x + \pm D\cdot\pi \\
&= 2\int_{-\infty}^{\infty} K_\mathrm{c}\cos^2\phi\ \mathrm{d}x \pm D\cdot\pi \\
&= 4\sqrt{AK_\mathrm{c}} \pm \begin{cases} 0 & ;\ \text{Bloch wall} \\ D\cdot\pi & ;\ \text{Néel wall} \end{cases}
\end{aligned}} \tag{3.20}$$

$$\boxed{\phi(x) = \arcsin\left(\tanh\left(\frac{x}{w_0/2}\right)\right), \qquad w_0 := 2\sqrt{\frac{A}{K_\mathrm{c}}}.} \tag{3.21}$$

Here, w_0 is a measure of the domain wall width, as used in the remainder of this thesis. In analogy to Eq. (3.14) the ±-sign denotes right and left rotating domain walls, respectively. Consequently, in the presence of the DM interaction right- and left-rotating Néel-type domain walls are not energetically degenerate. For large values of D the energy split can become large, such that for one sense of rotation the domain wall energy may eventually become negative for $D > D_c$. Note, that here D_c has the same value as in Eq. (3.16). Thus, a transition from positive to negative domain wall energies corresponds to a transition from the classical domain to the spin spiral regime.

In the presence of an external magnetic field B along the surface normal domains being magnetized parallel to the field are larger than those with an antiparallel magnetization. For high enough fields, pairs of domain walls are formed. The profile of such a wall pair, sometimes denoted as a 360° wall, can be calculated analytically [107]:

$$\boxed{\begin{gathered} \phi_{360}(x) = \sum_{+,-} \arcsin\left(\tanh\left(\frac{x \pm c}{w/2}\right)\right) \\ c := \frac{w}{2} \arcsin\left(\sqrt{\frac{2K_c}{M_s \cdot B}}\right) \quad , \quad w := 2\sqrt{\frac{A}{K_c + \frac{M_s}{2} \cdot B}} \end{gathered}} \tag{3.22}$$

Here, $\pm c$ denote the centers of the two 180° walls and w indicates their individual wall width that differs from the one given in Eq. (3.21) due to interactions between the walls.

According to Eq. (3.21)-(3.22), both the domain wall shape of a single domain wall and the profile of a domain wall pair are independent of D, i.e. they are not affected by the DM interaction. In Chapter 6 this property will turn out to be of highest significance, as it allows to generalize the results of a previous study [1] to the case of a non-vanishing energy contribution of the DM interaction although it has not been considered in the original work.

Demagnetizing energy

Thus far, for the calculation of the energy density only local interactions were considered while the long-range dipolar interactions were omitted. In order to overcome this deficiency it is crucial to incorporate the contribution of dipolar energy (Eq. (3.8)) into the micromagnetic model ansatz discussed before (Eq. (3.14)).

The dipolar energy of a magnetic body is equivalent to the energy of the demagnetizing field $\mathbf{H}_d$ since, according to Maxwell's equation, $\mathbf{H}_d$ and the magnetization $\mathbf{M}$ of the body are related quantities:

$$\text{div}\,[\mathbf{B}] = -\text{div}\left[\mu_0\left(\mathbf{H}_\text{d} + \mathbf{M}\right)\right] = 0. \tag{3.23}$$

Based on this relationship the demagnetizing energy, can be calculated in two different ways [108]:

$$E_\text{d} = \frac{\mu_0}{2} \cdot \int\limits_{\text{all space}} \mathbf{H}_\text{d}^2 \,\text{d}V = -\frac{\mu_0}{2} \cdot \int\limits_{\text{sample}} \mathbf{H}_\text{d} \cdot \mathbf{M} \,\text{d}V. \tag{3.24}$$

Here, the first integral extends over all space. The second integral is mathematically equivalent and refers to the finite sample volume. This mathematical equivalence may be illustrated by the following handwaving argument: The energy of the field H_d can be calculated by considering the complete field (first integral). However, the source of the field, i.e. the magnetization M inside the magnetic body, necessarily contains the same information as the complete field. Thus it must be possible to calculate the field energy on the basis of the magnetization inside the magnetic body (second integral). In analogy to Eq. (3.10) the averaged demagnetizing energy density can be calculated inside the sample volume V starting from Eq. (3.24):

$$\varepsilon_\text{d} = -\frac{1}{V} \cdot \int\limits_V \frac{\mu_0}{2} \cdot \mathbf{H}_\text{d} \cdot \mathbf{M} \,\text{d}V. \tag{3.25}$$

Fig. 3.5 shows the demagnetizing field $\mathbf{H}_\text{d}$ and the respective magnetization $\mathbf{M}$ for three different scenarios: an infinitely extended homogeneously magnetized plate (a), a finite plate with identical magnetization (b), and two magnetically interacting finite plates with magnetizations identical to the ones in (a) and (b). In (a) $\mathbf{H}_\text{d}$ is homogeneous, i.e one has $\mathbf{H}_\text{d} = -\mathbf{M}$. In contrast, $\mathbf{H}_\text{d}$ is inhomogeneous in (b) due to the finite plate size. In (c) the inhomogeneity of $\mathbf{H}_\text{d}$ is further increased with respect to (b) due to magnetic interactions with the second plate. Since in the framework of this thesis finite size effects on the demagnetizing field will turn out to be of major importance, it is elucidating to conceptually split $\mathbf{H}_\text{d}$ into its homogeneous and its inhomogeneous contribution:

$$\mathbf{H}_\text{d} = \mathbf{H}_\text{d}^{(\text{hom})} + \mathbf{H}_\text{d}^{(\text{inhom})} = -\mathbf{M} + \mathbf{H}_\text{d}^{(\text{inhom})} \tag{3.26}$$

The demagnetizing energy density Eq. (3.25) can be split accordingly:

$$\varepsilon_\text{d} = \underbrace{\frac{1}{V}\int\limits_V \frac{\mu_0}{2}\mathbf{M}^2 \,\text{d}V}_{\varepsilon_\text{shape}} - \underbrace{\frac{1}{V}\int\limits_V \frac{\mu_0}{2}\mathbf{H}_\text{d}^{(\text{inhom})} \cdot \mathbf{M} \,\text{d}V}_{\varepsilon_\text{d}^\text{inhom}}. \tag{3.27}$$

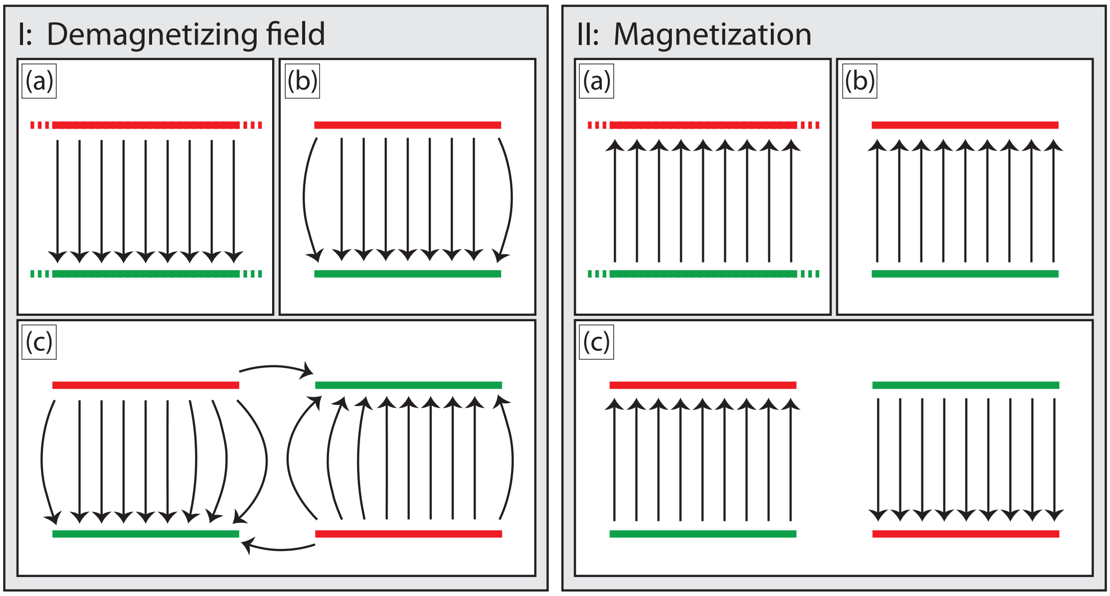

Figure 3.5: I: Dependence of the demagnetizing field on the magnetic charge distribution. (a) Demagnetizing field of a homogeneously magnetized infinite plate. (b) Field inhomogeneities due to finite size effects. (c) Modification of the demagnetizing field due to interactions with a neighboring plate. The corresponding homogeneous magnetizations are visualized in (II).

Here, the first integral describes the so called shape anisotropy energy density, while the second one refers to the energy density contribution due to domain formation and finite sample geometries. In previous studies [3, 48, 72, 73, 109] it was argued that in ultrathin magnetic films the second integral can be neglected. In Chapter 6 the validity of this approximation will be confirmed for extended Fe DL films on W(110). However, in Chapter 7 it is shown that in the case of finite stripe geometries the disregard of the second integral is no longer justified.

Shape anisotropy

With M_s being the saturation magnetization and $\phi\,(x)$ describing a periodic one dimensional magnetic configuration with period length λ_x, the first integral in Eq. (3.27) can be rewritten[2]:

$$\varepsilon_\mathrm{shape} = \frac{1}{\lambda_x}\int\limits_0^{\lambda_x}\frac{\mu_0}{2}M_\mathrm{s}^2\cdot\sin^2\phi\;\mathrm{d}x = -\frac{1}{\lambda_x}\int\limits_0^{\lambda_x}K_\mathrm{shape}\cdot\left(1-\cos^2\phi\right)\;\mathrm{d}x \qquad (3.28)$$

$$K_\mathrm{shape} := \frac{\mu_0}{2}M_\mathrm{s}^2.$$

---

[2] For the definition of ϕ cf. Fig. 3.2.

The shape anisotropy energy density $\varepsilon_{\text{shape}}$ is minimized for $\phi(x) = 90°$, i.e for all magnetic moments being aligned along the sample plane. The physical origin of this behavior is the reduced number of magnetic charges in an in-plane magnetized thin film as compared to an out-of-plane configuration. Consequently, the demagnetizing field, and thus the demagnetizing energy, is reduced by rotating the magnetization direction into the sample plane. However, if the crystalline anisotropy is out-of-plane and K_{c} is larger than K_{shape}, the shape anisotropy only reduces the effective anisotropy without changing the direction of the magnetic easy axis. This scenario has been observed for the Fe DL on W(110), where the experimentally observed effective anisotropy is out-of-plane [29, 101, 102], although, according to Eq. (3.28), the shape anisotropy prefers an in-plane configuration.

According to Eq. (3.28) the shape anisotropy is formally equivalent to the crystalline anisotropy energy density in Eq. (3.14), with the parameter K_{c} being replaced by K_{shape}. Consequently, both equations can be merged:

$$\boxed{\begin{gathered}\varepsilon[\phi(x)] = \frac{\int_0^{\lambda_x} A \cdot \left|\dot{\phi}\right|^2 \pm D \cdot \left|\dot{\phi}\right| + K_{\text{eff}} \cdot \cos^2\phi \, \mathrm{d}x}{\lambda_x} + \text{constant} \\ \\ K_{\text{eff}} = K_{\text{c}} - K_{\text{shape}}.\end{gathered}} \tag{3.29}$$

Starting from this equation, Eq. (3.15)-(3.22) can be recalculated in formal analogy to the previous discussion based on Eq. (3.14). In all equations the crystalline anisotropy K_{c} must be replaced by the effective anisotropy K_{eff}.

Domain formation and finite size effects

In contrast to the calculation of the first integral in Eq. (3.27), the calculation of the second integral is highly non-trivial. It can only be determined by calculating ε_{d} and subtracting the previously calculated shape anisotropy contribution (Eq. (3.28)). In general, ε_{d} can be separated into the energy density contribution of magnetic surface charges ($\varepsilon_{\text{d}}^{\text{surf}}$) and the energy density contribution of magnetic volume charges ($\varepsilon_{\text{d}}^{\text{vol}}$). In the following the calculation of $\varepsilon_{\text{d}}^{\text{surf}}$ and $\varepsilon_{\text{d}}^{\text{vol}}$ is discussed independently. Since all calculations in this thesis refer to magnetic thin films, the considerations are restricted to two-dimensional magnetic structures, where the magnetization $\mathbf{M}(x, y)$ varies only along the xy-plane.

The magnetic surface charge distribution $\sigma(x,y)$ in a magnetic thin film is proportional to the projection of the magnetization $\mathbf{M}(x,y)$ on the surface normal (z-direction in Fig. 3.2). Consequently, the corresponding contribution to the demagnetizing energy density ($\varepsilon_{\mathrm{d}}^{\mathrm{surf}}$) can be calculated as a functional of $\sigma(x,y)$. In general, it can only be calculated numerically. However, if the analysis is restricted to periodic magnetic charge distributions, the mathematical complexity reduces considerably. In particular, for this special case, $\sigma(x,y)$ can be expanded into a Fourier series, and $\varepsilon_{\mathrm{d}}^{\mathrm{surf}}$ is given as an analytical function of the respective Fourier coefficients c_{rs} [110]:[3]

$$\boxed{\begin{aligned} \varepsilon_{\mathrm{d}}^{\mathrm{surf}}\left[\sigma(x,y)\right] &= \frac{\mu_0}{2} M_{\mathrm{s}}^2 \cdot d \cdot \left\{ c_{00}^2 + {\sum_{rs}}' \left[c_{rs} \cdot c_{-r-s} \cdot \frac{1-\mathrm{e}^{-2\pi g_{rs}}}{2\pi g_{rs}} \right] \right\} \\ c_{rs} &:= \int_0^{\lambda_y} \int_0^{\lambda_x} \left[\frac{\sigma(x,y)}{\lambda_x \cdot \lambda_y} \cdot \mathrm{e}^{-2\pi\mathrm{i}\left(r\frac{x}{\lambda_x}+s\frac{y}{\lambda_y}\right)} \right] \mathrm{d}x\,\mathrm{d}y \\ g_{rs} &:= d\sqrt{\left(\frac{r}{\lambda_x}\right)^2 + \left(\frac{s}{\lambda_y}\right)^2} \end{aligned}} \tag{3.30}$$

The period of $\sigma(x,y)$ along the x- and y-direction is given by λ_x and λ_y, respectively. M_{s} is the saturation magnetization, d denotes the film thickness. The summation ${\sum}'_{rs}$ is defined for integers r and s from $-\infty$ to ∞, omitting $r = s = 0$. If the projection of $\mathbf{M}(x,y)$ on the surface normal is replaced by a projection on the x-direction (cf. Fig. 3.2), the function $\gamma(x,y)$ and the corresponding energy density contribution $\varepsilon_{\mathrm{d}}^{\mathrm{vol}}$ can be calculated in analogy to $\sigma(x,y)$ and $\varepsilon_{\mathrm{d}}^{\mathrm{surf}}$:[4]

$$\boxed{\begin{aligned} \varepsilon_{\mathrm{d}}^{\mathrm{vol}}\left[\gamma(x,y)\right] &= \frac{\mu_0}{2} M_{\mathrm{s}}^2 \cdot d \cdot \left\{ c_{00}^2 + {\sum_{rs}}' \left[c_{rs} \cdot c_{-r-s} \cdot \frac{\lambda_x^2}{\lambda_x^2+\lambda_y^2} \cdot \left(1 - \frac{1-\mathrm{e}^{-2\pi g_{rs}}}{2\pi g_{rs}}\right) \right] \right\} \\ c_{rs} &:= \int_0^{\lambda_y} \int_0^{\lambda_x} \left[\frac{\gamma(x,y)}{\lambda_x \cdot \lambda_y} \cdot \mathrm{e}^{-2\pi\mathrm{i}\left(r\frac{x}{\lambda_x}+s\frac{y}{\lambda_y}\right)} \right] \mathrm{d}x\,\mathrm{d}y \\ g_{rs} &:= d\sqrt{\left(\frac{r}{\lambda_x}\right)^2 + \left(\frac{s}{\lambda_y}\right)^2} \end{aligned}} \tag{3.31}$$

---

[3] In order to assure correct units of $\varepsilon_{\mathrm{d}}^{\mathrm{surf}}$, $\sigma(x,y)$ must be given in units of $\mu_0 M_{\mathrm{s}}$.

[4] Here, the calculation of $\varepsilon_{\mathrm{d}}^{\mathrm{vol}}$ is restricted to the special case of a vanishing projection of $\mathbf{M}$ on the y-direction (cf. Fig. 3.2), in agreement with the novel experimental results to be discussed in Chapter 5.

Demagnetizing energy of a spin spiral in a closed magnetic film

In the context of the previously discussed local interactions the spin spiral profile was assumed to vary only along the x-direction while it is constant along the y-direction. If, in addition, the rotation of the spiral is confined to a plane ($\theta = 0$, Eq. (3.14)-(3.15)), $\mathbf{M}$ can be expressed in terms of the spiral profile $\phi(x)$ (cf. Eq. (3.28)). Consequently, both $\sigma(x,y)$ and $\gamma(x,y)$ can be rewritten:

$$\begin{aligned} \sigma(x,y) &= \sigma_x(x) = \sin[\phi(x)] \\ \gamma(x,y) &= \gamma_x(x) = \cos[\phi(x)] \end{aligned} \tag{3.32}$$

For this one-dimensional special case the demagnetizing energy densities (Eq. (3.30)-(3.31)) simplify considerably:

$$\boxed{\begin{aligned} \varepsilon_{\mathrm{d}}^{\mathrm{surf}}[\phi(x)] &= \frac{\mu_0}{2} M_{\mathrm{s}}^2 \cdot d \cdot \left\{ c_0^2 + \sum_r{}' \left[c_r \cdot c_{-r} \cdot \frac{1 - \mathrm{e}^{-2\pi d \left| \frac{r}{\lambda_x} \right|}}{2\pi d \left| \frac{r}{\lambda_x} \right|} \right] \right\} \\ c_r &= \frac{1}{\lambda_x} \int_0^{\lambda_x} \sin[\phi(x)] \cdot \mathrm{e}^{-\mathrm{i} r \frac{2\pi}{\lambda_x} x} \mathrm{d}x \end{aligned}} \tag{3.33}$$

$$\boxed{\begin{aligned} \varepsilon_{\mathrm{d}}^{\mathrm{vol}}[\phi(x)] &= \frac{\mu_0}{2} M_{\mathrm{s}}^2 \cdot d \cdot \left\{ c_0^2 + \sum_r{}' \left[c_r \cdot c_{-r} \cdot \left(1 - \frac{1 - \mathrm{e}^{-2\pi d \left| \frac{r}{\lambda_x} \right|}}{2\pi d \left| \frac{r}{\lambda_x} \right|} \right) \right] \right\} \\ c_r &= \frac{1}{\lambda_x} \int_0^{\lambda_x} \cos[\phi(x)] \cdot \mathrm{e}^{-\mathrm{i} r \frac{2\pi}{\lambda_x} x} \mathrm{d}x \end{aligned}} \tag{3.34}$$

Like the local contribution to the total energy density (Eq. (3.14), the demagnetizing energy densities $\varepsilon_\mathrm{d}^\mathrm{surf}$ and $\varepsilon_\mathrm{d}^\mathrm{vol}$ are given as functionals of $\phi(x)$. Consequently, all energy density contributions can be easily combined[5]:

$$\boxed{\begin{aligned} \varepsilon\left[\phi(x)\right] &= \frac{\int A\left|\dot{\phi}\right|^2 \pm D\cdot\left|\dot{\phi}\right| + K_\mathrm{c}\cdot\cos^2\phi\,\mathrm{d}x}{\lambda_x} + \varepsilon_\mathrm{d}\left[\phi(x)\right] \\ \varepsilon_\mathrm{d}\left[\phi(x)\right] &= \varepsilon_\mathrm{d}^\mathrm{surf}\left[\phi(x)\right] + \varepsilon_\mathrm{d}^\mathrm{vol}\left[\phi(x)\right] \end{aligned}} \tag{3.35}$$

Demagnetizing energy of a spin spiral in a magnetic stripe array

For the more complex scenario of finite magnetic stripes, as investigated experimentally in previous studies [29, 111], Eq. (3.33)-(3.35) are no longer applicable, since the one-dimensional approach does not account for inhomogeneous topographic structures. However, this deficiency can be overcome by refocusing on the two-dimensional functions $\sigma(x,y)$ and $\gamma(x,y)$, as defined in Eq. (3.32). Both $\sigma(x,y)$ and $\gamma(x,y)$ can always be written as the product of the previously defined functions $\sigma_x(x)$ and $\gamma_x(x)$ (Eq. (3.32)), defining the spin spiral profile, and an additional function $\tau(x,y)$, describing the topography of the sample.

$$\begin{aligned} \sigma(x,y) &= \sigma_x(x)\cdot\tau(x,y) = \sin\left[\phi(x)\right]\cdot\tau(x,y) \\ \gamma(x,y) &= \gamma_x(x)\cdot\tau(x,y) = \cos\left[\phi(x)\right]\cdot\tau(x,y) \end{aligned} \tag{3.36}$$

For the special case of a closed magnetic film one has $\tau(x,y) = 1$ and Eq. (3.36) reduces to Eq. (3.32). In the general case of a magnetic film that covers only parts of the sample surface, $\tau(x,y)$ is defined as:

$$\tau(x,y) = \begin{cases} 1 & \mid \text{inside areas covered by the magnetic film} \\ 0 & \mid \text{inside areas not covered by the magnetic film} \end{cases} \tag{3.37}$$

---

[5] Note, that here ε_d implicitly contains the energy density contribution of the shape anisotropy. Thus, the first summand in Eq. (3.35) refers to K_c instead of K_eff.

Using Eq. (3.36), $\varepsilon_{\mathrm{d}}^{\mathrm{surf}}$ and $\varepsilon_{\mathrm{d}}^{\mathrm{vol}}$ (Eq. (3.30)-(3.31)), and thus the total demagnetizing energy density ε_{d}, can be rewritten as functionals of $\phi(x)$ and $\tau(x,y)$:

$$\varepsilon_{\mathrm{d}}\left[\phi(x),\tau(x,y)\right] \;=\; \varepsilon_{\mathrm{d}}^{\mathrm{surf}}\left[\phi(x),\tau(x,y)\right] \;+\; \varepsilon_{\mathrm{d}}^{\mathrm{vol}}\left[\phi(x),\tau(x,y)\right] \tag{3.38}$$

In this form the demagnetizing energy density can be combined with the local contribution to the energy density Eq. (3.14) in analogy to Eq. (3.35):

$$\boxed{\varepsilon\left[\phi(x),\tau(x,y)\right] = \frac{\int A\left|\dot{\phi}\right|^{2} \pm D\cdot\left|\dot{\phi}\right| + K_{\mathrm{c}}\cdot\cos^{2}\phi\,\mathrm{d}x}{\lambda_{x}} + \frac{1}{p}\cdot\varepsilon_{\mathrm{d}}\left[\phi(x),\tau(x,y)\right]} \tag{3.39}$$

Here p denotes the surface fraction covered by magnetic material. It accounts for the fact that the demagnetizing energy of Eq. (3.30) refers to the volume of a closed magnetic film while the local energy density contribution implicitly refers to the magnetic volume that corresponds to the partial coverage. In particular the prefactor $1/p$ converts the demagnetizing energy density such that it refers to the true magnetic volume as well.

While in the case of shape anisotropy (Eq. (3.29) the spiral profile and energy of the magnetic ground state can be calculated using variational techniques this is no longer possible in the case of Eq. (3.35) and Eq. (3.39). Instead numerical methods must be applied. Consequently, the computational complexity increases significantly if, in addition to the shape anisotropy, the influence of inhomogeneities in the demagnetizing field is taken into account. It will be shown in this thesis that the effects of such field inhomogeneities can be neglected in closed Fe DL films on W(110) but play a decisive role in the case of finite Fe DL stripe geometries.

Chapter 4

Fe double layer on W(110): previous studies

With the theoretical background of the previous chapter it is now possible to give an overview of the experimental and theoretical studies on the Fe DL on W(110). With the advent of the SP-STM [21–24, 53] the Fe DL on W(110) became one of the first magnetic systems that was investigated with nanoscale magnetic resolution and remained the subject of various experimental and theoretical studies ever since. In this chapter the results of these studies are compared and existing contradictions are discussed. Finally, the remaining experimental and theoretical challenges are summarized.

4.1 Topographic structure

The lattice structure of W crystals is body centered cubic (bcc) with a lattice parameter $a_{\mathrm{W}} = 3.165$ Å [112]. The surface unit cell of the (110)-surface has a rectangular bi-atomic structure, as illustrated by the filled blue circles in Fig. 4.1 (a). Fe also has a bcc lattice structure, with a lattice parameter $a_{\mathrm{Fe}} = 2.866$ Å [112]. When combining both materials by evaporating Fe on a clean W(110) surface one observes that the first atomic layer (AL) of Fe grows pseudomorphically, i.e. it follows the lattice structure of the underlying W(110) crystal [113] (orange dots). In the second layer the growth continues to be pseudomorphic (b). However, in order to reduce the strain due to the lattice mismatch of $(a_{\mathrm{W}} - a_{\mathrm{Fe}})/a_{\mathrm{W}} = 9.4\%$, dislocation lines, where the growth deviates from the pseudomorphic structure, are induced. The dislocation lines are aligned along the crystallographic [001] direction and thus form the characteristic pattern shown in Fig. 4.1 (d) [114–116]. In panel (c) the dislocation lines are not visible due to the narrow Fe DL stripe width and the relatively poor resolution. For an Fe coverage above 2.0 AL more sophisticated two-dimensional dislocation networks can be observed (cf. panel (d)) [115, 116].

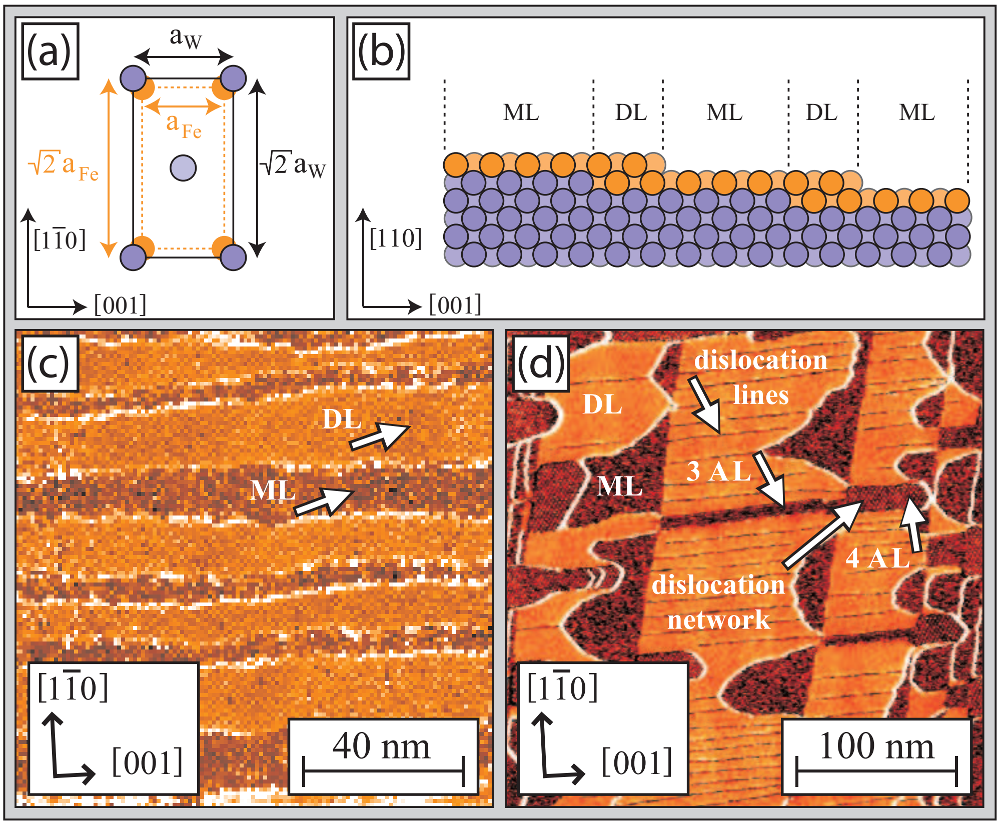

Figure 4.1: Pseudomorphic growth of Fe on a W(110) substrate. (a) surface unit cell of the W(110) substrate (blue). For comparison the undistorted surface unit cell of Fe was added (orange). (b) Atomic coordination of Fe ML and DL regions (orange) on W(110) (blue). (c) Spin-averaged $\mathrm{d}I/\mathrm{d}U$ map of about 1.6 AL of Fe on W(110). The step edges are roughly aligned along [001]. The DL areas form a well defined stripe pattern. (d) Spin-averaged $\mathrm{d}I/\mathrm{d}U$ map of 1.6 AL of Fe on W(110). Now, the step edges are roughly aligned along $\left[1\bar{1}0\right]$. Due to the prevailing preferential growth direction along [001] the stripe geometry is ragged. Regions with ML and DL coverage coexist with patches of the third and fourth AL. ((c) from [29]).

The topographic structure of the Fe DL on W(110) mainly depends on three parameters: Fe coverage, growth temperature and miscut of the W(110) surface. For a nominal coverage below 1.0 AL one observes the growth of ML islands at room temperature. In addition, the Fe decorates the step edges of the W(110) substrate. At elevated substrate temperature extended ML stripes are formed [117]. With increasing coverage the stripe width increases until the ML film is completed for a nominal coverage of 1.0 AL. In the coverage regime between 1.0 AL and 2.0 AL, DL islands grow at room temperature. The islands are preferentially elongated along the [001] direction [116]. At elevated temperature extended DL areas are formed. With the step edges being aligned along [001] one observes a step flow growth of well defined stripes being aligned along the step edges (Fig. 4.1 (c)) [118, 119]. For step edges being oriented along $\left[1\bar{1}0\right]$ the

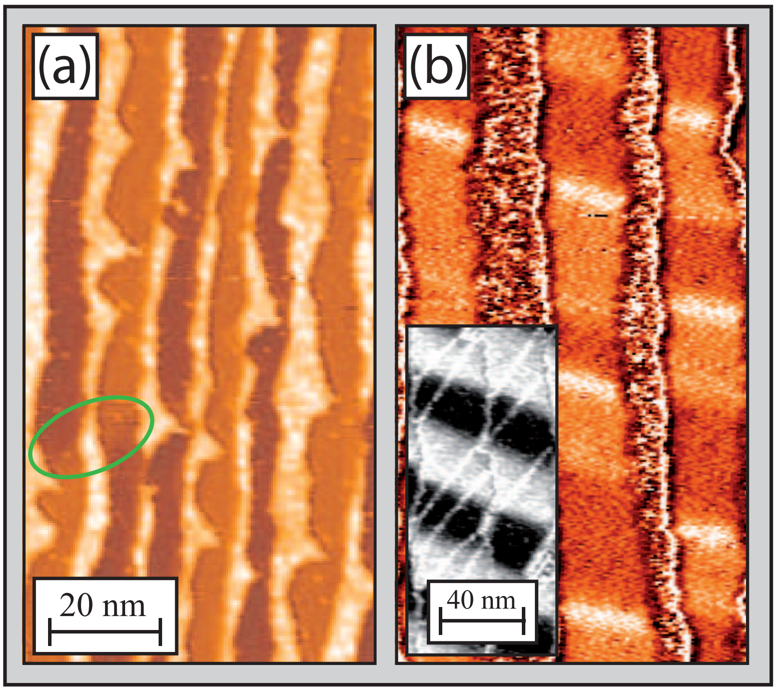

Figure 4.2: Spin-polarized dI/dU maps visualizing the magnetic structure of Fe DL stripes on W(110) [29]: (a) stripe width: 10 – 15 nm. The image was recorded using a Gd coated W tip being sensitive to the out-of-plane magnetization of the Fe DL stripes. The magnetization within each individual stripe is essentially single domain with few exceptions due to domain wall pinning at surface imperfections (green mark). Neighboring stripes show an antiparallel magnetization. (b) stripe width: 20 – 25 nm. The image was recorded using an Fe coated W tip, being sensitive to both the in-plane and the out-of-plane component of the magnetization in the stripes. The magnetic pattern within each individual stripe is given by a unirotational spiral structure. As for the narrow stripes neighboring stripes show a checkerboard-like antiparallel magnetization. For closed Fe DL films the checkerboard pattern is no longer visible and neighboring stripes couple ferromagnetically (inset). ((a,b) from [29], inset from [1]).

stripe edges become frayed due to the prevailing preferential growth direction along [001] (Fig. 4.1 (d)).

4.2 Geometry dependence of the magnetic ground state

Fig. 4.2 shows spin-polarized dI/dU maps visualizing the magnetic structure of Fe DL stripes on W(110). In (a) and (b) the stripe width amounts to 10 – 15 nm and 20 – 25 nm, respectively. Both images were taken at a measurement temperature of 14 K.

Narrow Fe DL stripes The image in (a) was recorded using an out-of plane sensitive Gd-coated W-tip. Thus, from the image one can conclude that along individual stripes the magnetization is characterized by long out-of-plane magnetized domains. Only rarely, one observes a magnetic contrast change within one individual stripe, indicating the existence of more than one domain (green mark). Between neighboring stripes there is a general tendency towards an antiparallel alignment of the magnetization direction. This stripewise antiparallel structure was determined before the advent of SP-STM using the magneto-optical Kerr effect (MOKE) [119] and served as a first reliable reference to establish the technique of SP-STM in its early days. At that time the magnetic structure was discussed as a rowwise antiferromagnetic state. There is full agreement in the literature that the antiparallel order is induced by dipolar inter-stripe coupling [119].

Wide Fe DL stripes and extended Fe DL films The image in (b) was recorded using an Fe-coated W-tip being sensitive to both the in-plane and the out-of-plane component of the magnetization. Thus both an out-of-plane magnetic contrast between neighboring domains and an in-plane magnetic contrast in the domain wall areas is observed. In contrast to the narrow Fe DL stripes (a), now the magnetic structure of one individual stripe can no longer be described in terms of long domains. Instead one observes a regular pattern of very short domains with a typical length of only 20 – 25 nm. The critical stripe width for the transition between both regimes amounts to 10 – 20 nm. Following one single stripe from the bottom to the top, one observes a unique sequence of domains and domain walls, i.e. bright domain, bright wall, dark domain, dark wall. This unique sequence is observed for all stripes independent of the position on the crystal. It was concluded that above the critical stripe width the Fe DL on W(110) has a spiral-like magnetic structure with a unique rotational sense [29, 30]. In Fig. 4.2 (b) the spiral structure of neighboring stripes is phase shifted by π. Consequently, one observes a characteristic checkerboard pattern being slightly distorted due to magnetic pinning centers induced by surface defects. As for the magnetic coupling between narrow stripes the formation of the checkerboard pattern can be ascribed to dipolar inter-stripe coupling. For extended Fe DL films the checkerboard pattern does no longer exist. Instead one observes one single magnetic spiral structure extending all over the sample (inset in panel (b)) [30].

Despite all the knowledge about the magnetic structure of Fe DL films and stripes on W(110) there are essentially two properties of the spiral state that could not be measured so far due to experimental limitations[1]. Thus it is yet unknown whether the observed spiral state is of cycloidal or helical type, as visualized in Fig. 2.9 (c), or if it is even non-planar as discussed in the context of Fig. 3.4. Furthermore the rotational sense of the spiral-structure remains puzzling.

---

[1] Both questions could not be tackled in previous studies, since in all available experimental setups the in-plane magnetization direction at the tip apex appeared as an unknown parameter that could not be controlled during the measurement. With the experimental setup discussed in Part I this experimental limitation has been overcome. Consequently, the magnetic configuration of the observed spiral state can be investigated in detail (cf. Chapter 5).

4.3 Field dependence of the spiral profile

According to Fig. 4.2 (b), the unirotational spin spiral in the Fe DL on W(110) consists of a regular sequence of up and down magnetized out-of-plane domains separated by in-plane magnetized domain walls. While in zero magnetic field the size of the domains is independent of their magnetization direction this changes if an external magnetic field is applied along the surface normal, i.e. along the magnetization axis in the domains. In particular, one observes that domains being magnetized parallel to the field grow in size, while domains with an antiparallel magnetization shrink.

Fig. 4.3 shows the in-plane component of the magnetic profile in the field range between zero and 800 mT as measured by SP-STM [1]. The gray shaded area corresponds to a non-vanishing magnetization component antiparallel to the external field. As discussed before, the domain size decreases with increasing field. For $B = 800$ mT it essentially reduces to zero, thus the profile describes a continuous rotation of the magnetization by 360°. By even larger external fields this 360° domain wall can annihilate, resulting in one single domain magnetized parallel to the field.

It was shown in [1] that the experimentally observed 360° domain wall profile is nicely reproduced by Eq. (3.22) for $B \geq 50$ mT and the fitting parameters $A = 1.8 \cdot 10^{-11}$ J/m and $K_{\mathrm{eff}} = 1.25 \cdot 10^{6}$ J/m^3 (white solid curves in Fig. 4.3). However, the model fails completely in explaining the experimentally observed unique rotational sense. Moreover, in the limit $B \to 0$, Eq. (3.22) predicts a single domain ground state ($c \to \infty$), in contradiction to the experimental results. In conclusion, despite the convincing accordance for $B \geq 50$ mT, the micromagnetic model underlying Eq. (3.22) is obviously incomplete. Consequently, the validity of the determined values of A and K_{eff}, as well as their general applicability within the framework of more comprehensive micromagnetic models, such as Eq. (3.35)-(3.39), remains disputable.

4.4 Temperature dependence of the spiral state

The previously discussed SP-STM experiments were done at a constant temperature of 14 K. At this temperature one observes a characteristic unirotational spin spiral ground state that vanishes for stripe widths below 10 – 20 nm. However, according to a recent experimental SP-STM study [120], this behavior is not universal with the existence of the spiral state depending on temperature in addition to the stripe width. In particular, the spin spiral disappears at elevated temperatures even in the case of wide stripes and

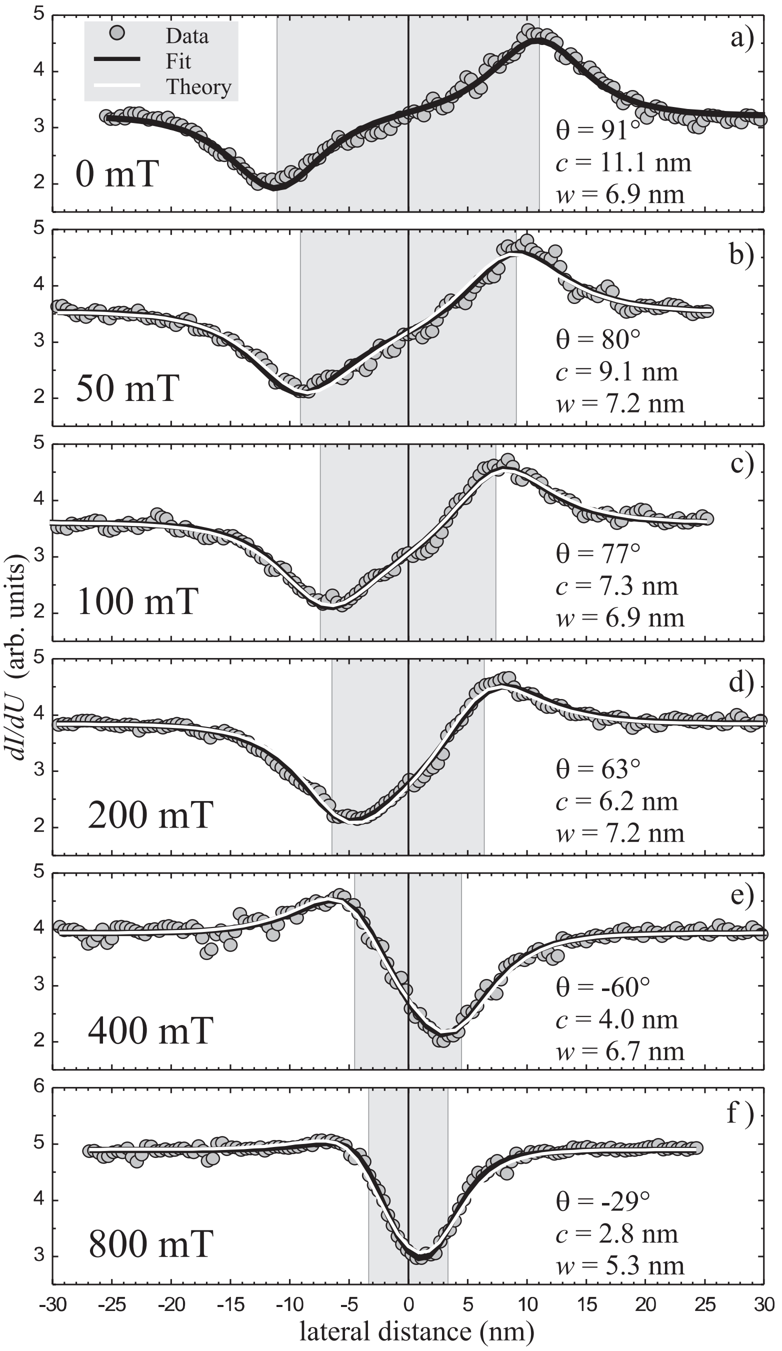

Figure 4.3: Line sections (circles) across a single 360° wall measured in an external magnetic field applied along the surface normal in the field range between zero and 800 mT. The solid curves represent the calculated wall profiles as fitted to the data on the basis of Eq. (3.22). The shaded areas correspond to the wall's inner 180° spin rotation. (from [1]).

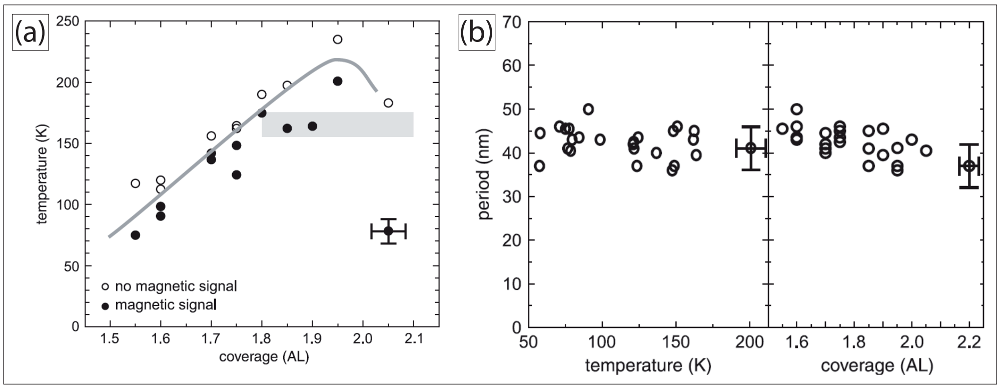

Figure 4.4: (a) Temperature and coverage dependent vanishing of the spin spiral in 1.6 AL Fe on W(110). The experimentally determined critical temperature is indicated by the gray curve. An estimate of the error is indicated for one data point. The gray rectangle refers to MOKE measurements of the magnetic remanence [100]. (b) Temperature and coverage dependence of the observed spiral period. While the period is independent of temperature, it increases moderately with decreasing Fe coverage. (from [120]).

closed Fe DL films. It was claimed that the critical temperature is a function of the nominal Fe coverage.

The major results concerning these issues are summarized in Fig. 4.4 (a). Here, filled dots indicate the highest temperature, for which the domain structure could still be identified. Empty dots correspond to the lowest temperature, for which the domain structure is still absent before it reappears. Thus, the gray solid line illustrates the transition boundary between the unirotational domain state and some other, yet unknown, magnetic state. In [120] it was claimed that the observed transition is due to a spin reorientation transition from an out-of-plane magnetic easy axis at low temperatures to an in-plane anisotropy at elevated temperature. Although the argumentation in [120] is based on previous MOKE measurements [100], it turns out that in fact the drawn conclusions are contradictory to the MOKE results that confirm an out-of-plane anisotropy in the full coverage regime between one and two AL even at a temperature as high as 165 K.[2] In contrast to the interpretation in [120] the gray rectangle in Fig. 4.4 (a) indicates an area of vanishing hysteresis rather than vanishing out-of-plane anisotropy [100]. Using torsion oscillation magnetometry the out-of-plane anisotropy in the Fe DL on W(110) was measured quantitatively with an anisotropy parameter $K = 1.0 \cdot 10^6$ J/m^3 [119, 121].

---

[2] cf. [100], page 3212, line 29-33: "We conclude, that the perpendicular magnetization in the range $1 < \Theta < 2$ must result from a perpendicular anisotropy of this DL caused by its 10% in-plane strain previously inferred from DL island data, but now clearly confirmed for the case of the DL stripes." Note that here Θ denotes the Fe coverage. The measurement temperature in [100] was 165 K.

Only in the regime of ultra-narrow Fe DL stripes, i.e. for stripe widths below 2 nm, the preferential magnetization direction is in-plane [119, 121]). However, even in this case the observed behavior is not the result of a reorientation of the magnetic easy axis. Instead it can be ascribed to the exchange coupling between the Fe DL and the surrounding ML sea with its in-plane anisotropy [102]. Below a critical stripe width the exchange coupling overcomes the out-of-plane anisotropy of the DL, resulting in a reorientation of the magnetic moments into the surface plane. This coupling mechanism could be confirmed by SP-STM experiments on small Fe DL islands on W(110) [101].

Fig. 4.4 (b) shows the period of the magnetic domain structure (defined as the average distance between two neighboring bright domain walls in Fig. 4.2 (a), as a function of temperature and Fe coverage. While the period is independent of temperature one observes a weak coverage dependence, i.e the period increases with decreasing coverage [120]. However, on the basis of the available experimental data this interpretation is speculative, since the varying period could just as well be ascribed to the variation of the stripe width instead of the Fe coverage.

4.5 The physical origin of the spiral state

Before the advent of SP-STM there was a broad consensus in the physical community that domain sizes in the nanometer regime do not exist in magnetic thin films, since the gain of dipolar energy can only compensate for the cost of magnetic exchange and crystalline anisotropy energy for domain sizes on the order of several hundred nanometers. After the experimental discovery of the nanometer scale magnetic structure in the Fe DL on W(110) the discussion became controversial.

According to Eq. (3.27), the demagnetizing energy of a ferromagnetic film can be reduced by the formation of domains. However, with an increasing number of domains the magnetic exchange and the crystalline anisotropy energy increase, due to the growing number of domain walls. For typical bulk values of the exchange stiffness A, the crystalline anisotropy K_c, and the saturation magnetization density M_s the typical domain size is on the order of at least several microns. Starting from this scenario, the observed nanometer scale domain sizes in the Fe DL on W(110) can only be explained by a significantly increased value of M_s, a significantly decreased domain wall energy $4\sqrt{AK_{\mathrm{eff}}}$ (cf. Eq. (3.20) and Eq. (3.29)) or an additional energy contribution, such as the DM interaction discussed in Chapter 3 (cf. Eq. (3.29), Eq. (3.35), Eq. (3.39)). In the following the various proposed explanations for the observed magnetic ground state configuration will be summarized and mutually compared.

Magnetic domains induced by demagnetizing fields

In some of the previous studies on the subject the DM interaction was considered to be negligible [1, 2]. Based on this assumption two very much contradictory conclusions were drawn. In [2], it was claimed that the experimentally observed domain sizes can be explained as a consequence of long-range demagnetizing fields[3]. Starting from the assumption that the value of M_s is well known, the values of A and K_eff were varied until the observed domain size and domain wall width in zero field could be reproduced ($A = 0.7 \cdot 10^{-11}$ J/m, $K_\mathrm{eff} = 0.4 \cdot 10^{6}$ J/m^3) [122]. On the basis of these parameters the direction of the domain walls was ascribed to the anisotropy of magnetic exchange, i.e. to different values of A along the propagation direction and perpendicular to it. However, the determined micromagnetic parameter set had been ruled out before by investigations of the magnetic field dependence [1] of the observed magnetic structure. On the other hand, as discussed before, the general validity of the alternative parameter set determined in [1] is disputable, since the micromagnetic model used for its calculation is incomplete and fails completely to explain the observed spiral state in zero field. In addition to the contradictory values of A and K_eff, in both studies the observed unique rotational sense remained unexplained. It was speculated that it may be a consequence of the hitherto neglected DM interaction [123].

Dzyaloshinskii-Moriya driven spiral structures

In order to account for the discussed deficiencies the DM interaction was addressed in recent theoretical studies [3, 72, 73]. Based on DFT calculations and the micromagnetic model Eq. (3.29) the magnetic ground state of the Fe DL on W(110) was calculated numerically using a one-dimensional model ansatz. The homogeneous contribution to the demagnetizing energy ($\varepsilon_\mathrm{shape}$, first term on the right hand side of Eq. (3.27)) was considered via an effective anisotropy parameter K_eff, whereas the inhomogeneous contribution ($\varepsilon_\mathrm{d}^\mathrm{inhom}$, second term on the right hand side of Eq. (3.27)) was neglected. In contrast to the experimentally observed spiral state, the magnetic ground state of the Fe DL on W(110) was determined to be collinear. However, within the numerical accuracy of the calculations a non-collinear spin spiral ground state could not be ruled out either. The relevant micromagnetic parameters were determined as: $A = 1.9 \cdot 10^{-11}$ J/m, $K_\mathrm{eff} = 0.4 \cdot 10^{6}$ J/m^3, and $D = 2.85 \cdot 10^{-3}$ J/m^2.

According to Eq. (3.21) these parameters correspond to a domain wall width of 13 nm, which is about twice the value measured in SP-STM experiments [1]. Thus, like for the previously discussed studies [1, 2], the determined parameter set does not give a consistent description of the experimental data. However, now the unirotational character of the magnetic ground state can be explained as a consequence of the DM interaction. Thus for the case of two domains of opposite magnetization induced by appropriate boundary conditions the separating domain wall was predicted to be a right-rotating ($\underline{\uparrow\nearrow\rightarrow\searrow\downarrow}$), in contrast to a left rotating ($\underline{\uparrow\nwarrow\leftarrow\swarrow\downarrow}$), Néel-type wall. In contrast to [2] the domain wall alignment along the $[1\overline{1}0]$ direction of the underlying crystal was ascribed to the direction of the effective **D**-vector, instead of anisotropic exchange.

---

[3] According to Fig. 2 in [2], the experimentally observed domain size was reproduced, although the simulations exclusively considered the energy contributions of magnetic exchange, anisotropy and demagnetizing fields.

4.6 Open questions

Experimental challenges Although the Fe DL on W(110) was the subject of intense studies during the past decades a couple of questions have not been answered, yet. To date, the certainly most important experimental challenges are the direct measurement of the spiral type (helical or cycloidal), and the rotational sense in an SP-STM experiment. In particular, it is of great importance to measure if the rotation of the spiral is confined to a plane or if it is more complex and must be described according to Eq. (3.13) with $\theta \neq 0$.

Fe Double Layer on W(110): Micromagnetic Parameters

Publication	A [J/m]	K_c $\left[\mathrm{J/m^3}\right]$	K_{eff} $\left[\mathrm{J/m^3}\right]$	D $\left[\mathrm{J/m^2}\right]$	M_s [A/m]
Vedmedenko et al. [2, 122]	$0.7 \cdot 10^{-11}$	$1.7 \cdot 10^{6}$	$0.4 \cdot 10^{6}$	0	?
Kubetzka et al. [1]	$1.8 \cdot 10^{-11}$	$2.6 \cdot 10^{6}$	$1.3 \cdot 10^{6}$	0	$2.0 \cdot 10^{6}$
Heide et al. [3]	$1.9 \cdot 10^{-11}$	$1.7 \cdot 10^{6}$	$0.4 \cdot 10^{6}$	$2.9 \cdot 10^{-3}$	$1.4 \cdot 10^{-6}$
Weber et al. [121]	-	$2.3 \cdot 10^{6}$	-	-	-

Table 4.1: Micromagnetic parameters determined for the Fe DL on W(110) according to various studies.

Theoretical challenges Besides the experimental issues discussed before it is of high relevance to develop a consistent physical model explaining the observed spin spiral ground state with all its properties. Due to the nearly mesoscopic spiral period a micromagnetic model seems to be a good starting point to achieve this goal. However, all previous approaches into this direction failed and could only partially explain the experimental observations while in the context of other experiments they produced contradictory predictions. Thus, from a theoretical point of view it is of major importance to develop a micromagnetic model being powerful enough to reproduce all experimental observations on the basis of a unique set of micromagnetic parameters (A, K_c, D, M_s). A summary of previously determined parameter values for A, K_c and K_{eff} is given in Tab. 4.1.

Table 4.2 summarizes the previously discussed properties of the magnetic ground state in the Fe DL on W(110). Agreement and disagreement with the micromagnetic models discussed in the literature [2, 3, 101] is indicated by + and -, respectively.

	Kubetzka et al. [1]	Vedmedenko et. al. [2]	Heide et al. [3]
spiral period	-	+	-
rotational sense	-	-	+
domain wall width	+	+	-
domain wall direction	-	+	+
magnetic field dependence	+	-	-
vanishing spiral in narrow stripes	-	-	-
vanishing spin contrast at elevated temperature	-	-	-
coverage dependence of the spiral period	-	-	-

Table 4.2: Agreement (+) and disagreement (-) of current micromagnetic models with the previously discussed experimental observations.

Chapter 5

Real-space measurement of spiral type and rotational sense

In order to investigate if the spin spiral in the Fe DL on W(110) is of cycloidal or helical type (cf. Fig. 2.9), or if it must be described as a more complex non-planar configuration ($\theta \neq 0$, cf. Fig. 3.4) a series of SP-STM experiments was performed in the triple axes vector magnet system described in Part I. In a second series of measurements the rotational sense of the spin spiral was measured. All experiments were done under ultra-high vacuum conditions at $T = 4.7$ K. The tungsten tip used in the experiment was flashed to remove surface oxides and coated with about 50 AL[1] of Fe resulting in an in-plane magnetic sensitivity. During the acquisition of the SP-STM images the external magnetic field was used to align the tip magnetization along a well defined spatial direction as described in Part I. With the direction of the tip magnetization being a well defined and controllable parameter, it is now possible to draw detailed conclusions concerning the local magnetization direction of the sample with respect to a well known external coordinate system.

5.1 Topography

The W(110) crystal being used in the experiments has a miscut being different compared to the crystals used in most previous studies. However, it is well known [2] that the magnetic spiral state being the subject of this thesis is independent of the crystal miscut, although the Fe DL grows in a different morphology. The W(110) substrate was cleaned according to [56]. After cleaning, 1.7 atomic layers (AL) of Fe were evaporated at a deposition rate of 0.6 AL per minute, with subsequent annealing at 500 K

---

[1] The film thickness was chosen based on previous measurements [124], where it was shown that for a film thickness of about 50 AL the system undergoes reorientation transition of the magnetic easy axis between the crystallographic [001] and [$1\bar{1}0$] direction. It can therefore be assumed that in this coverage regime the energy barrier for the alignment of the tip magnetization in the external in-plane field is relatively small.

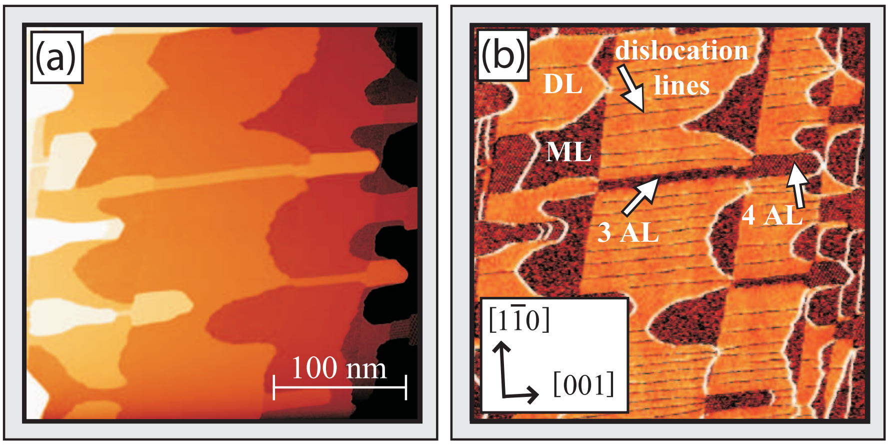

Figure 5.1: 1.7 atomic layers of Fe on W(110) with a local Fe coverage of 1-4 atomic layers. (a) Constant-current STM image showing the topography. (b) $\mathrm{d}I/\mathrm{d}U$ map showing the details of the varying local coverage with dislocation lines in the double layer areas. Tunneling parameters: $I = 500$ pA, $U_{\text{bias}} = 550$ mV.

for five minutes. Fig. 5.1 shows the morphology of the sample with various local Fe coverages. Regions of pseudomorphic ML and DL coverage coexist with patches of the third and fourth AL. To relief the strain resulting from the 9 % lattice mismatch between W and Fe, dislocation lines along the [001] axis are induced in the DL areas [114–116]. While in Fig. 4.2 the direction of the step edges was roughly along the crystallographic [001] direction, their direction is now almost perpendicular to it. Since [001] is the preferred growth direction of the Fe DL on W(110) the stripe edges in Fig. 5.1 are frayed as compared to the stripes in Fig. 4.2.

5.2 The cycloidal character of the spin spiral

Fig. 5.2 presents a first field-dependent series of spin-polarized $\mathrm{d}I/\mathrm{d}U$ maps showing the in-plane domain wall contrast in the DL areas. An external magnetic field was applied along different in-plane directions, as indicated, to align the tip magnetization $\mathbf{m}_\mathrm{t}$ accordingly. This is a well established procedure for SP-STM experiments in fields oriented along the surface normal [1], which is generalized here to arbitrary field directions. The magnetic field $B = 150$ mT was chosen such that it is weak enough not to affect the magnetic structure of the sample but strong enough for the alignment of $\mathbf{m}_\mathrm{t}$. For $\mathbf{m}_\mathrm{t}$ pointing along the [001] axis (a,c) we observe a strong domain wall contrast (black and white lines along the $[1\bar{1}0]$ axis). By comparison of (a) and (c) one observes a contrast reversal due to the reversal of $\mathbf{m}_\mathrm{t}$. The domain wall contrast vanishes with $\mathbf{m}_\mathrm{t}$ being rotated by 90° (b,d) along the $[1\bar{1}0]$ axis. Instead, one observes a weak stripe-like pattern in the areas of the out-of-plane magnetized domains due to a residual perpendicular component of $\mathbf{m}_\mathrm{t}$.

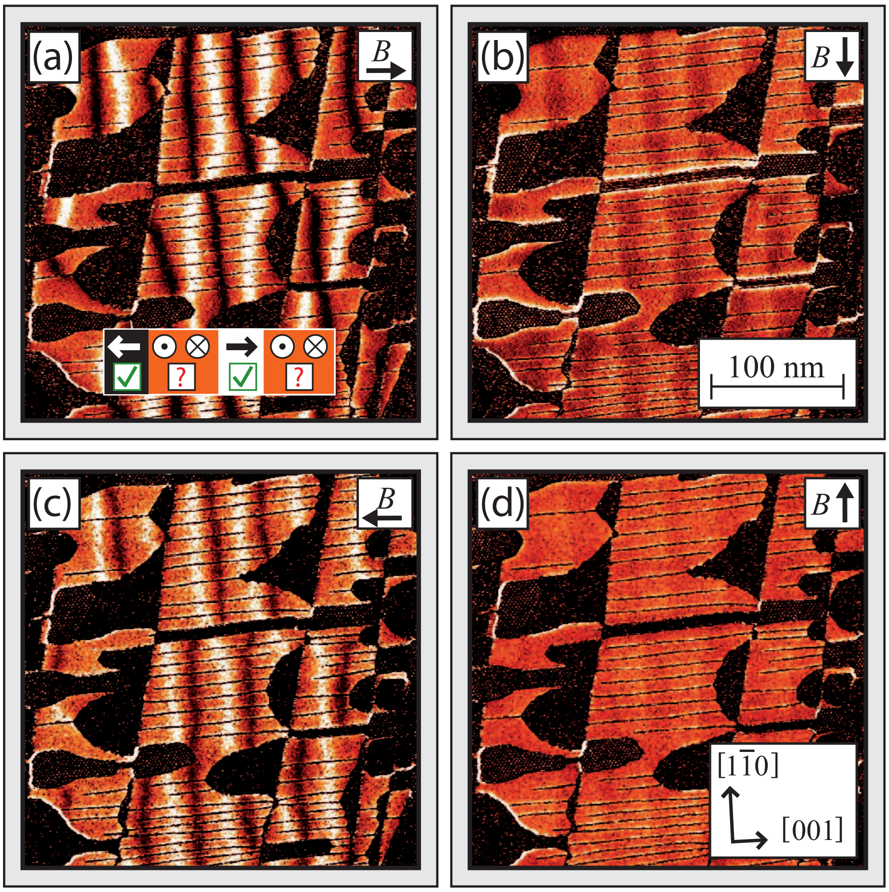

Figure 5.2: Spin-polarized dI/dU maps measured for different in-plane orientations of the external magnetic field B = 150 mT and the tip magnetization, respectively. (a, c) Domain walls showing up in the DL as black and white lines along the [1$\bar{1}$0] axis with contrast inversion from (a) to (c). (b, d) Vanishing domain wall contrast. This behavior is characteristic for Néel-type walls (cycloidal spin spirals). Tunneling parameters: I = 500 pA, U_{bias} = 550 mV. Inset: illustration of the cycloidal spiral type and the yet unknown rotational sense.

In conclusion, the magnetization in the domain walls rotates through the [001] rather than any other direction, proving that the domain walls are of Néel-type, i.e. the spiral is a flat cycloid with the rotation of the magnetic moments being confined to the (x,y)-plane, as defined in Fig. 3.2.

5.3 The rotational sense of the spin spiral

Fig. 5.3 displays a second series of field dependent measurements to investigate the sense of rotation of the spin spiral. The measurements were done on the same sample and using the same tip, bias voltage and tunneling current as for the series shown in

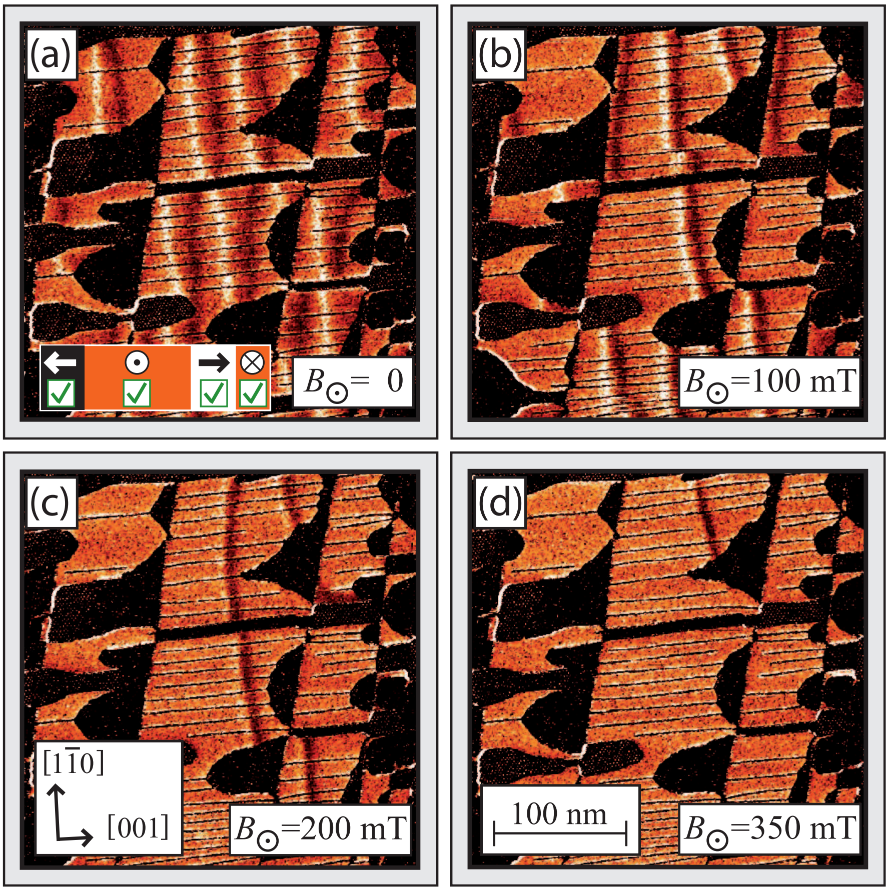

Figure 5.3: Spin-polarized dI/dU maps of the Fe DL on W(110) measured for variable field values applied normal to the surface plane. The domain sizes are affected by the external field. In addition, the tip magnetization is increasingly rotated from parallel to normal to the sample plane due to the field, resulting in a gradual change from in-plane to out-of-plane magnetic sensitivity. Tunneling parameters: I = 500 pA, U_{bias} = 550 mV. Inset: illustration of the right-rotating cycloidal spiral type.

Fig. 5.2. Now, the field was applied normal to the sample surface and swept in the range $B_z = 0 - 350$ mT. In contrast to the measurement series shown in Fig. 5.2 now both $\mathbf{m}_\text{t}$ and the magnetic structure of the sample are affected by the external field. Domains with the magnetization $\mathbf{m}_\text{s}$ being parallel (antiparallel) to the field grow (shrink). Thus, the direction of $\mathbf{m}_\text{s}$ can be identified for all domains. On the tip side, sweeping the field causes $\mathbf{m}_\text{t}$ to increasingly rotate into the perpendicular direction. Consequently, the in-plane domain wall contrast gradually disappears and is eventually replaced by an out-of-plane contrast, allowing to image the domains rather than the domain walls (Fig. 5.3 (c, d)). The large domains with $\mathbf{m}_\text{s}$ being parallel to the field appear bright whereas residual domains, being shrunken to mere lines and with $\mathbf{m}_\text{s}$ being antiparallel to the field, appear dark. This observation can be generalized such that for the

tip-sample combination in our experiment, at the given bias voltage, bright colors (high $\mathrm{d}I/\mathrm{d}U$ signal) indicate a parallel alignment of $\mathbf{m}_\mathrm{s}$ and $\mathbf{m}_\mathrm{t}$ while dark (low $\mathrm{d}I/\mathrm{d}U$ signal) corresponds to an antiparallel alignment. Applying this result to the magnetic structure as visualized in Fig. 5.2(a) one can conclude that $\mathbf{m}_\mathrm{s}$ in the bright (dark) domain walls is pointing to the right (left), i.e. parallel (antiparallel) to the external field. Combining this knowledge with that of the spin orientation in the domains allows the conclusion that the observed magnetic ground state is a right-rotating cycloidal spin spiral propagating along the [001] axis, with the spin rotation being confined to the *xy*-plane (cf. Fig. 3.2).

5.4 Homochirality

The following considerations are based on the notion of chirality, as it is most widely accepted in science. In particular the argumentation refers to the definition proposed by Barron [125]:

> *A chiral object and its mirror image are called enantiomers. True chirality is exhibited by systems that exist in two distinct enantiomeric states that are interconverted by space inversion, but not by time reversal combined with any proper spatial rotation.*

Starting from this definition the term *homochirality* describes the phenomenon that in nature one enantiomeric state is favored with respect to the other.

Homochirality is not just a strange peculiarity of nature. It is rather an ubiquitous phenomenon influencing wide areas of our everyday live. In particular, the complex biomolecules, such as DNA, amino acids, sugars, and proteins are homochiral objects. One observes that their biomolecular chirality is unique for all known organisms with the respective mirror symmetric molecules playing no role in biology. To date the physical origin of this biological homochirality is unknown and remains one of the most fundamental questions of life science. Besides its fundamental importance homochirality is also of great industrial relevance, in particular for the pharmaceutical industry. Thus it is well known that drugs must necessarily match the chirality of the biomolecules in the organism to be treated. The terrible consequences of non matching chiralities became evident in 1961 when several thousands of children were born with physical abnormalities as an adverse reaction of the tranquilizer *CONTERGAN* [126] being consumed by their mothers during pregnancy.

It was shown above that the spin spiral in the Fe DL on W(110) has a unique rotational sense. This raises the important question if the observed spin spiral is an example of homochirality in physics thus being an ideal system to investigate the underlying physical mechanisms governing its existence. Fig. 4.2 (c) shows right- and left-rotating spin spirals of helical and cycloidal type. While the right- and left-rotating helical spirals are enentiomeric according to the definition given above, the cycloidal spirals are not, since the right- and left-rotating version are not interconverted by space inversion[2]. Consequently, the spin spiral, as observed in the Fe DL on W(110), does not have a chirality, i.e it is not homochiral although it has a unique sense of rotation. With respect to the fundamental importance of homochirality this distinction is of highest relevance and the synonymous use of the terms unirotational and homochiral is inappropriate and misleading in the context of cycloidal spin spirals.

---

[2] Note, that space inversion is equivalent to the consecutive application of a mirror symmetry operation and a proper rotation.

Chapter 6

Infinitely extended Fe double layer films

It was discussed in Chapter 3 that within the framework of a micromagnetic model ansatz the magnetic ground state of closed Fe DL films on W(110) can be discussed on the basis of the micromagnetic model described by Eq. (3.35). Compared to the models used in previous studies on the subject [1, 2, 48, 109, 127], Eq. (3.35) represents a significant extension, since both the DM interaction and dipolar interactions are considered as potential driving forces towards a non-collinear spin spiral ground state. However, a priori the values of the micromagnetic parameters, A, K_c, D, and M_s are not known. In several previous studies they were determined as fit parameters that best reproduce (i) the experimentally observed spiral shape and period [1, 2] or (ii) the energy density dispersions calculated by DFT [48, 109, 127].

The first approach (i) is conceptually correct as long as all interactions, that determine the measured spiral profiles, are adequately considered in the used micromagnetic model. For the best fit the calculated spiral profile coincides with the experimental one and all micromagnetic parameters have unique values that can be related to physically meaningful quantities. If certain relevant magnetic interactions are neglected in the micromagnetic model the fitting procedure can still be applied formally. However, then the micromagnetic parameters are mere fitting parameters that can no longer be related to physically meaningful quantities. Instead, they must be considered as *effective* parameters of an *effective* micromagnetic model. In particular, the values obtained for these effective parameters are not necessarily unique, i.e. they may differ if the fitting procedure is applied to spiral profiles measured under different experimental conditions such as variable external magnetic fields or variable temperatures.

If a DFT-model describes the experimental observations correctly, the second approach (ii) is equivalent to the first one and the fitting procedure results in the same values of the micromagnetic parameters. If the predictions of a DFT-model are contradictory to the experimental results, the obtained fitting parameters are different and describe the DFT-model rather than the experiment. Therefore, the quality of the DFT-results must always be checked for consistency with existing measurements before the fitting procedure is applied.

The following discussion is based on the first approach discussed above. All considerations are initially restricted to the case of extended Fe DL films. In Chapter 7 the results will be extended to the case of finite Fe DL stripes. Following previous studies [72, 73, 127] the analysis is initially restricted to a simplified micromagnetic model where the demagnetizing energy is approximated by the shape anisotropy (cf. Eq. (3.29)). In a subsequent step it is investigated how the determined values of A, K_c, M_s, and D must be modified if the micromagnetic model additionally accounts for the energy contribution of inhomogeneities in the demagnetizing field (Eq. (3.35)). In particular, it is shown that for extended Fe DL films on W(110) the initial approximation of the demagnetizing energy by the shape anisotropy, and thus the application of Eq. (3.29) instead of Eq. (3.35), is well justified.

6.1 Exchange stiffness and effective anisotropy

The approach underlying the micromagnetic analysis in this Chapter was applied to the magnetic structure of the Fe DL on W(110) already before [1, 2]. However, according to the discussion in Chapter 4 the conclusions of these studies are contradictory and can only partly explain the experimental observations (cf. Table 4.2). In particular, the contradictory conclusions of [1] and [2] can be attributed to two issues:

- In both studies the DM interaction was omitted, i.e. Eq. (3.29) was applied for the special case $D = 0$.
- In [1] the micromagnetic parameters were determined by data fits with respect to the spiral *shape*, while in [2] they were obtained by fits to the spiral *period*.

The influence of these aspects on the validity of the determined values of the exchange stiffness (A), the magnetic anisotropy (K_c, K_eff), the Dzyaloshinskii parameter D and the saturation magnetization M_s is discussed in the following.

Data fits with respect to the shape of the spiral profile [1] According to the discussion in Chapter 3.2 the DM interaction can destabilize collinear magnetic order and induce a spin spiral ground state that is described by Eq. (3.15). In the spiral regime the Dzyaloshinskii parameter D only affects the spiral period, while the shape of the spiral profile is independent of D. It is fully determined by the exchange stiffness A and the effective anisotropy K_{eff}[1]. However, according to Eq. (3.15), A and K_{eff} cannot be considered as independent fit parameters, since the spiral profile only depends on the quotient A/K_{eff}. This changes in the presence of an external magnetic field along the surface normal that modifies Eq. (3.15) according to Eq. (3.22). Consequently, A and K_{eff} can be determined independently by fitting Eq. (3.22) to the experimentally observed spiral profiles in the external magnetic field, as done in [1]. Since the spiral profile is independent of D this fitting procedure remains applicable even in the presence of a significantly strong DM interaction. Thus, although the DM interaction was not considered in [1] the drawn conclusions remain valid even in the case of finite D.

Data fits with respect to the spiral period [2] While the shape of a spin spiral profile essentially depends on the quotient A/K_{eff} but not on D, its period is related to the domain wall energy (Eq. (3.20), i.e. the product $A \cdot K_{\text{eff}}$ and the Dzyaloshinskii parameter D. The spiral period increases with increasing values of A and K_{eff} and decreases with increasing values of D. Thus, the spiral period can be reproduced on the basis of infinitely many micromagnetic parameter sets (A, K_{eff}, D). In [2] one of these parameter sets ($D = 0$) was chosen arbitrarily by omitting the DM interaction. However, according to recent experimental results [48, 109] the assumption of a vanishing D is problematic in the context of ultrathin magnetic films.

In summary, the values of A and K_{eff}, as determined in [1], remain conceptually correct even in the presence of a finite DM interaction, while the values of [2] rely on the arbitrary assumption of a vanishing DM interaction. Thus, the following analysis will be based on the parameters determined in [1].

$$\boxed{\begin{aligned} A &= 1.8 \cdot 10^{-11} \quad \text{J/m} \\ K_{\text{eff}} &= 1.25 \cdot 10^{6} \quad \text{J/m}^3 \\ M_{\text{s}} &= 2.0 \cdot 10^{6} \quad \text{A/m} \end{aligned}} \tag{6.1}$$

---

[1] The spiral profile is determined by K_{eff} instead of K_{c} because of the non-vanishing shape anisotropy contribution in the Fe DL on W(110). In addition to the shape anisotropy, the spiral profile may also be affected by the energy contribution related to inhomogeneities in the demagnetizing field (cf. Eq.(3.27)). However, this effect is negligible, as discussed in Chapter 6.3.

Note, that the value of M_s, as determined in [1], differs from the values used in other studies [3] by about 30%. This discrepancy is mainly due to the problem that the boundary between the Fe and the vacuum, and thus the thickness of the Fe DL film, is not well defined. Consequently, the determination of the volume that refers to the calculation of M_s is difficult, resulting in a large error bar of M_s. It is therefore not possible to decide which value is more appropriate.

6.2 The Dzyaloshinskii-Moriya vector

Using the micromagnetic parameter values of Eq. (6.1) the shape of the experimentally observed spiral profile and its magnetic field dependence for $B \geq 50$ mT can be reproduced using a micromagnetic model that does not consider the DM interaction [1]. However, in zero-field such a model fails completely and predicts an infinitely long spiral period. In addition, the observed unique rotational sense cannot be explained and must be induced by appropriate boundary conditions. In the following it will be shown that this deficiency can be overcome by including the DM interaction according to Eq (3.29). According to the discussion in Chapter 3 the DM vector **D** must point along the crystallographic $[1\bar{1}0]$ direction in order to be consistent with the experimentally observed propagation direction, i.e. the alignment of the domain walls (cf. Fig. 5.2), while the magnitude of **D**, i.e. the Dzyaloshinskii parameter D, remains unknown. In the following, D is determined by reproducing the measured zero-field spiral period in addition to the spiral shape and its magnetic field dependence. Following previous studies [72, 73, 127] the analysis is initially restricted to sinusoidal (homogeneous) spiral profiles. In a subsequent step the analysis is generalized to non-sinusoidal (inhomogeneous) spiral profiles. By comparison of both cases the implications of inhomogeneity in the spiral profile are discussed in detail.

Homogeneous spiral profiles

In analogy to the theoretical analysis of other spin spirals described previously [3, 48, 109], the discussion is initially restricted to homogeneous, i.e. to continuously rotating, magnetization profiles[2]:

$$\phi_\lambda (x) = \pm \frac{2\pi}{\lambda} x \tag{6.2}$$

Here, the sign of $\phi (x)$ determines the rotational sense of the spin spiral, i.e (+) accounts for right-rotating and (-) for left-rotating spirals. Using Eq. (6.2), Eq. (3.29) can be rewritten:

---

[2] Note, that according to Eq. (3.15) the ground state spiral profile resulting from Eq. (3.29) is inhomogeneous. It approaches the homogeneous case only in the limit of small spiral periods.

$$
\boxed{
\begin{aligned}
&\varepsilon\left[\phi_\lambda\right] = \varepsilon_A\left[\phi_\lambda\right] + \varepsilon_{\mathrm{DM}}\left[\phi_\lambda\right] + \varepsilon_{K_\mathrm{c}}\left[\phi_\lambda\right] + \varepsilon_{\mathrm{shape}}\left[\phi_\lambda\right] \\[1em]
&\begin{aligned}
\varepsilon_A\left[\phi_\lambda\right] &= \frac{\int A\cdot\left|\dot{\phi}_\lambda(x)\right|^2\,\mathrm{d}x}{\lambda} &&= 4\pi^2 A\cdot\lambda^{-2}\\
\varepsilon_{\mathrm{DM}}\left[\phi_\lambda\right] &= \frac{\int \pm D\cdot\left|\dot{\phi}_\lambda(x)\right|\,\mathrm{d}x}{\lambda} &&= \pm 2\pi D\cdot\lambda^{-1}\\
\varepsilon_{K_\mathrm{c}}\left[\phi_\lambda\right] &= \frac{\int K_\mathrm{c}\cdot\cos^2\left[\phi_\lambda(x)\right]\,\mathrm{d}x}{\lambda} &&= \frac{K_\mathrm{c}}{2}\\
\varepsilon_{\mathrm{shape}}\left[\phi_\lambda\right] &= \frac{\int K_{\mathrm{shape}}\cdot\cos^2\left[\phi_\lambda(x)\right]\,\mathrm{d}x}{\lambda} &&= \frac{\mu_0}{2}M_\mathrm{s}^2.
\end{aligned}
\end{aligned}
}
\tag{6.3}
$$

Fig. 6.1 shows all contributions to the energy density dispersion, as calculated for the Fe DL on W(110) on the basis of the parameter set determined in the previous section (Eq. (6.1)). Here, the energy density dispersions of right-rotating (left-rotating) spin spiral profiles are displayed in the right (left) half-plane of the graph. For the energy density contribution of magnetic exchange one observes a parabolic behavior (solid black curve). The energy density dispersion of the effective anisotropy is independent of the spiral period (dashed green line) except for a discontinuous jump at $\lambda^{-1} = 0$ (green dot). This discontinuity is an artifact of the ad-hoc restriction to homogeneous spiral profiles that implies a finite spiral period λ and does not allow for a continuous transition between the spiral regime and the collinear ferromagnetic state. The energy density dispersion of the effective anisotropy can be separated into the two contributions of the crystalline (solid green line) and shape anisotropy (solid blue line) according to Eq. (6.3). Finally, the DM interaction results in a linear dispersion relation with the slope being given by the Dzyaloshinskii parameter D (yellow line). The figure displays three scenarios that correspond to three different values of the Dzyaloshinskii parameter D. In each case the energy density of the collinear single domain state is given by the dot at the origin of the coordinate system.

For $D = 0$ the total energy density is described by a parabola with its minimum at $\left(0|\frac{K_{\mathrm{eff}}}{2}\right)$. For finite D the parabola undergoes an additional linear displacement with the minimum of the parabola being shifted to

$$\left(-\frac{D}{4\pi A}\,\middle|\,-\frac{D^2}{4A}+\frac{K_{\mathrm{eff}}}{2}\right). \tag{6.4}$$

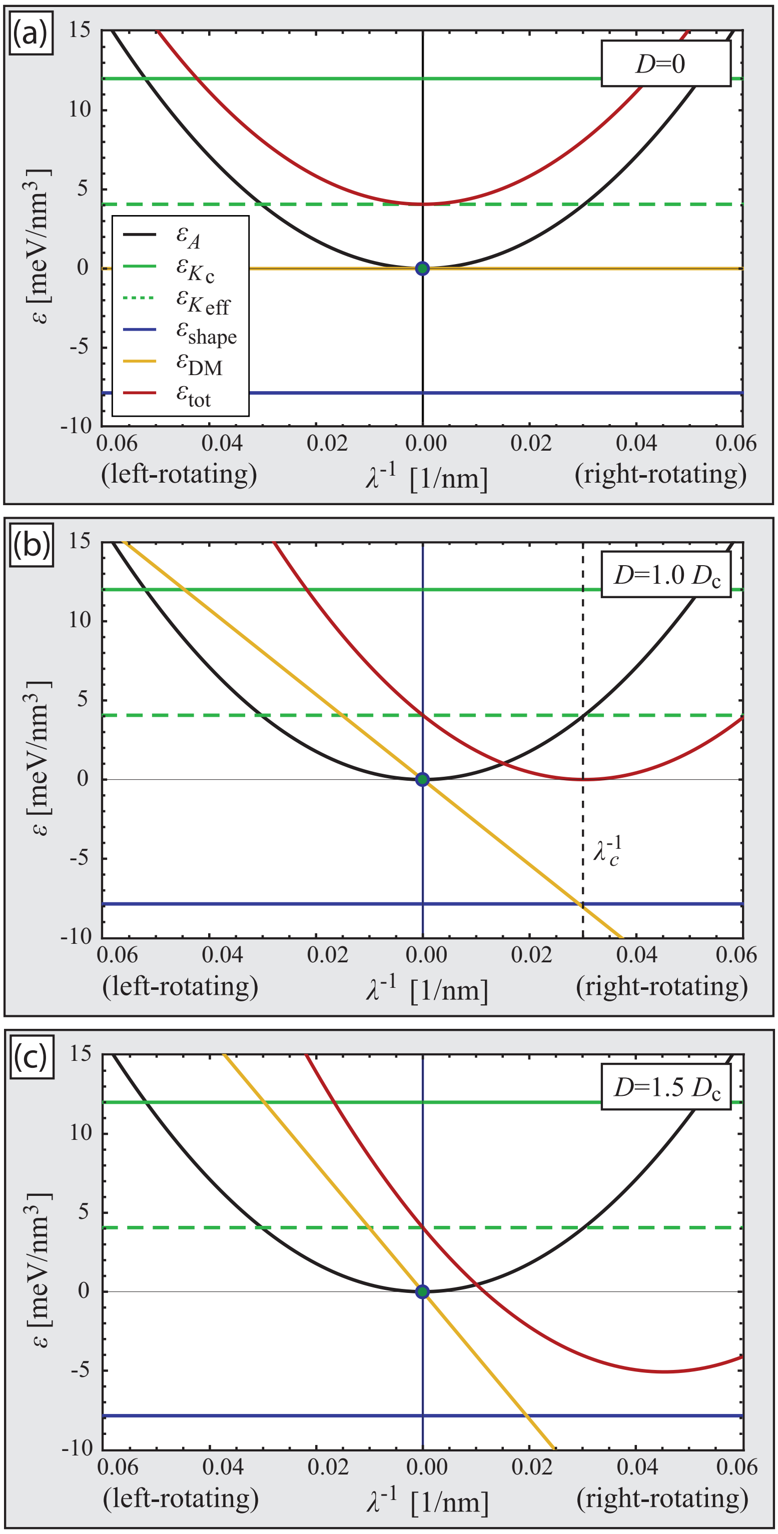

Figure 6.1: Energy density dispersions, as calculated for the special case of homogeneous. i.e. sinusoidal, spiral profiles and various values of the Dzyaloshinskii parameter *D*. The solid green dot at the origin indicates the total energy density of the collinear single domain state. Energy density dispersions of right-rotating (left-rotating) spin spiral profiles are displayed in the right (left) half-plane of the graph. λ_c: maximum spiral period in the spiral regime.

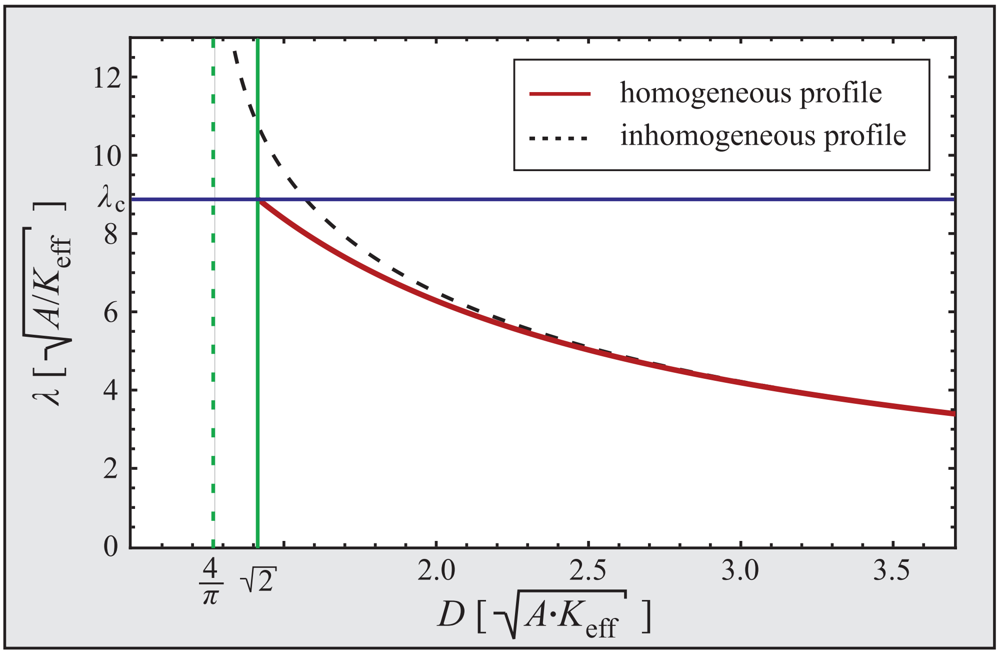

Figure 6.2: Spiral period λ as a function of the Dzyaloshinskii parameter D. The red curve was calculated on the basis of Eq. (6.4), i.e. using a micromagnetic model being restricted to homogeneous spiral profiles. For comparison the dashed curve visualizes the more general case of inhomogeneous spiral profiles (cf. Fig. 3.3(a)). In contrast to the inhomogeneous case the spiral period does not converge if the model is restricted to homogeneous spirals. In particular, spiral periods above a critical value λ_c (blue horizontal line) cannot be described in the framework of homogeneous spiral profiles. In addition, the value of the D_c is slightly increased.

The spin spiral state becomes favorable with respect to the ferromagnetic single domain state if the minimum of the parabola is shifted to energy densities below the one of the ferromagnetic configuration, i.e if the Dzyaloshinskii parameter D is larger than a certain critical value D_c that can be determined on the basis of Eq. (6.4) [48]:

$$D > D_c = \sqrt{2} \cdot \sqrt{AK_{\text{eff}}}. \tag{6.5}$$

Here D_c deviates from the previously determined value of $D_c = \frac{4}{\pi} \cdot \sqrt{AK_{\text{eff}}}$ (Eq. (3.16)) due to the restriction to homogeneous spiral profiles. At $D = D_c$ the magnetic ground state undergoes a phase transition between the collinear state (dot in Fig. 6.1) and the spin spiral regime. The transition is accompanied by a discontinuous jump of the spiral period, as visualized in Fig. 6.1(b). The corresponding critical spiral period λ_c can be determined from the minimum of the energy dispersion Eq. (6.4):

$$\lambda_c = \frac{4\pi}{\sqrt{2}} \cdot \sqrt{\frac{A}{K_{\text{eff}}}} \tag{6.6}$$

With further increasing values of D the spiral period decreases continuously starting from λ_c, as visualized in Fig. 6.2 (red curve)[3]. For comparison, the functional dependence, as obtained for the more general inhomogeneous case (cf. Fig. 3.3), is displayed additionally (black dashed curve). For large values of D the homogeneous model results in essentially the same spiral period, as obtained for the inhomogeneous case. However, for D approaching D_c the models are contradictory. While λ diverges in the inhomogeneous case, it remains finite and approaches λ_c in the case of homogeneous spiral profiles. This behavior implies that large spiral periods can only be reproduced by simultaneously increasing the value of λ_c. However, according to Eq. (6.6) and Eq. (3.21), λ_c is directly related to the domain wall width w_0:

$$\lambda_c = \frac{2\pi}{\sqrt{2}} \cdot w_0 \tag{6.7}$$

Consequently, within the framework of a homogeneous spin-spiral model, large spiral periods and narrow domain wall profiles cannot be reproduced simultaneously, i.e. on the basis of a single unique set of micromagnetic parameters. In particular this problem applies to the spin spiral in the Fe DL on W(110) ($\lambda = 45$ nm, $w_0 = 7.6$ nm).

In the case of long spiral periods and narrow domain wall profiles the homogeneous spiral model cannot be considered as an appropriate approximation that describes the magnetic properties in a consistent way. Nevertheless, the model can be fitted to the experimental observations or the results of DFT-calculations. However, using such an approach, the micromagnetic parameters are mere fitting parameters. In particular, the spiral period and the domain wall shape is reproduced by two different parameter sets, as discussed above. The obtained parameter values can therefore not be considered as physically meaningful quantities such as exchange stiffness, magnetic anisotropy or the Dzyaloshinskii parameter. They are mere fitting parameters that depend on the applied fitting procedure. In the context of the Fe DL on W(110) this explains the deviation of the micromagnetic parameters of Eq. 6.1 and the *effective* parameters determined in [3] (cf. Tab. 4.1) that result in a domain wall width of about twice the experimental value.

Inhomogeneous spiral profiles

In order to overcome the discussed deficiencies the following considerations refer to the general case of inhomogeneous spin spiral profiles. It is shown that the domain wall width and the spiral period are independent quantities, in contrast to the homogeneous spiral model discussed before. This allows for the calculation of a unique set of micromagnetic parameters by fitting the model to the experimental data. In particular, the Dzyaloshinskii parameter D is determined in addition to the parameters of Eq. (6.1).

---

[3] Note, that Eq. (6.4) indicates a linear dependence of λ^{-1} on D, i.e. $\lambda^{-1} = -D/4\pi A$. This linear dependence is reflected in the hyperbolic dependence of λ on D according to Fig. 6.2.

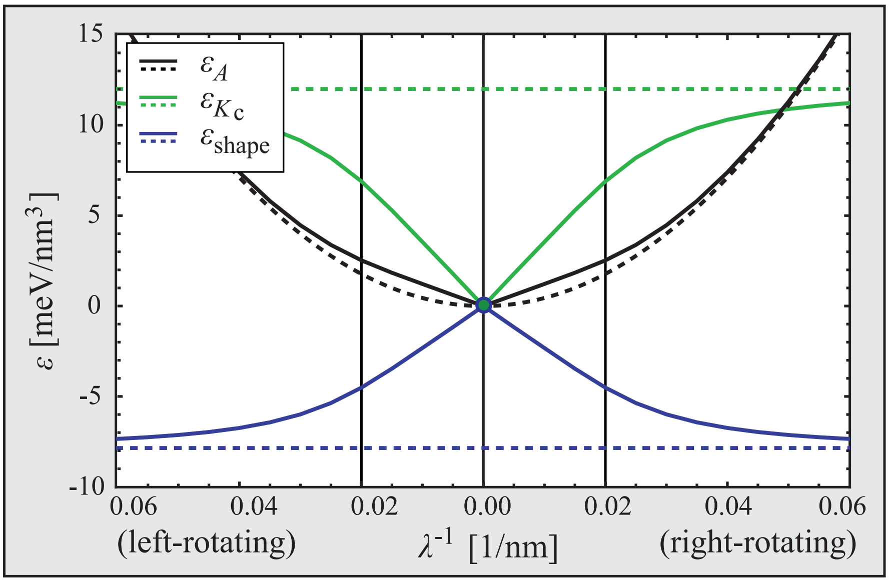

Figure 6.3: Energy density dispersions, as calculated for the general case of inhomogeneous spiral profiles according to Eq. (6.8). For comparison the respective solutions for the homogeneous scenario, as displayed in Fig. 6.1, are given as dashed curves. The collinear single domain state is indicated by the solid dot at the origin. Energy density dispersions of right-rotating (left-rotating) spin spiral profiles are displayed in the right (left) half-plane of the graph.

For the generalized scenario of inhomogeneous spin spiral profiles the analysis of the various contributions to the energy density dispersion Eq. (3.29) can be performed in formal analogy to the homogeneous case (Eq. (6.3)). However, now the spiral profile is given by Eq. (3.15) instead of Eq. (6.2):

$$\phi(x) = \pm\mathrm{am}\left(\frac{1}{\delta\sqrt{\frac{A}{K_{\mathrm{eff}}}}}\cdot x, \delta\right) \quad , \quad \lambda = 4\delta\cdot\sqrt{\frac{A}{K_{\mathrm{eff}}}}\cdot F\left(\frac{\pi}{2},\delta\right). \tag{6.8}$$

In contrast to the homogeneous spiral profile (Eq. (6.2)), $\phi(x)$ can no longer be written as a direct function of λ, since the second expression in Eq. (6.8) cannot be resolved for δ. However, for a given value of δ, both λ and $\phi(x)$ can be determined. Consequently, the spiral profile and the energy density dispersions can be calculated pointwise.

As discussed before, the DM energy only depends on the spiral period but is independent of the spiral shape (cf. Chapter 3). Consequently it is not affected by the discussed transition to inhomogeneous spin spiral profiles. The respective energy density dispersion $\varepsilon_{\mathrm{DM}}(\lambda^{-1})$ remains unchanged with respect to the homogeneous scenario visualized in Fig. 6.1. All other energy density contributions change significantly. Fig. 6.3 shows $\varepsilon_A(\lambda^{-1})$ (solid black), $\varepsilon_{K_c}(\lambda^{-1})$ (solid green) and $\varepsilon_{\mathrm{shape}}(\lambda^{-1})$ (solid blue). The respective curves, as calculated under the assumption of homogeneous spiral profiles, are given as dashed curves of the same colors. All calculations were done on the basis of the micromagnetic parameter set Eq. (6.1). The energy density dispersions of right-rotating (left-rotating) spin spiral profiles are displayed in the right (left) half-plane of the graph. With increasing values of λ^{-1} the spiral profile approaches the homogeneous limit. Thus, the solid curves converge towards the dashed ones. In the opposite limit the inhomogeneity of the spiral profile becomes dominating. Consequently, the energy density dispersions deviate significantly from the ones calculated for the homogeneous scenario discussed before. Even in the transition regime between the two limit cases, i.e for intermediate values of λ, the inhomogeneity of the spiral profile can modify the energy density dispersions significantly. The vertical lines at $\lambda^{-1} = 0.2\ \mathrm{nm}^{-1}$ visualize the experimentally observed spiral period in the Fe DL on W(110).

In Fig. 6.4 all energy contributions are combined in analogy to the homogeneous case. The total energy density $\varepsilon_{\mathrm{tot}}$ (red curve) is visualized for three different values of the Dzyaloshinskii parameter D. For all three scenarios the energy density of the collinear single domain state is given by the dot at the origin of the coordinate system. In contrast to the homogeneous case the total energy density dispersion is now pinned at the origin, i.e it is no longer shifted due to crystalline and shape anisotropy. While the total energy density dispersion $\varepsilon_{\mathrm{tot}}(\lambda^{-1})$ is symmetric for $D = 0$ (a) it is deformed towards an asymmetric shape for $D \neq 0$ (b, c). At $D = D_{\mathrm{c}}$ the magnetic ground state undergoes a phase transition between the collinear state and the spin spiral regime[4]. In particular, right-rotating spin spirals are favored with respect to left-rotating ones due to the asymmetric character of the DM interaction (±-sign in Eq. (3.29)). The phase transition is continuous in contrast to the homogeneous scenario discussed before. Thus, even if A, K_{c} and M_{s} are already determined by the spiral shape this allows for arbitrary spin spiral periods depending on the Dzyaloshinskii parameter D, as visualized by the black dashed curve in Fig. 6.2. Consequently, both the spiral shape and the spiral period can be reproduced on the basis of the same unique set of micromagnetic parameters.

According to the discussion in the previous section the micromagnetic parameters A, K_{c}, and M_{s} can be determined by fitting the calculated profile of a 360° domain wall (Eq. (3.22)) to the experimentally observed spiral profiles, as measured in an external magnetic field. In contrast to the analytical function describing the spin spiral profile in the case $D > D_{\mathrm{c}}$ (Eq. (3.15)) the mathematical expression for the 360° domain wall profile was determined for the case $D = 0$. However, this does not impose any limitation, since the spiral profile is independent of D, as discussed before. Consequently, the fitting procedure on the basis of the 360° domain wall profiles corresponds to a fitting procedure on the basis of inhomogeneous spin spiral profiles driven by a non-vanishing DM interaction. It is therefore meaningful to calculate the energy density dispersions

---

[4] Note, that here D_{c} is given by Eq. (3.16) that was calculated for the general, i.e. inhomogeneous, case. The value differs from the value of Eq. (6.5), as calculated for the homogeneous case.

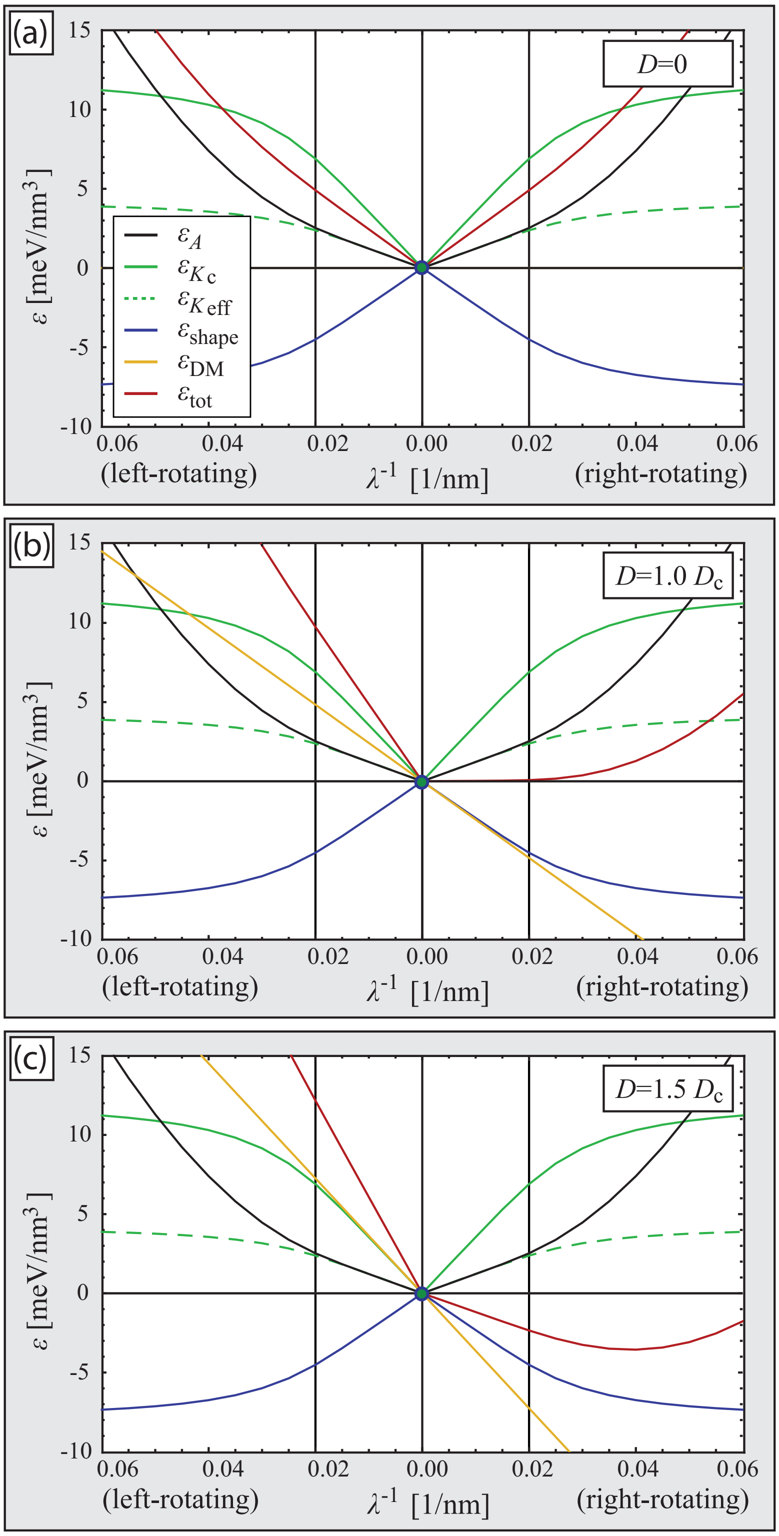

Figure 6.4: Energy density dispersions, as calculated for the case of inhomogeneous spiral profiles according to Eq. (6.8) and various values of the Dzyaloshinskii parameter D. The total energy density of the collinear single domain state is visualized by the dot at the origin. Energy density dispersions of right-rotating (left-rotating) spin spiral profiles are displayed in the right (left) half-plane of the graph.

ε_A, $\varepsilon_{K_\mathrm{c}}$, and $\varepsilon_\mathrm{shape}$ on the basis of the determined parameters (Eq. (6.1)). The DM parameter D can finally be determined such that the minimum of ε_tot in Fig. 6.4 corresponds to the experimentally observed spiral period of about 45 nm.

$$\boxed{D = 0.61 \cdot \frac{4}{\pi}\sqrt{AK_\mathrm{c}} = 1.05 \cdot \frac{4}{\pi}\sqrt{AK_\mathrm{eff}} = 6.4 \cdot 10^{-3}\ \mathrm{J/m^2}.} \qquad (6.9)$$

This value is by a factor of 2.26 larger than the value determined by density functional theory calculations with a subsequent fitting procedure on the basis of homogeneous spin spiral profiles [127]. According to the previous discussion of the homogeneous spiral model this deviation is due to the fact that the parameters determined in [127] must be considered as mere fitting parameters of an *effective* micromagnetic model. In particular, these fitting parameters are not unique and depend on the fitting procedure, as discussed above. They can therefore not be related to physically meaningful quantities, such as exchange stiffness, magnetic anisotropy, and the Dzyaloshinskii parameter, in contrast to the unique set of parameters determined in this thesis[5].

It was shown that the spin spiral ground state in the Fe DL on W(110) can be explained within the framework of a micromagnetic model that considers four different magnetic energy contributions (magnetic exchange, crystalline anisotropy, shape anisotropy, and the DM interaction) and allows for inhomogeneous spin spiral profiles. In particular, the model explains the observed spiral period, the unique rotational sense, the measured domain wall width, the propagation direction, the direction of the domain walls and the magnetic field dependence of the spiral profile in a consistent way. By comparison to Tab. 4.2 it becomes clear that this is a first major step towards a comprehensive description of magnetism in the Fe DL on W(110). According to Eq. (6.9) the observed spin spiral state is induced, because the DM interaction is strong enough to dominate the other interactions. However, this is only possible because of dipolar interaction that reduces the effective anisotropy by means of the shape anisotropy. Without this dipolar energy contribution the DM interaction would be too weak to destabilize the collinear state. Thus, it is the joint effect of both interactions that induces the spiral state.

---

[5] The micromagnetic model used in this thesis is based on magnetic exchange, crystalline anisotropy, demagnetizing energy and the DM interaction. All other physical interactions are neglected. Thus, strictly speaking the model is an effective model as well. However, in contrast to the previously suggested models, all major interactions are included.

6.3 Inhomogeneities of the demagnetizing field

All calculations in the previous section were done on the basis of the micromagnetic model of Eq. (3.29). In addition to magnetic exchange, crystalline anisotropy, and the DM energy, the model considers the energy contribution of shape anisotropy ($\varepsilon_{\text{shape}}$, first term on the right hand side of Eq. (3.27)) while the energy contribution of inhomogeneities of the demagnetizing field ($\varepsilon_{\text{d}}^{\text{inhom}}$, second term on the right hand side of Eq. (3.27)) is neglected. It was shown that, besides the DM interaction, the shape anisotropy is an important driving force towards the observed spin spiral ground state. On the other hand, it is not a priori clear that the omitted demagnetizing energy contribution is negligible, as assumed in Eq. (3.29). In the following the analysis of the previous section is repeated on the basis of Eq. (3.33)-(3.35) that extend the model of Eq. (3.29) by the energy density contribution of inhomogeneities in the demagnetizing field. By comparison of the results of both models it is shown that the application of Eq. (3.29), as done in the previous section, is well justified in extended Fe DL films on W(110). From a methodical perspective, the following considerations are important as well, since the following calculations are based on a numerical procedure that will turn out to be of highest significance in Chapter 7.

Numerical calculation of energy density dispersions

All micromagnetic model equations discussed in this thesis (Eq. (3.29), Eq. (3.33), Eq. (3.35), Eq. (3.39)) are functionals of the spin spiral profile $\phi(x)$ and simultaneously depend on the spiral period λ. Thus, the energy density dispersions $\varepsilon_A(\lambda^{-1})$, $\varepsilon_{K_c}(\lambda^{-1})$, $\varepsilon_{\text{shape}}(\lambda^{-1})$, and $\varepsilon_{K_{\text{eff}}}(\lambda^{-1})$ can in principle be calculated pointwise, i. e. for a discrete set of spiral periods. For each spiral period the calculation follows a two-step process. In a first step the spiral profile $\phi(x)$ is determined such that it minimizes the total energy. In a second step this spiral profile is used to calculate the energy densities ε_A, ε_{K_c}, $\varepsilon_{\text{shape}}$, and $\varepsilon_{K_{\text{eff}}}$. In the previous section the spin spiral profiles were determined using standard variational techniques (Eq. (3.15)). However, this procedure cannot be applied in general, since in most cases an appropriate variational procedure is not known. In particular, this is the case when inhomogeneities in the demagnetizing field come into play. In the present context, it is therefore crucial to replace the variational calculus and pass on to a more versatile numerical procedure.

The most fundamental idea behind the following considerations is the transition from analytical to numerical integration in order to calculate the energy density dispersions. In particular, this transition comes along with the discretization of the integration interval in the respective micromagnetic model equation, and a corresponding discretization of the spiral profile $\phi(x)$. With n being the number of sampling points in the integration interval, the transition can be summarized as:

$$\boxed{\varepsilon\left[\phi\left(x\right)\right] \longrightarrow \varepsilon\left(\left\{\phi_1, \phi_2, ..., \phi_n\right\}\right) \;\Big|\; \phi_i = \phi\left(i \cdot \frac{\lambda}{n}\right)} \tag{6.10}$$

The transition from analytical to numerical integration is equivalent to the replacement of the energy density functional $\varepsilon\left[\phi\left(x\right)\right]$ by a multivariate function $\varepsilon\left(\phi_1, \phi_2, ..., \phi_n\right)$ that can be minimized numerically instead of using variational techniques. As discussed before, this minimization procedure can be applied pointwise in order to obtain $\varepsilon_{\mathrm{min}} = \varepsilon\left(\phi_1, \phi_2, ..., \phi_n\right)$, the minimum of the total energy density, for all considered values of λ. As a byproduct of the numerical procedure, the discretized spiral profile $\boldsymbol{\phi}_{\mathrm{min}} = \{\phi_1, \phi_2, ..., \phi_n\}$ is additionally obtained for all considered spiral periods. Starting from these spiral profiles, all energy density dispersions can be calculated point by point. The discussed numerical process is visualized in Fig. 6.5.

The energy density dispersions to be discussed in the following were calculated for $\lambda^{-1} \in \{0.005\ \mathrm{nm}^{-1}, 0.010\ \mathrm{nm}^{-1}, ..., 0.060\ \mathrm{nm}^{-1}\}$. They are represented by lists of tuples $(\lambda^{-1}|\varepsilon(\lambda^{-1}))$. For every tuple the numerical calculation starts from a homogeneous spiral profile with spiral period λ that is discretized according to Eq. (6.10). The resulting multivariate function $\varepsilon\left(\phi_1, \phi_2, ..., \phi_n\right)$ is minimized using the quasi-Newton formalism [128], as implemented in the *FindMinimum*-method of the commercially available software *Mathematica* [129]. The numerical reliability of the results depends on two determinants:

- The number of sampling points for the discretization (n).
- The numerical accuracy of the *FindMinimum*-method, as implemented in the Mathematica software. It is determined by the values of the Mathematica specific parameters *AccuracyGoal* and *PrecisionGoal*.

Software test: The software implementation of the discussed numerical procedure, as developed in the framework of this thesis, was initially applied to the micromagnetic model investigated in the previous section (Eq. (3.29)). For the parameter set ($n = 50$, *AccuracyGoal* = 5, *PrecisionGoal* = 20) it was verified that the numerically calculated dispersion relations coincide with the analytically calculated curves of Fig. 6.4 within the error of the graphical representation.

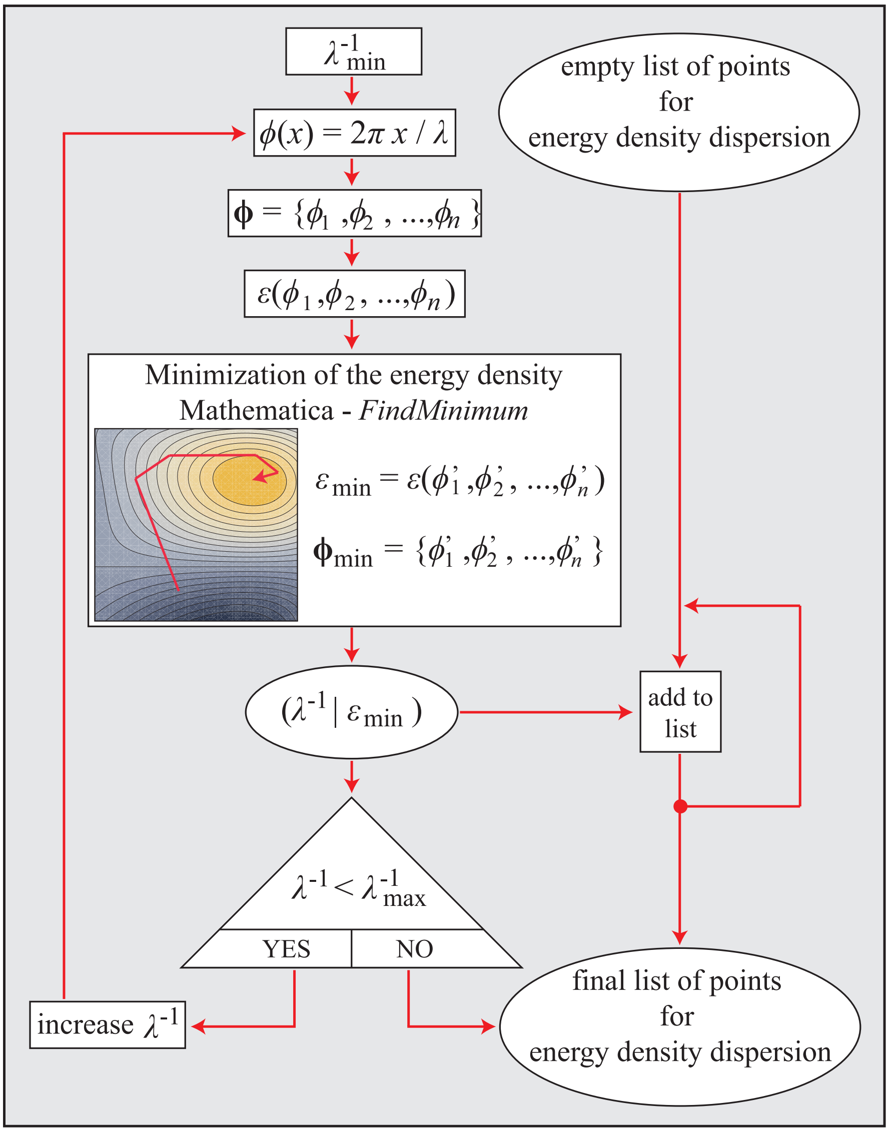
$\lambda^{-1}_{\text{min}}$
empty list of points
for
energy density dispersion
$\phi(x) = 2\pi\, x / \lambda$
$\Phi = \{\phi_1, \phi_2, \ldots, \phi_n\}$
$\varepsilon(\phi_1, \phi_2, \ldots, \phi_n)$
Minimization of the energy density
Mathematica - *FindMinimum*
$\varepsilon_{\text{min}} = \varepsilon(\phi'_1, \phi'_2, \ldots, \phi'_n)$
$\Phi_{\text{min}} = \{\phi'_1, \phi'_2, \ldots, \phi'_n\}$
$(\lambda^{-1} | \varepsilon_{\text{min}})$
add to
list
$\lambda^{-1} < \lambda^{-1}_{\text{max}}$
YES
NO
increase λ^{-1}
final list of points
for
energy density dispersion

Figure 6.5: Structure diagram visualizing the numerical process for the pointwise calculation of the energy density dispersions. Each point of the energy dispersion is given by a tuple $(\lambda\,|\varepsilon_{\text{min}}(\lambda))$. Starting from the homogeneous limit the spiral profile is modified until the energy density minimum is reached. In this thesis the minimization is based on the quasi-Newton formalism [128], as implemented in the *FindMinimum*-method of the commercially available software *Mathematica* [129].

Negligible influence of inhomogeneities of the demagnetizing field

In the previous section the calculation of the demagnetizing energy density was simplified by neglecting the contribution of inhomogeneities of the demagnetizing field ($\varepsilon_{\mathrm{d}}^{\mathrm{inhom}}$, second summand on the right hand side of Eq. (3.27)). In the following, this limitation is dropped, i.e. the previously used micromagnetic model (Eq. (3.29)) is replaced by the more general model of Eq. (3.33)-(3.35) that considers all contributions to the demagnetizing energy. As discussed in Chapter 3, this generalized model is valid for the special case of a closed magnetic film and a magnetic ground state being periodic along the x-direction, such as the spin spiral configuration observed in the Fe DL on W(110). While the functionals $\varepsilon_A\left[\phi\left(x\right)\right]$, $\varepsilon_{\mathrm{DM}}\left[\phi\left(x\right)\right]$, and $\varepsilon_{K_{\mathrm{c}}}\left[\phi\left(x\right)\right]$ remain unchanged compared to the previously used model, the functional form of $\varepsilon_{\mathrm{d}}\left[\phi\left(x\right)\right]$ is considerably more complicated than the functional $\varepsilon_{\mathrm{shape}}\left[\phi\left(x\right)\right]$ used in the simplified model.

For the calculation of the energy density dispersions this increased complexity imposes two complications:

- The spiral profile can no longer be determined in a mathematically closed functional form by applying variational techniques.
- Even if the spiral profile is known, ε_{d}, can in general not be calculated exactly due to the infinite summation in Eq. (3.33)+(3.34).

Using the numerical procedure discussed in the previous section, the first limitation can in principle be overcome. However, due to the second limitation the numerical procedure cannot be applied. It is therefore necessary to first approximate ε_{d} by considering only a finite number of summands in Eq. (3.33)+(3.34). In the following it will be discussed how such an approximation can be done and how the respective error can be quantified.

Approximation of the demagnetizing energy density

According to Eq. (3.35) the demagnetizing energy density can be split into the contributions of magnetic surface and volume charges ($\varepsilon_{\mathrm{d}}^{\mathrm{surf}}$ and $\varepsilon_{\mathrm{d}}^{\mathrm{vol}}$). The following discussion initially refers to the approximation of $\varepsilon_{\mathrm{d}}^{\mathrm{surf}}$ and the quantification of the corresponding error. The energy density contribution of the magnetic volume charges ($\varepsilon_{\mathrm{d}}^{\mathrm{vol}}$) can be treated in an analogous way.

A periodic surface charge distribution $\sigma_x\left(x\right) = \sin\left[\phi\left(x\right)\right]$ (cf. Eq. (3.32)), like the one describing the spin spiral ground state of the Fe DL on W(110), can always be expanded into a Fourier series:

$$\begin{aligned}\sigma_x(x) &= \sum_{r=-\infty}^{\infty} c_r \mathrm{e}^{\mathrm{i}r\frac{2\pi}{\lambda}x} \\ c_r &:= \frac{1}{\lambda}\int_0^{\lambda} \sigma_x(x)\cdot \mathrm{e}^{-\mathrm{i}r\frac{2\pi}{\lambda}x}\mathrm{d}x.\end{aligned} \tag{6.11}$$

In agreement with the experimental observations the spiral profile can be assumed to be continuously differentiable. Thus, the Fourier series converges at least pointwise and $\sigma_x(x)$ can be approximated by a finite Fourier sum:

$$\sigma_x(x) \approx \sum_{r=-\tilde{r}}^{\tilde{r}} c_r \mathrm{e}^{\mathrm{i}r\frac{2\pi}{\lambda}x}. \tag{6.12}$$

The quality of the approximation depends on the number of Fourier coefficients being considered ($2\tilde{r}$). It can by quantified by the error of convergence $R(\tilde{r})$ that is defined here using Parseval's identity:

$$\frac{1}{\lambda}\int_0^{\lambda} |\sigma_x(x)|^2 \ \mathrm{d}x = \sum_{r=-\infty}^{\infty} |c_r|^2 = \sum_{r=-\tilde{r}}^{\tilde{r}} |c_r|^2 + R(\tilde{r}). \tag{6.13}$$

The following considerations will be based on the relative error of convergence $\overline{R}(\tilde{r})$ that can be derived from $R(\tilde{r})$ according to:

$$\boxed{\overline{R}(\tilde{r}) = \frac{R(\tilde{r})}{\frac{1}{\lambda}\int_0^{\lambda} |\sigma_x(x)|^2 \ \mathrm{d}x} = \frac{R(\tilde{r})}{\sum_{r=-\infty}^{\infty} |c_r|^2}.} \tag{6.14}$$

The calculation of the demagnetizing energy density ε_{d} (Eq. (3.33)) is based on the Fourier coefficients c_r, as obtained from the Fourier expansion of the surface charge distribution (Eq. (6.11)). Each Fourier coefficient corresponds to one of the summands in (Eq. (3.33). Thus, the approximation of $\sigma_x(x)$ by a finite number of Fourier coefficients can be directly related to a corresponding approximation of ε_{d}:

$$\boxed{\begin{gathered}\varepsilon_{\mathrm{d}}^{\mathrm{surf}}\left[\phi_{\lambda}(x)\right]=\frac{1}{V}\cdot\frac{\mu_0}{2}M_{\mathrm{s}}^2\cdot\left\{c_0^2+\sum_{r=-\tilde{r}}^{\tilde{r}}\left[c_r\cdot c_{-r}\cdot\frac{1-\mathrm{e}^{-2\pi d\left|\frac{r}{\lambda}\right|}}{2\pi d\left|\frac{r}{\lambda}\right|}\right]\right\}\\ c_r:=\frac{1}{\lambda}\int_0^{\lambda}\sigma_x(x)\cdot\mathrm{e}^{-\mathrm{i}r\frac{2\pi}{\lambda}x}\mathrm{d}x\quad,\quad\sigma_x(x):=\sin\left[\phi_{\lambda}(x)\right]\end{gathered}}\tag{6.15}$$

In particular, the errors of σ_x and ε_{d} are related quantities. Thus, in both cases the quality of the approximation is essentially described by the relative error of convergence $\overline{R}(\tilde{r})$, as defined in Eq. (6.14).

As discussed above, the energy density contribution of the magnetic volume charges can be treated in an analogous way:

$$\boxed{\begin{gathered}\varepsilon_{\mathrm{d}}^{\mathrm{vol}}\left[\phi_{\lambda}(x)\right]=\frac{1}{V}\cdot\frac{\mu_0}{2}M_{\mathrm{s}}^2\cdot\left\{c_0^2+\sum_{r=-\tilde{r}}^{\tilde{r}}\left[c_r\cdot c_{-r}\cdot\left(1-\frac{1-\mathrm{e}^{-2\pi d\left|\frac{r}{\lambda}\right|}}{2\pi d\left|\frac{r}{\lambda}\right|}\right)\right]\right\}\\ c_r:=\frac{1}{\lambda}\int_0^{\lambda}\gamma_x(x)\cdot\mathrm{e}^{-\mathrm{i}r\frac{2\pi}{\lambda}x}\mathrm{d}x\quad,\quad\gamma_x(x):=\cos\left[\phi_{\lambda}(x)\right]\\ \overline{R}(\tilde{r})=\frac{R(\tilde{r})}{\frac{1}{\lambda}\int_0^{\lambda}\left|\gamma_x(x)\right|^2\,\mathrm{d}x}=\frac{R(\tilde{r})}{\sum_{r=-\infty}^{\infty}\left|c_r\right|^2}.\end{gathered}}\tag{6.16}$$

Numerical calculation of the energy density dispersions and the spin spiral profiles

As discussed before, the following calculations are based on a micromagnetic model (Eq. (3.33)-(3.35)) that extends the previously used model (Eq. (3.29)) by the additional consideration of $\varepsilon_{\mathrm{d}}^{\mathrm{inhom}}\left[\phi_{\lambda}\right]$. In order to make the model applicable to the numerical procedure discussed before, the functional $\varepsilon_{\mathrm{d}}\left[\phi(x)\right]$ (Eq. (3.34) must be approximated according to Eq. (6.15)+(6.16). The complete model can be summarized as follows:

$$\boxed{\begin{aligned}
\varepsilon\left[\phi_\lambda\right] &= \varepsilon_A\left[\phi_\lambda\right] + \varepsilon_{\mathrm{DM}}\left[\phi_\lambda\right] + \varepsilon_{K_\mathrm{c}}\left[\phi_\lambda\right] + \varepsilon_{\mathrm{shape}}\left[\phi_\lambda\right] + \varepsilon_{\mathrm{d}}^{\mathrm{inhom}}\left[\phi_\lambda\right] \\[1em]
\varepsilon_A\left[\phi_\lambda\right] &= \lambda^{-1}\cdot\int A\cdot\left|\dot{\phi}_\lambda(x)\right|^2\,\mathrm{d}x \\
\varepsilon_{\mathrm{DM}}\left[\phi_\lambda\right] &= \lambda^{-1}\cdot\int \pm D\cdot\left|\dot{\phi}_\lambda(x)\right|\,\mathrm{d}x \\
\varepsilon_{K_\mathrm{c}}\left[\phi_\lambda\right] &= \lambda^{-1}\cdot\int K_\mathrm{c}\cdot\cos^2\phi_\lambda(x)\,\mathrm{d}x \\
\varepsilon_{\mathrm{shape}}\left[\phi_\lambda\right] &= \lambda^{-1}\cdot\int K_{\mathrm{shape}}\cdot\cos^2\phi_\lambda(x)\,\mathrm{d}x \\
\varepsilon_{\mathrm{d}_\perp}^{\mathrm{inhom}}\left[\phi_\lambda\right] &= \varepsilon_{\mathrm{d}}^{\mathrm{surf}}\left[\phi_\lambda\right] - \varepsilon_{\mathrm{shape}}\left[\phi_\lambda\right] \\
\varepsilon_{\mathrm{d}_\parallel}^{\mathrm{inhom}}\left[\phi_\lambda\right] &= \varepsilon_{\mathrm{d}}^{\mathrm{vol}}\left[\phi_\lambda\right] \\[1em]
\varepsilon_{\mathrm{d}}^{\mathrm{surf}}\left[\phi_\lambda\right] \; &: \; \text{cf. Eq. (6.15)} \quad , \quad \varepsilon_{\mathrm{d}}^{\mathrm{vol}}\left[\phi_\lambda\right] \; : \; \text{cf. Eq. (6.16)}
\end{aligned}} \tag{6.17}$$

According to Eq. (6.14)+(6.16), the errors of $\varepsilon_{\mathrm{d}}^{\mathrm{surf}}[\phi(x)]$, $\varepsilon_{\mathrm{d}}^{\mathrm{vol}}[\phi(x)]$, $\varepsilon_{\mathrm{d}_\perp}^{\mathrm{inhom}}[\phi(x)]$, and $\varepsilon_{\mathrm{d}_\parallel}^{\mathrm{inhom}}[\phi(x)]$ decrease with the number of considered Fourier coefficients ($\tilde{r}$). For the following calculations $\tilde{r}$ was chosen such that $\overline{R}(\tilde{r}) < 0.001$ ‰[6] in all four cases.

As discussed before, $\varepsilon_{\mathrm{DM}}(\lambda^{-1})$ is independent of the spiral shape (cf. Chapter 3). It is therefore not affected by inhomogeneities in the demagnetizing field and remains unchanged with respect to the previous calculations. All other energy density dispersions, as calculated on the basis of Eq. (6.17), are shown in Fig. 6.6 (a). Compared to the simplified model, $\varepsilon_A(\lambda^{-1})$, $\varepsilon_{K_\mathrm{c}}(\lambda^{-1})$, $\varepsilon_{K_\mathrm{eff}}(\lambda^{-1})$, and $\varepsilon_{\mathrm{shape}}(\lambda^{-1})$ remain unchanged within the precision of the graphical representation. The additional energy density dispersions $\varepsilon_{\mathrm{d}_\perp}^{\mathrm{inhom}}(\lambda^{-1})$ and $\varepsilon_{\mathrm{d}\parallel}^{\mathrm{inhom}}(\lambda^{-1})$ are symmetric with respect zero energy density and cancel out completely within the precision of the graphical representation, i.e. $\varepsilon_{\mathrm{shape}}$ is the only significant energy density contribution of the demagnetizing field. It is therefore well justified to neglect inhomogeneities of the demagnetizing field right from the beginning and describe the spin spiral ground state in the Fe DL on W(110) in terms

---

[6] In contrast to the previous discussion the denominator in Eq. (6.14) can no longer be evaluated exactly, since for non-vanishing values of $\varepsilon_{\mathrm{d}}^{\mathrm{inhom}}$ there is no analytical expression describing the magnetization profile $\phi(x)$, and thus $\sigma(x)$ and $\gamma(x)$. Here, this problem is overcome by replacing the infinite sum in the definition of $\overline{R}$ by a finite one. The summation boundaries ($\tilde{r} = \pm 250$) are chosen such that with a further increase of $\tilde{r}$ at every point of the numerically calculated energy dispersions the spiral profile only changes within the precision of the graphical representation.

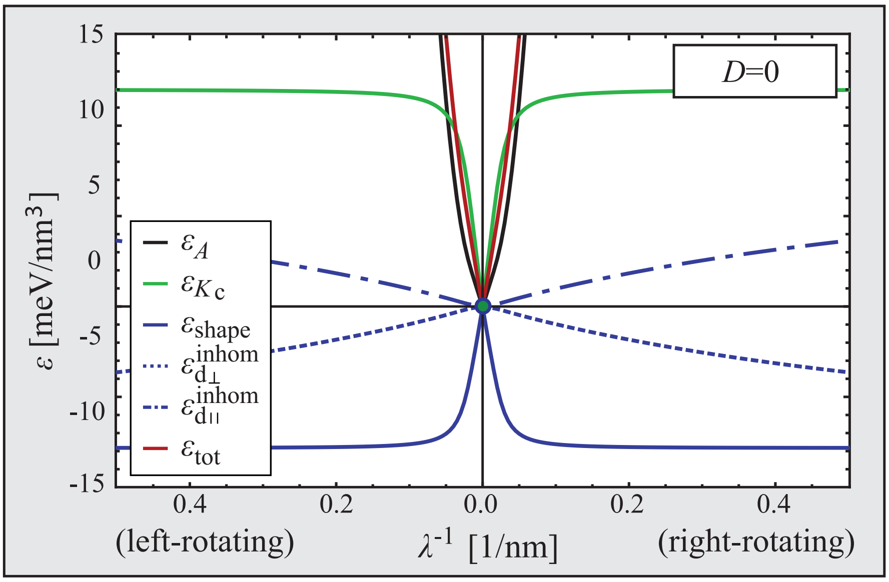

Figure 6.6: (a) Energy density dispersions, as calculated for the case of a non-vanishing energy density contribution of inhomogeneities in the demagnetizing field. The curves of $\varepsilon_A(\lambda^{-1})$, $\varepsilon_{K_\mathrm{c}}(\lambda^{-1})$, $\varepsilon_{K_\mathrm{eff}}(\lambda^{-1})$, and $\varepsilon_{\mathrm{shape}}(\lambda^{-1})$ coincide with the curves of Fig. 6.4 (a) within the error of the graphical representation. The curves of $\varepsilon_{\mathrm{d}_\perp}^{\mathrm{inhom}}(\lambda^{-1})$ and $\varepsilon_{\mathrm{d}_\parallel}^{\mathrm{inhom}}(\lambda^{-1})$ are symmetric with respect to zero energy density within the resolution of the graphs.

of the simplified micromagnetic model (Eq. (3.29)), as discussed before. In particular, the vanishing contribution of $\varepsilon_{\mathrm{d}}^{\mathrm{inhom}} = \varepsilon_{\mathrm{d}_\perp}^{\mathrm{inhom}} + \varepsilon_{\mathrm{d}\parallel}^{\mathrm{inhom}}$ also justifies the procedure that was applied in [1] to determine the exchange stiffness A and the effective anisotropy parameter K_{eff} (Eq. (6.1)).

Numerical accuracy: The energy density dispersions shown in Fig. 6.6 were calculated pointwise starting from the micromagnetic model defined by Eq. (6.15)-(6.17). According to the previous discussion, the corresponding spiral profiles were approximated by a finite Fourier sum at each point of the curve (Eq. (6.12)), i.e. by a finite number of Fourier coefficients. In the homogeneous limit the spin spiral profile is perfectly sinusoidal and can therefore be described by only one Fourier coefficient. Consequently, the error due to the application of the finite Fourier sum vanishes. With increasing inhomogeneity the size of the domain areas increases while the size of the domain walls remains essentially constant. Due to this asymmetry the number of Fourier coefficients needed in order to keep $\overline{R}$ at a constant value increases with increasing inhomogeneity. It is therefore necessary to investigate the dependence of $\overline{R}$ on the number of considered Fourier coefficients at each point.

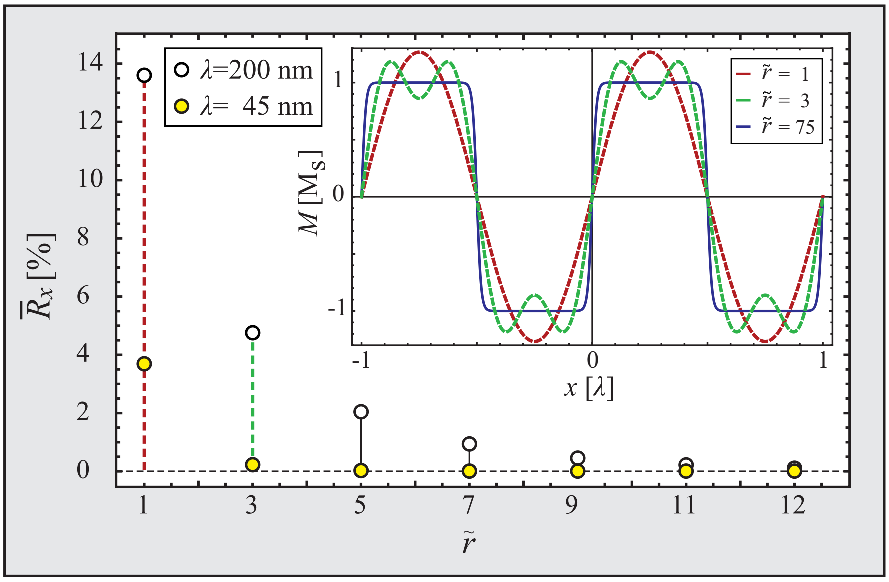

Figure 6.7: Relative error of convergence as a function of the number of Fourier coefficients ($\tilde{r}$) being considered for the approximation of the spiral profile. The error decreases with increasing $\tilde{r}$. For a spiral period of $\lambda = 200$ nm the convergence of the real-space spiral profile is shown in the inset.

Fig. 6.7 displays this dependence for the experimentally observed spiral period ($\lambda = 45$ nm) and the largest spiral period considered in Fig. 6.7 ($\lambda = 200$ nm). As discussed before, in both cases $\overline{R}$ decreases with the number of considered Fourier coefficients. It is systematically larger in the case of the longer spiral period due to the increased asymmetry of the spiral shape. In both cases for $\tilde{r} > 12$ the error becomes very small. For $\tilde{r} > 75$, i.e. the value used for the calculation of the curves in Fig. 6.6 it is below 0.001 ‰. The inset visualizes the dependence of the approximated spin spiral profile (out-of-plane magnetization) on the number of Fourier coefficients for the case $\lambda = 200$ nm. For $\tilde{r} = 1$ (red dashed curve) the approximated spiral profile is of sinusoidal shape. The error of the approximation amounts to $\overline{R} = 13.6\%$, as shown in the main panel. For $\tilde{r} = 3$ (green dashed curve) the profile deviates from the sinusoidal shape with $\overline{R}$ decreasing to 4.8%. The blue curve finally shows the profile ($\tilde{r} = 75$), as used for the calculations shown in Fig. 6.6. As mentioned before, the error of the discussed approximation is below 0.001 ‰

Chapter 7

Finite Fe double layer stripes

In Chapter 6 the focus was put on the analysis of the spin spiral in the extended Fe DL on W(110). It was shown that the spin spiral is induced by the interplay of magnetic exchange, anisotropy and the DM interaction. The demagnetizing energy was considered in terms of an effective anisotropy parameter. In particular, it was shown that the observed spiral period, the unique rotational sense, the domain wall width, the domain wall orientation and the magnetic field dependence (first five lines in Tab. 4.2) can be reproduced consistently on the basis of an extended micromagnetic model and a unique set of micromagnetic parameters. In this chapter the micromagnetic model is extended to finite Fe DL stripes on W(110), as investigated in previous SP-STM experiments [29, 120, 130]. The main focus is put on the investigation of the observed vanishing of the spin spiral ground state in narrow stripes, the stripe width dependent vanishing of the spin contrast at elevated temperatures, and the stripe width dependence of the spiral period (last three lines in Tab. 4.2). In particular, it is shown that the observations can be explained as a consequence of inhomogeneities of the demagnetizing field at the stripe edges (cf. Fig. 3.5 I (b)), in contrast to the previously discussed closed film geometry where inhomogeneities of the demagnetizing field were shown to be negligible.

7.1 Extended micromagnetic model calculations

Up to now, all micromagnetic calculations were restricted to the case of extended Fe DL films on W(110), i.e. the magnetization was assumed to be constant along the direction perpendicular to the propagation direction of the spin spiral. Consequently, inhomogeneities of the demagnetizing field at the edges of the Fe DL areas could be neglected. For an appropriate description of finite Fe DL stripes these simplifications must be dropped in the following. Thus, it is assumed that inside the Fe DL stripes the magnetization remains constant along the direction perpendicular to the propagation direction while it is assumed to be zero in the gaps between the stripes. Compared to

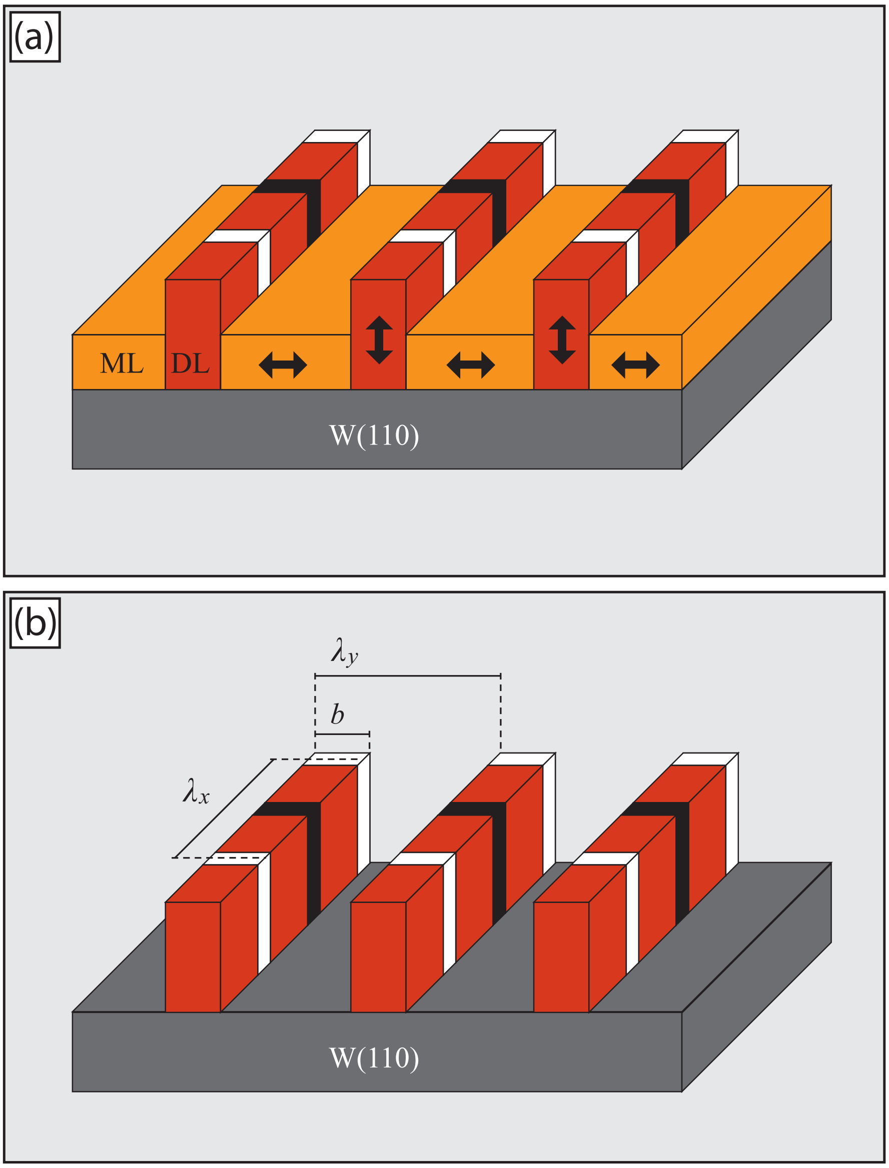

Figure 7.1: (a) Magnetic configuration of the Fe DL stripes on W(110) and the intermediate Fe ML. In the ML areas the magnetic easy axis points perpendicular to the propagation direction of the spin spiral in the DL. (b) Magnetic configuration, as used for the calculations in this chapter. The ML areas are not considered, since the spiral profile in the DL is essentially unaffected by the ML due to the perpendicular orientation of the magnetic easy axis.

the experimentally investigated samples this assumption constitutes a simplification, since in real world systems the DL stripes are separated by in-plane magnetized ML areas (cf. Fig. 7.1). According to [131] the ML is ferromagnetic below its Curie temperature $T_\mathrm{c} = 225\,\mathrm{K}$ with an in-plane-anisotropy along $[1\bar{1}0]$. Nevertheless, neglecting the magnetic structure of the ML seems to be well justified, since due to the in-plane anisotropy the Fe ML only has a weak stray field that is oriented perpendicular to the magnetization in the DL, and therefore should not affect the magnetization of the DL stripes significantly. The following calculations are based on the micromagnetic model described by Eq. (3.39), that extends the model used in the context of closed Fe DL films (Eq. (3.35)) to the case of non-trivial surface topographies. In particular, this is achieved by calculating the surface and volume charge contributions to the demagnetizing energy density ($\varepsilon_\mathrm{d}^\mathrm{surf}$ and $\varepsilon_\mathrm{d}^\mathrm{vol}$) on the basis of Eq. (3.30)-(3.31), instead of the previously used Eq. (3.33)-(3.34). Here, the micromagnetic model is repeated for the sake of clarity[1]:

$$\boxed{\begin{aligned}
\varepsilon\left[\phi_\lambda\right] &= \varepsilon_A\left[\phi_\lambda\right] + \varepsilon_\mathrm{DM}\left[\phi_\lambda\right] + \varepsilon_{K_\mathrm{c}}\left[\phi_\lambda\right] + \varepsilon_\mathrm{shape}\left[\phi_\lambda\right] + \varepsilon_\mathrm{d}^\mathrm{inhom}\left[\phi_\lambda\right] \\
\\
\varepsilon_A\left[\phi_\lambda\right] &= \lambda^{-1}\cdot\int A\cdot\left|\dot{\phi}_\lambda(x)\right|^2\,\mathrm{d}x \\
\varepsilon_\mathrm{DM}\left[\phi_\lambda\right] &= \lambda^{-1}\cdot\int \pm D\cdot\left|\dot{\phi}_\lambda(x)\right|\,\mathrm{d}x \\
\varepsilon_{K_\mathrm{c}}\left[\phi_\lambda\right] &= \lambda^{-1}\cdot\int K_\mathrm{c}\cdot\cos^2\phi_\lambda(x)\,\mathrm{d}x \\
\varepsilon_\mathrm{shape}\left[\phi_\lambda\right] &= \lambda^{-1}\cdot\int K_\mathrm{shape}\cdot\cos^2\phi_\lambda(x)\,\mathrm{d}x \\
\varepsilon_\mathrm{d}^\mathrm{inhom}\left[\phi_\lambda\right] &= \frac{1}{p}\cdot\left(\varepsilon_\mathrm{d}^\mathrm{surf}\left[\phi_\lambda,\tau\right] + \varepsilon_\mathrm{d}^\mathrm{vol}\left[\phi_\lambda,\tau\right]\right) - \varepsilon_\mathrm{shape}\left[\phi_\lambda\right] \\
\\
\varepsilon_\mathrm{d}^\mathrm{surf}\left[\phi_\lambda\right] &: \text{ cf. Eq. (3.30)} \quad , \quad \varepsilon_\mathrm{d}^\mathrm{vol}\left[\phi_\lambda\right] : \text{ cf. Eq. (3.31)}
\end{aligned}} \tag{7.1}$$

---

[1] Eq. (7.1) was rewritten such that it becomes formally equivalent to Eq. (6.17). In contrast to Eq. (6.17), here $\varepsilon_\mathrm{d}^\mathrm{surf}\left[\phi_\lambda,\tau\right]$ and $\varepsilon_\mathrm{d}^\mathrm{vol}\left[\phi_\lambda,\tau\right]$ are functionals of both $\phi(x)$ and the topography of the DL stripe array, as described by the function $\tau(y)$ (cf. Eq. 3.37).

For an Fe DL stripe array, like the one shown in Fig. 7.1, the topography $\tau(x,y)$, as introduced in Eq. (3.37), reduces to a function varying only along the direction perpendicular to the stripes:

$$\tau(x,y) = \tau(y) = \left\{ \begin{array}{lcl} 1 & : & n\cdot\lambda_y \geq y \geq n\cdot\lambda_y + b \\ 0 & : & n\cdot\lambda_y + b > y > (n+1)\cdot\lambda_y \end{array} \right| n \in \mathbb{Z} \tag{7.2}$$

In contrast, the spiral profile only varies along the propagation direction of the spin spiral. Thus, the two-dimensional functions $\sigma(x,y)$ and $\gamma(x,y)$, as needed for the calculation of $\varepsilon_{\mathrm{d}}^{\mathrm{surf}}$ and $\varepsilon_{\mathrm{d}}^{\mathrm{vol}}$ can be written as product of $\tau(y)$ and the one-dimensional functions $\sigma_x(x)$ and $\gamma_x(x)$, as introduced in Chapter 6:

$$\begin{aligned} \sigma(x,y) &= \sigma_x(x)\cdot\tau(y) \\ \gamma(x,y) &= \gamma_x(x)\cdot\tau(y) \end{aligned} \tag{7.3}$$

Approximation of the demagnetizing energy density

In analogy to the case of closed Fe DL films on W(110), the magnetic ground state configuration of Fe DL stripe arrays can be calculated by applying the numerical procedure discussed in Chapter 6 to the micromagnetic model described by Eq. (7.1). However, in a preceding step the model must be simplified by considering only a finite number of summands for the calculation of the demagnetizing energy density, i.e. for the calculation of $\varepsilon_{\mathrm{d}}^{\mathrm{surf}}$ and $\varepsilon_{\mathrm{d}}^{\mathrm{vol}}$ (Eq. (3.30)-(3.31)). In analogy to the closed film scenario (Eq. (6.12)), the functions $\sigma_x(x)$, $\gamma_x(x)$, and $\tau(y)$ can be approximated by finite Fourier series:

$$\begin{aligned} \sigma_x(x) &= \sum_{r=-\tilde{r}}^{\tilde{r}} c_r^{(\sigma_x)} \mathrm{e}^{\mathrm{i}r\frac{2\pi}{\lambda_x}x} \quad , \quad c_r^{(\sigma_x)} = \frac{1}{\lambda_x}\int_0^{\lambda_x} \sin\left[\phi(x)\right]\cdot \mathrm{e}^{-\mathrm{i}r\frac{2\pi}{\lambda_x}x}\mathrm{d}x \\ \gamma_x(x) &= \sum_{r=-\tilde{r}}^{\tilde{r}} c_r^{(\gamma_x)} \mathrm{e}^{\mathrm{i}r\frac{2\pi}{\lambda_x}x} \quad , \quad c_r^{(\gamma_x)} = \frac{1}{\lambda_x}\int_0^{\lambda_x} \cos\left[\phi(x)\right]\cdot \mathrm{e}^{-\mathrm{i}r\frac{2\pi}{\lambda_x}x}\mathrm{d}x \\ \tau(y) &= \sum_{s=-\tilde{s}}^{\tilde{s}} c_s^{(\tau)} \mathrm{e}^{\mathrm{i}s\frac{2\pi}{\lambda_y}y} \quad , \quad c_s^{(\tau)} = \frac{1}{\lambda_y}\int_0^{\lambda_y} \tau(y)\cdot \mathrm{e}^{-\mathrm{i}s\frac{2\pi}{\lambda_y}y}\mathrm{d}y \overset{Eq.\ (7.2)}{=} \frac{\mathrm{e}^{\mathrm{i}s\frac{2\pi}{\lambda_y}d} - \mathrm{i}}{2\pi s} \end{aligned} \tag{7.4}$$

The corresponding relative errors of convergence $\overline{R}_{\sigma_x}(\tilde{r})$, $\overline{R}_{\gamma_x}(\tilde{r})$, and $\overline{R}_{\tau}(\tilde{r})$ can be calculated according to Eq. (6.14). For the product functions $\sigma(x,y)$ and $\gamma(x,y)$ the relative errors result from the summation of the errors of the respective factor functions:

$$\begin{aligned}\overline{R}_{\sigma}(\tilde{r},\tilde{s}) &= \overline{R}_{\sigma_x}(\tilde{r}) + \overline{R}_{\tau}(\tilde{s}) \\ \overline{R}_{\gamma}(\tilde{r},\tilde{s}) &= \overline{R}_{\gamma_x}(\tilde{r}) + \overline{R}_{\tau}(\tilde{s})\end{aligned} \tag{7.5}$$

Like in the case of extended Fe DL films, the approximation of $\sigma(x,y)$ and $\gamma(x,y)$ by finite Fourier sums is directly related to a corresponding approximation of $\varepsilon_{\mathrm{d}}^{\mathrm{surf}}$ and $\varepsilon_{\mathrm{d}}^{\mathrm{vol}}$:

$$\boxed{\begin{gathered}\varepsilon_{\mathrm{d}}^{\mathrm{surf}} = \frac{\mu_0}{2}M_{\mathrm{s}}^2 \cdot \left\{c_{00}^2 + \sum_{r=-\tilde{r}}^{\tilde{r}}\sum_{s=-\tilde{s}}^{\tilde{s}}\left[c_{rs}\cdot c_{-r-s}\cdot\frac{1-\mathrm{e}^{-2\pi g_{rs}}}{2\pi g_{rs}}\right]\right\} \\ c_{rs} := c_r^{(\sigma_x)}\cdot c_s^{(\tau)} \\ g_{rs} := d\sqrt{\left(\frac{r}{\lambda_x}\right)^2 + \left(\frac{s}{\lambda_y}\right)^2}\end{gathered}} \tag{7.6}$$

$$\boxed{\begin{gathered}\varepsilon_{\mathrm{d}}^{\mathrm{vol}} = \frac{\mu_0}{2}M_{\mathrm{s}}^2 \cdot \left\{c_{00}^2 + \sum_{r=-\tilde{r}}^{\tilde{r}}\sum_{s=-\tilde{s}}^{\tilde{s}}\left[c_{rs}\cdot c_{-r-s}\cdot\frac{\lambda_x^2}{\lambda_x^2+\lambda_y^2}\cdot\left(1-\frac{1-\mathrm{e}^{-2\pi g_{rs}}}{2\pi g_{rs}}\right)\right]\right\} \\ c_{rs} := c_r^{(\gamma_x)}\cdot c_s^{(\tau)} \\ g_{rs} := d\sqrt{\left(\frac{r}{\lambda_x}\right)^2 + \left(\frac{s}{\lambda_y}\right)^2}\end{gathered}} \tag{7.7}$$

In analogy to the closed film scenario the errors of σ and $\varepsilon_{\mathrm{d}}^{\mathrm{surf}}$ (γ and $\varepsilon_{\mathrm{d}}^{\mathrm{vol}}$) are related quantities. Thus, the quality of the approximation in Eq. (7.6)-(7.7) is essentially described by the relative errors of convergence as given in Eq. (7.5).

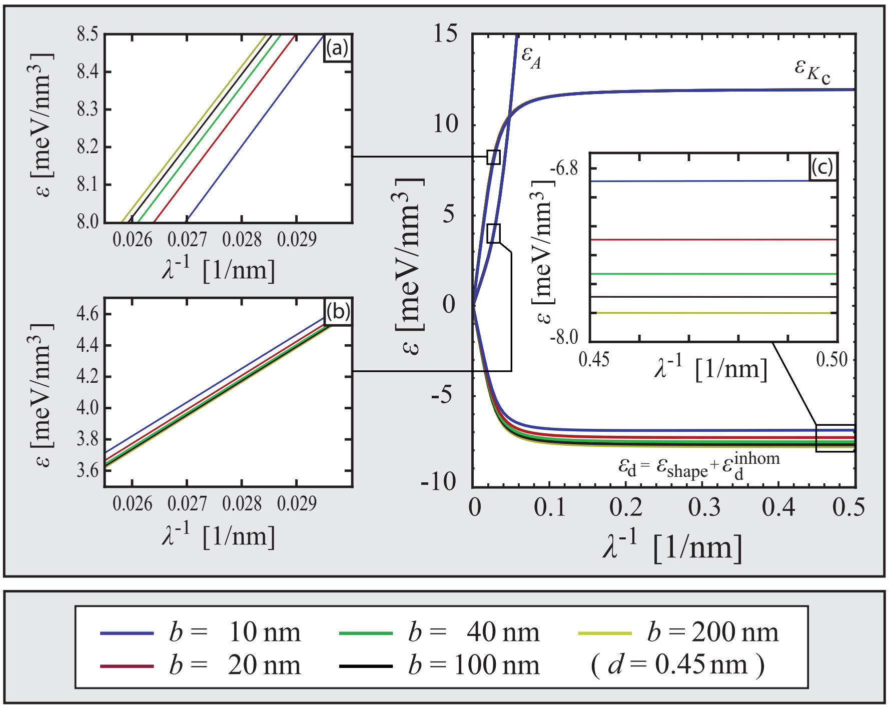

Figure 7.2: Magnetic exchange ε_A, crystalline anisotropy ε_{K_c} and demagnetizing energy density ε_d as a function of the inverse spiral period λ^{-1}. The curves were calculated for an array of Fe DL stripes with an inter-stripe distance $\lambda_y = 200$ nm. All dispersion relations show a clear stripe width dependence, as shown in the insets.

Numerical calculation of the energy density dispersions

Starting from the micromagnetic model Eq. (7.1) and the discussed approximations of $\varepsilon_\mathrm{d}^\mathrm{surf}$ and $\varepsilon_\mathrm{d}^\mathrm{vol}$ (Eq. (7.6)-(7.7)) the spiral profile and the energy density dispersions $\varepsilon_A(\lambda^{-1})$, $\varepsilon_{K_\mathrm{c}}(\lambda^{-1})$, $\varepsilon_\mathrm{DM}(\lambda^{-1})$, $\varepsilon_\mathrm{shape}(\lambda^{-1})$, and $\varepsilon_\mathrm{d}^\mathrm{inhom}(\lambda^{-1})$ can be calculated pointwise in formal analogy to the one-dimensional case, i.e. using the numerical procedure introduced in Chapter 6. Like in the closed film scenario the error due to the approximation of $\varepsilon_\mathrm{d}^\mathrm{surf}[\phi(x)]$ and $\varepsilon_\mathrm{d}^\mathrm{vol}[\phi(x)]$ decrease with the number of considered Fourier coefficients, i.e. $\tilde{r}$ and $\tilde{s}$, respectively. For the following calculations, $\tilde{r}$ and $\tilde{s}$ were chosen such that the error of convergence is below 1% for both $\varepsilon_\mathrm{d}^\mathrm{surf}[\phi(x)]$ and $\varepsilon_\mathrm{d}^\mathrm{vol}[\phi(x)]$[2].

---

[2] The values of $\overline{R}_{\sigma_x}$ and $\overline{R}_{\gamma_x}$ were chosen to be below 0.001‰, in analogy to the calculations in Chapter 6. However, in contrast to $\overline{R}_{\sigma_x}$ and $\overline{R}_{\gamma_x}$, the value of $\overline{R}_\tau$ decreases much more slowly with an increasing number of Fourier coefficients. Therefore, in order to keep the number of Fourier coefficients, and thus the computational effort, within reasonable limits, $\overline{R}_\tau$ was chosen to be below 1%.

The energy density dispersions in Fig. 7.2 were calculated for stripe widths between $b = 10$ nm and $b = 200$ nm, as indicated. The inter-stripe distance of $\lambda_y = 200$ nm was chosen such that, within the precision of the graphical representation, the calculated energy density dispersions do not change upon a further increasing value of λ_y. Thus, it is guaranteed that the results refer to individual stripes that are not affected by dipolar coupling to neighboring stripes. Note, that the limit case $b = 200$ nm does not refer to a stripe geometry, but is geometrically equivalent to the closed film geometry discussed in Chapter 6. The respective curves were checked for consistency. They coincide within the precision of the graphical representation.

The calculation of all curves in Fig. 7.2 is based on the micromagnetic parameters determined in Chapter 6 (Eq. (6.1)), i.e. it was assumed that the values of these parameters are independent of the stripe width. In view of the fact that the parameters describe local properties, and thus essentially depend on the local lattice structure in the Fe DL, a variation of A, K_c, D and M_s can only be expected in very close proximity to the stripe edges. Thus, it seems to be a reasonable assumption that the stripe width dependence of the parameters can be neglected for $b > 10$ nm (more than 40 atomic distances), as discussed in the present context.

Despite the discussed assumption of constant micromagnetic parameters, $\varepsilon_A(\lambda^{-1})$, $\varepsilon_{K_c}(\lambda^{-1})$ and especially $\varepsilon_\mathrm{d}(\lambda^{-1})$ show an explicit stripe width dependence (cf. insets in Fig. 7.2). The stripe width dependence of $\varepsilon_A(\lambda^{-1})$, $\varepsilon_{K_c}(\lambda^{-1})$ only exists in the regime of inhomogeneous spiral profiles and fully disappears in the homogeneous limit ($\lambda^{-1} = 0$). In contrast, the stripe width dependence of $\varepsilon_\mathrm{d}(\lambda^{-1})$ (inset (c)) prevails for homogeneous spiral profiles and decreases when approaching the inhomogeneous limit ($\lambda^{-1} = \infty$). This inverse behavior originates from two different mechanisms:

- In agreement with the calculations of Chapter 6 the total demagnetizing energy density ε_d decreases with increasing values of λ^{-1}. For closed films ($b = 200$ nm) and in the homogeneous limit, it converges to $-\frac{\mu_0}{2}M_\mathrm{s}^2$. According to Fig. 7.2 the convergence limit increases with decreasing stripe width, as shown in inset (c). This effect originates from the demagnetizing field inhomogeneities at the stripe edges that effectively reduce the demagnetizing energy density. In particular, the significance of this edge effect increases with decreasing stripe width.

- As a second order effect the stripe width dependence of the demagnetizing energy density results in a stripe width dependence of the spin spiral profile $\phi(x)$. The effect only plays a role in the regime of inhomogeneous spiral profiles and vanishes in the homogeneous limit, where the spiral profile is perfectly sinusoidal by definition. In narrow stripes, the variation of $\phi(x)$ reflects the reduced domain wall width due to the reduced demagnetizing energy density and in particular due to the reduced value of $\varepsilon_\mathrm{shape}$. As a consequence of this reduced domain wall width the exchange energy density ε_A increases with decreasing stripe width (inset (a)), while the crystalline anisotropy energy density ε_{K_c} decreases (inset(b)). In contrast, $\varepsilon_{\mathrm{DM}}(\lambda^{-1})$ is independent of the shape of the spiral profile and only depends on the spiral period, as discussed in Chapter 3. Consequently, it is not affected by the variation of $\phi(x)$ and remains unchanged with respect to Fig. 6.4.

Stripe width dependence of the spin spiral ground state

Starting from the energy density dispersions of Fig. 7.2 it is straightforward to calculate the total energy density dispersion and investigate its stripe width dependence. Fig. 7.3 shows the result for various stripe widths. Again the Dzyaloshinskii parameter ($D = 6.4 \cdot 10^{-3}$ J/m^2, in agreement with Eq. (6.9)) was chosen such that the position of the global energy density minimum reflects the experimentally observed spiral period $\lambda = 45$ nm in an infinitely extended closed Fe DL film ($b = 200$ nm, yellow curve). The result was checked for consistency with the result of the one-dimensional calculation in Chapter 6. The curves coincide within the accuracy of the graphical representation.

Stripe width dependence of the spiral period With decreasing stripe width the depth of the total energy density minimum gradually decreases and shifts towards smaller values of λ^{-1}, i.e. larger spiral periods (black dotted line in panel (a)). For stripe widths between 200 nm and 20 nm the spiral period varies between 45.5 nm and 58.8 nm, respectively. Below $b = 20$ nm the spiral period increases dramatically and eventually reaches values in the micrometer regime. The calculated dependence of the energy density minimum on the geometrical stripe width is in very good agreement with experimental observations [29, 120]. Thus, the model describes the hitherto unexplained vanishing of the spiral state for narrow stripe geometries (cf. Fig. 4.2 (a)) [29]. In particular, the calculations are in good quantitative agreement with the experimental finding of a critical stripe width of about 15 nm. In addition to the vanishing of the spin spiral, the results of Fig. 7.3 predict a continuous transition from the spiral state to the ferromagnetic state. The calculated transition path (black dotted line) is in good quantitative agreement with previous measurements (cf. Fig. 4.4 (b)) [120], where the discussed variation of the spiral period was observed by SP-STM. However, in [120] the varying period of the spiral state was attributed to the Fe coverage on the W(110) substrate, i.e. to the ratio of stripe width and inter-stripe distance. In contrast to this interpretation, the calculations discussed in this chapter indicate that the variation is related to the stripe width alone, with the inter-stripe distance playing essentially no role. Consequently, the spiral period does not depend on the coverage. The observed variation originates from inhomogeneities of the demagnetizing field due to the stripe edges and can be identified as a property of free standing Fe DL stripes on W(110).

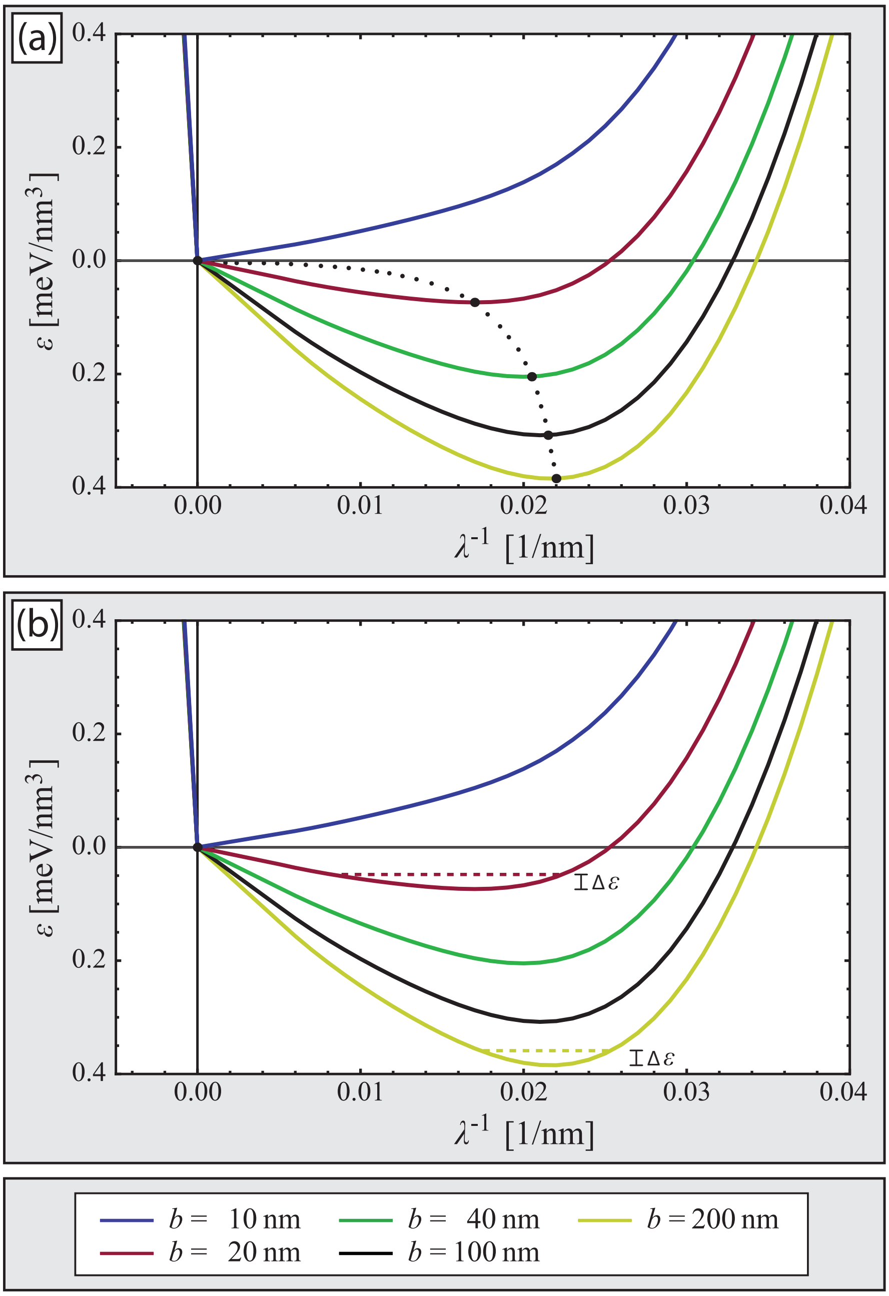

Figure 7.3: Stripe width dependence of the dispersion of the total energy density. The yellow curves represent the closed Fe DL film and coincide with the respective solution, as calculated in Chapter 6. (a) With decreasing stripe width the energy density minimum shifts to higher energy densities and larger spiral periods (black dotted curve). (b) At finite temperature, indicated by $\Delta\varepsilon$, the width of the energy density minimum depends on the stripe width, as indicated by the dashed horizontal lines.

Stripe width dependence of the ground state energy density In addition to the stripe width dependence of the ground state spiral period the calculations visualized in Fig. 7.3 also predict a stripe width dependence of the thermal stability of the spin spiral. The depth of the global energy density minimum decreases with decreasing stripe width. Consequently, the energy difference between the spiral state and the ferromagnetic state decreases as well and can eventually be overcome by thermal excitations at finite temperatures. According to Fig. 7.3 the spiral state in narrow stripes (red) can be excited at lower temperature as compared to wider stripes (green, black) and closed films (yellow). In addition, the energy minimum broadens with decreasing stripe width (dashed horizontal lines in panel (b)). Thus, even if the spiral state can not be excited to the ferromagnetic configuration, the range of accessible spiral periods at finite temperature increases with decreasing stripe width. Consequently, the calculations in this chapter are compatible with a temperature driven excitation of the magnetic state that results in the vanishing spin contrast observed in SP-STM experiments performed at elevated temperature. In particular, the calculations predict a critical temperature that increases with increasing stripe width, in good qualitative agreement with previous SP-STM measurements [120] (cf. Fig. 4.4 (a)). While in [120] the vanishing of the spin contrast was interpreted as a coverage-dependent temperature induced reorientation transition of the magnetic easy axis, the calculations discussed in this chapter, indicate a stripe width dependent thermal excitation, without any necessity for a changing anisotropy direction. In contrast to the previous interpretation this is in full agreement with all experimental observations [100, 120] (cf. discussion in Chapter 4).

Numerical accuracy

The dependence of $\overline{R}_{\sigma_x}$ and $\overline{R}_{\gamma_x}$ on the number of Fourier coefficients being considered for the approximation of $\sigma_x(y)$ and $\gamma_x(y)$ was discussed in detail in Chapter 6. Thus the following analysis can be restricted to the discussion of $\overline{R}_\tau$. Fig. 7.4 displays $\overline{R}_\tau$ as a function of the number of Fourier coefficients ($\tilde{s}$) for four different values of the stripe width b. All calculations are based on the same inter-stripe distance of $\lambda_y = 200$ nm. The inset shows the respective approximations of the stripe profiles, as given by the finite Fourier series for $\tilde{s} = 50$. Independent of the stripe width the value of $\overline{R}_\tau$ decreases with an increasing number of Fourier coefficients. In contrast to the previously discussed smooth magnetization profile along the x-direction (Fig. 6.7) the convergence is much worse due to the discontinuous jumps of $\tau(y)$ at the stripe edges. The critical number of Fourier coefficients ($\tilde{s}_c$) to be considered in order to reach the 1% limit for $\overline{R}_\tau$ is given in the figure. For a given number of Fourier coefficients, $\overline{R}_\tau$ depends significantly on the stripe width, i.e. it increases with decreasing values of b. This behaviour is a direct consequence of the increasing asymmetry of the profile due to the decreasing ratio b/λ_y. It is illustrated in the inset that the convergence in the center of the stripes is much better than at the edges, due to the Gibbs phenomenon. With decreasing ratio b/λ_y this effect becomes increasingly important. According to

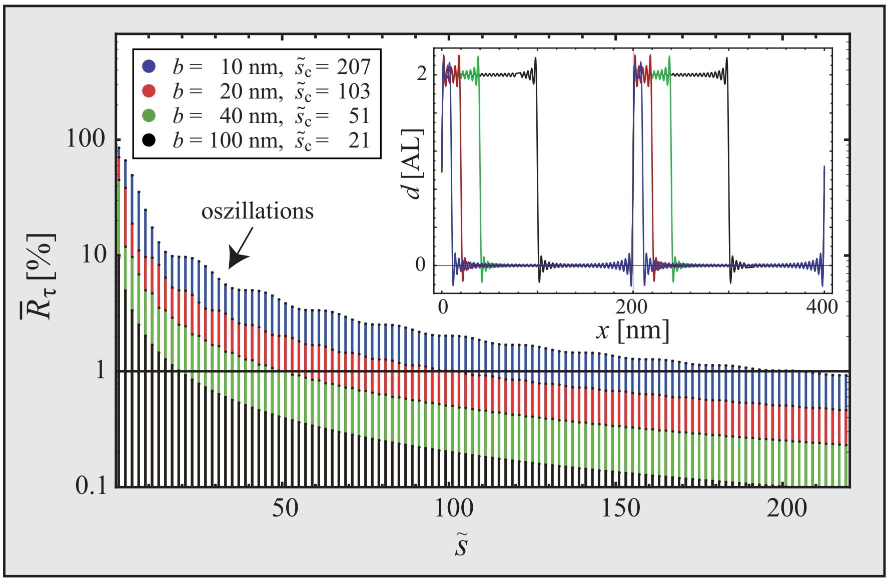

Figure 7.4: Relative error of convergence as a function of the number of Fourier coefficients being considered for the approximation of the profile of a stripe array, as indicated in the inset. The calculations were done for an inter-stripe distance of 200 nm. With increasing asymmetry of the array profile, i.e. for stripes being narrow compared to the inter-stripe distance, the well known Gibbs phenomenon becomes increasingly important. It can only be suppressed by increasing the number of Fourier coefficients in the finite Fourier sum. The critical numbers of coefficients $\tilde{s}_c$ being necessary to keep the error below 1% (black horizontal line) are given in the box on the upper left. The indicated oscillations reflect the varying significance of different Fourier coefficients.

Fig. 7.4, the decay of $\overline{R}_\tau$ as a function of the number of Fourier coefficients is not uniform. Instead one observes more or less pronounced oscillations. The phenomenon is most clearly visible for the most narrow stripes, as indicated. The oscillations reflect the fact that the Fourier components are not equally important. This property became most evident in Chapter 6 where it was discussed that sinusoidal spiral profiles can be perfectly described by only two Fourier coefficients with all other coefficients playing no role. Here, the situation is more complicated than four sinusoidal profiles, but nevertheless some coefficients have a higher significance for the approximation than others. Consequently, the consideration of one additional Fourier coefficient reduces $\overline{R}_\tau$ depending on its significance, thus explaining the oscillations in Fig. 7.4.

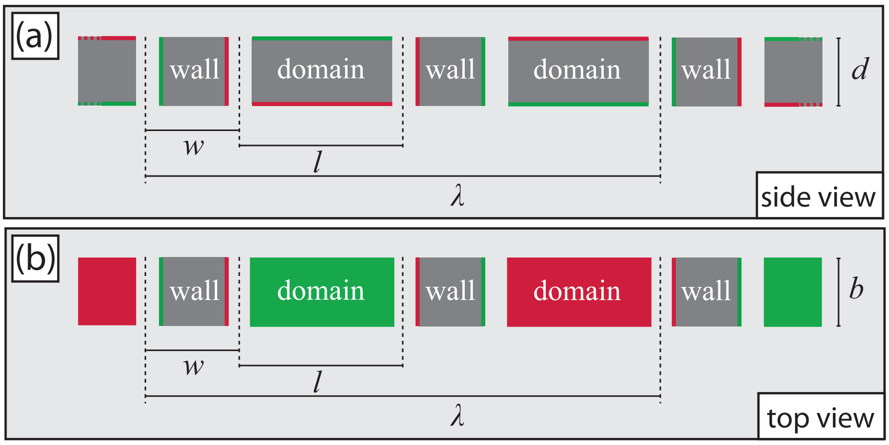

Figure 7.5: Side-view (a) and top-view (b) of the simplified spiral profile. Domains and domain walls are represented by homogeneously magnetized cuboid blocks. Positive and negative magnetic surface charges are visualized by red and green colors. The parameters w, λ, d, and b denote domain wall width, spiral period, film thickness, and stripe width, respectively.

7.2 A simplified box model

Up to now, the stripe width dependence was investigated on the basis of a sophisticated two-dimensional micromagnetic model, where the full complexity of the spin spiral profile was taken into account. However, it is a major drawback of this technique that some physical details of the calculated stripe width dependence remain hidden behind the mathematical complexity of the model. In order to account for this deficiency a very much simplified model was developed in the framework of this thesis. Although the model is less precise than the one applied before, it turns out to be valuable for the conceptual understanding of the physical mechanisms underlying the observed finite size dependence. The model is based on three assumptions:

- Domains and walls are represented by homogeneously magnetized cuboids.
- At the edges of each cuboid block the demagnetizing field is inhomogeneous.
- Dipolar interactions between the blocks are neglected[3].

The resulting modified spiral profile is visualized in Fig. 7.5. The magnetization is indicated by magnetic surface charges, as illustrated by red and green colors.

---

[3] For symmetry reasons the demagnetizing energy due to the interaction of neighboring blocks vanishes, i.e. it is independent of the domain length l and the domain width w. Only the relatively weak interactions between spatially separated blocks of the same type contribute to the demagnetizing energy. Thus, it seems to be justified to neglect these interactions. At the end of this chapter the assumption is supported by direct quantitative comparison of the box model and the more sophisticated model discussed before.

Demagnetizing energy density of a single cuboid block

Fig. 7.6 illustrates the demagnetizing field of the domain and the domain wall blocks in Fig. 7.5 for various block geometries. At the edges of the blocks the field is inhomogeneous. Due to these inhomogeneities the demagnetizing energy densities of domain-like blocks (ε_D) and domain-wall-like blocks (ε_W) are reduced compared to the case of infinitely extended blocks. With decreasing block length (l for domain blocks, w for wall blocks) and block width (b) the effect becomes increasingly significant.

Domain-like blocks: In the limit of infinitely extended magnetic films the inhomogeneities of the demagnetizing field are localized at the interfaces to the neighboring blocks (black ⊙ signs and arrows). Their influence on ε_D is negligible in the limit of infinitely long domains, whereas for finite domain lengths they reduce the value of ε_D, as indicated in Fig. 7.6 (a). With decreasing stripe width, additional field inhomogeneities at the stripe edges (blue ⊙ signs and arrows) come into play. In the limit of narrow stripes these edge inhomogeneities become dominating. Thus, ε_D reduces with decreasing stripe width.

Domain-wall-like blocks: In the limit of infinitely extended magnetic films the field inhomogeneities in the interface regions to the neighboring blocks are negligible also in the case of the domain wall blocks. Only the field inhomogeneities at the upper and lower surface of the thin film (brown arrows in the side view in Fig 7.6 (b)) reduce the demagnetizing energy density significantly. With increasing domain wall width their influence increases and ε_W decreases. As for the domain case, the stripe edges induce additional inhomogeneities of the demagnetizing field (blue arrows). With decreasing stripe width these additional inhomogeneities become increasingly significant and reduce the value of ε_W.

The quantitative dependence of ε_D and ε_W on the geometry of the block, as calculated using the method of three-dimensional finite element calculations [110, 132][4], is shown in Fig. 7.7. Both ε_D and ε_W are displayed as a functions of the block length x along the propagation direction of the spin spiral ($x = l$ for domain blocks, $x = w$ for wall blocks (cf. insets)). For each set of curves the dependence on the block width b is indicated by the color coding defined in the lower part of the figure. Both for the domain blocks and the domain wall blocks the demagnetizing energy density decreases with decreasing values of b, as discussed before (cf. zoom-ins). The b-dependence of ε_D is more than one order of magnitude larger than the b-dependence of ε_W.

---

[4] Note, that this method should not be confused with the method of finite element calculations, as used for engineering purposes.

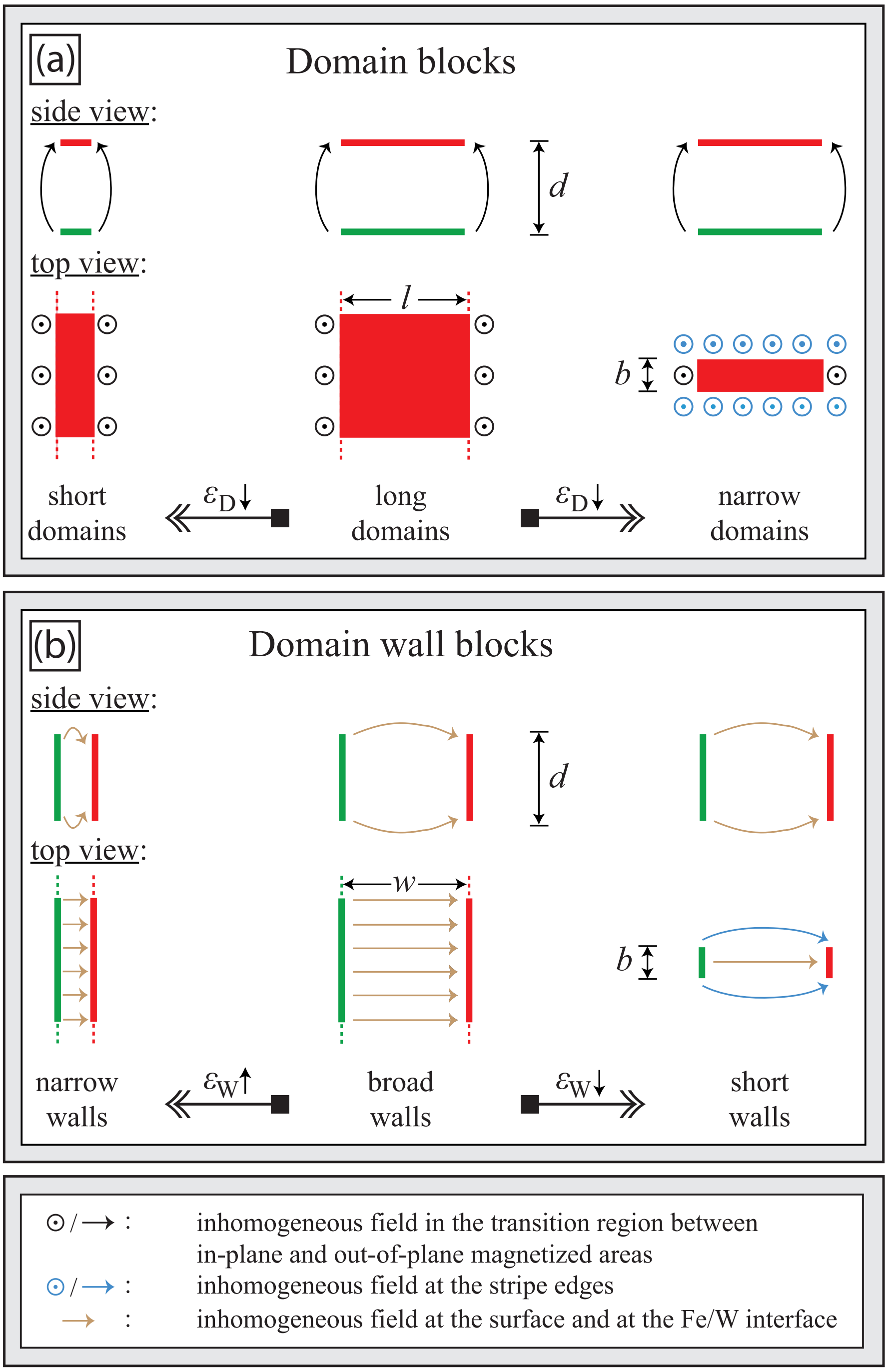
(a)
Domain blocks
side view:
d
top view:
l
b
short domains
$\varepsilon_D\downarrow$
long domains
$\varepsilon_D\downarrow$
narrow domains
(b)
Domain wall blocks
side view:
d
top view:
w
b
narrow walls
$\varepsilon_W\uparrow$
broad walls
$\varepsilon_W\downarrow$
short walls
⊙/⟶ : inhomogeneous field in the transition region between in-plane and out-of-plane magnetized areas
⊙/⟶ : inhomogeneous field at the stripe edges
⟶ : inhomogeneous field at the surface and at the Fe/W interface

Figure 7.6: Geometry dependence of the demagnetizing field in domain blocks (a) and domain wall blocks (b). In the domain case, there are two types of field inhomogeneities: those at the interfaces to neigboring blocks (black ⊙-signs and arrows) and those at the stripe edges (blue ⊙-signs). With decreasing domain length l, ε_D decreases due to the first type of inhomogeneities. With decreasing stripe width b it decreases due to the edge inhomogeneities. In the domain wall blocks, there are also two types of inhomogeneities: those at the surface and the Fe/W interface (brown arrows), and those at the stripe edges (blue arrows). In analogy to the domain case ε_W increases with decreasing domain wall width w due to the first type of inhomogeneities. With decreasing stripe width it decreases due to the increasing influence of the edge inhomogeneities.

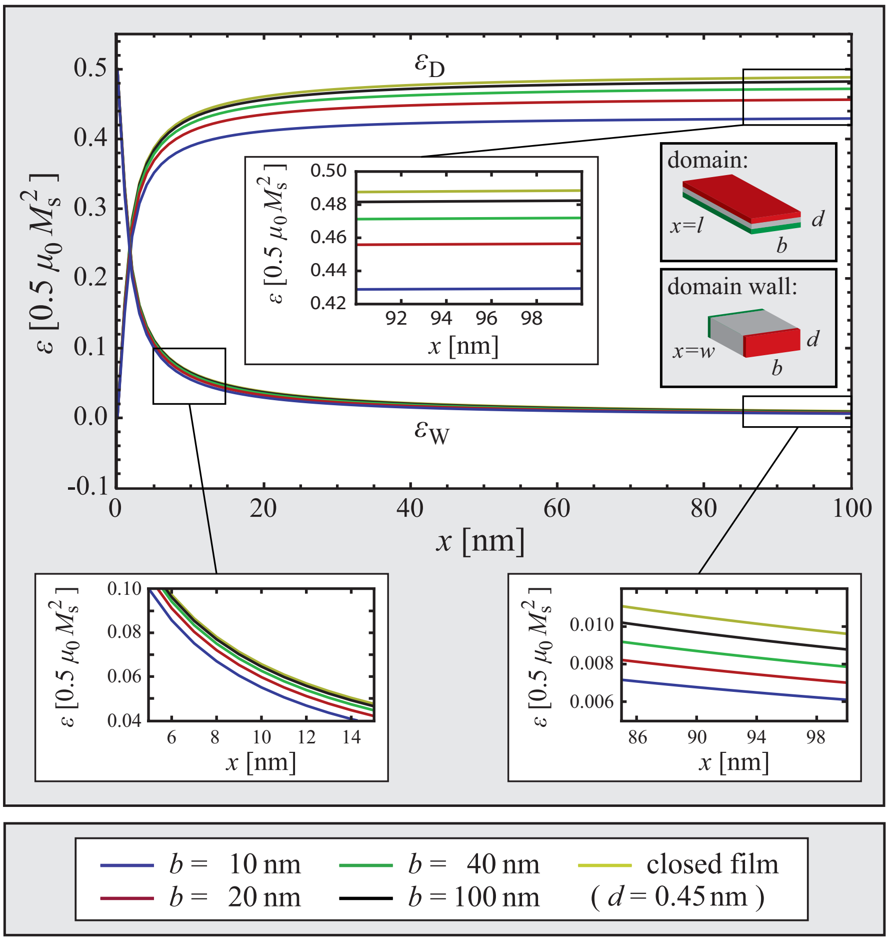

Figure 7.7: Geometry dependence of the demagnetizing energy density in the domain (ε_D) and domain wall blocks (ε_W). In agreement with Fig. 7.6 ε_D increases with increasing domain length l, ε_W decreases with increasing domain width w. In addition, both ε_D and ε_D decrease with decreasing stripe width b (zoom-ins). Note, that the b-dependence of ε_D is about one order of magnitude larger than the b-dependence of ε_W.

Demagnetizing energy density of homogeneous spin spirals

The spiral profile of Fig. 7.5 can now be modeled on the basis of the homogeneously magnetized cuboid blocks discussed before. For the special case of homogeneous spiral profiles the domain blocks and the domain wall blocks in Fig. 7.5 are of equal length. This length is directly related to the spiral period λ:

$$x = l = w = \frac{\lambda}{4} \tag{7.8}$$

The demagnetizing energy density ε_{D} of the domain-like blocks is closely related to the demagnetizing energy density of the surface charges, as discussed in the context of the more sophisticated micromagnetic model discussed before. Likewise, ε_{W} is related to the demagnetizing energy density of the volume charges[5]. Thus, the corresponding energy density dispersions can be calculated starting from the curves in Fig. 7.7. In particular, $\varepsilon_{\mathrm{d}\perp}^{\mathrm{inhom}}(\lambda^{-1}, b)$ and $\varepsilon_{\mathrm{d}\|}^{\mathrm{inhom}}(\lambda^{-1}, b)$ (cf. Eq. (6.17)) result as spatial averages of $\varepsilon_{\mathrm{D}}(\lambda/4)$ and $\varepsilon_{\mathrm{W}}(\lambda/4)$ over the magnetic volume of one spiral period, respectively.

$$\begin{aligned} \varepsilon_{\mathrm{d}\|}^{\mathrm{inhom}}\left(\lambda^{-1}, b\right) &= \frac{1}{2} \cdot \varepsilon_{\mathrm{W}}\left(\frac{\lambda}{4}, b\right) \\ \varepsilon_{\mathrm{d}\perp}^{\mathrm{inhom}}\left(\lambda^{-1}, b\right) &= \frac{1}{2} \cdot \varepsilon_{\mathrm{D}}\left(\frac{\lambda}{4}, b\right) - \frac{1}{2} \cdot \varepsilon_{\mathrm{D}}\left(\infty, b\right) \end{aligned} \tag{7.9}$$

Here, the prefactor 1/2 refers to the spatial averaging. The additive term $-\frac{1}{2} \cdot \varepsilon_{\mathrm{D}}(\infty, b)$ normalizes $\varepsilon_{\mathrm{d}\perp}^{\mathrm{inhom}}(0, b)$ to zero.

The energy density dispersions $\varepsilon_{\mathrm{d}\|}^{\mathrm{inhom}}(\lambda^{-1}, b)$ and $\varepsilon_{\mathrm{d}\perp}^{\mathrm{inhom}}(\lambda^{-1}, b)$, as calculated for various values of the stripe width b, are shown in Fig. 7.8 (a). In analogy to Fig. 7.7 the b-dependence is indicated by the color coding defined in the lower part of the figure. For $b = \infty$ the energy densities vanish for the collinear configuration ($\lambda^{-1} = 0$) and converge to $\pm\frac{\mu_0}{2} M_{\mathrm{s}}^2$ in the homogeneous limit ($\lambda^{-1} = \infty$). This behavior is in good agreement with the previously calculated energy density dispersions shown in Fig. 6.6. The energy density dispersions are reproduced despite the major simplifications of the box model. It therefore appears to be well justified to describe the spin spiral as a sequence of independent blocks without any interactions. Consequently, the understanding of the stripe width dependence of $\varepsilon_{\mathrm{d}}(\lambda^{-1}, b)$ reduces to the understanding of the shape dependence of ε_{D} and ε_{W}, as discussed before (cf. Fig.7.6).

---

[5] Note, that ε_{W} does not originate from magnetic volume charges, since in the box model the volume charges are essentially replaced by rotated surface charges in the wall regions. Nevertheless, ε_{W} is closely related to the volume charges. It is therefore used in order to recalculate $\varepsilon_{\mathrm{d}}^{\mathrm{vol}}$ in the framework of the box model.

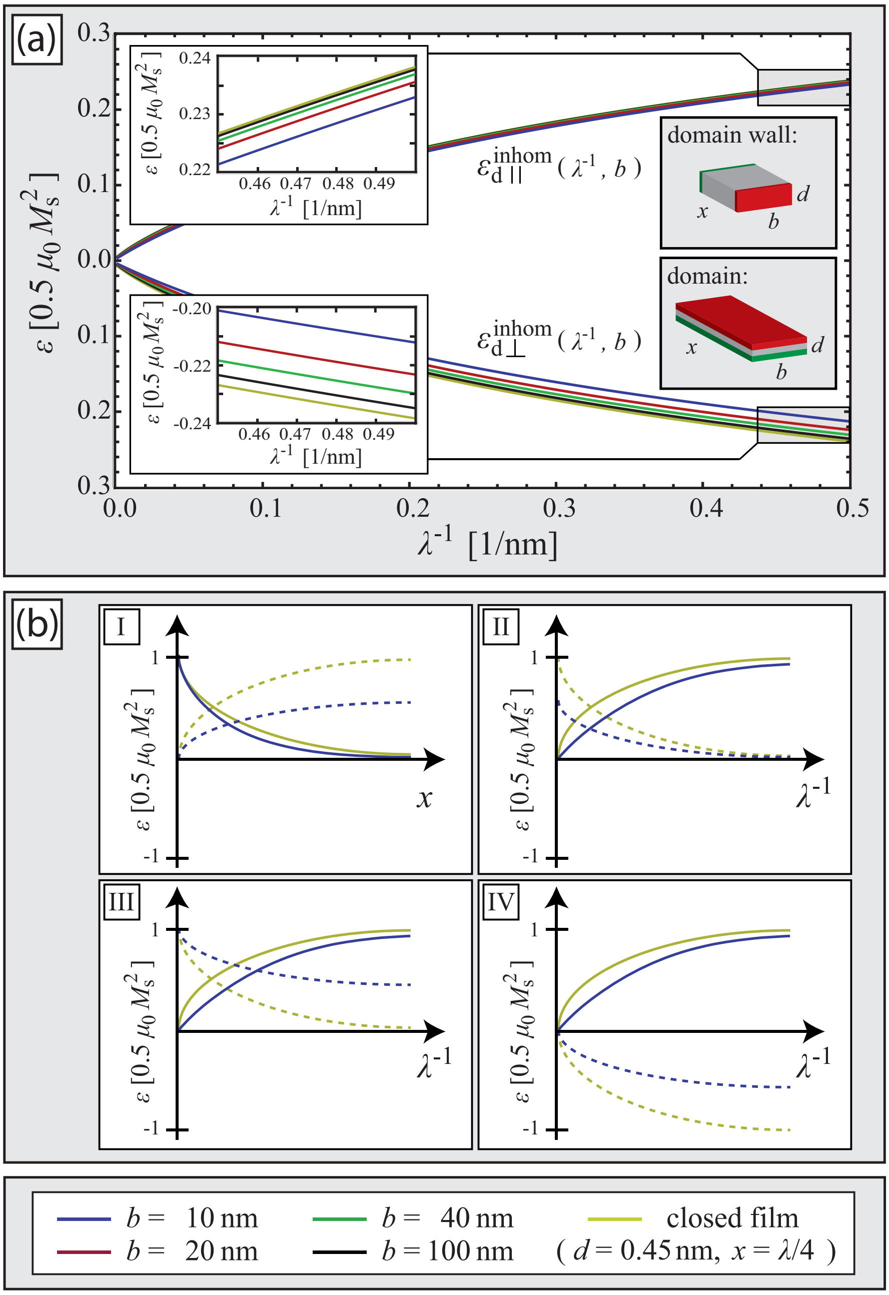

Figure 7.8: (a) Demagnetizing energy density contributions originating from surface charges($\varepsilon^{\text{inhom}}_{\text{d}\perp}(\lambda^{-1}, b)$) and volume charges ($\varepsilon^{\text{inhom}}_{\text{d}\|}(\lambda^{-1}, b)$), as calculated on the basis of ε_{D} and ε_{W}, respectively. The stripe width dependence is indicated by the color coding in analogy to Fig. 7.7. (b) Schematic illustration of the transition from Fig. 7.7 to the curves shown in (a). *I* → *II* represents recalibration of the horizontal axis from x to the inverted spiral period λ^{-1}. *II* → *III* → *IV* reflect the renormalization of $\varepsilon^{\text{inhom}}_{\text{d}\perp}(\lambda^{-1}, b)$ such that all curves coincide at the origin of the coordinate system.

According to Fig. 7.8 (a), $\varepsilon_{\mathrm{d}\|}^{\mathrm{inhom}}(\lambda^{-1}, b)$ decreases with decreasing values of b, in agreement with the behavior of $\varepsilon_{\mathrm{W}}(x, b)$ in Fig. 7.7. In contrast, $\varepsilon_{\mathrm{d}\perp}^{\mathrm{inhom}}(\lambda^{-1}, b)$ decreases with decreasing values of b, and thus shows the inverse behavior of $\varepsilon_{\mathrm{D}}(x, b)$. The discussed inversion originates from the fact that in both figures the energy density dispersions are normalized such that they coincide at the origin of the coordinate system. However, in Fig. 7.7 the origin represents the case of infinitely short domain and domain wall blocks, while in Fig. 7.8 it represents the inhomogeneous limit, i.e. the case of infinitely long domains and domain wall blocks of length w_0. The transition from Fig. 7.7 to Fig 7.8 (a) is schematically illustrated in panel (b).

Starting from $\varepsilon_{\mathrm{d}\|}^{\mathrm{inhom}}(\lambda^{-1}, b)$ and $\varepsilon_{\mathrm{d}\perp}^{\mathrm{inhom}}(\lambda^{-1}, b)$ the total demagnetizing energy density dispersion $\varepsilon_{\mathrm{d}}^{*}(\lambda^{-1}, b)$ can be calculated:

$$\varepsilon_{\mathrm{d}}^{*}\left(\lambda^{-1}, b\right) \;=\; \varepsilon_{\mathrm{d}\|}^{\mathrm{inhom}}\left(\lambda^{-1}, b\right) + \varepsilon_{\mathrm{d}\perp}^{\mathrm{inhom}}\left(\lambda^{-1}, b\right) \;\overset{b\to\infty}{=}\; 0 \tag{7.10}$$

Here, the asterisk indicates that the energy density dispersion refers to the special case of homogeneous spiral profiles. In agreement with Fig. 6.6, $\varepsilon_{\mathrm{d}}^{*}(\lambda^{-1}, b)$ vanishes in the limit of closed film geometries ($b \to \infty$). However, for finite stripe geometries this is no longer the case due to the asymmetric stripe width dependence of $\varepsilon_{\mathrm{d}\|}^{\mathrm{inhom}}(\lambda^{-1}, b)$ and $\varepsilon_{\mathrm{d}\perp}^{\mathrm{inhom}}(\lambda^{-1}, b)$ discussed before. Thus, for $b \neq \infty$ the total energy density is positive and increases with increasing values of λ^{-1}. In particular, this means that in narrow stripes $\varepsilon_{\mathrm{d}}^{*}$ may not be negligible, in contrast to the extended film geometry discussed in Chapter 6. This issue will be discussed in more detail, after the additional consideration of inhomogeneous spin spiral shapes and the shape anisotropy contribution to the demagnetizing energy density.

Demagnetizing energy density of inhomogeneous spin spirals

In order to account for inhomogeneity in the spiral profiles, the length of the domain and domain wall blocks must be varied as a function of λ^{-1} in an appropriate way (cf. Chapter (6)). In particular, the box model allows to distinguish two regimes[6]:

---

[6] In the previously discussed more sophisticated micromagnetic model the strict separation of a homogeneous and an inhomogeneous regime was not possible. Instead, the discussion was based on the continuous transition from the inhomogeneous limit at $\lambda^{-1} = 0$ to the homogeneous limit at $\lambda^{-1} = \infty$.

Homogeneous regime ($\lambda < 4w_0$): The variation of λ is related to the joint variation of the domain length l and the domain wall width w, with $l = w$, as discussed in the previous section. Consequently, the demagnetizing energy density dispersions are given by Eq. (7.9)-(7.10).

Inhomogeneous regime ($\lambda > 4w_0$): The variation of λ is exclusively related to the variation of the domain length l. The domain wall width $w = w_0$ is given by magnetic exchange and anisotropy (cf. Eq. (3.21)), i.e. it is independent of λ. Consequently, the demagnetizing energy density dispersions are given by:

$$\begin{aligned}
\varepsilon_{\mathrm{d}\|}^{\mathrm{inhom}}\left(\lambda^{-1}, b\right) &= \frac{2w_0}{\lambda} \cdot \varepsilon_{\mathrm{W}}\left(w_0, b\right) \\
\varepsilon_{\mathrm{d}\perp}^{\mathrm{inhom}}\left(\lambda^{-1}, b\right) &= \frac{\lambda - 2w_0}{\lambda} \cdot \varepsilon_{\mathrm{D}}\left(\frac{\lambda - 2w_0}{2}, b\right) - \frac{1}{2} \cdot \varepsilon_{\mathrm{D}}\left(\infty, b\right)
\end{aligned} \tag{7.11}$$

In contrast to Eq. (7.9) the domain length and the domain wall width are no longer equal ($l \neq w$). Consequently, the spatial averaging is more complicated. This is reflected by the weighting coefficients $2w_0/\lambda$ and $(\lambda - 2w_0)/\lambda$. The additive normalization term $-\frac{1}{2} \cdot \varepsilon_{\mathrm{D}}(\infty, b)$ was chosen such that the demagnetizing energy density is a continuous function of λ^{-1} even at the transition line between the homogeneous and the inhomogeneous regime ($\lambda = 4w_0$).

By combining the expressions for the demagnetizing energy density in the homogeneous and inhomogeneous regime (Eq. (7.9)-(7.11)), $\varepsilon_{\mathrm{d}}(\lambda^{-1}, b)$ can be written as:

$$\boxed{\varepsilon_{\mathrm{d}}\left(\lambda^{-1}, b\right) = \begin{cases} \varepsilon_{\mathrm{d}}^{*}\left(\lambda^{-1}, b\right) & \Big|\ \lambda < 4w_0 \\ \frac{2w_0}{\lambda} \cdot \varepsilon_{\mathrm{W}}\left(w_0, b\right) + \frac{\lambda-2w_0}{\lambda} \cdot \varepsilon_{\mathrm{D}}\left(\frac{\lambda-2w_0}{2}, b\right) - \frac{1}{2} \cdot \varepsilon_{\mathrm{D}}\left(\infty, b\right) & \Big|\ \lambda > 4w_0 \end{cases}} \tag{7.12}$$

Using the expression for the energy density dispersion $\varepsilon_\mathrm{d}^*(\lambda^{-1})$ of the purely homogeneous case (Eq. (7.10)), $\varepsilon_\mathrm{d}(\lambda^{-1}, b)$ can be split into the homogeneous contribution $\varepsilon_\mathrm{d}^*(\lambda^{-1})$ and an additional summand $\varepsilon_\mathrm{shape}(\lambda^{-1}, b)$ that purely originates from the transition from inhomogeneous to homogeneous spin spiral profiles[7]:

$$\boxed{\begin{aligned}
\varepsilon_\mathrm{d}\left(\lambda^{-1}, b\right) &= \varepsilon_\mathrm{d}^*\left(\lambda^{-1}, b\right) + \varepsilon_\mathrm{shape}\left(\lambda^{-1}, b\right) \\
\varepsilon_\mathrm{shape}\left(\lambda^{-1}, b\right) &= \left\{\begin{array}{l|l}
\qquad\qquad 0 & \lambda < 4w_0 \\
\frac{2w_0}{\lambda} \cdot \varepsilon_\mathrm{W}\left(w_0, b\right) & \\
+ \frac{\lambda - 2w_0}{\lambda} \cdot \varepsilon_\mathrm{D}\left(\frac{\lambda - 2w_0}{2}, b\right) - \frac{1}{2} \cdot \varepsilon_\mathrm{D}\left(\infty, b\right) & \lambda > 4w_0 \\
- \varepsilon_\mathrm{d}^*\left(\lambda^{-1}, b\right) &
\end{array}\right. \\
&\quad -\frac{1}{2} \cdot \varepsilon_\mathrm{D}\left(\infty, b\right) \\
\varepsilon_\mathrm{d}^*\left(\lambda^{-1}, b\right) &: \quad \text{cf. Eq. (7.10)}
\end{aligned}} \tag{7.13}$$

Fig. 7.9 shows $\varepsilon_\mathrm{shape}(\lambda^{-1}, b)$ for various values of the stripe width b. In addition, the figure shows $\varepsilon_{\mathrm{d}\|}^\mathrm{inhom}$ and $\varepsilon_{\mathrm{d}\perp}^\mathrm{inhom}$ (dashed curves), as copied from Fig. 7.8. In analogy to Fig. 7.7-7.8 the b-dependence is indicated by the color coding defined in the lower part of the figure. In the inhomogeneous regime ($\lambda > 4w_0$, blue shaded area) the value of $\varepsilon_\mathrm{shape}$ decreases almost linearly for all values of b. This decrease originates from the fact that, upon increasing the ratio of in-plane magnetized domain wall areas to out-of-plane magnetized domain areas (w/l), the system can gain shape anisotropy energy, as already discussed in Chapter 6. In the homogeneous regime ($\lambda < 4w_0$, white area) the ratio of in-plane to out-of-plane magnetized areas amounts to $w/l = 0.5$ and does not change with varying values of λ. Thus, $\varepsilon_\mathrm{shape}$ remains constant in the homogeneous regime. For closed film geometries ($b = \infty$), this constant value in the homogeneous regime amounts to $\varepsilon_\mathrm{shape} = 0.5\mu_0 M_\mathrm{s}^2$, in agreement with the results of the more complicated micromagnetic model discussed before. It increases with decreasing stripe width, as visualized in the inset.

---

[7] The gray shaded additive term $-\frac{1}{2} \cdot \varepsilon_\mathrm{D}(\infty, b)$ assures the normalization: $\varepsilon_\mathrm{shape}(0, b) = 0$.

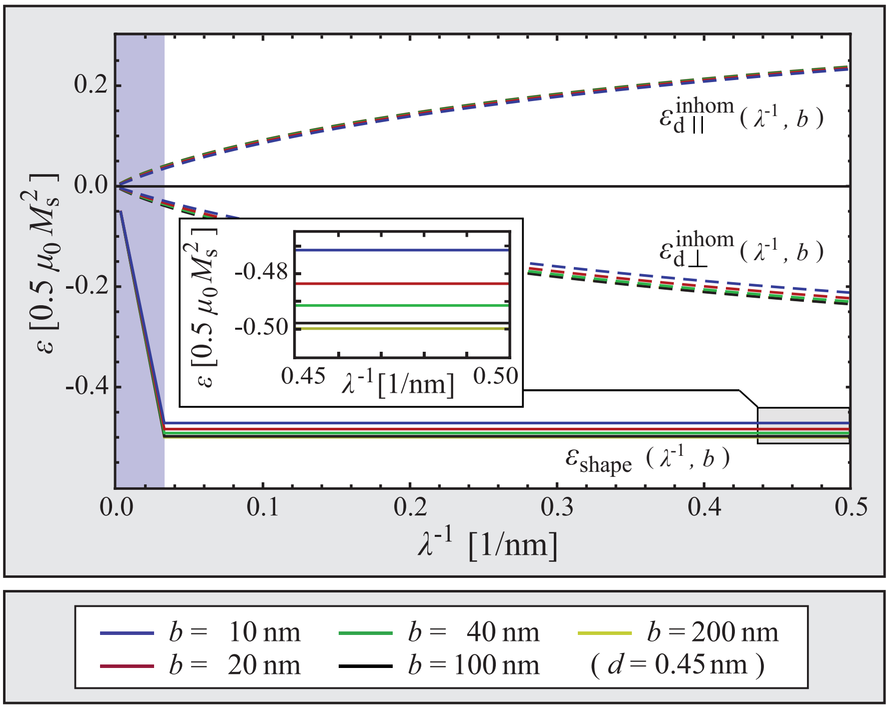

Figure 7.9: (a) Geometry dependence of the shape anisotropy contribution $\varepsilon_{\mathrm{shape}}(\lambda^{-1}, b)$ to the demagnetizing energy density. In the homogeneous regime (blue shaded area) $\varepsilon_{\mathrm{shape}}$ decreases almost linearly and takes a constant value in the regime of homogeneous spiral profiles (white area). With decreasing stripe width $\varepsilon_{\mathrm{shape}}(\lambda^{-1}, b)$ increases, as shown in the inset. For comparison, $\varepsilon_{\mathrm{d}\|}^{\mathrm{inhom}}(\lambda^{-1}, b)$ and $\varepsilon_{\mathrm{d}\perp}^{\mathrm{inhom}}(\lambda^{-1}, b)$ were copied from Fig. 7.8 (a) (dashed curves).

According to Fig. 7.9 the stripe width dependence of the total demagnetizing energy density is essentially determined by the stripe width dependence of $\varepsilon_{\mathrm{d}}^{*}(\lambda^{-1}, b)$ and $\varepsilon_{\mathrm{shape}}(\lambda^{-1}, b)$. In the homogeneous limit the effect is comparable for both energy density contributions. With decreasing values of λ^{-1} the stripe width dependence of $\varepsilon_{\mathrm{d}}^{*}(\lambda^{-1}, b)$ reduces whereas it remains initially unchanged for $\varepsilon_{\mathrm{shape}}(\lambda^{-1}, b)$. Only in the inhomogeneous regime (blue shaded area) the stripe width dependence of $\varepsilon_{\mathrm{shape}}(\lambda^{-1}, b)$ decreases as well. For the experimentally observed spiral period in the Fe DL on W(100), 11% of the stripe width dependence can be attributed to the stripe width dependence of $\varepsilon_{\mathrm{d}}^{*}(\lambda^{-1}, b)$ whereas 89% are related to the stripe width dependence of $\varepsilon_{\mathrm{shape}}(\lambda^{-1}, b)$.

Fig. 7.10 shows the stripe width dependence of the total demagnetizing energy density dispersion $\varepsilon_{\mathrm{d}}(\lambda^{-1}, b)$, i.e. the sum of the energy density dispersions shown in Fig. 7.9. For comparison the respective dispersions, as calculated using the more sophisticated micromagnetic model, were copied from Fig. 7.2 (dashed curves). For all values of b the results of the two models converge both in the homogeneous ($\lambda^{-1} = \infty$) and in the inhomogeneous limit ($\lambda^{-1} = 0$). In the intermediate regime the solutions of the

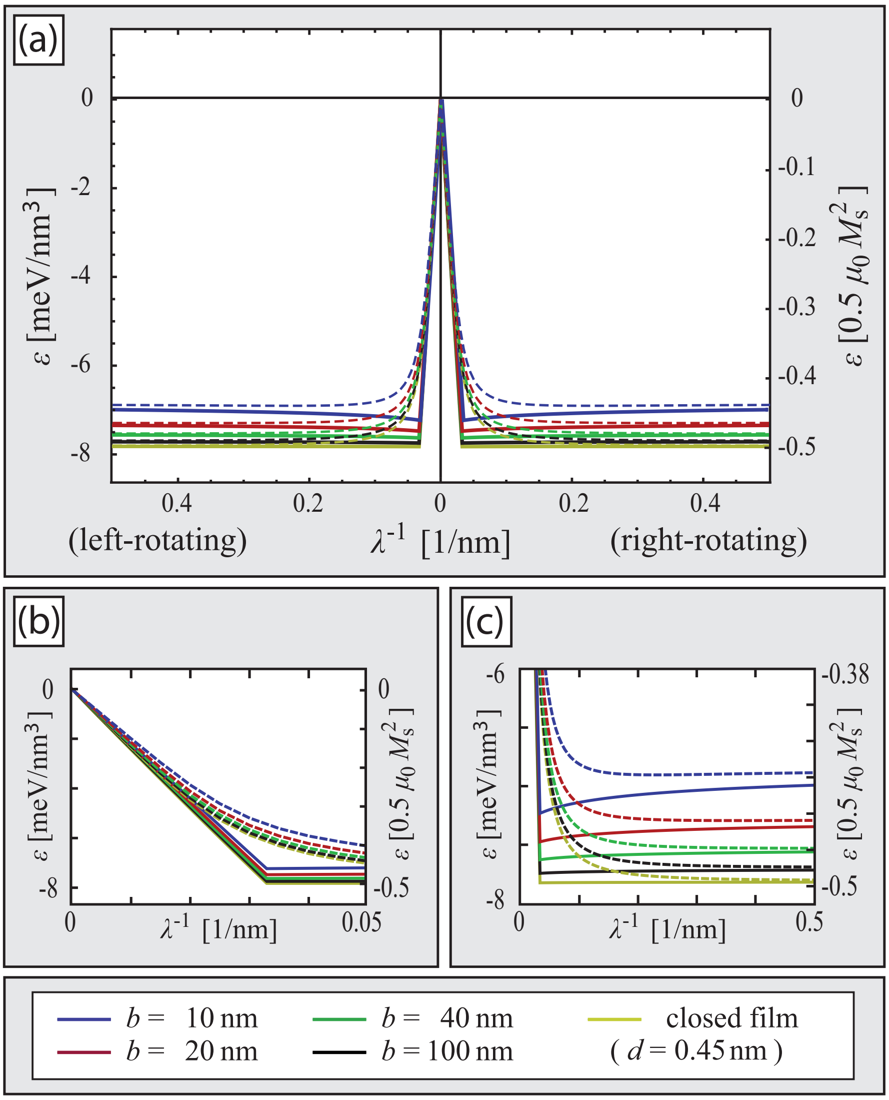

Figure 7.10: (a) Stripe width dependence of the total demagnetizing energy density, as calculated by the box model (solid curves). For comparison, the respective solutions of the previously discussed more sophisticated micromagnetic model were copied from Fig. 7.2. The solutions of both models converge both in the inhomogeneous (b) and in the homogeneous limit (c). In the transition regime the solutions of the box model are systematically below the ones of the more sophisticated model. For the experimentally observed spiral period in the Fe DL on W(110) the deviation varies between 7% in closed films and 13% for a stripe width of b = 10 nm.

box model are systematically below the ones of the more sophisticated model. For the experimentally observed spiral period in the Fe DL on W(110) the deviation varies between 7% in the case of closed films and 13% for a stripe width of $b = 10$ nm. Consequently, the discussed box model essentially reproduces the results of the more sophisticated micromagnetic model discussed before, and can therefore be applied alternatively in order to investigate the stripe width dependence of the demagnetizing energy density, and thus the stripe width dependence of the spin spiral ground state.

As already discussed in the context of the more sophisticated micromagnetic model, the stripe width dependence of the demagnetizing energy density results in a variation of the spin spiral period as a function of the stripe width. Thus, it explains the observed vanishing of the spiral state in narrow stripes, the measured stripe width dependence of the spiral period and the disappearing spin contrast at elevated temperature (last three lines in Tab. 4.2), as already discussed in the context of the more sophisticated micromagnetic model. According to the previous considerations all observations can also be explained in the framework of the very much simplified box model discussed before. Due to the reduced complexity of the model it could be shown that the observed stripe width dependence originates from two effects: the stripe width dependence of the shape anisotropy (89%), and the asymmetric geometry dependence of the demagnetizing energy density inside the domains and domain walls, i.e. the asymmetric geometry dependence of the surface and volume charge contributions to the demagnetizing energy density (11%).

Part III

Two-dimensional complex spin textures in Fe/W(110)

In the preceding chapters the discussion was restricted to the experimentally observed spin spiral in the Fe DL on W(110). The magnetic structure of the Fe ML, as well as magnetic interaction between the ML and DL areas, were not taken into account. As discussed before, such an approach is well justified for the discussion of the DL. In particular, it was shown that the spiral structure in the DL is not affected significantly by dipolar interactions between the ML and DL regions, since the magnetic easy axis in the ML is perpendicular to the magnetization in the DL all the way along the spin spiral. Only for very narrow DL stripe widths below 2 nm the magnetic structure of the Fe DL is significantly affected by the underlying ML due to the magnetic inter-layer exchange interaction [119, 121]

On the other hand, the magnetic structure in the ML can be strongly correlated to the magnetization in the DL. In the framework of this thesis these magnetic correlations were addressed in more detail using the experimental setup discussed in Part I. In particular a complex two-dimensional magnetic structure could be observed. It is the subject of the following chapter. After a short summary of some relevant previous observations the following discussion refers to the description of the novel experimental results and the discussion of the non-trivial topological structure of the observed spin configuration. Two alternative mechanisms are discussed in order to give an explanation of the experimental observations. Finally, some experiments based on the discussed spin configuration are suggested.

Chapter 8

Skyrmion-lattice-like spin textures

8.1 Previous studies

According to previous measurements of the magneto-optical Kerr effect (MOKE), the magnetic easy axis of the Fe ML on W(110) is oriented in-plane along the crystallographic $[1\bar{1}0]$ direction [100, 102, 119]. Due to the almost vanishing dipolar stray field in in-plane magnetized films of only one AL thickness the magnetic structure of the Fe ML is essentially single-domain. However, it turns out that domains can be induced by additional second layer Fe islands on top of the closed Fe ML film, as visualized in Fig. 8.1 (a) [123]. The image was recorded using a Gd coated W-tip with a canted magnetization direction and a magnetic sensitivity to both the in-plane and the out-of-plane component of the magnetization at the sample surface. By combining the observed magnetic contrast and the previously determined magnetic easy axis, it was concluded that the spin rotation in the area of the Fe DL island must be of cycloidal type, as indicated by the arrows and the crossed circle. However, at that time the rotational sense of this cycloidal spin configuration could not be determined due to the lack of external magnetic fields of arbitrary direction. The indicated right-rotating spiral type was chosen arbitrarily in order to allow for an intuitive illustration. Panel (b) shows an Fe ML/DL stripe array, as prepared by evaporation of 1.4 AL Fe and subsequent annealing [29]. Again a canted tip magnetization provides contrast in the DL as well as in the ML areas. The observed magnetic structure shows a characteristic and unique sequence of contrast levels (from left to right: dark DL, dark ML, bright DL, bright ML) that is independent of the position on the sample. As in the case of (a) the observed magnetic structure was identified as a cycloidal spin spiral of unknown rotational sense by combining the observed spin contrast with the previously measured direction of the magnetic easy axis in the Fe ML.

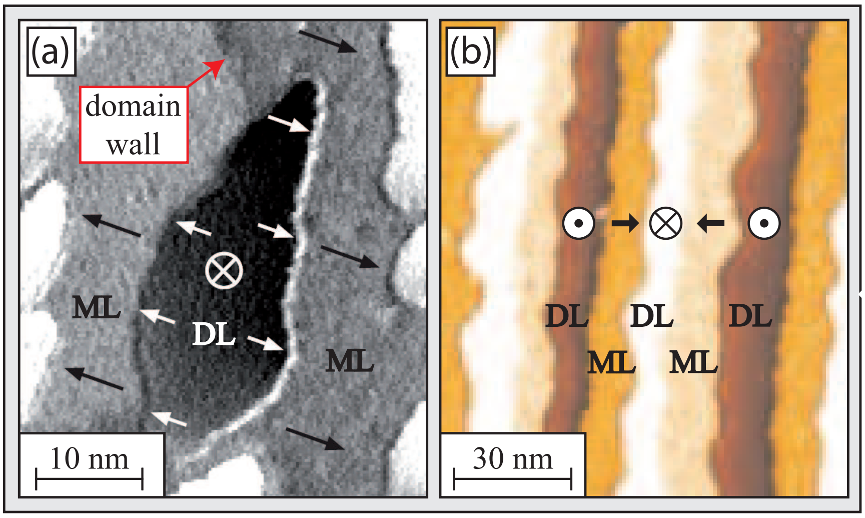

Figure 8.1: (a) Spin-polarized dI/dU-map of 1.4 AL Fe on W(110). The image was recorded using a Gd-coated W-tip with a canted magnetization direction and a combined in-plane and out-of plane magnetic sensitivity. The dI/dU-map shows an out-of-plane magnetized Fe DL island (black) that is fully surrounded by the Fe ML film, that shows a magnetic contrast, indicating the formation of a magnetic domain pattern induced by the DL island. Note, that the arrows suggest a left-rotating cycloidal spin-rotation, although the rotational sense could not be deduced from the experimental data due to the lack of external magnetic fields of arbitrary direction. (b) Spin-polarized dI/dU-map of 1.4 AL Fe on W(110). The image shows in-plane and out-of-plane magnetic contrast in the ML and DL areas, respectively. Due to the unique sequence of magnetic contrast levels (from left to right: dark DL, dark ML, bright DL, bright ML) and the previously observed ML easy axis along [1$\bar{1}$0] the magnetic structure can be identified as a spin spiral of cycloidal type. Like in the case of (a) the rotational sense could not be measured. ((a) from [123], (b) from [29]).

8.2 SP-STM experiments in the triple axes magnet

The following SP-STM measurements give the first experimental documentation of a coexistence of the spin spiral in the Fe DL on W(110), as discussed in Part II, and the spin spiral propagating along the perpendicular in-plane direction, as shown in Fig. 8.1. In particular, this coexistence implies a complex magnetic configuration that is topologically equivalent to the recently discussed skyrmion lattices [4, 5, 133–135] and goes beyond other types of magnetic whirls, as observed at interfaces between magnetic domains in ferromagnets or specially tailored magnetic nanosystems [136].

Fig. 8.2 (a) shows the topographic STM-image of 1.6 atomic layers of Fe on W(110). As for the previously discussed measurements, ML and DL regions can be identified. The second atomic layer grows on top of the closed ML with a preferred growth direction along [001]. The panels (b)-(d) show a series of spin-polarized dI/dU-maps in the same sample area, using an in-plane sensitive Fe coated W-tip. In zero field

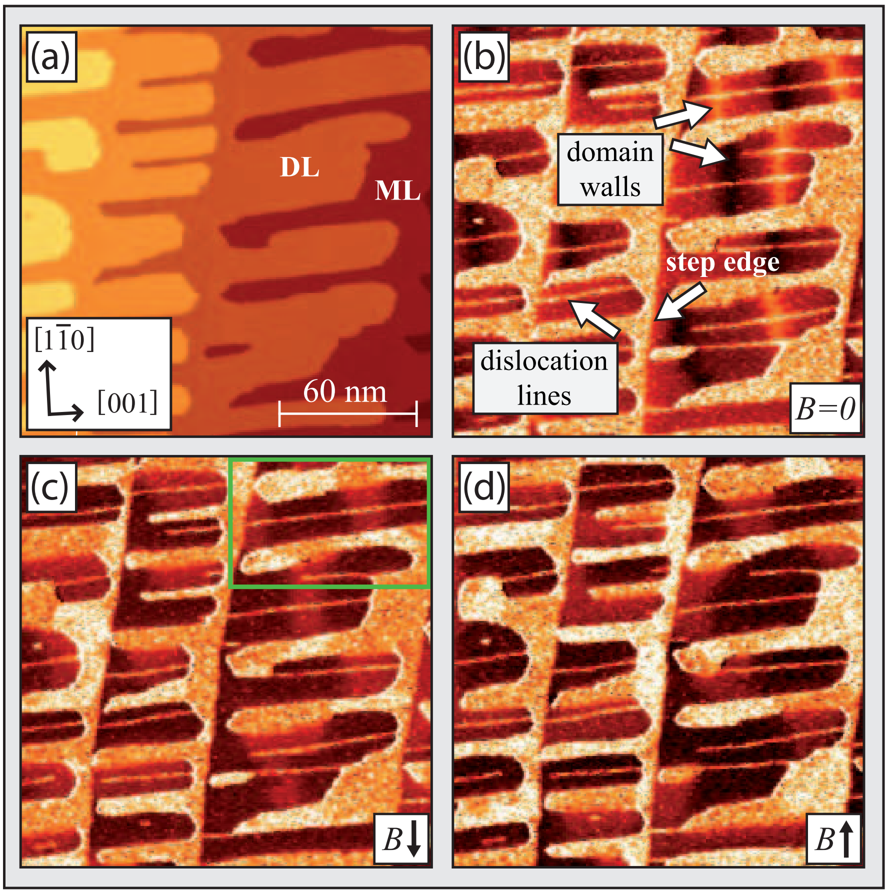

Figure 8.2: Spin-polarized dI/dU-maps of 1.6 atomic layers of Fe on W(110) using an in-plane sensitive Fe coated W-tip. ML and DL regions can be identified (a). In zero field the domain walls in the Fe double layer can be observed (b). Upon applying an external magnetic field along [1$\bar{1}$0] the domain wall contrast in the DL disappears (c). Instead domains with a magnetization direction along [1$\bar{1}$0] become visible in the ML due to the rotation of the tip magnetization in the external field. The contrast of this pattern is inverted upon reversal of the tip magnetization in the external magnetic field (d). Tunnel parameters: U = 550 mV, I = 500 pA. The green box indicates the reference area for the zoom-in shown in Fig. 8.3.

(b) one observes the well known domain wall contrast in the DL areas, in agreement with Fig. 5.2-5.3. The magnetic structure of the ML appears almost featureless. Upon switching on an in-plane magnetic field along [1$\bar{1}$0] (c) the domain wall contrast in the DL vanishes, in agreement with the discussions in Part II. Instead, a clear domain contrast appears in the ML areas. It almost vanishes when switching off the field (not shown) and inverts upon the reversal of the field direction (d).

The shown measurement series, as done using the triple axes magnet of the experimental setup described in Part II, constitutes the first direct SP-STM measurement of the magnetic easy axis along $[1\bar{1}0]$. In addition, the images show that the domain structure in the ML areas is closely related to the spiral state in the DL. Thus, following the $[1\bar{1}0]$ direction from the bottom to the top of Fig. 8.2 (c) one observes a regular and unique sequence of ML and DL domain contrast (bright ML, bright DL, dark ML, dark DL). Since a weak residual ML domain contrast can be observed even in zero-field (b) it can be excluded that the observed domain structure is induced by the external field. As for the measurement series shown in Fig. 5.2, the observed contrast variations can be attributed to the rotation of the magnetization at the tip apex due to the external field. In conclusion, the magnetic structure of the combined ML/DL system is interpreted as a coexistence of the previously discussed DL spiral propagating along [001] and an additional unirotational spiral structure of cycloidal type propagating along $[1\bar{1}0]$.

The observed close relationship of the magnetization in the Fe ML and DL on W(110) is not observed in all samples. It seems as if the observed two-dimensional checkerboard-like structure can only develop for certain ratios of the Fe DL stripe width and interstripe distance. However, on the basis of the existing data a detailed analysis of this issue is not possible. The detailed conditions for the formation of the observed structure remain puzzling and should be the subject of further investigations.

8.3 The complex topology of the observed spin texture

The topology of the observed magnetic structure, as resulting from the discussed coexistence of spiral-like spin rotations along [001] and $[1\bar{1}0]$, is illustrated in Fig. 8.3. The $\mathrm{d}I/\mathrm{d}U$-map on the left-hand side is a zoom-in to the $\mathrm{d}I/\mathrm{d}U$-map in Fig. 8.2 (c). The corresponding image sections are marked by a green box. The zoom-in visualizes a characteristic area of the sample that serves as a starting point for the schematic illustration on the right-hand side of Fig. 8.3. From the measurements discussed in Chapter 5 it is known that the DL spiral along [001] is a right-rotating cycloid. However, for the spiral along the perpendicular [001] direction only the cycloidal character of the spiral could be measured (Fig. 8.2), whereas the rotational sense remains unknown[1]. Thus, the observed $\mathrm{d}I/\mathrm{d}U$-contrast is consistent with two magnetic configurations, as illustrated on the right-hand side of Fig. 8.3.

Compared to the one-dimensional spin spiral configuration discussed before, the observed two-dimensional spin configuration is topologically different. Mathematically, the topological structure can be expressed in terms of the so-called skyrmion number:

---

[1] The rotational sense of the spiral along $[1\bar{1}0]$ can in principle be determined using the experimental setup described in Part I. However, due to technical problems the necessary measurements could not be done for the sample under discussion. Nevertheless, some interesting conclusions can be drawn.

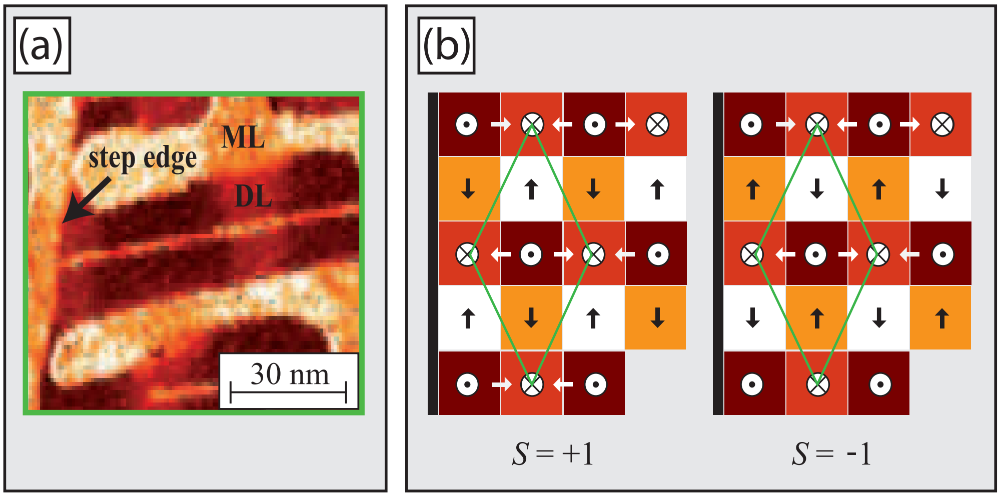

Figure 8.3: Topology of the magnetic ground state in the combined system of Fe ML and DL on W(110). (a) Zoom-in to the area marked by the green box in Fig. 8.2 (c). (b) Schematic illustration of the magnetization directions in the sample area shown in (a). The magnetic structure shows a unique spiral-like rotation along both the [001] and the [$1\bar{1}0$] direction. On the basis of the measurement series in Fig. 8.2 the configurations on the right and left-hand side cannot be distinguished. The configurations are topologically equivalent to a skyrmion lattice ($S = +1$), and an anti-skyrmion lattice ($S = -1$), respectively.

$$\boxed{S = \frac{1}{4\pi} \int \mathbf{M}(x,y) \cdot \left(\frac{\partial \mathbf{M}(x,y)}{\partial x} \times \frac{\partial \mathbf{M}(x,y)}{\partial y} \right) \mathrm{d}x\,\mathrm{d}y} \tag{8.1}$$

Here, $\mathbf{M(x,y)}$ is the normalized vector field that indicates the magnetization direction as a function of the spatial position in the (x,y)-plane (cf. Chapter 3.2, Eq. (3.9)-(3.10)). The integral is taken over one unit cell as visualized by the green lozenges in Fig. 8.3. For a collinear spin configuration the skyrmion number vanishes, due to the vanishing partial derivatives in the integrand of Eq. (8.1). For the previously discussed one-dimensional spin spiral configurations one can chose a coordinate system with the x-direction being defined as the propagation direction of the spiral. Consequently, one obtains finite values for $\frac{\partial \mathbf{M}(x,y)}{\partial x}$, whereas $\frac{\partial \mathbf{M}(x,y)}{\partial y}$ is again identical to zero. The integrand vanishes and the skyrmion number becomes equal to zero, as for the collinear case. In contrast, for the spin configurations in Fig. 8.3 both partial derivatives are finite and the skyrmion number achieves values of $S = \pm 1$, as indicated in Fig. 8.3. Consequently, the observed spin configuration is topologically different from the ferromagnetic state and the discussed spin spiral configurations. In particular, it cannot be described as a simple superposition of spin-spirals, a so-called multi-q state, which would have a skyrmion number $S = 0$. Instead, the observed two-dimensional spin configuration is topologically comparable to the recently observed skyrmion ($S = +1$) and anti-skyrmion ($S = -1$) lattices [4, 5, 133–135].

Despite the discussed topological similarities of the combined Fe ML/DL system on W(110) and the recently discussed skyrmion and anti-skyrmion lattices there are three major differences between these systems:

- Due to the combination of ML and DL areas the Fe/W(110) system is structurally and electronically inhomogeneous. As a consequence, the magnetic easy axis is a function of the spatial position on the sample, i.e. it points along $[1\overline{1}0]$ in the ML and along [110] in the double DL areas. This is in contrast to the recently discussed concept of skyrmion-lattices that was originally introduced, in order to describe stable excitations in homogeneous fields [137].

- The observed topologically non-trivial magnetic configuration is closely related to the topography of the arrangement of Fe DL patches and stripes on top of the ML film. In particular, the magnetic configuration cannot be displaced along the crystallographic $[1\overline{1}0]$ direction and any variation of the structure is restricted to the [001] direction, where domain walls can move freely. This is in contradiction to the free-particle-like behavior of skyrmionic excitations along all directions, as discussed in the literature [137].

- The two-dimensional spin configuration in the Fe/W(110) system is restricted to the sample surface. Like the surface spin spiral discussed in Part II it is of non-chiral type (cf. Chapter 5.4)[2]. This is in contrast to the recently observed skyrmion and antiskyrmion lattices [4, 5, 133–135] that were observed in bulk magnetic systems with a chiral lattice structure that induces a chirality in the skyrmion lattices.

8.4 Driving forces of the complex spin topology

In view of the previously discussed similarities between the observed two-dimensional spin configuration in the combined system of Fe ML and Fe DL on W(110) and the recently observed magnetic skyrmion lattices, it is tempting to describe the Fe/W(110) system in terms of skyrmion lattices. On the other hand such a description may be misleading due to the discussed differences. Thus, in the following the essential requirements for the existence of stable skyrmion lattices will be summarized. Afterwards, it is discussed to what extent the requirements are met in the case of the combined Fe ML/DL system. Finally, an alternative model is suggested for the description of the observed topologically non-trivial magnetic structure. It is based on dipolar interaction and the spatially varying crystalline anisotropy in the Fe/W(110) system.

---

[2] Note, that both spin configurations in Fig. 8.3 are mirror-symmetric with respect to the diagonal of the unit cell. Consequently, the configurations are non-chiral.

Skyrmion-like ground state formation

Recently the chiral ferromagnets MnSi and $Fe_{1-x}Co_xSi$ (FeSi with a fraction x of the Fe atoms being replaced by Co atoms) attracted a lot of interest because of the magnetic spin spiral and skyrmion lattice configurations that could be observed in these materials [4–6]. Both in MnSi and in $Fe_{1-x}Co_xSi$ the chiral crystal structure results in a broken inversion symmetry giving rise to a non-vanishing contribution of the DM interaction that explains the formation of the observed complex magnetic structures. At first sight, the observation of magnetic skyrmion lattices in these materials is surprising, since, according to a seminal result by Wright and Mermin [138], stable skyrmion lattices cannot exist in chiral ferromagnets. Nevertheless it could be shown that, under certain circumstances that had not been taken into account by Wright and Mermin, skyrmionic magnetic textures may be observed. In particular, it was shown that such states can be induced by external magnetic fields [139], thermal fluctuations [4], a spatial variation of the magnetic moments [134], or appropriate values of the magnetic anisotropy [140]. Only very recently, it was shown by measurements in the Fe ML on Ir(111) that even in non-chiral surface ferromagnets skyrmion lattices can be stabilized [7]. The stability was attributed to the joint action of the DM interaction in the presence of the broken inversion symmetry at the crystal surface and magnetic four-spin interactions.

In closed Fe DL films as well as in Fe DL stripe systems on W(110) the DM interaction plays an important role as discussed in Part II of this thesis. In Fe ML films on W(110) the interaction was also predicted to be of significant size, although the spin spiral formation is suppressed by the high magnetic anisotropy [141, 142]. Consequently, it appears to be a reasonable assumption that in the combined system of Fe ML and Fe DL on W(110) the DM interaction can account for the observed unique rotational sense along both the [001] and the $[1\bar{1}0]$ direction. However, as for the case of the recently discussed magnetic skyrmion lattices, it remains puzzling why the observed topologically non-trivial spin configuration is stabilized. Since the spin configuration is observed even in zero magnetic field (Fig. 8.2 (b)), a stabilization by external magnetic fields can be ruled out. In contrast, thermal fluctuations, softened amplitude variations of the magnetization and higher-order magnetic interactions may be present and might be relevant driving forces towards the observed magnetic ground state, in analogy to the skyrmion lattices discussed before. However, it remains to be investigated in detail if the mechanisms, as discussed in the context of skyrmion lattices in homogeneous solid state systems, can be generalized such that they can be applied even for the observed spatially inhomogeneous Fe coverages and magnetic anisotropies in the combined system of Fe ML and Fe DL on W(110).

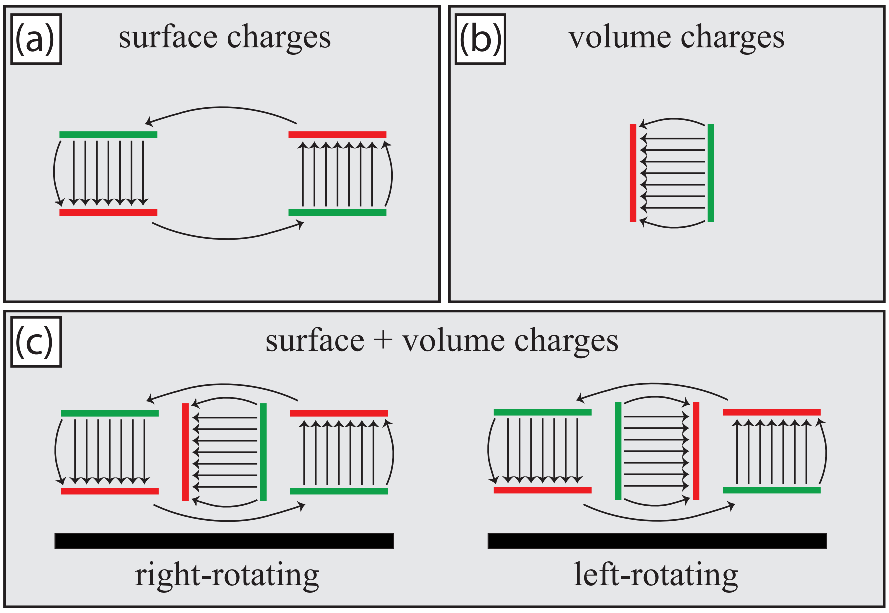

Figure 8.4: (a) Surface charge distribution and corresponding demagnetizing field for two neighboring out-of-plane magnetized magnetic domains. (b) Volume charge distribution and corresponding demagnetizing field for an in-plane magnetized domain wall. (c) Superposition of surface and volume charges and their corresponding demagnetizing fields. Due to the geometry of the demagnetizing fields in (a) and (b) the demagnetizing field configuration in the combined system depends on the spiral's sense of rotation. For left-rotating spiral profiles the fields add up at the Fe/W interface, for right-rotating spiral profiles they compete. Consequently, the energetic degeneracy of right- and left-rotating spirals may be lifted due to induced magnetic polarizations in the W layer closest to the Fe/W(110) interface.

Alternative ground state formation

As an alternative to the previously discussed skyrmion-like ground state formation it is suggested to explain the observed topologically non-trivial spin configuration on the basis of the DM interaction, spatially varying magnetic anisotropies, dipolar interactions and polarizations of the W(110) substrate. The discussion in this section relies on the idea that the spiral structure in the Fe DL is fully explained by the mechanisms discussed in Part II, whereas the additional spiral-like behavior along the perpendicular in-plane direction is explained by a second mechanism, which is introduced in the following [143].

Fig. 8.4 illustrates the magnetic charge distribution and the demagnetizing field of a short piece of a cycloidal spin spiral that consists of two out-of-plane magnetized domains separated by a Néel-type domain wall. In (a) and (b) the contributions of the surface and volume charges are visualized separately. The combination of both contributions is shown in (c). It turns out that the superposition of both field contributions results in an asymmetry of the total demagnetizing field. As a consequence of this asymmetry the resulting field at the Fe/W(110) interface depends on the rotational sense of the spin spiral. In the case of left-rotating spin spirals the fields originating from the surface and volume charges add up, for right-rotating spin spirals the fields are antiparallel and compete, as illustrated. Consequently, the energetic degeneracy of right- and left-rotating spirals can be lifted due to induced magnetic polarizations in the W layer closest to the Fe/W(110) interface. According to [144] such a polarization is most likely, since the topmost W layer acquires a small but significantly large magnetic moment of $-0.1\mu_\mathrm{B}$ due to strong hybridization between the 3*d* bands in the Fe and the 5*d* bands in the underlying W-substrate.

The lifting of the degeneracy of right- and left-rotating spin spirals at the surface of magnetically polarizable substrates only exists in the case of cycloidal spiral profiles. In the case of helical profiles, this symmetry breaking does not occur. Thus, the discussed mechanism can explain the unique rotational sense of cycloidal spin spirals on purely dipolar grounds, without considering the DM interaction. However, it does not explain why in the combined system of Fe ML and DL areas on W(110) the rotation along $[1\bar{1}0]$ is of cycloidal instead of helical type. As discussed before, in the combined system of Fe ML and Fe DL there are two different directions of the magnetic easy axis, i.e. $[1\bar{1}0]$ in the ML and [110] in the DL. Consequently, the cycloidal character of the spin rotation along $[1\bar{1}0]$ may result as a direct consequence of these different anisotropy directions. With the cycloidal structure being induced in this way, the previously discussed mechanism may account for the observed unique rotational sense.

8.5 Measurement of the topological stability

As discussed before, one-dimensional spiral configurations (Part II) have the same skyrmion number ($S = 0$) as the ferromagnetic state. As a consequence of this topological equivalence a spiral state can be transformed to the ferromagnetic state in a continuous fashion. For helical spin spiral configurations such a continuous transformation was simulated within the framework of a two dimensional micromagnetic model [123]. The cycloidal case discussed in Part II can be treated in an analogous way. In contrast to the spiral case, the observed skyrmion-lattice-like spin configuration ($S = \pm 1$) is a topologically protected state, i.e. it cannot be transformed continuously to the ferromagnetic state. Thus, the magnetic ground state of Fig. 8.2-8.3 is expected to be more stable with respect to perturbations than the previously discussed spin spiral configurations. In the following, it will be discussed how the increased topological stability of the observed two-dimensional spin configuration may be confirmed by SP-STM measurements in external magnetic fields. It is emphasized that the discussion is not intended as a detailed experimental description or feasibility study and should be considered as a preliminary collection of experimental concepts.

Lattice distortions in external magnetic fields

In order to confirm the topological stability of the two-dimensional spin configuration in Fe/W(110) it may be elucidating to compare its response to external magnetic fields with the response of the one-dimensional spin spiral configurations discussed in Part II. Fig. 8.5 illustrates the expected distortions for three different scenarios: zero field (top), external field along [110] (center), and external field along [001] (bottom).

In perpendicular magnetic fields along [110] the domains with a magnetization parallel to the external field grow in size while domains with an antiparallel magnetization shrink. When switching off the field both the spin spiral and the two-dimensional lattice structure return to the symmetric zero-field configurations. In the spiral case the distortions can be described in terms of a simple linear chain model, as introduced in standard textbooks of solid state physics. For small distortions the restoring force is dominated by dipolar interaction that favors equal domain sizes. Only for large distortions, i.e. in the regime of small domain wall separation, magnetic exchange comes into play and contributes significantly[3]. In the lattice case the situation is slightly more complex. In contrast to the spin spiral configuration, the distortion cannot be described by a simple linear chain model, since the lattice undergoes an additional shear distortion of the domain walls in neighboring Fe DL stripes. Consequently, in addition to the previously discussed restoring forces, the system experiences further restoring forces due to the shearing, as indicated by the spring symbols in Fig. 8.5 (b). In particular, these shearing forces are closely related to the strength of the inter-stripe coupling and thus the topological stability of the spin configuration. Consequently, the topological stability may be investigated in detail by comparing the field dependence of the one-dimensional spin spirals and the two-dimensional spin configuration. In addition, it may be elucidating to measure the critical field, above which domain walls annihilate. Due to the topological stability the critical field for the two-dimensional lattice configuration is expected to be enhanced with respect to the spin spiral state.

---

[3] The strong restoring force due to magnetic exchange was previously discussed in terms of a repelling force between neighboring 180° walls in the regime of 360° walls [1].

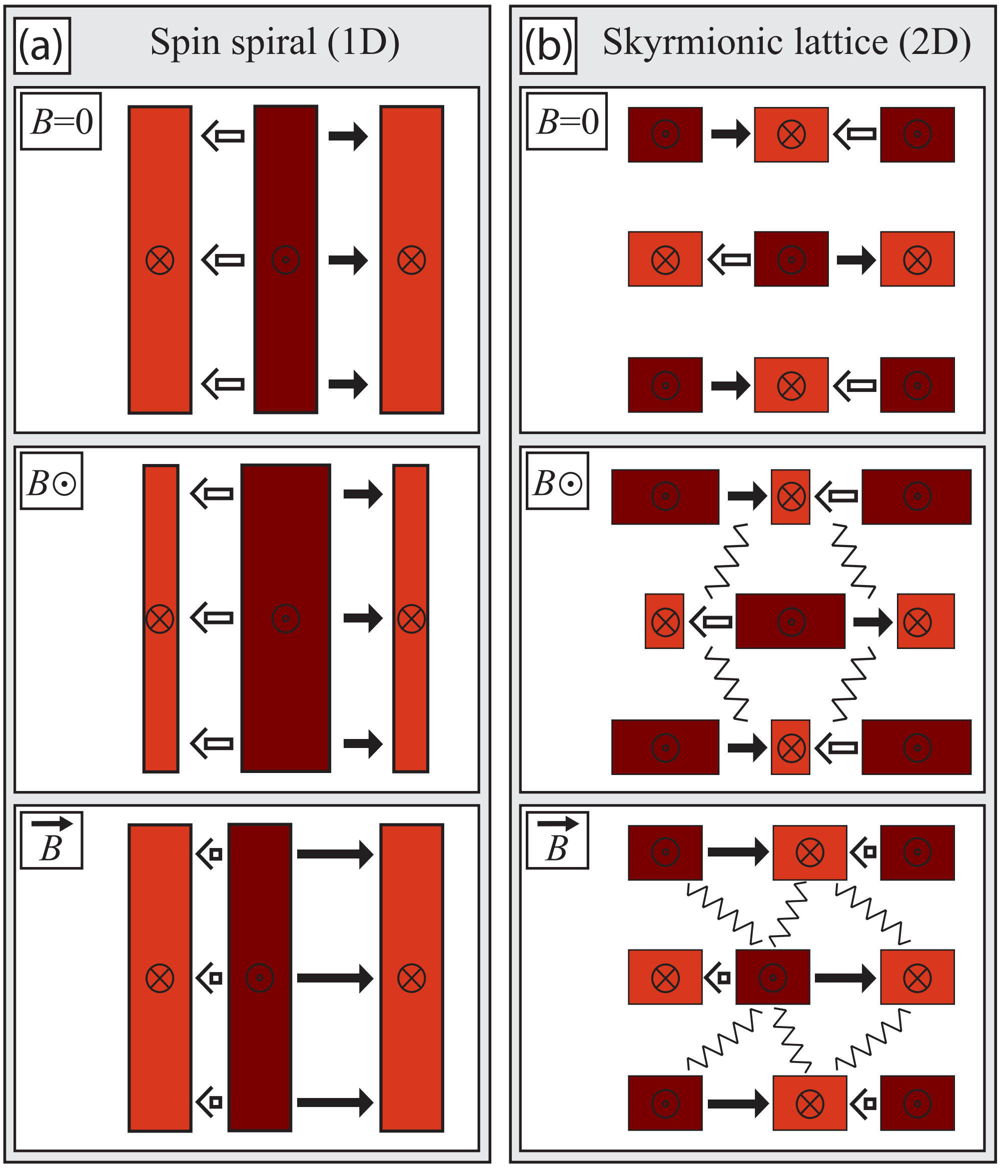

Figure 8.5: Field dependence of the one-dimensional spin spiral configuration (a) and the two-dimensional lattice configuration (b) in Fe/W(110). The upper panels show the spin configurations in zero field. The panels in the center illustrate the response to an external magnetic field along the surface normal. The lower panels visualize the response to an in-plane field along [001]. In the two-dimensional spin configuration additional restoring forces originate from the shear distortion and the topological coupling between neighboring Fe DL stripes (spring symbols).

In external in-plane magnetic fields along [001] the general mechanisms are comparable to the previously discussed case of perpendicular external fields. However, now the field acts on the in-plane magnetized domain walls rather than on the out-of-plane magnetized domains. Thus, in order to create a significant impact, the field must be strong enough to affect the domain wall width. Compared to the previous case, where the restoring force was (at least initially) dominated by the relatively weak dipolar coupling, the field must be stronger by about one order of magnitude. In particular, due to the strong restoring forces the additional effect due to the topological stability may be too weak to be observed.

In external in-plane magnetic fields along [$\mathbf{1\bar{1}0}$] the one-dimensional spin spirals remain unaffected, since they have no magnetization component along [$1\bar{1}0$]. In contrast, the two-dimensional lattice configuration exhibits such a magnetization component along [$1\bar{1}0$] in the ML areas. It may therefore be distorted by the magnetic field and the field dependence of this distortion may be measured in SP-STM experiments. Although the topological stability of the two-dimensional spin configuration cannot be compared to the stability of the spin spiral state, this type of measurements may provide insight into the coupling between the ML and DL areas, in particular when the external field becomes strong enough to break the coupling.

Thermal and current-induced magnetic switching experiments

In addition, the stability of both magnetic configurations may be compared with respect to their nanoscale thermal switching properties using SP-STM [145, 146]. In an analogous way the current-induced magnetic switching properties may be investigated [147, 148]. As for the previously suggested type of experiments it may be instructive to investigate the switching properties as a function of the direction of an external magnetic field using the experimental setup discussed in Part I.

8.6 Topological fields and topological Hall effect

In 1983 M. V. Berry discovered that quantum objects like electrons acquire a geometrical phase if they are transported adiabatically on a closed path in the parameter space spanned by the parameters in the system Hamiltonian [149]. The acquired phase depends on the topological structure of the parameter space and the shape of the chosen path. Thus, the concept of the Berry phase can give deep insight into the topological structure of quantum systems. It gives rise to various experimentally observable effects in diverse fields, such as quantum optics, elementary particle physics, and condensed matter physics [150, 151].

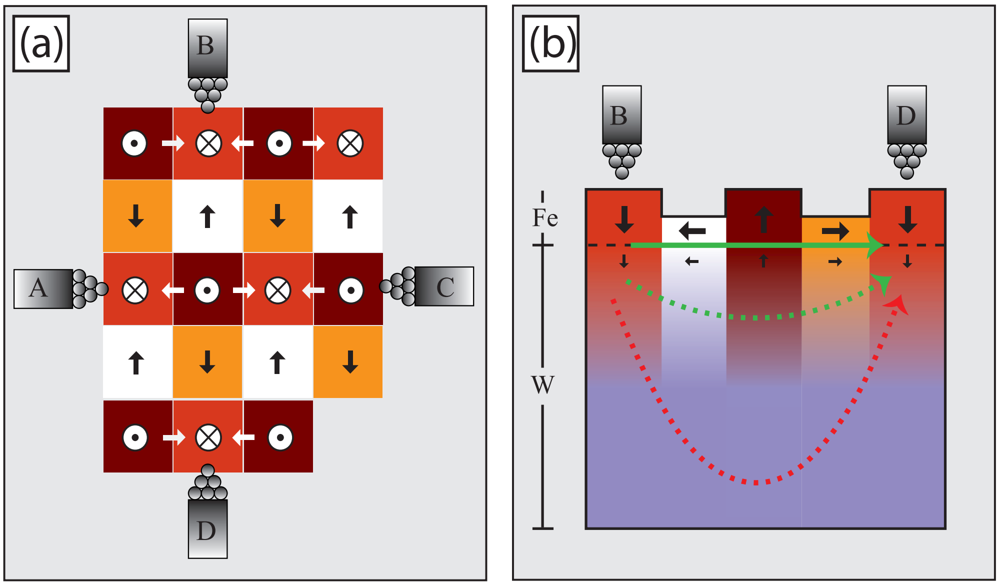

Figure 8.6: Hall measurements in the combined system of Fe ML and Fe DL. (a) Setup for a four probe measurement using four independent STM-tips. With a current flowing between B and D the Hall voltage can be measured between A and C. (b) Cross sectional view of the Fe coated W sample. The decay of the magnetic field with increasing distance from the surface is indicated by the color gradient. Three characteristic current paths are illustrated by arrows: The direct current path in the area where the magnetic field is strongest (solid green), a current path that is not significantly influenced by the magnetic field (red dotted), and an intermediate path (green dotted).

In a magnetic field electrons experience a Lorentz force perpendicular to both the field and the electron's direction of motion. One direct consequence of the Lorentz force is the normal Hall effect that was first observed by *Edwin Hall* in 1879. If in a Hall measurement the magnetic field is topologically non-trivial, the conduction electrons can acquire a Berry phase when their spin follows the direction of the field in an adiabatic way. The acquired Berry phase gives rise to a so-called topological field that results in an additional force experienced by the electrons [152, 153]. This topological force is again of Lorentz-type and gives rise to the so-called topological Hall effect [154, 155]. In contrast to the normal Hall effect the topological Hall effect can even be expected for a vanishing net magnetization along the current path. It is of purely topological origin and only requires a non-trivial field topology.

Recently, the topological Hall effect could be observed in the geometrically frustrated pyrochlore compound $Nd_2Mo_2O_7$ [156, 157] and the magnetic skyrmion lattice in the A-phase of the chiral ferromagnet MnSi [158]. In analogy to these experiments it appears promising to measure the topological Hall effect by transport measurements on the combined Fe ML/DL system on W(110), as illustrated in Fig. 8.6 (a). Compared to the previous measurements of the topological Hall effect the localization of the magnetic moments in the Fe and the interfacial W-layer [144], as indicated by black arrows in panel (b), may open novel experimental options. Thus, the magnetic moments may be manipulated intentionally by the artificial allocation of additional magnetic atoms or current-induced magnetic switching techniques [147, 148]. On the other hand, the localization of the magnetic moments at the sample surface also imposes experimental challenges, since due to this localization the magnetic field decays as a function of the distance from the Fe coating as illustrated by the color gradient [159]. Since the current between B and D is given by the sum of the partial currents along all possible paths between the probes, not all electrons will be affected by the field. For electrons flowing close to the surface the influence of the field is largest (solid green arrow in panel (b)). It reduces for electrons flowing farther away from the surface (green dotted) and finally becomes negligible for current paths that penetrate deeply into the W substrate. Since the electrical resistance is essentially proportional to the length of the current path, the electrons prefer paths close to the surface. Nevertheless, a certain amount of leakage current in the area of small magnetic field cannot be avoided. Thus, in contrast to the bulk magnetic structures in $Nd_2Mo_2O_7$ and MnSi, a certain fraction of the electrons may not be affected by the magnetic field and therefore may not contribute to the topological Hall effect. In order to deal with this problem, one should keep in mind that the average penetration depth depends significantly on the alignment of the probes, i.e. it reduces with decreasing inter-probe distance. It is therefore suggested to perform the discussed Hall measurements using a four probe STM [160] instead of using traditional probing techniques based on lithographically etched Hall bar geometries and traditional bonding methods. In addition, it might be helpful to replace the W single crystal by an epitaxial W thin film on an insulating substrate, in order to avoid leakage currents in the area where the magnetic field is weak.

Summary and perspectives

Instrumental developments

In the framework of this thesis a fully custom-designed SP-STM setup was developed. The SP-STM can be operated in the external field of a triple axes vector magnet at a base temperature of 4.2 K. The system was optimized to allow for a maximum of flexibility with respect to the self-assembled growth of atomic-scale magnetic structures in the temperature range between 10 K and 1100 K. In addition to the extended experimental capabilities the novel setup offers various options for automated substrate cleaning, data acquisition and data logging. In Part I the design concept was described in detail and the functionality was demonstrated.

The operation of an SP-STM in the external field of a triple axes vector magnet is an important extension of the technique towards measurements with angular resolution. In particular, the rotatable field allows for two novel types of SP-STM experiments:

Characterization of non-collinear magnetic structures with angular resolution

The instrument developed for this thesis allows to fully control the magnetization direction of ferromagnetically coated probe tips along all spatial directions. This extends the capabilities of SP-STM significantly since for the first time the local magnetization of the sample can be determined with respect to an external coordinate system. This unique capability of the novel setup allows for the real-space observation of atomic-scale magnetic structures with angular resolution. Thus, in particular in the field of non-collinear magnetism, it opens up the door for a whole class of experiments not being accessible by traditional SP-STM setups.

Manipulation of magnetic structures by magnetic fields of arbitrary direction

While in the case of ferromagnetic probe tips the direction of the tip magnetization is strongly affected by the external field this is not the case for antiferromagnetic tip coatings. Thus, for the latter case, the magnetic structure of the sample can be manipulated by the external field without any superimposed tip effects. Even for this class of experiments the vector magnet setup gives rise to experimental options not being accessible in traditional SP-STM setups, since now the response of the sample magnetization to the external field can be investigated as a function of the spatial orientation of the field. Since magnetic interactions are strongly determined by the lattice structure they are in general not isotropic. Thus the discussed measurements can give novel insight into the origin of magnetism at crystal surfaces.

The magnetic spin spiral ground state in the Fe DL on W(110)

The second part of the thesis was referring to the experimental investigation of the spin spiral ground state of the Fe DL on W(110). Using the newly developed experimental setup the right-rotating cycloidal character of the spin spiral could be measured directly for the first time. In addition, it was shown that the spiral rotation is confined to the plane spanned by the crystallographic [001] and [110] axes. Thus, it can be ruled out on the basis of real-space measurements that the spiral rotation follows a complex truly three-dimensional path as suggested recently [72]. Compared to previous investigations of other spin spirals, where the spiral configuration could only be deduced on the basis of density functional theory calculations, the real-space measurement of the spin spiral in the Fe DL on W(110) is a major progress. In particular, the measurements allow for the first time to directly compare experimental results and theoretical predictions. Thus, the presented results can serve as an experimental reference for the validation of the predictive power of the recently applied density functional theory models.

In order to bridge the gap between the results of density functional theory and the experimentally observed real space structure of the spin spiral state in the Fe DL on W(110), micromagnetic model calculations can be applied. Starting from either side the relevant micromagnetic parameters, i.e. the exchange stiffness A, the crystalline anisotropy K_c, the DM vector $\mathbf{D}$ and the saturation magnetization M_s, can be calculated and compared. However, the previous approaches along these lines [1, 2] were contradictory to at least some experimental observations (cf. Tab. 4.2). In the framework of this thesis the discussed contradictions could be resolved by the development of a micromagnetic model explaining all experimental observations on the basis of a unique set of micromagnetic parameters. In particular the previously suggested micromagnetic models were extended along two directions: (i) In addition to magnetic exchange, crystalline anisotropy, and shape anisotropy the model developed in this thesis also accounts for the DM interaction and the energy contribution of demagnetizing fields. (ii) The restriction to homogeneous sinusoidal spiral profiles was dropped and the considerations were extended to arbitrary, i.e. inhomogeneous, spiral profiles.

Based on this comprehensive micromagnetic model the micromagnetic parameters A, K_c, $\mathbf{D}$, and M_s were determined as fitting parameters to the experimentally observed spin spiral profile in the Fe DL on W(110). In contrast to all previous studies the parameter set is unique and the calculations are consistent with all experimental observations known to date. However, the determined micromagnetic parameters are contradictory to the respective parameters recently calculated on the basis of DFT methods [3]. It was discussed that this discrepancy may be explained by the restriction to homogeneous spiral profiles in the DFT calculations. It was shown that, in the case of the Fe DL on W(110), this restriction cannot be regarded as a minor simplification. In particular, the disregard of inhomogeneity in the profile shape results in an artificial coupling of the spiral period and the domain wall width, which is contradictory to the experimental observations. This improper coupling finally results in a coupling of the micromagnetic parameters A, K_c, $\mathbf{D}$, and M_s and accounts for the discrepancy between the recent DFT results and the results of this thesis that rely on the independence of the parameters.

The spin spiral in closed Fe DL films on W(110) was shown to be induced by the joint action of the DM interaction and dipolar coupling, whereas none of these interactions can explain the formation of the spin spiral on its own. This is in contrast to the previously observed antiferromagnetic spin spiral in the Mn ML on W(110) [48] that is purely induced by the DM interaction. In particular, it was shown that in the Fe DL on W(110) the strength of the DM interaction is close to the critical limit where a spin spiral state can be induced. As a consequence of this weak DM interaction the spin spiral profile is highly inhomogeneous in contrast to all previously observed spin spirals.

It is a major improvement compared to previous models that the micromagnetic model developed in this thesis is not only applicable to closed film geometries but also to finite size systems. In particular, this extended applicability allows to reproduce the hitherto unexplained vanishing of the spin spiral ground state in SP-STM measurements on narrow Fe DL stripes on W(110) [29]. It also gives a consistent explanation for the observed stripe width dependence of the disappearing spin contrast in SP-STM experiments at elevated temperatures [120]. In particular, it was shown that, with decreasing stripe width the spiral state becomes energetically less favorable while the ground state spiral period diverges. This behavior was attributed to the decreasing demagnetizing energy due to the increasing significance of demagnetizing field inhomogeneities at the stripe edges. Consequently, the joint effect of dipolar coupling and the DM interaction, that accounts for the spiral formation in closed films, reduces with decreasing stripe width and finally results in the diverging spiral period, in agreement with the experimental observations. In order to analyze the origin of the stripe width dependence in more detail a very much simplified box model was developed. Despite all simplifications the model reproduces the experimental observations very well. In addition, due to its reduced complexity, the model allows to separate finite-size effects originating from magnetic surface charges, volume charges, and shape anisotropy. Both micromagnetic models indicate a functional relationship between the spiral period and the stripe geometry that originates from the reduced demagnetizing energy density in narrow stripes. Thus based on the discussed models it is in principle feasible to tailor the spiral period by adjusting the geometry of the Fe DL stripes in an appropriate way. This may be of particular interest for future experiments and even technological applications such as microwave sources, based on the spin rotation of spin-polarized electron currents along the propagation direction of the spiral [48].

Skyrmion-lattice-like spin textures

In a certain range of Fe coverages, that remains to be determined by subsequent studies, a topologically complex two-dimensional magnetic structure appears in the combined system of Fe ML and Fe DL on W(110). Using the novel experimental setup described in Part II, it was shown experimentally that the structure is topologically equivalent to the recently observed skyrmion lattices in MnSi [4, 158], $Fe_{1-x}Co_xSi$ [5, 6], and the Fe ML on Ir(111) [7]. On the other hand it is topologically distinct from the collinear state and the spin spiral state discussed in Part II. Thus, its stability with respect to external perturbations is expected to be increased compared to the discussed spin spirals.

In order to explain the origin of the observed spin configuration two models were considered. On the one hand it was discussed if the observed structure can be described in terms of skyrmion lattices, in analogy to the previously observed magnetic configurations in MnSi and $Fe_{1-x}Co_xSi$. However, due to the complexity of the problem a closing answer is beyond the scope of this thesis. As an alternative to the skyrmion-like ground state formation it was suggested to explain the observed spin configuration on the basis of the DM interaction, spatially varying magnetic anisotropies, dipolar interactions and polarizations of the W(110) substrate. It was shown that the unique rotational sense of a spin spiral can be explained without taking the DM interaction into account, if the cycloidal spiral type is induced by other interactions such as spatially varying magnetic anisotropies, as observed along the $[1\overline{1}0]$ direction in the combined system of Fe ML and Fe DL on W(110).

For the measurement of the increased topological stability in the reported two-dimensional spin configuration several experiments were suggested. It was discussed how the new triple axes magnet system can be used for this purpose. In particular, it may be used to distort the observed magnetic lattice structure. Compared to the one-dimensional spin spiral configuration in closed Fe DL films, the two-dimensional skyrmion-lattice-like configuration is expected to experience a shear distortion between the spiral structures in neighboring DL stripes. The corresponding restoring forces originate from the inter-stripe coupling, which is strongly related to the non-trivial topology of the observed spin configuration and thus its topological stability. In addition to the investigation of the topological stability by the field dependent distortion of the spin configuration it was suggested to compare its thermal and current-induced switching properties to the switching properties of the spin spiral state.

Finally, it was proposed to exploit the non-trivial topology of the two-dimensional spin configuration in the Fe/W(110) system for electronic transport experiments. It was discussed that the spin configuration gives rise to a topologically non-trivial magnetic field that results in a non-vanishing Berry phase of the conduction electrons moving along the field. The Berry phase is closely related to the topological Hall effect, that may be measured by appropriate electronic transport experiments using an STM with four independent probe tips. In contrast to the recent measurements of the topological Hall effect in chiral ferromagnets, the two-dimensional spin configuration in Fe/W(110) is non-chiral. In addition, it is localized at the sample surface, thus giving rise to the possibility of its manipulation by the intentional agglomeration of additional magnetic atoms or current induced magnetic switching techniques

Bibliography

[1] A. Kubetzka, O. Pietzsch, M. Bode, and R. Wiesendanger, Phys. Rev. B **67**, 020401(R) (2003).

[2] E. Y. Vedmedenko, A. Kubetzka, K. von Bergmann, O. Pietzsch, M. Bode, J. Kirschner, H. P. Oepen, and R. Wiesendanger, Phys. Rev. Lett. **92**, 077207 (2004).

[3] M. Heide, G. Bihlmayer, and S. Blügel, Phys. Rev. B **78**, 140403 (2008).

[4] S. Mühlbauer, B. Binz, F. Jonietz, C. Pfleiderer, A. Rosch, A. Neubauer, R. Georgii, and P. Böni, Science **323**, 915 (2009).

[5] X. Z. Yu, Y. Onose, N. Kanazawa, J. H. Park, J. H. Han, Y. Matsui, N. Nagaosa, and Y. Tokura, Nature **465**, 901 (2010).

[6] W. Münzer, A. Neubauer, T. Adams, S. Mühlbauer, c. Franz, F. Jonietz, R. Georgii, P. Böni, B. Pedersen, M. Schmidt, et al., Phys. Rev. B **81**, 041203 (R) (2010).

[7] S. Heinze, K. v. Bergmann, M. Menzel, J. Brede, A. Kubetzka, R. Wiesendanger, G. Bihlmayer, and S. Blügel, submitted.

[8] G. Binnig, H. Rohrer, C. Gerber, and E. Weibel, Appl. Phys. Lett. **40**, 178 (1982).

[9] J. Bardeen, Phys. Rev. Lett. **6**, 57 (1961).

[10] J. Tersoff and D. R. Hamann, Phys. Rev. Lett. **50**, 1998 (1983).

[11] J. Tersoff and D. R. Hamann, Phys. Rev. B **31**, 805 (1985).

[12] N. D. Lang, Phys. Rev. B **34**, 5947 (1986).

[13] R. Wiesendanger, *Scanning Probe Microscopy and Spectroscopy* (Cambridge University Press, 1994).

[14] J. R. Hahn, H. J. Lee, and W. Ho, Phys. Rev. Lett. **85**, 1914 (2000).

[15] W. Ho, J. Chem. Phys. **117**, 11033 (2002).

[16] A. J. Heinrich, J. A. Gupta, C. P. Lutz, and D. M. Eigler, Science **306**, 466 (2004).

[17] A. F. Otte, M. Ternes, K. von Bergmann, S. Loth, H. Brune, C. P. Lutz, C. F. Hirjibehedin, and A. J. Heinrich, Nature Physics **4**, 847 (2008).

[18] S. Loth, M. Etzkorn, C. P. Lutz, D. M. Eigler, and A. J. Heinrich, Science **329**, 1628 (2010).

[19] C. F. Hirjibehedin, C. P. Lutz, and A. J. Heinrich, Science **312**, 1021 (2006).

[20] T. Balashov, A. F. Takács, W. Wulfhekel, and J. Kirschner, Phys. Rev. Lett. **97**, 187201 (2006).

[21] R. Wiesendanger, H.-J. Güntherodt, G. Güntherodt, R. J. Gambino, and R. Ruf, Phys. Rev. Lett. **65**, 247 (1990).

[22] R. Wiesendanger, D. Bürgler, G. Tarrach, A. Wadas, D. Brotbeck, D. Güntherodt, R. J. Gambino, and R. Ruf, J. Vac. Sci. Technol. B **9**, 519 (1991).

[23] R. Wiesendanger, I. V. Shvets, D. Bürgler, G. Tarrach, H.-J. Güntherodt, J. M. D. Coey, and S. Gräser, Science **255**, 583 (1992).

[24] M. Bode, Rep. Prog. Phys. **66**, 523 (2003).

[25] S. Heinze, M. Bode, A. Kubetzka, O. Pietzsch, X. Nie, S. Blügel, and R. Wiesendanger, Science **288**, 1805 (2000).

[26] M. Julliere, Phys. Rev. Lett. **54A**, 225 (1975).

[27] J. C. Slonczewski, Phys. Rev. B **39**, 6995 (1989).

[28] S. Heinze, Ph.D. thesis, University of Hamburg (2000).

[29] O. Pietzsch, Ph.D. thesis, University of Hamburg (2001).

[30] A. Kubetzka, M. Bode, O. Pietzsch, and R. Wiesendanger, Phys. Rev. Lett. **88**, 057201 (2002).

[31] O. Pietzsch, A. Kubetzka, D. Haude, M. Bode, and R. Wiesendanger, Rev. Sci. Instrum. **71**, 424 (2000).

[32] J. Wiebe, A. Wachowiak, F. Meier, D. Haude, T. Foster, M. Morgenstern, and R. Wiesendanger, Rev. Sci. Instrum. **75**, 4871 (2004).

[33] A. P. Fein, J. R. Kirtley, and R. M. Feenstra, Rev. Sci. Instrum. **58**, 1918 (1994).

[34] R. R. Schulz and C. Rossel, Rev. Sci. Instrum. **65**, 1918 (1994).

[35] J. G. A. Dubois, J. W. Gerritsen, J. G. H. Hermsen, and H. van Kempen, Rev. Sci. Instrum. **66**, 4146 (1995).

[36] S. I. Vasilev, S. I. Oreshkin, V. P. Panov, S. V. Savinov, C. van Haesendonck, and A. Depuydt, Instrum. Exp. Tech. **40**, 566 (1997).

[37] E. W. H. S. H. Pan and J. C. Davis, Rev. Sci. Instrum. **70**, 1459 (1999).

[38] M. Kugler, C. Renner, O. Fischer, V. Mikheev, and G. Batey, Rev. Sci. Instrum. **71**, 1475 (2000).

[39] D. F. G. K. K. Sagisaka, M. Kitahara and N. Koguchi, Nanotechnology **15**, 371 (2004).

[40] H. Kambara, T. Matsui, Y. Niimi, , and H. Fukuyama, J. Phys. Chem. Solids **66**, 1552 (2005).

[41] S. Ernst, S. Wirth, M. Rams, V. Dolocan, , and F. Steglich, Sci. Technol. Adv. Mater **8**, 347 (2007).

[42] C. Wittneven, R. Dombrowski, S. H. Pan, and R. Wiesendanger, Rev. Sci. Instrum. **68**, 3806 (1997).

[43] Y. Kondo, E. T. Foley, T. Amakusa, N. Shibata, M. Iwatsuki, and H. Tokumoto, Rev. Sci. Instrum. **72**, 2977 (2001).

[44] W. Cai, F. Pang, J. Wang, H. Liu, X. J. Liang, Q. K. Xue, , and D. M. Chen, Rev. Sci. Instrum. **78**, 065108 (2007).

[45] T. Mashoff, M. Pratzer, and M. Morgenstern, Rev. Sci. Instrum. **80**, 053702 (2009).

[46] O. Pietzsch, A. Kubetzka, M. Bode, and R. Wiesendanger, Science **292**, 2053 (2001).

[47] A. Wachowiak, J. Wiebe, M. Bode, O. Pietzsch, and R. Wiesendanger, Science **298**, 577 (2002).

[48] M. Bode, M. Heide, K. von Bergmann, P. Ferriani, S. Heinze, G. Bihlmayer, A. Kubetzka, O. Pietzsch, S. Blügel, and R. Wiesendanger, Nature **447**, 190 (2007).

[49] F. Meier, L. Zhou, J. Wiebe, and R. Wiesendanger, Science **320**, 82 (2008).

[50] L. Zhou, F. Meier, J. Wiebe, and R. Wiesendanger, Phys. Rev. Lett. **105**, 012409 (2010).

[51] D. Serrate, P. Ferriani, Y. Yoshida, S.-W. Hla, M. Menzel, K. von Bergmann, S. Heinze, A. Kubetzka, and R. Wiesendanger, Nature Nanotechnology **5**, 350 (2010).

[52] S. F. Alvarado and P. Renaud, Phys. Rev. Lett. **68**, 1387 (1992).

[53] W. Wulfhekel and J. Kirschner, Appl. Phys. Lett. **75**, 1944 (1999).

[54] O. Pietzsch, A. Kubetzka, M. Bode, and R. Wiesendanger, Phys. Rev. Lett. **92**, 057202 (2004).

[55] Omicron Nanotechnology GmbH, Taunusstein, Germany.

[56] M. Bode, S. Krause, L. Berbil-Bautista, S. Heinze, and R. Wiesendanger, Surf. Sci. **601**, 3308 (2007).

[57] Distributed by Omicron Nanotechnology GmbH, Taunusstein, Germany.

[58] J. Kirschner, H. Engelhard, and D. Hartung, Rev. Sci. Instrum. **73**, 3853 (2002).

[59] M. Volmer and A. Weber, Z. Phys. Chem. **119**, 277 (1926).

[60] Cryovac GmbH, Troisdorf, Germany.

[61] Scientific Magnetics, Abingdon, UK.

[62] Lake Shore Cryotronics Inc., Westerville, OH, USA.

[63] Isotec Kabel GmbH, Norderstedt, Germany.

[64] J. G. Hust, Rev. Sci. Instrum. **41**, 622 (1970).

[65] EBL Products Inc., East Hartford, CT, USA.

[66] M. E. Taylor, Rev. Sci. Instrum. **64**, 154 (1993).

[67] National Instruments, Austin, TX, USA.

[68] Nanonis GmbH, Zurich, Switzerland.

[69] Specs GmbH, Berlin, Germany.

[70] C. Liu and S. D. Bader, Phys. Rev. B **41**, 553 (1990).

[71] I. Horcas, R. Fernández, J. M. Gómez-Rodríguez, and J. Colchero, Rev. Sci. Instrum. **78**, 013705 (2007).

[72] M. Heide, Ph.D. thesis, RWTH Aachen (2006).

[73] M. Heide, G. Bihlmayer, P. Mavropoulos, A. Bringer, and S. Blügel, *Spin orbit driven physics at surfaces*, psi-k Newsletter **78**, Scientific Highlight of the Month, Forschungszentrum Jülich (2006).

[74] M. Bode, S. Heinze, A. Kubetzka, O. Pietzsch, X. Nie, G. Bihlmayer, S. Blügel, and R. Wiesendanger, Phys. Rev. Lett. **89**, 237205 (2002).

[75] S. Heinze, S. Blügel, R. Pascal, M. Bode, and R. Wiesendanger, Phys. Rev. B **58**, 16432 (1998).

[76] M. Bode, A. Kubetzka, S. Heinze, O. Pietzsch, R. Wiesendanger, M. Heide, X. Nie, G. Bihlmayer, and S. Blügel, J. Phys.: Condens. Matter **15**, 679 (2003).

[77] A. Montorsi, *The Hubbard Model* (World Scientific, Singapore, 1992).

[78] U. von Barth adn L. Hedin, J. Phys. C: Solid State Phys. **5**, 1629 (1972).

[79] M. M. Pant and A. K. Rajagopal, Solid State Commun. **10**, 1157 (1972).

[80] A. Kubetzka, P. Ferriani, M. Bode, S. Heinze, G. Bihlmayer, K. von Bergmann, O. Pietzsch, S. Blügel, and R. Wiesendanger, Phys. Rev. Lett. **94**, 087204 (2005).

[81] C. L. Gao, W. Wulfhekel, and J. Kirschner, Phys. Rev. Lett. **101**, 267205 (2008).

[82] M. Wasniowska, S. Schröder, P. Ferriani, and S. Heinze, Phys. Rev. B **82**, 012402 (2010).

[83] D. Hobbs and J. Hafner, J. Phys.: Condens. Matter **12**, 7025 (2000).

[84] D. Hobbs, G. Kresse, and J. Hafner, Phys. Rev. B **62**, 11556 (2000).

[85] A. H. MacDonald, S. M. Girvin, and D. Yoshioka, Phys. Rev. B **37**, 9753 (1988).

[86] T. A. Kaplan, Z. Phys. B.: Condens. Matter **49**, 313 (1983).

[87] T. Iwashita and N. Uryû, J. Phy. Soc. Japan **36**, 48 (1974).

[88] C. Timm, *Professor Bernhard Heß Lecture 2005*, http://www.physik.tu-dresden.de/˜timm/personal/Hess.html.

[89] I. E. Dzyaloshinskii, Sov. Phys. JETP **5**, 1259 (1957).

[90] I. Dzyaloshinskii, J. Phys. Chem. Solids **4**, 241 (1958).

[91] T. Moriya, Phys. Rev. **120**, 91 (1960).

[92] T. Moriya, Phys. Rev. Lett. **4**, 228 (1960).

[93] T. Thio, T. R. Thurston, N. W. Preyer, P. J. Picone, M. A. Kastner, H. P. Jenssen, D. R. Gabbe, C. Y. Chen, R. J. Birgeneau, and A. Aharony, Phys. Rev. B **38**, 905 (1988).

[94] D. Coffey, T. M. Rice, and F. C. Zhang, Phys. Rev. B **44**, 10112 (1991).

[95] L. Shekhtmann, O. Entin-Wohlmann, and A. Aharony, Phys. Rev. Lett. **69**, 836 (1992).

[96] N. E. Bonesteel, Phys. Rev. B **47**, 11302 (1993).

[97] A. Rouco, X. Obradors, M. Tovar, F. Perez, D. Chateigner, and P. Bordet, Phys. Rev. B **50**, 9924 (1994).

[98] D. A. Smith, J. Magn. Magn. Mater. **1**, 214 (1976).

[99] A. Fert and P. M. Levy, Phys. Rev. Lett. **44**, 1538 (1980).

[100] J. Hauschild, U. Gradmann, and H. J. Elmers, Appl. Phys. Lett. **72**, 3211 (1998).

[101] A. Kubetzka, O. Pietzsch, M. Bode, and R. Wiesendanger, Phys. Rev. B **63**, 1404071 (2001).

[102] H. J. Elmers, J. Magn. Magn. Mater. **185**, 274 (1998).

[103] I. E. Dzyaloshinskii, Sov. Phys. JETP **20**, 665 (1965).

[104] Y. A. Izyumov, Sov. Phys. Usp. **27**, 845 (1984).

[105] M. Abramowitz and I. M. Stegun, *Handbook of Mathematical Functions* (Dover Publications Inc., New York, 1965).

[106] L. Landau and E. Lifshitz, Phys. Z. Sowjetunion **8**, 153 (1935).

[107] H.-B. Braun, Phys. Rev. B **50**, 16485 (1994).

[108] A. Aharoni, *Introduction to the Theory of Ferromagnetism* (Clarendon Press, Oxford, 1996).

[109] P. Ferriani, K. von Bergmann, E. Y. Vedmedenko, S. Heinze, M. Bode, M. Heide, G. Bihlmayer, S. Blügel, and R. Wiesendanger, Phys. Rev. Lett. **101**, 027201 (2008).

[110] A. Hubert and R. Schäfer, *Magnetic Domains* (Springer, Berlin, Heidelberg, 1998).

[111] O. Pietzsch, A. Kubetzka, M. Bode, and R. Wiesendanger, Phys. Rev. Lett. **84**, 5212 (2000).

[112] *Crystal Data*, edited by J. D. H. Donnay and H. M. Ondik (National Bureau of Standards), Gaithersburg, MD, 1973.

[113] P. J. Berlowitz, J.-W. He, and D. W. Goodman, Surf. Sci. **231**, 315 (1990).

[114] M. Bode, K. von Bergmann, A. Kubetzka, O. Pietzsch, and R. Wiesendanger, J. Magn. Magn. Mater. **304**, 1 (2006).

[115] C. Jensen, K. Reshöft, and U. Köhler, Appl. Phys. A **62**, 217 (1996).

[116] H. Bethge, D. Heuer, C. Jensen, K. Reshöft, and U. Köhler, Surf. Sci. **331**, 878 (1995).

[117] J. Hauschild, H. J. Elmers, and U. Gradmann, Phys. Rev. B **57**, R677 (1998).

[118] H. J. Elmers, J. Hauschild, and U. Gradmann, J. Magn. Magn. Mater. **198**, 222 (1999).

[119] H. J. Elmers, J. Hauschild, and U. Gradmann, Phys. Rev. B **59**, 3688 (1999).

[120] K. von Bergmann, M. Bode, and R. Wiesendanger, J. Magn. Magn. Mater. **305**, 279 (2006).

[121] N. Weber, K. Wagner, H. J. Elmers, J. Hauschild, and U. Gradmann, Phys. Rev. B **55**, 14121 (1997).

[122] E. Y. Vedmedenko, private communication.

[123] A. Kubetzka, Ph.D. thesis, Universität Hamburg (2002).

[124] U. Gradmann, J. Korecki, and G. Waller, Appl. Phys. A **39**, 101 (1986).

[125] L. D. Barron, Chem. Soc. Rev. **15**, 189 (1986).

[126] CONTERGAN was produced by *Grünenthal GmbH, Aachen, Germany*. The victims of the tragedy are organised as *Bundesverband Contergangeschädigter e.V., Allmendingen, Germany*. The reader is referred to the publications from either side.

[127] M. Heide, G. Bihlmayer, and S. Blügel, Phys. Rev. B (R) **78**, 140403(R) (2008).

[128] W. H. Press, S. A. Teukolsky, W. T. Vetterling, and B. P. Flannery, *Numerical Recipes: The Art of Scientific Computing* (Cambridge University Press, Cambridge, 2007).

[129] Wolfram Research Inc., Mathematica Version 7.0, Champaign, IL (2007).

[130] M. Bode, A. Kubetzka, O. Pietzsch, and R. Wiesendanger, Appl. Phys. A **72**, 149 (2001).

[131] H. J. Elmers, J. Hauschild, H. Höche, U. Gradman, H. Bethge, D. Heuer, and U. Köhler, Phys. Rev. Lett. **73**, 898 (1994).

[132] P. Rhodes and G. Rowlands, Proc. Leeds Phil. Liter. Soc. **6**, 191 (1954).

[133] A. N. Bogdanov and D. A. Yablonskiî, Sov. Phys. JETP **68**, 101 (1989).

[134] U. K. Rößler, A. N. Bogdanov, and C. Pfleiderer, Nature **442**, 797 (2006).

[135] U. K. Rößler, A. A. Leonov, and A. N. Bogdanov, J. Phys.: Conf. Ser. **200**, 022029 (2010).

[136] S. D. Bader, Rev. Mod. Phys. **78**, 1 (2006).

[137] T. H. Skyrme, Proc. R. Soc. Lond. Ser. A **260**, 127 (1961).

[138] D. C. Wright and N. D. Mermin, Rev. Mod. Phys. **61**, 385 (1989).

[139] A. Bogdanov and A. Hubert, J. Magn. Magn. Mater. **138**, 255 (1994).

[140] S. D. Yi, S. Onoda, N. Nagaosa, and J. Han, Phys. Rev. B **80**, 054416 (2009).

[141] K. Nakamura, N. Mizuno, T. Akiyama, T. Ito, and A. J. Freeman, J. Appl. Phys. **101**, 09G521 (2007).

[142] K. Nakamura, T. Akiyama, and T. Ito, Appl. Surf. Sci. **256**, 1249 (2009).

[143] N. Mikuszeit, S. Meckler, R. Wiesendanger, and R. Miranda, in preparation.

[144] S. C. Hong and A. J. Freeman, Phys. Rev. B **38**, 12156 (1988).

[145] M. Bode, O. Pietzsch, A. Kubetzka, and R. Wiesendanger, Phys. Rev. Lett. **92**, 67201 (2004).

[146] S. Krause, G. Herzog, T. Stapelfeldt, L. Berbil-Bautista, M. Bode, E. Y. Vedmedenko, and R. Wiesendanger, Phys. Rev. Lett. **103**, 127202 (2009).

[147] S. Krause, L. Berbil-Bautista, G. Herzog, M. Bode, and R. Wiesendanger, Science **317**, 1537 (2007).

[148] G. Herzog, S. Krause, and R. Wiesendanger, Appl. Phys. Lett. **96**, 102505 (2010).

[149] M. V. Berry, Proc. Roy. Soc. London A **392**, 45 (1984).

[150] A. Shapere and F. Wilczek, *Geometric Phases in Physics* (World Scientific, Singapore, 1989).

[151] A. Bohm, A. Mostafazadeh, H. Koizumi, Q. Niu, and J. Zwanziger, *The Geometric Phase in Quantum Systems* (Springer, Berlin, 2003).

[152] Y. Aharonov and A. Stern, Phys. Rev. Lett. **69**, 3593 (1992).

[153] F. J. Huang, R. Qi, Y. D. Li, and W. M. Liu, Europhys. Lett. **79**, 10004 (2007).

[154] J. Ye, Y. B. Kim, A. J. Millis, B. I. Shraiman, P. Majumdar, and Z. Tešanović, Phys. Rev. Lett. **83**, 3737 (1999).

[155] P. Bruno, V. K. Dugaev, and M. Taillefumier, Phys. Rev. Lett. **93**, 096806 (2004).

[156] K. Ohgushi, S. Murakami, and N. Nagaosa, Phys. Rev. B **62**, R6065 (2000).

[157] Y. Taguchi, Y. Oohara, H. Yoshizawa, N. Nagaosa, and Y. Tokura, Science **291**, 2573 (2001).

[158] A. Neubauer, C. Pfleiderer, B. Binz, A. Rosch, R. Ritz, P. G. Niklowitz, and P. Böni, Phys. Rev. Lett. **102**, 186602 (2009).

[159] R. L. Wallace, Bell Syst. Tech. J. **30**, 1145 (1951).

[160] X. Lin, X. B. He, J. L. Lu, L. Gao, Q. Huan, D. X. Shi, and H. J. Gao, Chinese Phys. **14**, 1536 (2005).

Publications

- S. Meckler, M. Gyamfi, O. Pietzsch and R. Wiesendanger, *A low-temperature spin-polarized scanning tunneling microscope operating in a fully rotatable magnetic field*, Rev. Sci. Instrum. **80** 023708 (2009).
- S. Meckler, N. Mikuszeit, A. Preßler, E. Y. Vedmedenko, O. Pietzsch and R. Wiesendanger, *Real-space observation of a right-rotating inhomogeneous cycloidal spin spiral by spin-polarized scanning tunneling microscopy in a triple axes vector magnet*, Phys. Rev. Lett. **103**, 157201 (2009).
- S. Meckler, N. Mikuszeit, and R. Wiesendanger, *Spin spiral in Fe double layer on W(110): Experimental tunability of the spiral period*, in preparation.
- N. Mikuszeit, S. Meckler, R. Wiesendanger and R. Miranda, *Magneto-static self-energy and the sense of rotation of cycloidal spin spirals*, in preparation.

Conference contributions

Contributed talks

- 2008-07-17:
  S. Meckler, A. Preßler, M. Gyamfi, O. Pietzsch, and R. Wiesendanger
  Bloch or Néel-like walls in Fe double-layer nanowires
  NSS5/SP-STM2,
  Athens, Ohio (USA).

- 2008-07-23:
  S. Meckler, A. Preßler, M. Gyamfi, O. Pietzsch, and R. Wiesendanger
  Bloch or Néel-like walls in Fe double-layer nanowires
  International Conference on Nanoscience and Technology,
  Keystone, Colorado (USA)

- 2009-03-22:
  S. Meckler, A. Preßler, M. Gyamfi, O. Pietzsch, and R. Wiesendanger
  Right-rotating Néel-type domain walls in the Fe double-layer on W(110)
  73rd Spring Conference, Deutsche Physikalische Gesellschaft,
  Dresden (Germany).

Poster presentations

- 2009-09-20:
  Experimental Determination of the Dzyaloshinskii-Moriya Vector by Spin-Polarized Scanning Tunneling Microscopy in a Triple Axes Vector Magnet
  Nanostructures at Surfaces,
  Ascona (Switzerland).

Acknowledgements

Prof. Dr. Wiesendanger danke ich für seine Unterstützung in den vergangenen Jahren. Besonders hervorzuheben sind dabei die herausragenden Rahmenbedingungen in seiner Arbeitsgruppe, ohne die ein Laboraufbau in der beschriebenen Größenordnung und damit auch die in dieser Arbeit vorgestellten wissenschaftlichen Ergebnisse, nicht realisierbar gewesen wären. Ich wünsche ihm und all denen, die den neuen experimentellen Aufbau künftig nutzen werden, dass dieser eine ähnliche Fülle experimenteller Ergebnisse hervorbringen wird, wie die bereits in der Arbeitsgruppe existierenden Apparaturen, die für die neue Anlage in wesentlichen Punkten als Vorbild dienten.

Mein Dank geht besonders auch an *Dr. Oswald Pietzsch*, der mir in den vergangenen Jahren immer hilfreich zur Seite stand. Ihm verdanke ich eine umfangreiche und fundierte Ausbildung im Bereich Ultrahochvakuumtechnik und die Vermittlung vieler sehr hilfreicher handwerklicher Tricks. Darüber hinaus konnte ich sehr von seiner langjährigen Erfahrung mit spin-polarisierter Rastertunnelmikroskopie profitieren und mit meiner Arbeit an seine vorangehenden experimentellen Untersuchungen des Magnetismus in der Eisen-Doppellage auf W(110) anknüpfen. Unsere zahlreichen und oft auch hitzigen Diskussionen haben wesentlich zum Gelingen der vorliegenden Arbeit beigetragen.

Dr. Nikolai Mikuszeit danke ich für seine Unterstützung bei der mikromagnetischen Analyse der Messdaten. Ohne seine Unterstützung und sein Verständnis für meine anfangs nur unklar ausformulierten Analyseansätze gäbe es die mikromagnetischen Rechnungen in dieser Arbeit nicht. Seinen Umzug nach Madrid bedaure ich bis heute. Andererseits bin ich dankbar, dass ich vor seinem Umzug so viel von ihm lernen durfte, dass am Ende dann doch eine zufriedenstellende Analyse der Messdaten geglückt ist.

Besonders herausheben möchte ich an dieser Stelle auch die erstklassige Kooperation mit *Herrn Dr. Seifritz* bei der Planung und anschließenden Fertigung der Ultrahochvakuum-Anlage. Ihm danke ich ganz besonders für seine sehr qualifizierte Unterstützung bei der Konstruktion des Vakuumsystems. Ich werde die nahezu tägliche und sehr intensive Kooperation mit ihm während der vielleicht spannendsten und lehrreichsten Zeit meiner Doktorarbeit immer in bester Erinnerung behalten.

Herrn Dr. Krzyzowski und *Herrn Wolfram* danke ich neben ihrem Einsatz beim Bau des Magnetkryostatsystems vor allem für ihre Aufmerksamkeit in der Planungsphase. Ihnen ist es zu verdanken, dass ein wesentliches Problem bei der Integration des Magnetkryostaten und des Vakuumkammersystems frühzeitig genug erkannt wurde um gemeinsam eine zufriedenstellende Lösung zu finden, die sich im Praxistest sehr gut bewährt hat.

Mike Gyamfi bin ich vor allem dankbar für seine Geduld und seinen Einsatz beim Bau des Rasterunnelmikroskops. Das Mikroskop hat sich im Messbetrieb ausgesprochen gut bewährt. Besonders beeindruckt hat mich immer wieder die unglaubliche Robustheit und mechanische Stabilität des Mikroskops gegenüber äußeren Störungen. An dieser Stelle sei einmal ausdrücklich gesagt: Glückwunsch, das Teil ist gut gelungen!

Thomas Eelbo und *Anett Preßler* danke ich aus zwei Gründen. Zum einen war es die gute und kollegiale Zusammenarbeit mit ihnen, die den Betrieb des Labors und damit die Messungen für meine Doktorarbeit erst ermöglichte. Wichtiger ist aber der zweite Punkt. Wir drei mussten im Laboralltag zahlreiche herbe Rückschläge erleben, die wir letztendlich gemeinsam gemeistert haben. Beiden danke ich besonders für ihr Verständnis in Zeiten, wo bei mir die Nerven mehr blank lagen als bei ihnen.

Besonderen Dank schulde ich auch den Kolleginnen und Kollegen in der Feinmechanik- und der Elektronikwerkstatt. Ohne ihr handwerkliches Geschick, aber auch ihre Ideen und Erfahrungen wäre der Aufbau des neuen Labors undenkbar gewesen. Insbesondere möchte ich mich für die immer vorhandene Bereitschaft bedanken, im Notfall auch sehr kurzfristig mit anzupacken. Bei der Vielzahl der zu koordinierenden Projektschritte war es diese Flexibilität, die auch bei unvorhergesehenen Problemen immer eine reibungslose Zusammenarbeit aller Beteiligten ermöglichte.

Herrn Hatje und *Katrin Groth* danke ich für ihren unermüdlichen Einsatz für die ausreichende Bereitstellung von flüssigem Helium. Der hohe Verbrauch des neuen Magnetkryostaten stellte beide dabei vor so manche unlösbare Aufgabe, für die aber am Ende doch immer irgendwie eine Lösung gefunden wurde. Ich verstehe bis heute nicht, wie das manchmal ging, aber es hat funktioniert und war eine wertvolle Hilfe.

Nicht zuletzt möchte ich allen Doktoranden, Diplomanden, Postdocs und sonstigen Kollegen in unserer Arbeitsgruppe für eine lange gemeinsame Zeit danken, in der ich immer auf die Unterstützung aller zählen konnte. Besonders bedanken möchte ich mich vor allem für die vielen Schrauben, Muttern, Filamente, Kabel und sonstigen Kleinigkeiten, die ich von Kollegen ausleihen durfte und die mit der Zeit schliesslich in Dauerleihgaben umgewandelt wurden.

Die Jahre meiner Doktorarbeit waren für mich neben all den faszinierenden Erfahrungen auch von zahlreichen Rückschlägen und durch einige scheinbar aussichtslose Situationen geprägt. Es sind diese Momente, in denen auch Kollegen nicht mehr weiterhelfen können. Ich möchte mich deshalb zu guter Letzt ganz besonders bei meinen Eltern, meiner Schwester und meinen Freunden bedanken, die mir an den diversen Tiefpunkten der letzten Jahre immer gezeigt haben, dass es auch noch andere schöne Dinge im Leben gibt, neben Spinspiralen, Heliumtanks und Vakuumkammern.